



UNIVERSITY OF BIRMINGHAM

SYNTHESIS AND CHARACTERISATION OF δ -Bi₂O₃ RELATED MATERIALS STABILISED BY SUBSTITUTIONS OF Ca, Ga, Nb AND Re.

by

Maria Thompson

*A Thesis Submitted to
the College of Engineering and Physical Sciences
of the
University of Birmingham
for the degree of
DOCTOR OF PHILOSOPHY*

School of Chemistry,
University of Birmingham,
Edgbaston,
Birmingham,
B15 2TT
United Kingdom

June 2010

UNIVERSITY OF
BIRMINGHAM

University of Birmingham Research Archive

e-theses repository

This unpublished thesis/dissertation is copyright of the author and/or third parties. The intellectual property rights of the author or third parties in respect of this work are as defined by The Copyright Designs and Patents Act 1988 or as modified by any successor legislation.

Any use made of information contained in this thesis/dissertation must be in accordance with that legislation and must be properly acknowledged. Further distribution or reproduction in any format is prohibited without the permission of the copyright holder.

SYNOPSIS

The work reported in this thesis is based around substitutions into bismuth oxide, which has proven to be highly adaptable chemically as it can accommodate a wide variety of substituents. The synthesis and characterisation of stabilised δ -Bi₂O₃ related materials containing small amounts of Ca, Ga, Nb and Re are described. A body of work is presented exploring the structural and physical properties of such materials, characterised by neutron powder diffraction, X-ray powder diffraction, electron diffraction, extended X-ray absorption of fine structure measurements, differential thermal analysis and impedance spectroscopy.

The structure of two new fluorite-related materials, Bi₆Ca₃ReO_{15.5} and Bi₁₀Ca₅ReO_{23.5}, were studied. Bi₆Ca₃ReO_{15.5} formed a face-centred cubic (Fm $\bar{3}$ m) fluorite-related structure ($a = 5.416$ Å), and Bi₁₀Ca₅ReO_{23.5} a body-centred cubic (I $\bar{4}$ 3d) material ($a = 21.940$ Å) that is a 4 x 4 x 4 superstructure of the Bi₆Ca₃ReO_{15.5} phase. The structure of novel isostructural materials Bi₂₀Ca₇NbO_{39.5} and Bi_{10.75}Ca_{4.375}GaO₂₂ were also investigated. Both materials formed distorted δ -Bi₂O₃ related superstructures, derived as a monoclinic supercell (P2₁/m) based on a fluorite-related hexagonal subcell, where $a = 9.3334(4)$, $b = 3.7956(1)$, $c = 9.6195(3)$ Å, $\beta = 110.101(2)^\circ$ for Bi₂₀Ca₇NbO_{39.5} and $a = 9.3293(3)$, $b = 3.7943(1)$, $c = 9.6136(2)$ Å, $\beta = 110.084(2)^\circ$ for Bi_{10.75}Ca_{4.375}GaO₂₂. Detailed structural analysis and local environments of cations in the ordered monoclinic fluorite-related superstructure of Bi₉ReO₁₇ are also explored. In addition, the structural stability of each material is investigated. All materials synthesised in this thesis have structures related to that of δ -Bi₂O₃, which is known to have high oxide ion conducting properties at elevated temperatures. Oxide ion conducting properties are therefore also described.

To: My husband Scott and our daughter Leah.

ACKNOWLEDGEMENTS

First and foremost, I would like to express my sincere gratitude to my supervisor, Professor Colin Greaves, for his outstanding help and guidance during the course of my studies.

Heartfelt appreciation also goes to Professor Frank Berry, for his exceptional support and invaluable discussions.

I would also like to thank Dr Jenny Readman, Dr Louise Male and Dr Jackie Deans for their experimental support and guidance. Thanks go to Dr Emma Suard of the ILL, Grenoble, France for her assistance with neutron diffraction experiments, and Dr G Castro for his assistance in using Beamline 25 at ESRF, Grenoble, France. Thanks also go to Dr Jose Marco for his help not only obtaining EXAFS data, but also for assistance with data processing, and to Dr Tirma Herranz and Dr Benito Santos for their help with EXAFS collection. Furthermore, I would like to thank Dr Joke Hadermann of EMAT, University of Antwerp, Belgium, for her assistance in obtaining electron microscopy data.

Equipment used in this research was obtained/upgraded through the Science City Advanced Materials project: "Creating and Characterising Next Generation Advanced Materials", with support from Advantage West Midlands and part funded by the European Regional Development Fund.

Recognition must also go to my friends and colleagues on the 5th floor for their help and friendship, and to my family for their utmost support and encouragement.

Finally, I would like to thank EPSRC and the University of Birmingham for funding my PhD studentship.

CONTENTS

CHAPTER 1

Introduction

1.1	The Phases of Bismuth Oxide	1
1.1.1	α -Bi ₂ O ₃	2
1.1.2	β -Bi ₂ O ₃	4
1.1.3	δ -Bi ₂ O ₃	6
1.1.4	γ -Bi ₂ O ₃	10
1.2	Stabilisation of the High Temperature δ -Phase	11
1.3	Conductivity	13
1.4	Bismuth Oxides Containing Small Amounts of Rhenium	16
1.5	Bismuth Oxides Containing Small Amounts of Niobium	19
1.6	Bismuth Oxides Containing Small Amounts of Calcium	23
1.7	Aims	25
1.8	References	27

CHAPTER 2

Experimental Techniques

2.1	Materials Synthesis	31
2.2	Diffraction Techniques	32
2.2.1	X-ray Powder Diffraction	32
2.2.1.1	Instrumentation	35
2.2.1.1.1	Siemens D5000 Diffractometer	36
2.2.1.1.2	Bruker AXS D5005 Diffractometer	37
2.2.1.1.3	Bruker D8 Autosampler Diffractometer	39

2.2.2	Neutron Powder Diffraction	40
2.2.2.1	Instrumentation	42
2.2.2.1.1	D2b Neutron Powder Diffractometer	43
2.3	Rietveld Structural Refinement	44
2.4	Spectroscopic Techniques	47
2.4.1	Impedance Spectroscopy	47
2.4.1.1	Theory of Impedance Spectroscopy	48
2.4.1.2	Oxide Ion Conductivity Measurements	51
2.4.2	X-ray Absorption Spectroscopy	54
2.4.2.1	Extended X-ray Absorption of Fine Structure (EXAFS)	55
2.5	Differential Thermal Analysis (DTA)	58
2.6	Electron Microscopy	60
2.7	References	61

CHAPTER 3

The Structure, Ionic Conductivity and Local Environment of Cations in $\text{Bi}_9\text{ReO}_{17}$

3.1	Introduction	62
3.2	Experimental	64
3.3	Results and Discussion	64
3.3.1	The Structure of $\text{Bi}_9\text{ReO}_{17}$	64
3.3.2	Local Environment of Cations in $\text{Bi}_9\text{ReO}_{17}$	74
3.3.3	High Temperature Structural Studies of $\text{Bi}_9\text{ReO}_{17}$	81
3.3.4	Ionic Conductivity	95
3.4	References	100

CHAPTER 4

The Structure and Ionic Conductivity of Two New Fluorite Related Rhenium and Calcium doped Bismuth Oxide Materials, $\text{Bi}_6\text{Ca}_3\text{ReO}_{15.5}$ and $\text{Bi}_{10}\text{Ca}_5\text{ReO}_{23.5}$

4.1	Introduction	101
4.2	Experimental	102
4.3	Results and Discussion	103
4.3.1	The Structure of $\text{Bi}_6\text{Ca}_3\text{ReO}_{15.5}$	103
4.3.2	The Structure of $\text{Bi}_{10}\text{Ca}_5\text{ReO}_{23.5}$	107
4.3.3	Structural Changes in $\text{Bi}_{10}\text{Ca}_5\text{ReO}_{23.5}$	115
4.3.3.1	High Temperature Structural Studies of $\text{Bi}_{10}\text{Ca}_5\text{ReO}_{23.5}$	115
4.3.3.2	Thermal Stability of $\text{Bi}_{10}\text{Ca}_5\text{ReO}_{23.5}$	121
4.3.4	Ionic Conductivity	125
4.4	References	130

CHAPTER 5

The Structure and Ionic Conductivity of the Fluorite-Related Isostructural Materials $\text{Bi}_{20}\text{Ca}_7\text{NbO}_{39.5}$ and $\text{Bi}_{10.75}\text{Ca}_{4.375}\text{GaO}_{22}$

5.1	Introduction	131
5.2	Experimental	132
5.3	Results and Discussion	133
5.3.1	The Structure of $\text{Bi}_{20}\text{Ca}_7\text{NbO}_{39.5}$ and $\text{Bi}_{10.75}\text{Ca}_{4.375}\text{GaO}_{22}$	133
5.3.2	Thermal Stability	143
5.3.3	High Temperature Structural Studies of $\text{Bi}_{20}\text{Ca}_7\text{NbO}_{39.5}$	143
5.3.4	Ionic Conductivity	151
5.4	References	156

CHAPTER 6

Preliminary Studies of Bismuth-Niobium-Oxygen Solid Solutions

6.1	Introduction	157
6.2	Experimental	158
6.3	Results and Discussion	159
6.3.1	Solid Solution Range	159
6.3.2	Niobium-Rich Phase	165
6.3.3	Bismuth-Rich Phase	168
6.3.4	Structural Stability of Bi-Nb-O	171
6.3.4.1	High Temperature Structural Studies on $\text{Bi}_{14}\text{NbO}_{23.5}$	171
6.3.4.2	Structural Studies on $\text{Bi}_{13}\text{NbO}_{22}$	178
6.3.5	Ionic Conductivity	180
6.4	References	184

CHAPTER 7

Conclusions and Further Work	185
-------------------------------------	-----

Publications Arising from this Thesis	190
----------------------------------------------	-----

ABBREVIATIONS AND SYMBOLS

AC	Alternating Current
bcc	Body-centred cubic
DTA	Differential Thermal Analysis
E_a	Activation energy
EXAFS	Extended X-ray Absorption of Fine Structure
fcc	Face-centred cubic
GSAS	General Structure Analysis System
HREM	High Resolution Electron Microscopy
λ	Wavelength
NPD	Neutron Powder Diffraction
PSD	Position Sensitive Detector
R_p	Profile factor
R_{wp}	Weighted profile factor
σ	Conductivity
SAED	Selected Area Electron Diffraction
SOFC	Solid Oxide Fuel Cell
U_{iso}	Isothermal temperature factor
XAS	X-ray Absorption Spectroscopy
XPD	X-ray Powder Diffraction

CHAPTER 1

Introduction

Bismuth oxide has raised much interest for industrial applications over recent years, particularly in the fields of fuel cells and catalysis. The high temperature δ -Bi₂O₃ is the best known oxide ion conductor, with a conductivity of $\sim 1 \text{ } \Omega^{-1} \text{ cm}^{-1}$ at 1003 K, approximately two orders of magnitude higher than that of yttria stabilised zirconia, currently the favoured electrolyte in SOFCs. However its use is limited in such devices due to the instability to reduction at the anode.

1.1 The Phases of Bismuth Oxide

Bismuth oxide exists as four crystallographic polymorphs^{1,2}. The low temperature α form is monoclinic. It converts at 1002 K into the face-centred cubic δ form, which is stable up to the melting point at 1097 K. On cooling, large thermal hysteresis occurs and the metastable tetragonal β or body-centred cubic γ form can be obtained, depending on the cooling conditions, transforming to the β -phase at 923 K or the γ -phase at 912 K. On cooling, the β -phase transforms to the α -phase at 576 K, and the γ -phase at 773 K, although the γ -phase may persist to room temperature with slow cooling rates. The α -monoclinic and γ -bcc forms are semiconductors, whereas the β -tetragonal and δ -fcc forms are oxide ion conductors, the highest conductivity occurring with the δ -phase.

1.1.1 α -Bi₂O₃

The crystal structure of the monoclinic α -phase was first investigated by Sillen³ from Weissenberg photographs, determining the metal atom positions from Patterson analysis and the possible oxygen positions from space considerations. He was in this way able to determine the space group as P2₁/c. Malmros⁴, using single crystal X-ray diffraction, determined more information regarding the oxygen positions, suggesting those proposed by Sillen³ to be incorrect. The monoclinic structure was found to have a unit cell where $a = 5.8486(5)$ Å, $b = 8.166(1)$ Å, $c = 7.5097(8)$ Å, and $\beta = 113.00(1)^\circ$ ⁴. Later work by Harwig², using high temperature powder X-ray diffraction and neutron powder diffraction, confirmed the space group as P2₁/c, given by Sillen³ and Malmros⁴, and gave cell dimensions $a = 5.8496(3)$ Å, $b = 8.1648(4)$ Å, $c = 7.5101(4)$ Å, $\beta = 112.977(3)^\circ$. The structure consists of layers of bismuth ions, parallel to the [100] plane of the monoclinic unit cell, separated by layers of oxide ions, having an ordered defect fluorite structure with one quarter of the oxygen sites vacant^{2,5}. α -Bi₂O₃ has a distorted trigonal bipyramidal structure, where the lone pair of electrons share equatorial positions with two shorter Bi-O bonds, and two larger Bi-O bonds occupy the axial positions. The structure of α -Bi₂O₃ is shown in Figure 1.1, along with structural data in Table 1.1.

Table 1.1 Refined atomic parameters for α -Bi₂O₃.²

Site				
Atom	Symmetry	<i>x</i>	<i>y</i>	<i>z</i>
Bi1	4e	0.5242(6)	0.1843(4)	0.3615(4)
Bi2	4e	0.0404(5)	0.0425(4)	0.7767(4)
O1	4e	0.7783(8)	0.3037(5)	0.7080(7)
O2	4e	0.2337(8)	0.0467(5)	0.1266(6)
O3	4e	0.2658(7)	0.0294(6)	0.5115(6)

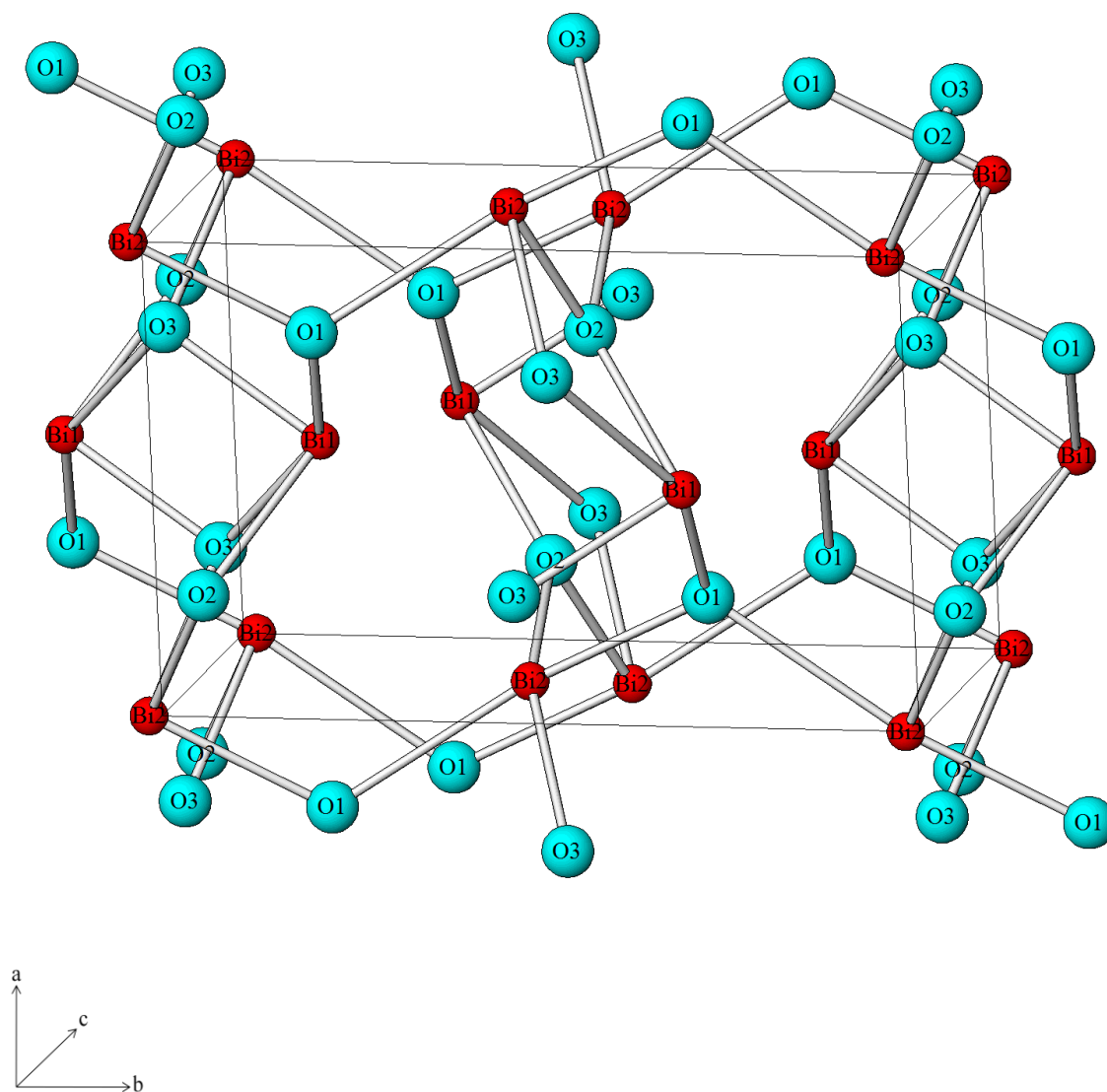


Figure 1.1 The structure of α -Bi₂O₃, determined by Harwig².

1.1.2 β -Bi₂O₃

The transition to the metastable β -Bi₂O₃, on cooling from the high temperature-phase, can occur at approximately 923 K¹. Sillen reported the formation of a tetragonal phase when super-cooling a Bi₂O₃ aerosol prepared by passing an O₂ stream over liquid bismuth metal³. He was able to determine the positions of the Bi atoms, and using space considerations was able to suggest possible positions for the O atoms, reporting the structure to belong to the space group $P\bar{4}b2$.

Using single crystal XPD Aurivillius and Malmros⁶ were able to determine the unit cell parameters and structure, showing the space group to be different to that suggested by Sillen³, suggesting space group $P\bar{4}2_1c$.

Harwig and Gerards¹ confirmed, using high temperature X-ray diffraction, that the β -phase is tetragonal, with cell dimensions $a = 7.738(3)$ Å and $c = 5.731(8)$ Å, at 916 K, supporting the work by Aurivillius and Malmros⁶. Further work by Harwig² revealed that the voids in the oxygen sublattice of the structure were ordered in the [001] direction.

Studies of β -Bi₂O₃, performed by Blower and Greaves⁷ by both XPD and NPD investigations, were able to definitely correct the structural data produced by Aurivillius and Malmros⁶, of which the model was found to have converged to a false minimum in the R factors. The structure was redetermined to have a tetragonal unit cell where $a = 7.741(3)$ Å and $c = 5.634(2)$ Å, space group $P\bar{4}2_1c$. Structural parameters for β -Bi₂O₃ are given in Table 1.2. The β -Bi₂O₃ structure is shown in Figure 1.2. The tetragonal structure displays pseudo trigonal bipyramidal coordination, with a lone pair of electrons occupying an equatorial position with two shorter bonds, and two longer bonds occupying the axial positions. This is shown in Figure 1.3.

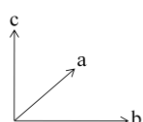
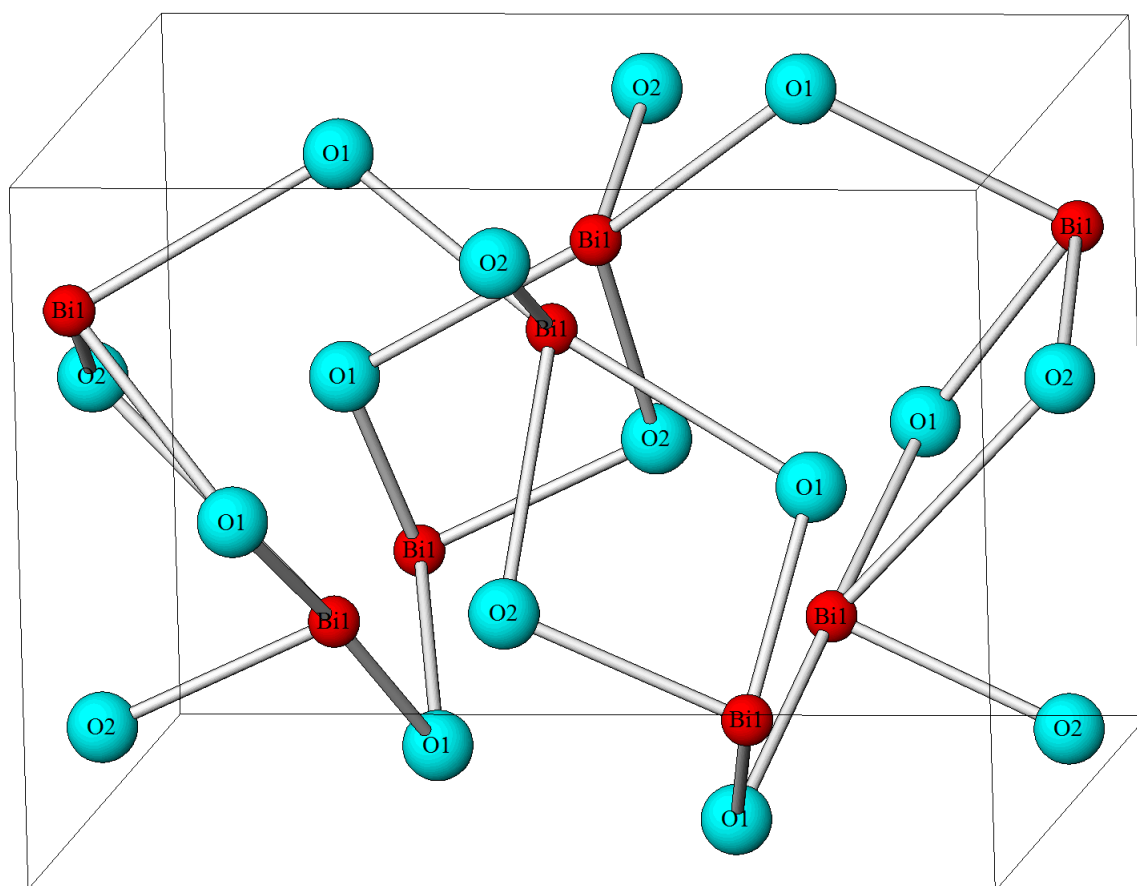


Figure 1.2 Unit cell for β - Bi_2O_3 determined by Blower and Greaves⁷.

Table 1.2 Atomic parameters for β - Bi_2O_3 determined by Blower and Greaves⁷.

Site					
Atom	Symmetry	x	y	z	$B / \text{\AA}^2$
Bi	8e	0.0174(5)	0.2545(4)	0.2385(6)	1.11(7)
O1	8e	0.2905(7)	0.3125(7)	0.0286(10)	1.71(11)
O2	4d	0	0.5	0.3939(11)	1.27(13)

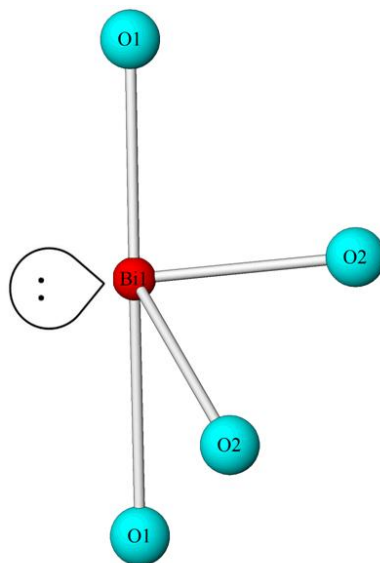


Figure 1.3 Diagram of BiO_4 trigonal bipyramidal coordination, with a lone pair of electrons occupying an equatorial position.

1.1.3 $\delta\text{-Bi}_2\text{O}_3$

When heated, the α -phase transforms at 1002 K to the face-centred cubic δ -phase, which is stable up to the melting point at 1097 K². The high temperature fluorite-related δ -phase of Bi_2O_3 was found to be an excellent oxide ion conductor and may be regarded as an anion deficient fluorite structure, where bismuth occupies the fcc sites, having a defect oxygen sublattice². The structure of this oxygen sublattice has caused controversy.

Sillen reported on a primitive cubic phase, space group $\text{Pn}\bar{3}\text{m}$, obtained by quenching Bi_2O_3 ³. This cubic structure is related to the fluorite structure but has ordered defects in the oxygen sublattice in the $[111]$ direction (Figure 1.4). Each Bi^{3+} ion has six oxygen neighbours arranged at six corners of a cube; two oxygens at diagonally opposite corners of the cube are missing.

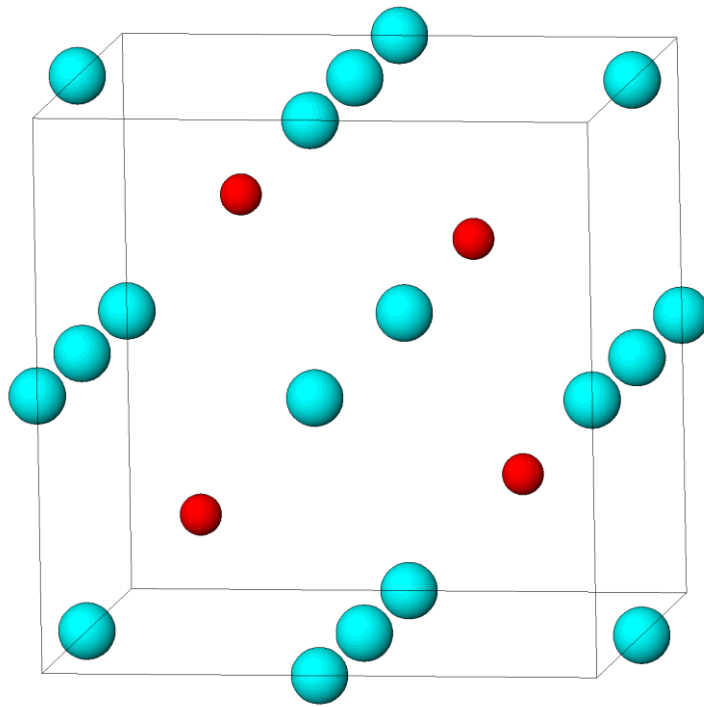


Figure 1.4 The Sillen model³, where the red spheres represent bismuth and the light blue represent oxygen.

The study by Gattow and Schröder⁸ into the δ -Bi₂O₃ system revealed by means of high-temperature X-ray powder diffraction that the δ -phase of Bi₂O₃ is face-centred cubic. They rejected the model of an ordered defect oxygen sublattice with defects in the [111] direction which had been proposed by Sillen³, and instead suggested that the structure was based upon the cubic CaF₂ structure with the space group Fm $\bar{3}$ m, illustrated in Figure 1.5. The cations occupied the 4*a* site and the oxygen atoms the 8*c* site with an average occupancy of 75% and a random distribution of vacancies⁸. The high oxide ion conductivity exhibited by δ -Bi₂O₃ is consistent with a structural model in which the oxide ion sites are 75% occupied in a statistical fashion^{2, 8}.

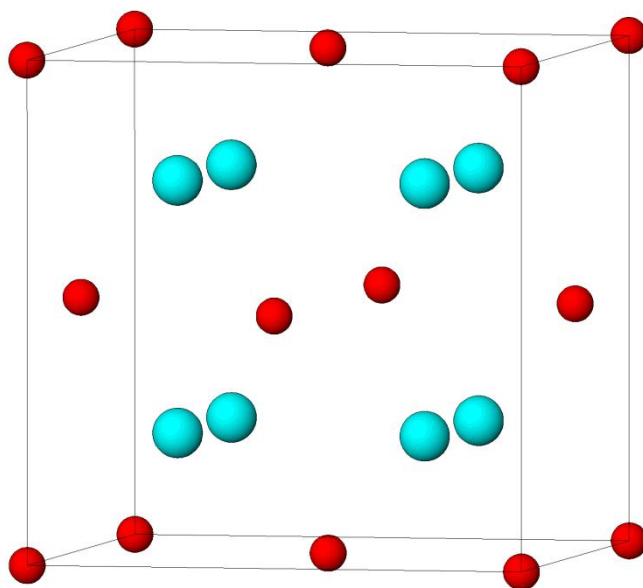


Figure 1.5 The Gattow and Schröder model⁸, where bismuth is represented by red spheres and oxygen represented by blue spheres.

Willis⁹ also proposed a model where the six oxygen atoms are randomly distributed along four of the $[111]$ directions from the regular tetrahedral sites towards the central octahedral vacant site, $32f$, of the $Fm\bar{3}m$ space group.

All three models are inconsistent with the observed experimental results, and consequently need modification to explain the complex structural changes. Studies performed by Battle *et al.*¹⁰ show the anion sublattice is a combination of the Gattow and Willis models (ie occupancy of both the $8c$ and $32f$ sites) and suggest the tendency for vacant oxygen sites to be arranged in a $[111]$ configuration around the Bi atoms, as the formation of a $[111]$ vacancy string is a well known feature of anion deficient fluorite materials. Refined atomic parameters from this NPD study, where $a = 5.648 \text{ \AA}$ space group $Fm\bar{3}m$, are given in Table 1.3, along with the structure of the unit cell in Figure 1.6.

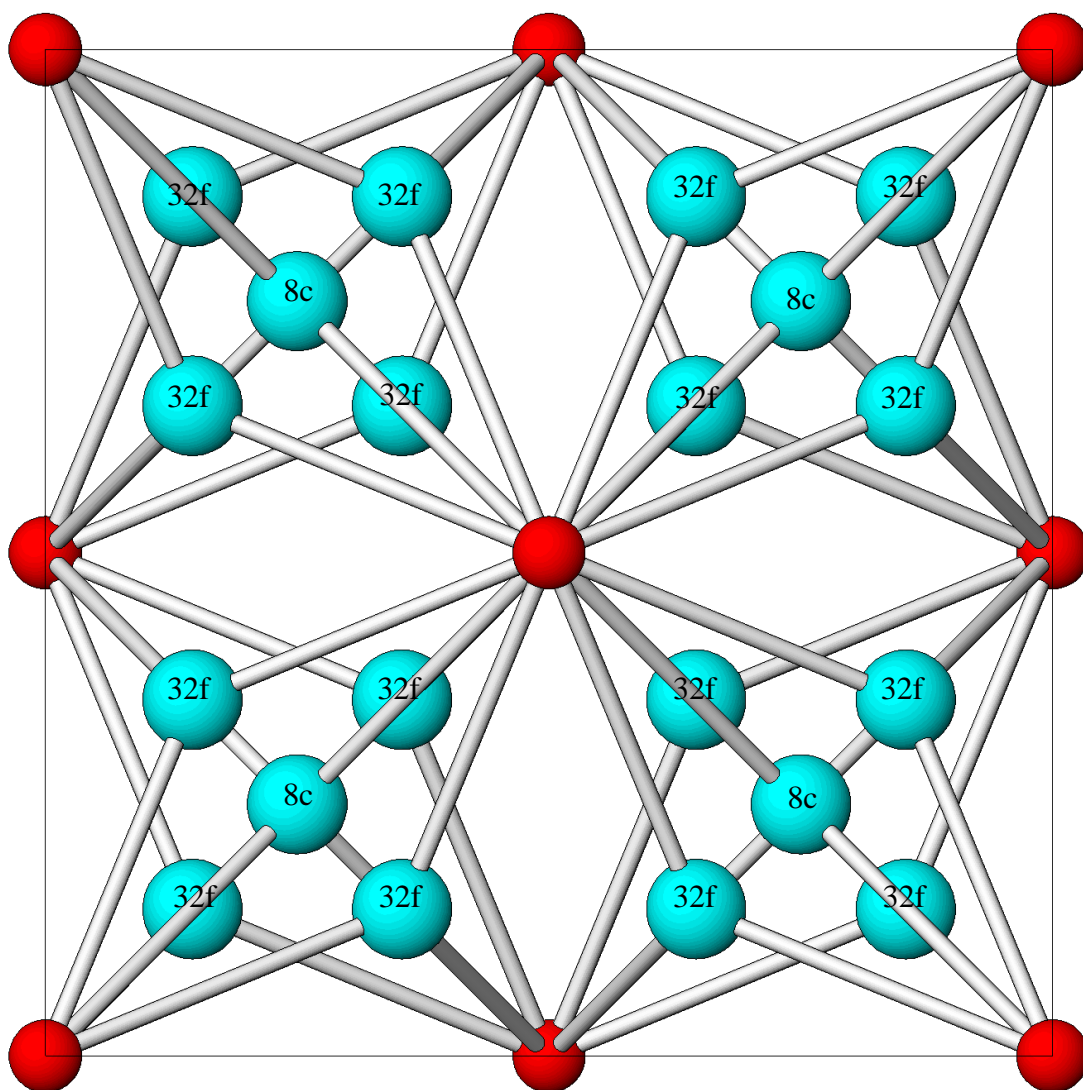


Figure 1.6 Unit cell for $\delta\text{-Bi}_2\text{O}_3$ ¹⁰, viewed along [100].

Table 1.3 Refined structural parameters for $\delta\text{-Bi}_2\text{O}_3$ ¹⁰.

Site						Fractional
Atom	Symmetry	x	y	z	$B / \text{\AA}^2$	Occupancy
Bi	4a	0	0	0	7.3(1)	1
O1	8c	0.25	0.25	0.25	11.8(7)	0.43(2)
O2	32f	0.354(3)	0.354(3)	0.354(3)	9.9(9)	0.08(1)

1.1.4 γ -Bi₂O₃

A transition to a metastable body centred cubic phase is also possible on cooling δ -Bi₂O₃, or from the melt, to 912 K¹. This phase is known as γ -Bi₂O₃, and can persist down to room temperature. Schumb and Rittner¹¹ were the first to prepare pure γ -Bi₂O₃. Levin and Roth¹² observed the bcc metastable phase at temperatures below 912 K, and compared with other compounds they were studying, found that γ -Bi₂O₃ had the larger unit cell. Harwig⁵ showed that γ -Bi₂O₃ had a cell dimension of 10.268(1) Å at room temperature, which was in good agreement with that suggested by Levin and Roth¹². The authors also found that γ -Bi₂O₃ was isomorphous with the system of Bi₁₂GeO₂₀, in the space group I 23, with BiO₄ tetrahedra located at (0, 0, 0) and (½, ½, ½) and BiO₃ groups which retain the cubic symmetry of the crystal. The structure of the unit cell and the atomic parameters of γ -Bi₂O₃ are given in Table 1.4 and Figure 1.7.

Table 1.4 Refined structural parameters for γ -Bi₂O₃⁵.

Site		Fractional			
Atom	Symmetry	<i>x</i>	<i>y</i>	<i>z</i>	Occupancy
Bi1	24f	0.858(2)	0.687(1)	0.972(1)	1
Bi2	2a	0	0	0	1
O1	24f	0.921(1)	0.738(2)	0.514(2)	0.975
O2	8c	0.716(2)	0.716(2)	0.716(2)	0.975
O3	8c	0.148(4)	0.148(4)	0.148(4)	0.975

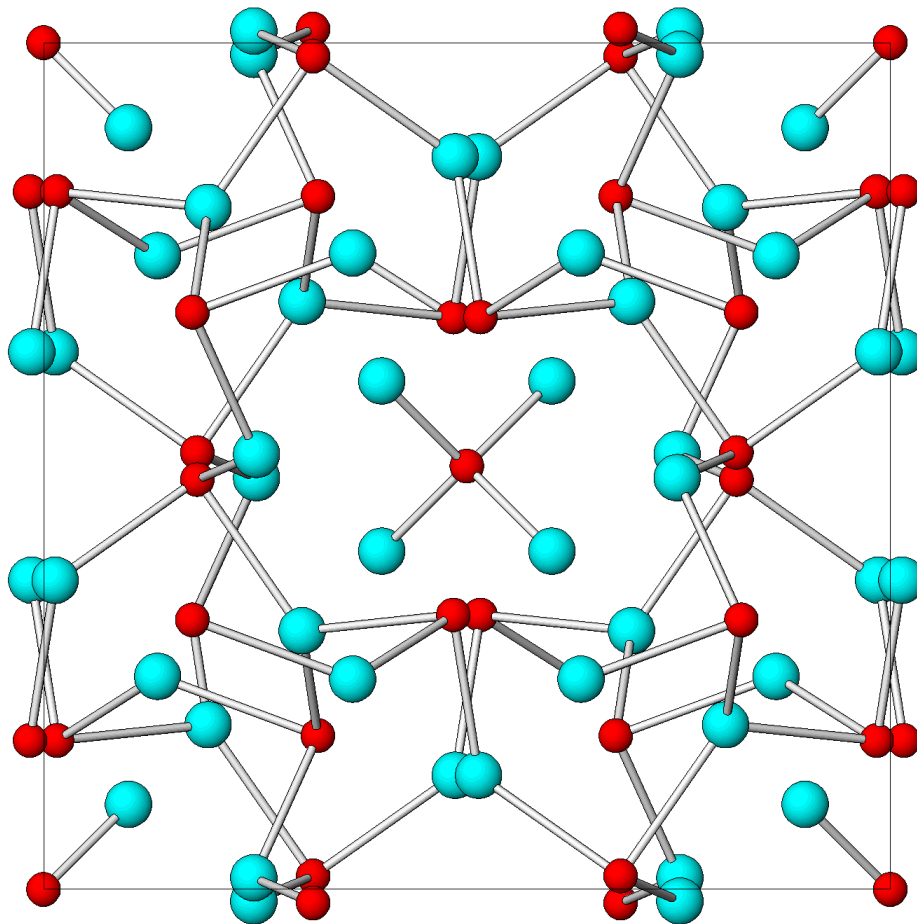


Figure 1.7 Unit cell for γ - Bi_2O_3 determined by Harwig⁵, viewed along $[100]$.

1.2 Stabilisation of the High Temperature δ -Phase

The high-temperature δ -form of bismuth oxide is recognised as one of the best solid state oxygen ion conductors¹³ and would be an interesting material for practical purposes, e.g. as a solid electrolyte in galvanic cells or in an oxygen sensor, if it could be obtained at lower temperatures without too much loss of its exceptionally high oxide ionic conductivity.

Although the pure phase cannot be quenched to room temperature, a variety of oxides have been claimed to be able to stabilise δ - Bi_2O_3 towards room temperature^{11-14,16-19} when

added to Bi_2O_3 as the minor component, forming binary oxides which often preserve a structure related to $\delta\text{-Bi}_2\text{O}_3$. However, these doped bismuth oxides show lower conductivity and undergo an order-disorder transition of the oxygen sublattice below 873 K, which leads to a decay in conductivity. This phenomenon is referred to as aging²⁰⁻²².

The use of rare earth ions as a dopant to stabilise bismuth oxide down to room temperature has been widely explored. They stabilise the high temperature fcc or rhombohedral phases to room temperature, depending on the cation type and dopant concentration. Iwahara *et al.*¹⁹ found that smaller rare earth ions were more effective in stabilising the δ -phase to room temperature, and the larger rare earth ions yielded the rhombohedral phase or a LaOF type structure. The stabilisation of bismuth oxide with rare earth ions has been comprehensively reviewed²³ and will not be discussed here in detail.

Isovalent and aliovalent dopants including Y, Ga, V, Nb, Ta and W have also been shown to stabilise $\delta\text{-Bi}_2\text{O}_3$, forming rhombohedral, fcc or tetragonal phases at room temperature^{11,16,17,23}. Table 1.5 shows the type of dopant and concentration range required to stabilise the fcc phase at low temperature¹³.

Table 1.5 fcc solid solution range at low temperatures¹³.

Dopant material	x
$(\text{Bi}_2\text{O}_3)_{1-x}(\text{Y}_2\text{O}_3)_x$	0.25-0.43
$(\text{Bi}_2\text{O}_3)_{1-x}(\text{Gd}_2\text{O}_3)_x$	0.35-0.50
$(\text{Bi}_2\text{O}_3)_{1-x}(\text{Nb}_2\text{O}_5)_x$	0.15-0.26
$(\text{Bi}_2\text{O}_3)_{1-x}(\text{Ta}_2\text{O}_5)_x$	0.20-0.25
$(\text{Bi}_2\text{O}_3)_{1-x}(\text{WO}_3)_x$	0.22-0.27

1.3 Conductivity

The conductivities of the α , β , γ and δ -phases were systematically measured by Harwig²⁴. The electrical conductivity of bismuth oxide increases by around four orders of magnitude at the $\alpha \rightarrow \delta$ transition at 1002 K. In the cooling direction, a hysteresis occurs and the transition to the intermediate β - and γ -phases are observed at about 80-90 K lower than 1002 K. This is shown in Figure 1.8.

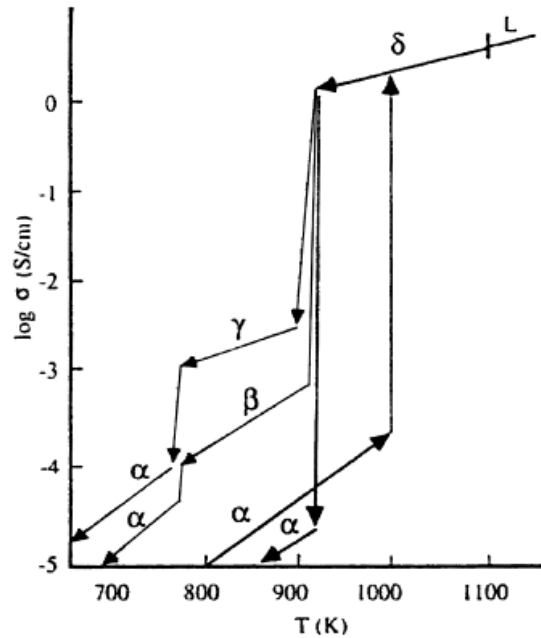


Figure 1.8 Electrical conductivity of Bi₂O₃ as a function of temperature²⁴.

δ -Bi₂O₃ has a conductivity of $\sim 1 \Omega^{-1} \text{ cm}^{-1}$ at 1003 K – one to two orders of magnitude higher than that of stabilised zirconia at this temperature – and owes its excellent oxide conductivity to the highly disordered oxygen sublattice. The conductivity of bismuth oxide

was initially discovered by Takahashi *et al.*²⁵, where it was shown that δ -Bi₂O₃ has the highest oxide ion conductivity of all oxide ion conductors known.

Recent computational simulations of δ -Bi₂O₃ performed by Yashima *et al.*²⁶ revealed that the oxygen sublattice has a complicated disorder. A diffusion mechanism was identified along the [111] directions where the oxide ions move along a path towards an empty octahedral site at the cube centre. However this minimum energy conduction pathway does not pass through the centre of this octahedron, but continues into a vacant neighbouring anion site. The pathway is made more energetically favourable by the presence of this empty octahedral site, creating displacement of the anions towards the central vacant site along the [111] direction²⁷. They therefore present complimentary results to those proposed by Koto *et al.*²⁸ based upon the β -PbF₂ material. Earlier investigations by Jacobs and Mac Donaill²⁹ support the concept of a [111] ordering of vacant anion sites and, whilst not precisely defining the structure of the oxygen sublattice, concluded that a [111] arrangement of vacancies is a realistic description of the lattice of δ -Bi₂O₃.

The use of δ -Bi₂O₃ as an oxide ion conductor is limited because it is only stable in the narrow temperature range of 1002-1097 K. As a consequence, cation substitution may be performed to stabilise the highly conductive δ form below the phase transition temperature. The conductivity as a function of dopant type and temperature has been studied widely, isovalent cations being the most extensively investigated (M=Y, Ln)^{10,13,19,30-33}. The addition of di-, tri-, penta- or hexavalent metal oxides in bismuth oxide result in conductive phases analogous to δ -Bi₂O₃ or a rhombohedral type phase. The oxide ion conductivity at 773 K of some typical solid electrolytes based on δ -Bi₂O₃ are given in Table 1.6¹³.

Table 1.6 The oxide ion conductivity at 773 K of solid electrolytes based on Bi_2O_3 ¹³.

Electrolyte	$\sigma / \Omega^{-1} \text{ cm}^{-1}$	Unit cell
$(\text{Bi}_2\text{O}_3)_{0.8}(\text{SrO})_{0.2}$	6.0×10^{-3}	rhombohedral
$(\text{Bi}_2\text{O}_3)_{0.8}(\text{BaO})_{0.2}$	1.1×10^{-2}	rhombohedral
$(\text{Bi}_2\text{O}_3)_{0.75}(\text{Y}_2\text{O}_3)_{0.25}$	1.3×10^{-2}	fcc
$(\text{Bi}_2\text{O}_3)_{0.65}(\text{Gd}_2\text{O}_3)_{0.35}$	3.5×10^{-3}	fcc
$(\text{Bi}_2\text{O}_3)_{0.85}(\text{Nb}_2\text{O}_5)_{0.15}$	1.1×10^{-2}	fcc
$(\text{Bi}_2\text{O}_3)_{0.8}(\text{Ta}_2\text{O}_5)_{0.2}$	5.0×10^{-3}	fcc
$(\text{Bi}_2\text{O}_3)_{0.78}(\text{MoO}_3)_{0.22}$	2.6×10^{-3}	tetragonal
$(\text{Bi}_2\text{O}_3)_{0.78}(\text{WO}_3)_{0.22}$	1.0×10^{-2}	fcc

The amount of dopant required to stabilise the $\delta\text{-Bi}_2\text{O}_3$ phase varies and the resultant conductivity varies greatly with dopant. Iwahara *et al.* found that an increase in dopant concentration led to a decrease in conductivity¹⁹. This can be related in part to the lower polarisability of the dopant cation compared to that of Bi^{3+} . Also, there is a tendency for the formation of small ordered microdomains around the dopant⁴ which increase with dopant concentration and lead to a reduction in the overall disorder of the materials, resulting in lowered conductivity³¹.

The conductivity of stabilised bismuth oxides decrease with aging. This may be partly attributed to phase transformation to lower symmetry, or from ordering of the oxygen sublattice in the $\delta\text{-Bi}_2\text{O}_3$ phase^{20,22,27}. Since ionic conductivity in these materials is dependent on random distribution of the oxygen ions between their regular 8c and interstitial 32f sites^{26,27}, displacement of oxygen ions from the 8c to 32f site, caused by the tendency for

alignment of oxygen vacancies in the [111] direction³⁴, will subsequently lead to a decrease in ionic conductivity.

1.4 Bismuth Oxides Containing Small Amounts of Rhenium

Previous studies in the $\text{Bi}_2\text{O}_3\text{-Re}_2\text{O}_7$ system have revealed several Bi-rich materials with fluorite-related crystal structures.

The structure of Bi_3ReO_8 , investigated by Cheetham and Smith, was shown to have cubic symmetry with $a = 11.590(1) \text{ \AA}$ ($a = 2 a_F$, where a_F is the cell parameter of the face-centred cubic fluorite subcell) and space group P2_13 ³⁵. The system, illustrated in Figure 1.9, contains an ordered array of ReO_4 tetrahedra in a distorted fluorite structure, with the major distortion from the ideal fluorite structure arising from the short Re-O bonds in the ReO_4 tetrahedra. These tetrahedra are rotated 40° about the [111] direction in order to accommodate the Bi lone pair activity.

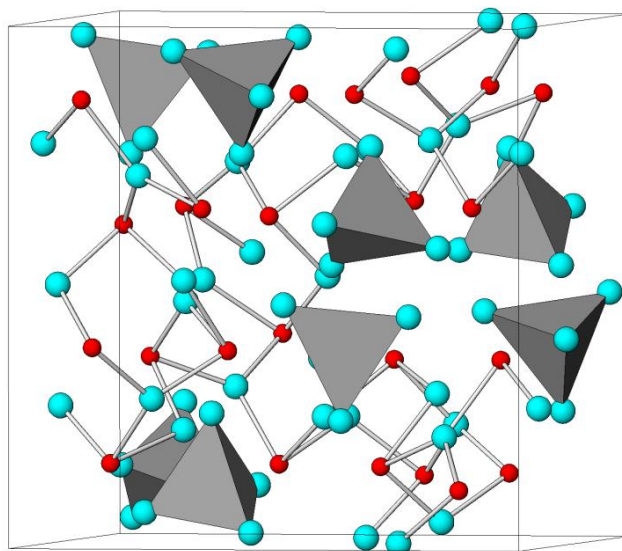


Figure 1.9 The structure of Bi_3ReO_8 ³⁵, where the red spheres represent Bi, the light blue spheres represent O and the ReO_4 tetrahedra are shown in grey.

Recently the structure of a new Bi-Re-O phase $\text{Bi}_9\text{ReO}_{17}$ has been resolved, which may be crystallographically related to $\text{Bi}_8\text{O}_{11}(\text{SO}_4)^{36}$, having fluorite-related monoclinic symmetry, where $a = 9.89917(5) \text{ \AA}$, $b = 19.70356(10) \text{ \AA}$, $c = 11.61597(6) \text{ \AA}$, $\beta = 125.302(2)^\circ$, space group $\text{P}2_1/\text{c}^{37}$. The system features clusters of ReO_4 tetrahedra embedded in a distorted Bi-O fluorite-like network and is thermodynamically stable at room temperature up to 998 K, above which it transforms to a distorted $\delta\text{-Bi}_2\text{O}_3$ like phase of cubic symmetry where $a = 5.7809(1) \text{ \AA}$, space group $\text{Fm}\bar{3}\text{m}$.

Crumpton *et al.* demonstrated that $\text{Bi}_{28}\text{Re}_2\text{O}_{49}$ also had a fluorite related superstructure, with tetragonal symmetry where $a = 8.7216(1) \text{ \AA}$, $c = 17.4177(2) \text{ \AA}$ and space group $\text{I}4/\text{m}^{38}$, having a structure related to that of $\text{Bi}_{14}\text{O}_{20}(\text{SO}_4)^{39}$. In contrast to previously reported phases containing MO_4^{2-} tetrahedral groups⁴⁰, $\text{Bi}_{28}\text{Re}_2\text{O}_{49}$ contains both octahedral and tetrahedral rhenium, and can be written as $\text{Bi}_{14}[(\text{ReO}_4)_{0.75}(\text{ReO}_6)_{0.25}]\text{O}_{20}$. The structure, shown in Figure 1.10, comprises an ordered framework of linked BiO_4 trigonal bipyramids and square pyramids with discrete Re oxoanions at the origin and body centre of the unit cell. The compound displayed relatively high conductivity ($5.4 \times 10^{-4} \Omega^{-1} \text{ cm}^{-1}$ at 673 K), despite its ordered structural framework. This may arise from oxide ion transfer between the tetrahedral ReO_4^- and octahedral ReO_6^{5-} units.

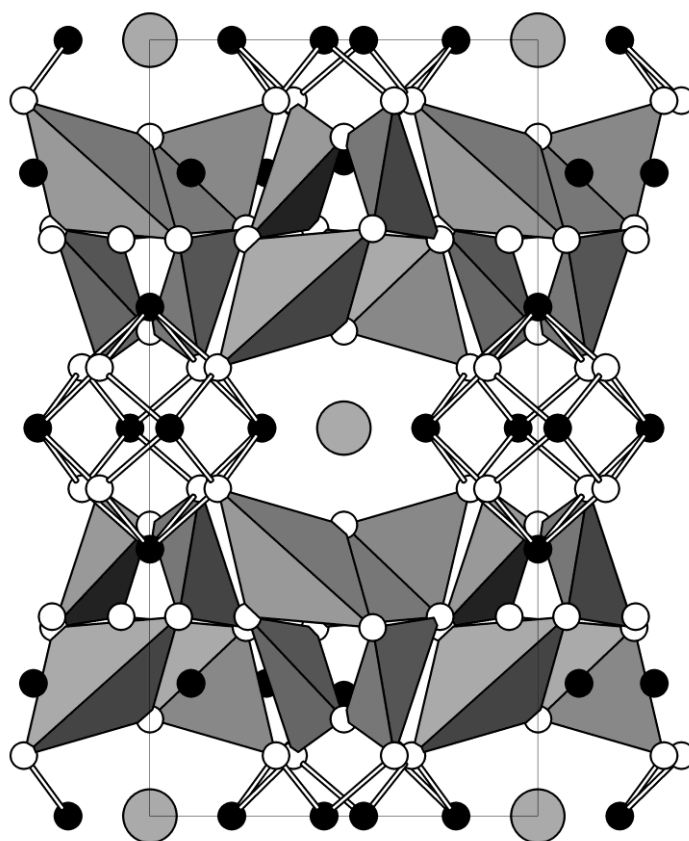


Figure 1.10 The structure of $\text{Bi}_{28}\text{Re}_2\text{O}_{49}$ ³⁸ projected along [100]. The BiO_4 trigonal bipyramidal polyhedra (grey) and square pyramids (Bi-O bonds indicated) are highlighted. The Re atoms are the large grey spheres and O atoms small open spheres (the O atoms bonded to Re are not shown).

Recently, a series of materials were synthesised by doubly doping Bi_2O_3 with both rhenium and a rare earth cation, forming $\text{Bi}_{12.5}\text{Ln}_{1.5}\text{ReO}_{24.5}$ ⁴¹ (i.e. replacing some of the Bi with Ln in $\text{Bi}_{28}\text{Re}_2\text{O}_{49}$). Observed conductivities were shown to be significantly higher than other stabilised $\delta\text{-Bi}_2\text{O}_3$ phases, with a reduction in the total amount of dopant required to stabilise the high temperature δ -phase at ambient temperature to around 16% (single substituents require $\sim 20 - 40\%$)^{13,42}. The $\delta\text{-Bi}_2\text{O}_3$ phase was also shown to be stabilised using even the largest lanthanides in this rhenium doped system, a phenomenon not previously observed. Structural analysis revealed these materials were of face-centred cubic

symmetry, space group $Fm\bar{3}m$, with the cations statistically distributed on the $4a$ (0, 0, 0) site and the oxygen atoms occupying their regular $8c$ ($\frac{1}{4}$, $\frac{1}{4}$, $\frac{1}{4}$) and displaced $32f$ (x , x , x) sites. The local environment of the cations in the erbium stabilised material $Bi_{12.5}Er_{1.5}ReO_{24.5}$ was recently reported⁴³. The Bi LIII- and Er LIII- edge EXAFS data revealed a high level of oxygen disorder and the Re LIII edge data endorsed the highly disordered nature of the oxygen system and showed rhenium to adopt four fold oxygen coordination and to be significantly different from that of the local environment of rhenium in $Bi_{28}Re_2O_{49}$.

Two further materials in the Bi_2O_3 - Re_2O_7 system have been identified by Fries *et al.*⁴⁴, those being $Bi_{39}ReO_{62}$ and $Bi_{19}ReO_{32}$. The structure of $Bi_{19}ReO_{32}$ is fluorite-related, with a $3 \times 3 \times 3$ superstructure from δ - Bi_2O_3 with a tetragonal subcell where $a = 5.503(5)$ Å and $c = 5.778(5)$ Å, and $Bi_{39}ReO_{62}$ is characterised by a $\sqrt{2} \times \sqrt{2} \times 1$ tetragonal supercell of β - Bi_2O_3 , where $a = 7.747(5)$ Å and $c = 5.641(5)$ Å.

1.5 Bismuth Oxides Containing Small Amounts of Niobium

In recent years, much research has been carried out into bismuth oxide materials doped with small amounts of niobium oxide, many yielding fluorite-type phases based on superlattice ordering of the cubic subcell of δ - Bi_2O_3 . Despite previously being designated a continuous solid solution with a fluorite structure, the complex structural chemistry of the Bi_2O_3 - Nb_2O_5 system, first studied by Roth and Waring⁴⁵, is of four types.

The first of these, designated a type I superstructure, is based upon the composition $15Bi_2O_3:Nb_2O_5$ and forms a $2 \times 2 \times 2$ body centred supercell based on the δ - Bi_2O_3 subcell, with Nb cations existing in isolated but ordered NbO_6 octahedral units^{46,47}. However, this

conclusion is questioned by Ling *et al.*⁴⁸, where the formation of a sillenite-related phase of composition $\text{Bi}_{12}\text{Nb}_{0.29}\text{O}_{18.7+x}$ is suggested, rather than fluorite-related.

Upon further addition of Nb_2O_5 , an incommensurate type II superstructure is formed, existing in the composition range from $12\text{Bi}_2\text{O}_3:\text{Nb}_2\text{O}_5$ to $4\text{Bi}_2\text{O}_3:\text{Nb}_2\text{O}_5$. Commensurate $11 \times 11 \times 11$ superstructures in $\text{Bi}_{17}\text{Nb}_3\text{O}_{33}$, $\text{Bi}_9\text{NbO}_{16}$, and an $8 \times 8 \times 8$ superstructure in $\text{Bi}_4\text{NbO}_{8.5}$ have been proposed by Tang *et al.*⁴⁶, derived from the $\delta\text{-Bi}_2\text{O}_3$ subcell. The Nb cations are believed to exist in some Nb_7O_{30} and $\text{Nb}_{18}\text{O}_{72}$ clusters in a partially ordered arrangement in the $\delta\text{-Bi}_2\text{O}_3$ matrix.

Castro *et al.*⁴⁹ demonstrated that Bi_3NbO_7 exhibits a defect fluorite type structure which crystallizes in the cubic system, space group $\text{Fm}\bar{3}\text{m}$, with unit cell parameter $a = 5.4788(9)$ Å, with electron microscopy studies confirming the presence of an incommensurate cubic F-lattice of type II. The system appears to show disorder in both the anionic and cationic lattices with 12.5% anion vacancies. Both cations are statistically distributed ($\text{Bi}:\text{Nb} = 3:1$) at the $4a$ site, with the oxygen atoms occupying the interstitial $48g$ site with an x coordinate $0.189(9)$ displaced slightly with respect to its normal value in CaF_2 ($8c$, $\frac{1}{4}$, $\frac{1}{4}$, $\frac{1}{4}$). The positional parameters for Bi_3NbO_7 are shown in Table 1.7, along with the structure in Figure 1.11.

Table 1.7 Structural parameters for Bi_3NbO_7 determined by Castro *et al.*⁴⁹.

Site		Fractional			
Atom	Symmetry	x	y	z	Occupancy
Bi	4a	0	0	0	0.75
Nb	4a	0	0	0	0.25
O	48g	0.189(9)	0.25	0.25	0.15

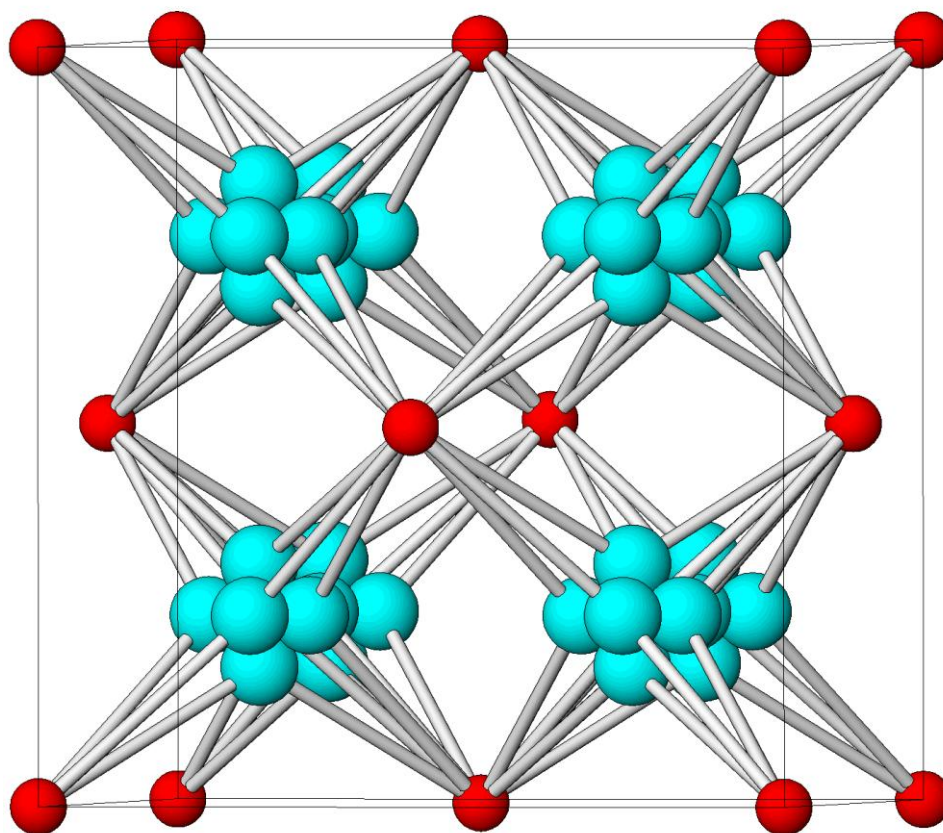


Figure 1.11 The structure of Bi_3NbO_7 ⁴⁹, where the red spheres represent the Bi/Nb site and the blue spheres represent oxygen.

The type III phase, with a composition of approximately $7\text{Bi}_2\text{O}_3:3\text{Nb}_2\text{O}_5$ is a layered fluorite-based phase, built up of fluorite, pyrochlore (strings of Nb atoms along [110] directions) and perovskite units⁴⁷.

Ling and Johnson have recently synthesized $\text{Bi}_{94}\text{Nb}_{32}\text{O}_{221}$ ⁵⁰, a slightly Nb rich composition of Bi_3NbO_7 , which comprises an ordered tetragonal cell with dimensions $a = 11.52156(18) \text{ \AA}$ and $c = 38.5603(6) \text{ \AA}$, space group $I\bar{4}m2$, displaying a type III structure. The structure, described as a hybrid of fluorite and pyrochlore types, consists of corner-

connected strings of NbO₆ octahedra along [110] directions of the δ -Bi₂O₃ subcell, and is shown in Figure 1.12. This work suggests that small differences in synthesis conditions can lead to a phase that shows significant tetragonal distortion of the cubic fluorite cell.

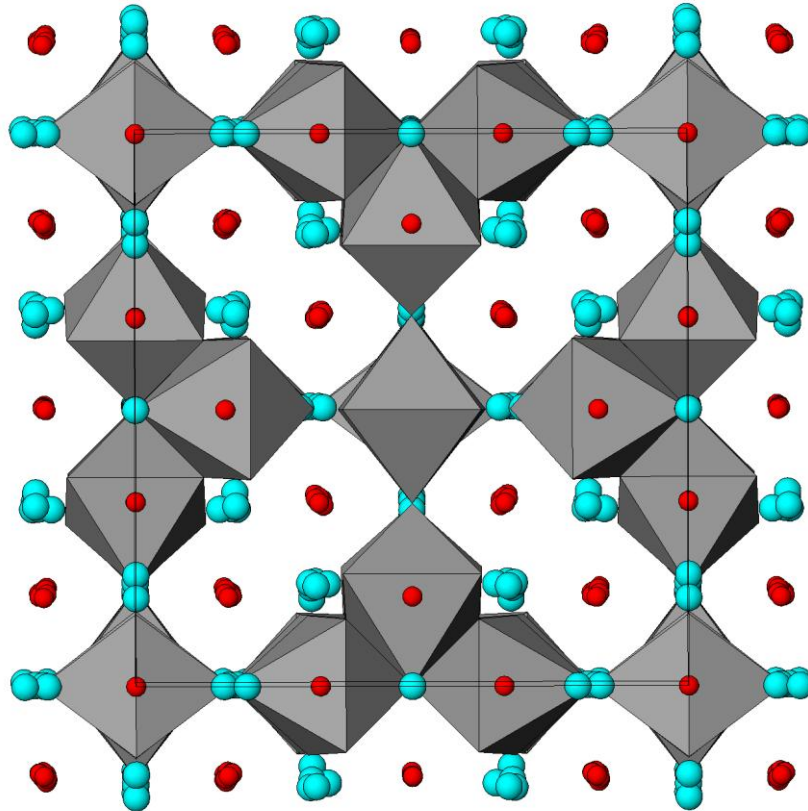


Figure 1.12 The structure of Bi₉₄Nb₃₂O₂₂₁⁵⁰, viewed along [110], where the red spheres represent Bi, the blue spheres represent O and the NbO₆ octahedra are shown in grey.

The remaining phase, designated Type IV, is centred at a composition 5Bi₂O₃:3Nb₂O₅. Bi₅Nb₃O₁₅ adopts a mixed layer Aurivillius-related phase structure with an orthorhombic cell, consisting of a [Bi₂O₂] + [NbO₄] + [Bi₂O₂] + [BiNb₂O₇] stacking sequence⁵¹.

Due to the fluorite-related structures of many of the $\text{Bi}_2\text{O}_3\text{-Nb}_2\text{O}_5$ materials, good oxide ion conductivity is observed. Table 1.8 displays the conductivities of several $\text{Bi}_2\text{O}_3\text{-Nb}_2\text{O}_5$ compositions at 773 K, along with corresponding activation energies^{13,49}.

Table 1.8 Conductivity at 773 K and activation energies for $\text{Bi}_2\text{O}_3\text{-Nb}_2\text{O}_5$ materials^{13,49}.

Composition	$\sigma / \Omega^{-1} \text{ cm}^{-1}$	E_a / eV
$(\text{Bi}_2\text{O}_3)_{0.85}(\text{Nb}_2\text{O}_5)_{0.15}$	1.1×10^{-2}	0.9
$(\text{Bi}_2\text{O}_3)_{0.78}(\text{Nb}_2\text{O}_5)_{0.22}$	2.3×10^{-4}	1.2
$(\text{Bi}_2\text{O}_3)_{0.75}(\text{Nb}_2\text{O}_5)_{0.25}$	4.2×10^{-4}	0.88
$(\text{Bi}_2\text{O}_3)_{0.70}(\text{Nb}_2\text{O}_5)_{0.30}$	2.3×10^{-5}	1.4

$\text{Bi}_2\text{O}_3\text{-Nb}_2\text{O}_5$ solid solutions have also been shown to serve as parent compounds for a range of solid solutions based upon substitution of either Bi^{3+} or Nb^{5+} by appropriate cations⁵²⁻⁵⁵, increasing the vacancy concentration. Oxide ion conductivity measurements of such doped compounds reveal that conductivity increases with the increased vacancy concentration introduced by substitution of suitable cations.

1.6 Bismuth Oxides Containing Small Amounts of Calcium

Doping of Bi_2O_3 with calcium to give $\text{Bi}_{1-x}\text{Ca}_x\text{O}_{1.5-x/2}$, where $0.12 < x < 0.18$, was found to result in the formation of a rhombohedral phase. The early work of Takahashi *et al.*²⁵ suggested this material to be a good ionic conductor, hence of considerable interest.

Aurivillius⁵⁷ initially investigated $\text{Bi}_2\text{O}_3\text{-CaO}$, suggesting that $\text{Bi}_{7.02}\text{Ca}_{1.98}\text{O}_{12.51}$ has a fluorite related structure, with hexagonal symmetry where $a = 3.92 \text{ \AA}$, $c = 27.84 \text{ \AA}$, crystallising in space group $R\bar{3}m$. The structure revealed that calcium was located every third close packed metal layer. However, this corresponds to a stoichiometry of $(\text{Ca/Bi})\text{O}_2$, hence a satisfactory description of the anion sublattice could not be established.

Boivin and Thomas⁵⁸ investigated $\text{Bi}_{0.87}\text{Ca}_{0.13}\text{O}_{1.435}$. Structural analysis suggested a rhombohedral material where $a = 3.950 \text{ \AA}$, $c = 27.87 \text{ \AA}$. The structure revealed layers of cations stacked along the c -axis with the sequence Bi-Bi-(Ca, Bi)-Bi-Bi-(Ca, Bi)-. Two kinds of oxide ions were detected inside the blocks consisting of a mixed layer surrounded by two Bi layers. The conduction properties were ascribed to the migration of the remaining anions in the space between two successive Bi layers. The authors also suggested⁵⁹, by means of single crystal XPD, the existence of conduction planes, and the preservation of the cation network.

Powder XPD and NPD investigations were conducted by Blower and Greaves⁶⁰, on a closely related phase $\text{Bi}_{0.824}\text{Ca}_{0.176}\text{O}_{1.412}$. Data proved incompatible with previous structural descriptions, with refinement suggesting a supercell of the simple rhombohedral cell, with monoclinic symmetry, where $a = 13.653(3) \text{ \AA}$, $b = 7.866(2) \text{ \AA}$, $c = 9.554(1) \text{ \AA}$, $\beta = 103.76(2)^\circ$, and space group $C2/m$. The structure comprises close packed layers of Ca/Bi atoms in distorted cubic 8-coordinate sites (2 being only partially occupied), separated by close packed layers of Bi atoms. The partially occupied anion layers are presumably responsible for the high oxide ion conductivity of this phase. The structure of $\text{Bi}_{0.824}\text{Ca}_{0.176}\text{O}_{1.412}$ is illustrated in Figure 1.13.

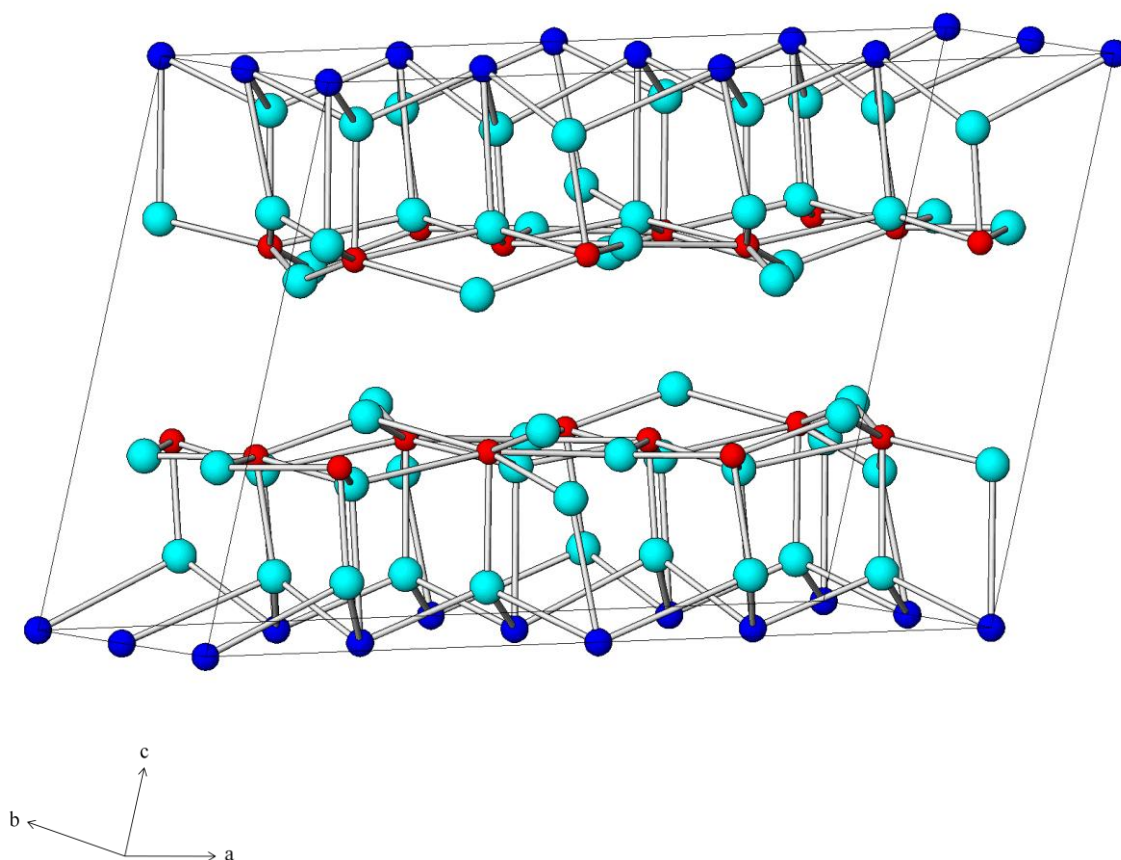


Figure 1.13 The structure of $\text{Bi}_{0.824}\text{Ca}_{0.176}\text{O}_{1.412}$, where the red spheres represent Bi sites, the dark blue spheres represent Bi/Ca shared sites and the light blue O.

1.7 Aims

The work reported in this thesis is concerned with the synthesis of new materials based around substitutions into bismuth oxide, which has proven to be highly adaptable chemically as it can accommodate a wide variety of substituents. The previously reported material $\text{Bi}_{28}\text{Re}_2\text{O}_{49}$ ³⁸ prompted these investigations, since new materials containing bismuth and small amounts of rhenium oxoanions could be synthesized. As a development of that work, further studies of the structural and conduction properties of other fluorite-related superstructures in

the bismuth-rich portion of the $\text{Bi}_2\text{O}_3\text{-Re}_2\text{O}_7$ phase diagram have been investigated, including the material of composition $\text{Bi}_9\text{ReO}_{17}$ which, when formed by quenching from high temperature, has been suggested⁴⁴ as containing both ReO_4 and ReO_6 environments similar to those observed in $\text{Bi}_{28}\text{Re}_2\text{O}_{49}$ ³⁸, although the actual ordered structure was not known at this time. However, during the course of this work the structure of $\text{Bi}_9\text{ReO}_{17}$ was described³⁷. Hence the structural characterisation of $\text{Bi}_9\text{ReO}_{17}$, together with the results of an examination of the local environments of the cations, is reported. The structural description is slightly different to that previously given³⁷ and emphasises the preferred stereochemical preference of Bi^{3+} .

It was also intended to use solid state reactions between bismuth, rhenium and other suitable reagents to synthesize new materials and investigate the structure and physical properties of any single-phase products. Substitution of Bi in Bi-Re-O for a 2+ cation would create a charge discrepancy that would be compensated by temperature independent extrinsic oxygen vacancies. Importantly, the 2+ cation must give discrete metal exchange to maintain the overall fluorite structure. Since Ca^{2+} has similar ionic radius⁶¹ to Bi^{3+} , studying the effect of doping bismuth oxide with both Re and Ca could achieve interesting results. The substitution of rhenium by other transition metals has also been studied, since structures related to that of $\text{Bi}_{28}\text{Re}_2\text{O}_{49}$ ³⁸ can also be achieved with S, W, Mo and Cr⁴⁰.

Detailed structural analysis of all single-phase products has been undertaken. Any phase changes occurring at different temperatures were additionally investigated. With previous observations of high oxide ion conductivity in bismuth oxide based materials^{38,41}, oxide ion conductivity measurements were also performed.

1.8 References

- 1 Harwig, H. A.; Gerards, A. G. *Thermochim. Acta* **28** (1979) 121
- 2 Harwig, H. A. *Z. Anorg. Chem.* **444** (1978) 151
- 3 Sillen, L. G. *Ark. Kemi Mineral. Geol.* **12A** (1937) 1
- 4 Malmros, G. *Acta. Chem Scand.* **24** (1970) 384
- 5 Harwig, H. A. *Z. Anorg. Chem.* **444** (1978) 167
- 6 Aurivillius, B.; Malmros, G. *Trans. Roy. Inst. Technol. Stockholm* **291** (1972) 544
- 7 Blower, S. K.; Greaves, C. *Acta Cryst.* **C44** (1988) 587
- 8 Gattow, G.; Schutze, D. *Z. Anorg. Allg. Chem.* **328** (1964) 44
- 9 Willis, B. T. M. *Acta. Cryst.* **18** (1965) 75
- 10 Battle, P. D.; Catlow, C. R. A.; Drennan, J.; Murray, A. D. *J. Phys. C* **16** (1983) L561
- 11 Schumb, W. C.; Rittner, E. S. *J. Am. Chem Soc.* **65** (1943) 1055
- 12 Levin, E. M.; Roth, R. S. *J. Res. N. B. S. A Physics and Chem.* **68A** (1964) 197
- 13 Takahashi, T.; Iwahara, H. *Mat. Res. Bull.* **13** (1978) 1447
- 14 Gattow, G.; Schroder, H. *Z Anorg. Allg. Chem.* **318** (1962) 176
- 15 Radaev, S. F.; Simonov, V. I.; Kargin, Y. F. *Acta. Cryst.* **B48** (1992) 604
- 16 Takahashi, T.; Iwahara, H. J.; Arao, T. *J. Appl. Electrochem.* **5** (1975) 187
- 17 Takahashi, T.; Iwahara, H. J.; Esaka, T. *J. Electrochem. Soc.* **124** (1977) 1563
- 18 Verkerk, M. J.; Keizer, K.; Burggraaf, A. J. *J. Appl. Electrochem.* **10** (1980) 81
- 19 Iwahara, H. J.; Esaka, T.; Takahashi, T.; *J. Solid State Chem.* **39** (1981) 173
- 20 Jiang, N.; Wachsman, E. D.; *J. Am. Ceram. Soc.* **82** (1999) 3057
- 21 Wachsman, E. D.; Boyapati, S.; Kaufman, M. J.; Jiang, N. *J. Am. Ceram. Soc.* **83** (2000) 1964

- 22 Wachsman, E. D.; Jiang, N.; Buchanan, R. M.; Hen, F. E. G.; Marshall, A. F.; Stevenson, D. A. *Mat. Res. Bull.* **29** (1994) 247
- 23 Sammes, N. M.; Tompsett, G. A.; Näfe, H.; Aldinger, F. *J. Eur. Ceram. Soc.* **19** (1999) 1801
- 24 Harwig, H. A.; Gerards, A. G. *J. Solid State Chem.* **26** (1978) 265
- 25 Takahashi, T.; Iwahara, H. *J. Appl. Electrochem.* **2** (1972) 97
- 26 Yashima, M.; Ishimura, D. *Chem. Phys. Letters* **378** (2003) 395
- 27 Boyapati, S.; Wachsman, E. D.; Jiang, N. *Solid State Ionics* **140** (2001) 149
- 28 Koto, K.; Schultz, H.; Huggins, R. A. *Solid State Ionics* **1** (1980) 355
- 29 Jacobs, P. W. M.; Mac Donall, D. A. *Solid State Ionics* **23** (1987) 279
- 30 Battle, P. D.; Catlow, C. R. A.; Heap, J. W.; Moroney, L. M. *J. Solid State Chem.* **63** (1986) 8
- 31 Verkerk, M. J.; Burggraaf, A. J. *J. Electrochem. Soc.* **128** (1981) 75
- 32 Verkerk, M. J.; Van de Velde, G. M. H.; Burggraaf, A. J. *J. Phys. Chem. Solids* **43** (1982) 1129
- 33 Battle, P. D.; Catlow, C. R. A.; Moroney, L. M. *J. Solid State Chem.* **67** (1987) 42
- 34 Boyapati, S.; Wachsman, E. D.; Chakoumakos, B. C. *Solid State Ionics* **138** (2001) 293
- 35 Cheetham, A. K.; Rae Smith, A. R.; *Acta. Cryst.* **B41** (1985) 225
- 36 Crumpton, T. E.; Greaves, C. *J. Mat. Chem.* **14** (2004) 2433
- 37 Sharma, N.; Withers, R. L.; Knight, K. S.; Ling, C. D. *J. Solid State Chem.* **182** (2009) 2468
- 38 Crumpton, T. E.; Mosselmans, J. F. W.; Greaves, C. *J. Mater. Chem.* **15** (2005) 164
- 39 Francesconi, M. G.; Kirbyshire, A. L.; Greaves, C.; Richard, O.; Van Tendeloo, G. *Chem. Mater.* **10** (1998) 626

- 40 Crumpton, T. E.; Francesconi, M. G.; Greaves, C. J. *Solid State Chem.* **175** (2003) 197
- 41 Pun, R.; Feteira, A. M.; Sincliar, D. C.; Greaves, C. J. *Am. Chem. Soc.* **128** (2006) 15386
- 42 Jiang, N.; Wachsman, E. D.; Jung, S. H. *Solid State Ionics* **150** (2002) 347
- 43 Pun, R.; Gameson, I.; Berry, F.; Greaves, C. J. *Phys. Chem. Solids* **69** (2008) 2687
- 44 Fries, T.; Lang, G.; Kemmler-Sack, S. *Solid State Ionics* **89** (1996) 233
- 45 Roth, R. S.; Waring, T. L. *J. Res. Nat. Bur. Stand.* **A66** (1962) 451
- 46 Tang, D.; Zhou, W.; *J. Solid State Chem.* **119** (1995) 311
- 47 Zhou, W.; Jefferson, D. A.; Thomas, J. M. *J. Solid State Chem.* **70** (1987) 129
- 48 Ling, C. D.; Withers, R. L.; Schmid, S.; Thompson, J. G. *J. Solid State Chem* **137** (1998) 42
- 49 Castro, A.; Aguado, E.; Rojo, J. M.; Herrero, P.; Enjalbert, R.; Galy, J. *Mat. Res. Bull.* **33** (1998) 31
- 50 Ling, C. D.; Johnson, M. *J. Solid State Chem.* **177** (2004) 1838
- 51 Tahara, S.; Shimada, A.; Kumada, N.; Sugahara, Y. *J. Solid State Chem.* **180** (2007) 2517
- 52 Krok, F.; Abrahams, I.; Wrobel, W.; Chan, S. C. M.; Kozanecka, A.; Ossowski, T.; Dygas, J. R. *Solid State Ionics* **175** (2004) 335
- 53 Abrahams, I.; Kozanecka-Szmigiel, A.; Krok, F.; Wrobel, W.; Chan, S. C. M.; Dygas, J. R. *Solid State Ionics* **177** (2006) 1761
- 54 Abrahams, I.; Krok, F.; Wrobel, W.; Kozanecka-Szmigiel, A.; Chan, S. C. M.; *Solid State Ionics* **179** (2008) 2
- 55 Krok, F.; Abrahams, I.; Holdynski, M.; Kozanecka-Szmigiel, A.; Malys, M.; Struzik, M.; Liu, X.; Dygas, J. R. *Solid State Ionics* **179** (2008) 975

- 56 Yudin, A. N.; Pobedinskaya, E. A.; Terent'eva, L. E.; Petrova, I. V.; Kaplunnik, L. N.; Malakhova, G. V. *Izvestiya Akademii Nauk SSSR, Neorganicheskie Materialy* **25** (1989) 1715
- 57 Aurivillius, B. *Ark. Kemi Mineral. Geol.* **16A** (1943) 1
- 58 Boivin, J. C.; Thomas, D. J. *Solid State Ionics* **3/4** (1981) 457
- 59 Boivin, J. C.; Thomas, D. J. *Solid State Ionics* **5** (1981) 523
- 60 Blower, S. K.; Greaves, C. *Mat. Res. Bull.* **23** (1988) 765
- 61 Shannon, R. D. *Acta. Cryst.* **A32** (1976) 751

CHAPTER 2

Experimental Techniques

2.1 Materials Synthesis

Materials prepared in this thesis were synthesised using conventional solid state techniques, whereby intimately ground mixtures of high purity powdered reagents in stoichiometric quantities were heated at elevated temperatures to promote a solid state reaction.

High temperatures are required for synthesis as a large input of energy is needed to overcome the large lattice energy which tends to characterise these materials, and thereby facilitate a cation to leave its position within the lattice and diffuse to a different site. In order for the reaction to occur in the solid state it was necessary, during reactant heating cycles, not to exceed the melting point of bismuth oxide of 1097 K. The experimental procedure involved regrinding between heating cycles to ensure the formation of a homogeneous product, since solid state reactions take place at the interface, impeding diffusion. It was therefore crucial that starting materials were well ground to give a small particle size, and were well mixed to maximise the surface contact area and minimise the distance of diffusion.

Specific synthesis details are given in the Chapters that follow, as individual materials are discussed.

2.2 Diffraction Techniques

The materials discussed in this thesis were characterised using two types of crystal diffraction technique, X-ray powder diffraction XPD, and neutron diffraction, NPD.

When a finely ground crystalline powder, with its regularly repeating structure, is placed in the path of an X-ray or neutron beam, diffraction will occur. The Laue equations and Bragg's Law, which describe how diffraction occurs in a crystal, are well documented and will not be discussed here in detail^{1,2}.

2.2.1 X-ray Powder Diffraction

XPD was used for the preliminary investigation of all the materials synthesised to obtain phase and structure identification.

X-rays are electromagnetic radiation of wavelength $\sim 1 \text{ \AA}$ and are produced when high-energy electrons, typically 30 kV, are bombarded at a metal target which is usually made of copper. The resulting X-ray spectrum consists of white radiation, which is a broad spectrum of wavelengths, and a number of fixed, monochromatic wavelengths. White radiation arises when collision with the copper atoms slow or even stop the electrons, with the excess energy being radiated as X-radiation. Normally in X-ray diffraction monochromatic radiation is required. When the electron beam strikes the metal target the incident electrons have sufficient energy to ionise a Cu 1s electron, leaving a hole. This vacancy is in turn filled by an electron descending from the shell above (2p or 3p) with the energy released appearing as monochromatic X-radiation. Electrons descending from the 2p and 3p produce Cu K_α ($\lambda = 1.5418 \text{ \AA}$) and less intense Cu K_β ($\lambda = 1.3922 \text{ \AA}$) radiation respectively. The more

intense Cu K_α is used in diffraction experiments. As the $2p \rightarrow 1s$ transition has a slightly different energy for the 2 spin states of 2p, the K_α line is split as a doublet with Cu $K_{\alpha 1}$ ($\lambda = 1.5406 \text{ \AA}$) and Cu $K_{\alpha 2}$ ($\lambda = 1.5443 \text{ \AA}$). The more intense Cu $K_{\alpha 1}$ radiation can be selected for diffraction experiments using a monochromator, such as Ge, which filters out the unwanted radiation. When a sample of finely ground crystalline powder, orientated randomly in a sample holder, is placed in the path of a monochromatic X-ray beam, diffraction occurs from the lattice planes in the crystallites which are ordered in the correct orientation to fulfil the Bragg condition.

In order to solve crystal structures, quantitative measurements of intensity are necessary. As the intensity of these diffracted beams depends on the atoms type and positions within a unit cell, structural information is provided by the resultant diffraction pattern. The intensity of a diffracted beam, I_{hkl} , may be expressed as:

$$I_{hkl} \propto F_{hkl}^2 mALP$$

Equation 2.1

- F_{hkl} = structure factor

The structure factor contains information about the amplitude and phase of scattered X-ray waves from all atoms of a crystal plane hkl, thus providing the most important source of information extracted from the sample and having the most influence upon the intensity of the diffracted beam. It can be expressed mathematically as:

$$F_{hkl} = \sum_n f_n p_n \exp[2\pi i(hx_n + ky_n + lz_n)] \exp\left[-\frac{B_n \sin^2 \theta}{\lambda^2}\right]$$

Equation 2.2

- f_n = atomic scattering factor of the n^{th} atom in the unit cell with the coordinates (x_n, y_n, z_n) .

The atomic scattering factor is proportional to atomic number, Z .

- p_n = population factor

This accounts for the site occupancy.

- m = multiplicity factor

The multiplicity factor takes into account the number of equivalent reflections that give rise to a single powder line.

- A = absorption factor

This factor accounts for absorption occurring within the sample, equating the proportion of incident and diffracted X-rays absorbed. The amount absorbed is dependent upon sample composition, diffraction angle and thickness, and varies according to the geometry of the diffraction method used.

- L = Lorentz factor

The Lorentz factor is the correction for variation in the probability of a Bragg reflection occurring within a given diffraction angle. It corrects for the geometry of the diffractometer and is a simple function of θ .

- P = polarisation factor

This factor corrects for the unpolarised nature of X-rays produced by the X-ray tube. Diffracted beams are more intense when the electric field vector is parallel or anti-parallel to the sample and are weakest when perpendicular. This correction is also a simple function of θ .

- B_n = isotropic temperature factor

This accounts for the effect of thermal motion on intensity. B is proportional to the mean square oscillations of the atoms, u_{iso} .

$$B_n = 8\pi^2 \langle u_{iso}^2 \rangle_n$$

Equation 2.3

2.2.1.1 Instrumentation

In this work, XPD data were collected on Siemens D5000, Bruker AXS D5005 and Bruker D8 diffractometers. To characterise a product by X-ray diffraction, a thin layer of sample is packed on a layer of Scotch brand magic tape and is placed in the magnetic holder of the diffractometer. Diffrac plus³ software was used to perform XPD scans and XPD evaluation (Eva) to assist analysis of the obtained data. By measuring atomic spacings in crystals, the XPD data allow the unit cell of the sample to be indexed and the lattice parameters of the cell determined. Miller indices were assigned using the computer programs DSPACE⁴ or INDEX⁵. The lattice parameters were refined using the program CELL⁶, which corrects for the zero point error of the diffractometer. Longer scans were collected for more

detailed structural refinement by the program GSAS (General Structure Analysis System)⁷ using the Rietveld method⁸ to refine the structures.

2.2.1.1.1 Siemens D5000 Diffractometer

The Siemens D5000 diffractometer is a transmission instrument allowing very high resolution to be obtained. It is equipped with a position sensitive detector (PSD) which moves through 2θ degrees rotating around a circumference centred on the sample, allowing rapid data collection. It can therefore be used for rapid ‘fingerprinting’, identification, and characterisation of crystalline phases at ambient temperature, in addition to providing data of sufficient quality for more advanced applications of powder diffraction analysis. A photograph of the Siemens D5000 is shown in Figure 2.1.

A small amount of finely powdered sample is evenly coated onto the adhesive side of a piece of Scotch branded magic tape, which is fixed onto the central hole of an aluminium disc. The prepared sample is then placed into the sample holder and subsequently into the magnetic holder within the diffractometer. In order to minimise the effects of distortions in the reflection intensities caused by preferred orientations, the sample is rotated at 30 rps throughout the scan.

The D5000 X-ray tube contains a Cu target which is bombarded with electrons leading to a $2p \rightarrow 1s$ transition resulting in X-ray emission consisting of a doublet arising from the two spin states of the 2p orbital, $K_{\alpha 1}$ and $K_{\alpha 2}$, where $\lambda = 1.5406 \text{ \AA}$ and 1.5443 \AA respectively. A germanium beam monochromator was used to provide the Cu $K_{\alpha 1}$ radiation and a wavelength of 1.5406 \AA . The data for the X-ray pattern were collected over a range of $0-60^\circ 2\theta$ for primary indexing and $0-90^\circ 2\theta$ for more detailed analysis. By changing the parameter file and

lengthening the duration of the scan, i.e. the 2θ range, higher quality data necessary for more detailed measurements and structural refinement were obtained.

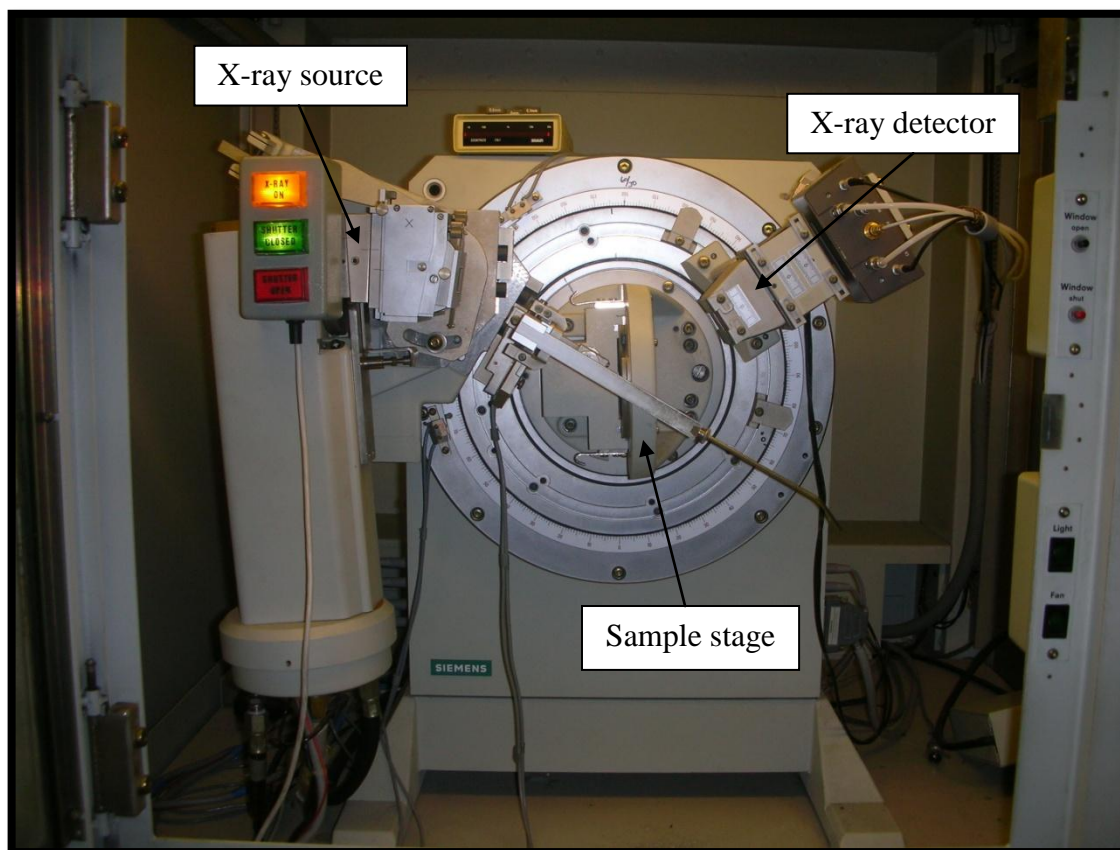


Figure 2.1 The Siemens D5000 X-ray Diffractometer.

2.2.1.1.2 Bruker AXS D5005 Diffractometer

Variable temperature XPD was carried out on the Bruker AXS D5005 diffractometer equipped with an Anton Paar HTK 1200 heating stage, shown in Figure 2.2. The ceramic sample holder consists of a shallow well into which a finely powdered sample is evenly loaded. Before being placed into position within the instrument the surface of the sample is carefully levelled using a glass slide.

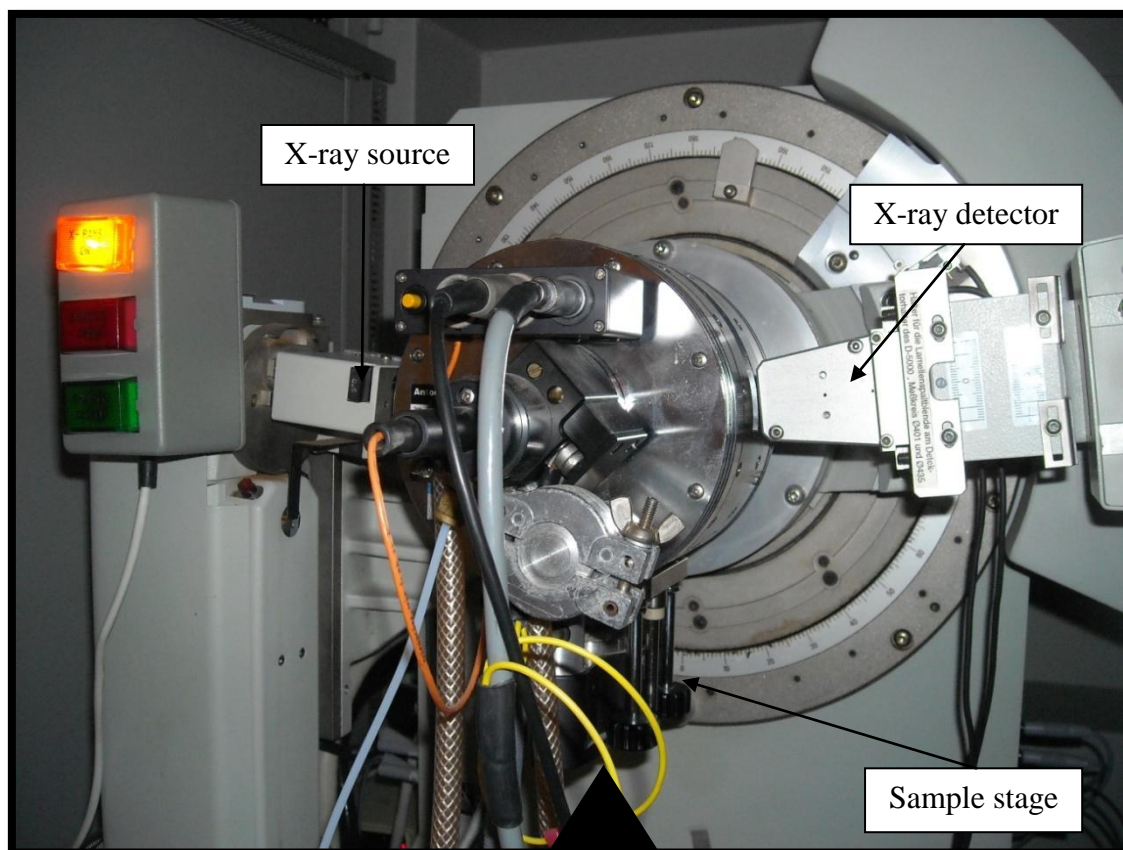


Figure 2.2 The Bruker AXS D5005 X-ray diffractometer.

The instrument operates in reflection mode and has a divergent primary beam of X-rays. The diffracted Cu K β radiation ($\lambda = 1.3922 \text{ \AA}$) is removed by a Ni filter placed in front of the detector, leaving only the diffracted Cu K α radiation ($\lambda = 1.5406 \text{ \AA}$ for Cu K α_1 and 1.5444 \AA for Cu K α_2). The data produced contained both Cu K α_1 and Cu K α_2 radiation. However, computer processing software allowed the Cu K α_2 radiation to be stripped from the data to leave only the Cu K α_1 peaks. The instrument operates in θ - θ geometry, meaning that both the X-ray source and detector rotate simultaneously through an angle θ around the sample. Diffraction data are collected using a Braun position sensitive detector (PSD) over a range of 298-1073 K and angles of 0 - $90^\circ 2\theta$.

2.2.1.1.3 Bruker D8 Autosampler Diffractometer

This high resolution instrument operates in transmission mode, in a similar manner to the Siemens D5000, with the main difference being that the D8 is equipped with an autosampler capability. Analogous to the D5000, the sample and detector move through angles of θ and 2θ , respectively, with the position of the source and the monochromator being fixed in order to preserve the geometric arrangement while the Bragg angle is varied. The diffraction data are acquired using a solid-state LynxEye PSD. A photograph of the Bruker D8 autosampler diffractometer is shown in Figure 2.3.

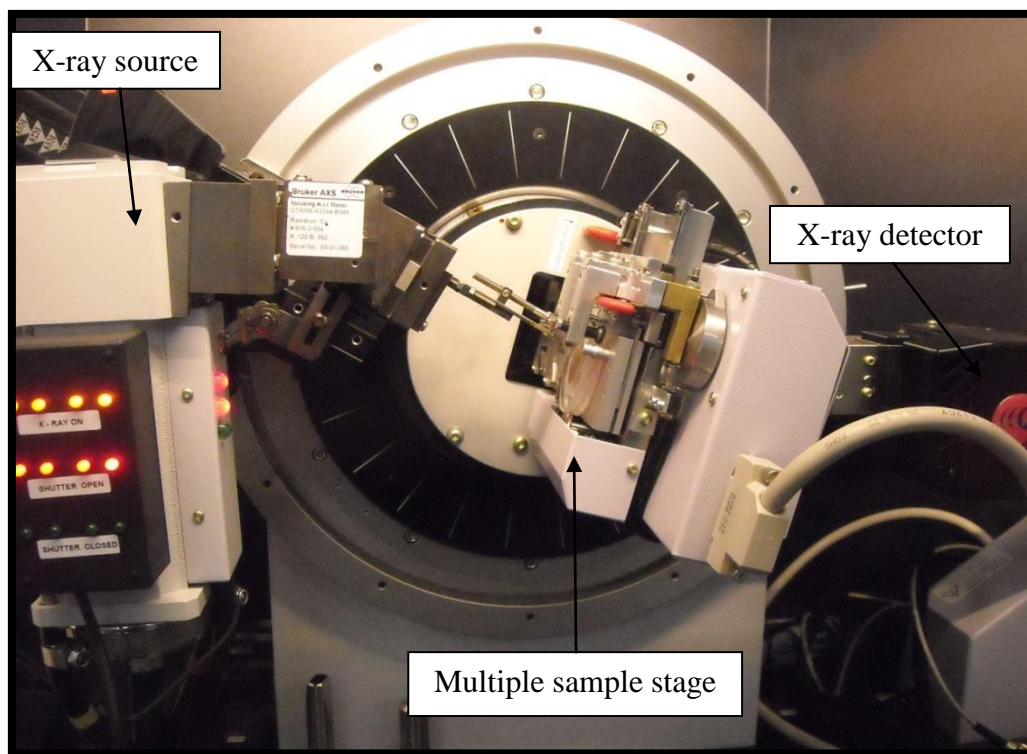


Figure 2.3 The Bruker D8 Autosampler Diffractometer.

2.2.2 Neutron Powder Diffraction

NPD was used to complement XPD and to give further structural information which allowed the determination of atomic positions and any deviations from ideal sites.

NPD has several characteristic differences from XPD. Firstly, the scattering powers of atoms towards neutrons are different from X-rays. Whereas in X-ray diffraction the scattering power is a function of atomic number, for neutron diffraction the atomic nuclei, rather than electrons, are responsible for the scattering. Hence, light elements such as hydrogen which diffract X-rays very weakly, make substantial contributions to neutron diffraction patterns, allowing the detection of light atoms in the presence of heavier atoms in

the crystal¹. This is of great importance to the work carried out in this thesis, since the oxygen atoms were difficult to locate in the presence of the heavy bismuth and rhenium cations by XPD. Therefore, in this research NPD was used to locate the positions of atoms which are light scatterers relative to bismuth.

A second difference between neutron and X-ray diffraction is that the neutrons obtained from a nuclear reactor give a continuous spectrum of radiation. Hence the selection of a particular wavelength is required, rendering it necessary to filter out the remainder using a crystal monochromator to produce a monochromatic beam of neutrons. Consequently, the neutron beam tends to be weak and most of the available neutron energy is wasted.

The intensity of a diffracted neutron beam is generally affected by the same factors as those affecting a diffracted X-ray beam. However, the intensity of a diffracted beam in NPD is independent of Z since the neutrons are diffracted by the nucleus. The relative intensity of a Bragg reflection due to neutron diffraction is given by:

$$I = \frac{CmAF_{hkl}^2}{L}$$

Equation 2.4

where

- C = instrument constant
- m = multiplicity factor
- A = absorption factor
- F_{hkl} = structure factor
- L = Lorentz factor

The expression for the structure factor, F_{hkl} , is similar to that for X-ray diffraction except that f_n is replaced by b_n , and is given by:

$$F_{hkl} = \sum_n b_n p_n \exp[2\pi i(hx_n + ky_n + lz_n)] \exp\left[-\frac{B_n \sin^2 \theta}{\lambda^2}\right]$$

Equation 2.5

where

- b_n represents the average scattering lengths of an atom, thereby allowing for the differing scattering lengths for the isotopes of an atom with respect to their relative abundances.

2.2.2.1 Instrumentation

The NPD measurements carried out in this thesis were performed at the ILL, Grenoble, France. Neutrons at the ILL are delivered by a reactor producing the most intense neutron flux in the world. High velocity neutrons with a very small wavelength are released in atomic fission processes from a uranium target. The neutrons generated in a nuclear reactor can be slowed using a moderator to give a suitable wavelength for use in diffraction experiments, and a single-crystal monochromator is utilised to give a monochromatic beam. A high-flux nuclear reactor is therefore required for structural studies as most of the available neutrons are wasted.

2.2.2.1.1 D2b Neutron Powder Diffractometer

Measurements were performed on the D2b diffractometer. D2b is a very high resolution powder diffractometer characterised by the very high take-off angle of 135° for the monochromator. It is 300 mm high, focusing vertically onto about 50 mm; this large incident vertical divergence is matched by 200 mm high detectors and collimators. Wavelengths can be changed under computer control, since they are all obtained by a simple rotation within the Ge [hkl] crystal plane. For the work in this thesis, the Ge 335 plane was utilised with $\lambda = 1.594 \text{ \AA}$ (optimum λ) at 298 K. A complete diffraction pattern is obtained after about 100 steps of 0.025° in 2θ , since the setup consists of 64 He detectors spaced at 2.5° intervals. A view of the instrument enclosure is shown in Figure 2.4, and a schematic view of the instrument layout is shown in Figure 2.5.

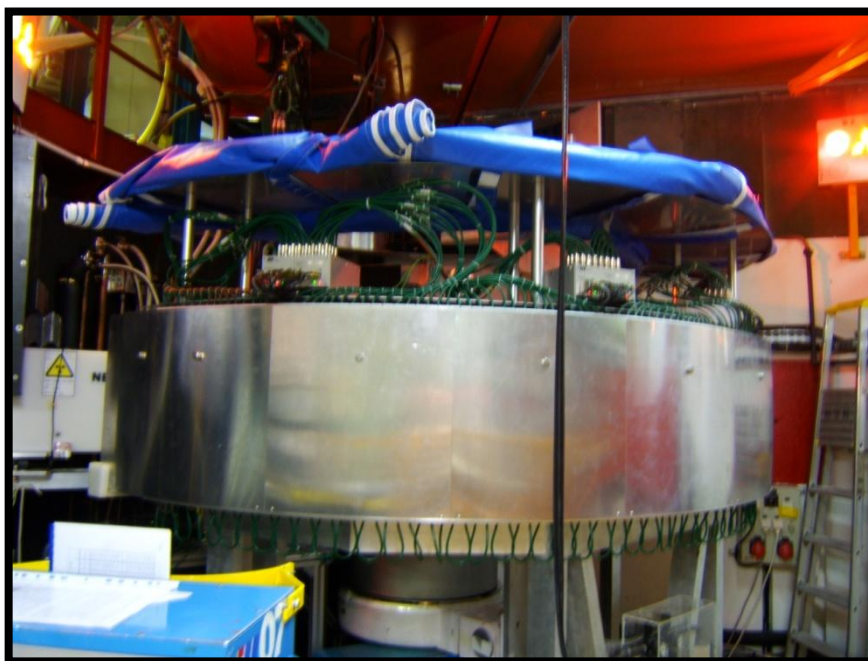


Figure 2.4 View of the D2b instrument enclosure.

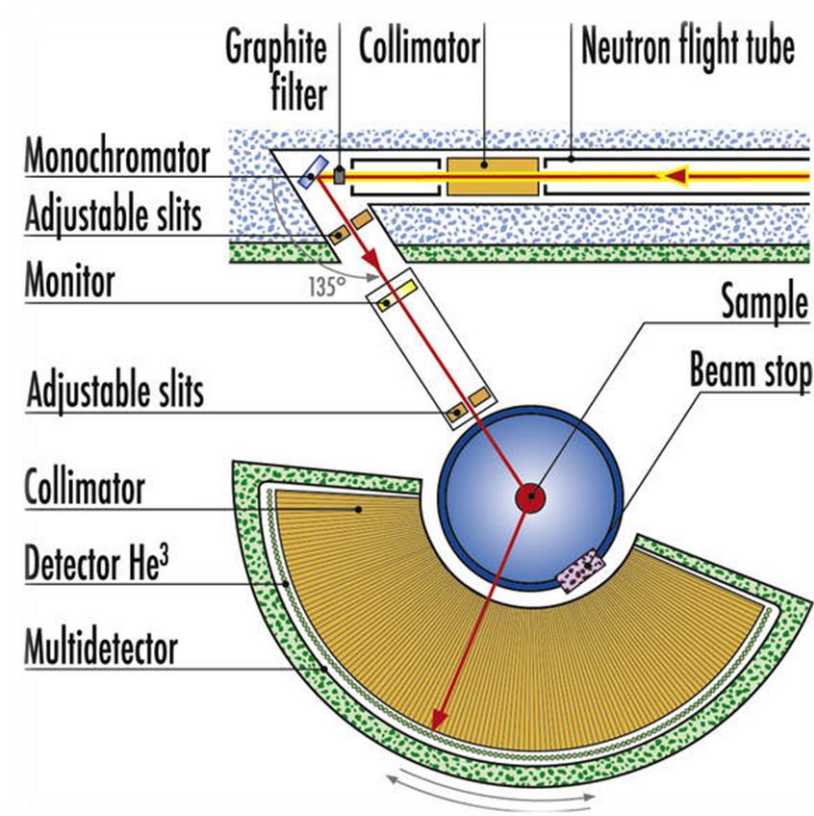


Figure 2.5 Schematic diagram illustrating the instrument layout⁹.

2.3 Rietveld Structural Refinement

The Rietveld method, a technique devised by Hugo Rietveld in 1967⁸, is widely used for the characterisation of crystalline materials. In Rietveld refinements structural parameters are refined in addition to other parameters which influence the diffraction pattern. In the refinement a diffraction profile is calculated for the proposed structure and is compared with the experimental data. The proposed structure is then refined using a least-squares approach

to give a best fit model structure, achieved by adjusting parameters of the proposed structure, in order to minimise the difference between the experimental and calculated intensities.

When undertaking a refinement, the diffraction pattern is recorded as a numerical intensity value, y_i , at each of several thousand equal steps, i , of either the scattering angle, 2θ , or velocity for time of flight neutron data, in the pattern. The best fit sought is the best least squares fit to each y_i simultaneously. The residual S_y , the quantity minimised in the least squares refinement, may be expressed as:

$$S_y = \sum_i w_i (y_i - y_{ci})^2$$

Equation 2.6

where

- $w_i = 1/y_i$
- y_i = observed intensity at the i^{th} step
- y_{ci} = calculated intensity at the i^{th} step

and the sum is over all data points.

The Rietveld refinement program therefore adjusts refineable parameters until the residual (Equation 2.6) is minimised to obtain a best fit between the observed and calculated profiles. Refineable parameters fall into 2 categories – the first containing structural parameters, including temperature factors, occupancy of sites and atomic coordinates; and the second containing profile parameters, such as peak shape and zero position of the diffractometer.

Various criteria are required to judge whether the refinement is successful, as the best fit obtained depends on adequacy of the model and whether a global rather than local minimum is reached¹⁰. This is achieved by the use of R factors,

$$R_p = \frac{\sum |y_i(obs) - (1/c)y_i(calc)|}{\sum y_i(obs)}$$

Equation 2.7

$$R_{wp} = \left[\frac{\sum w_i (y_i(obs) - (1/c)y_i(calc))^2}{\sum w_i (y_i(obs))^2} \right]^{1/2}$$

Equation 2.8

$$R_{exp} = \left[\frac{(N - P + c)}{\sum w_i y_i^2 (obs)} \right]^{1/2}$$

Equation 2.9

where

- R_p = profile factor
- R_{wp} = weighted profile factor
- R_{exp} = expected profile factor
- N = number of observations
- P = number of variables
- c = number of constraints

At the end of a successful refinement R_{wp} tends to be around twice the value of R_{exp} but greater than 1. χ^2 is a measure of the relationship between R_{wp} and R_{exp} and is often used as a guide to the fit,

$$\chi^2 = \left(\frac{R_{wp}}{R_{exp}} \right)^2$$

Equation 2.10

For the work described in this thesis, all structural refinements were carried out using the General Structure Analysis System (GSAS)⁷. GSAS is a multi-purpose refinement program ideal for working with both X-ray and neutron data.

2.4 Spectroscopic Techniques

2.4.1 Impedance Spectroscopy

Impedance spectroscopy is a valuable electrochemical technique that can be used to characterise the electrical properties of materials and their interfaces with electronically conducting electrodes. Impedance measurements are a sensitive indicator of a wide variety of chemical and physical properties, such as oxide ion conduction in materials.

2.4.1.1 Theory of Impedance Spectroscopy

Impedance is a measure of the ability of a circuit to resist the flow of electrical current, and is measured by applying an AC potential to an electrochemical cell and measuring the current through the cell. A sinusoidal potential excitation is applied. From the fundamentals of AC theory¹¹, a pure sinusoidal voltage can be expressed as,

$$E(t) = E_0 \cos(\omega t)$$

Equation 2.11

where

- $E(t)$ = the potential at time t
- E_0 = amplitude of the signal
- ω = radial frequency

The relationship between radial frequency ω / radians per second, and frequency f / hertz is described by,

$$\omega = 2\pi f$$

Equation 2.12

The response to this applied potential is AC current signal containing the excitation frequency and its harmonics. In a simple circuit the resulting sinusoidal current will have an identical frequency but, depending on the type of electrical components involved in the circuit, will have different phase and amplitude. The response signal, $I(t)$, can be described by,

$$I(t) = I_0 \cos(\omega t - \theta)$$

Equation 2.13

where

- I_0 = amplitude
- θ = phase difference. When the voltage is leading the current this value is positive, and is negative when the voltage is trailing the current.

The impedance, Z , of an electrical component is defined by Ohm's Law as,

$$Z = \frac{E(t)}{I(t)}$$

Equation 2.14

The impedance of the system can then be calculated using an expression analogous to Ohm's Law, given as,

$$Z = \frac{E_0 \cos(\omega t)}{I_0 \cos(\omega t - \theta)} = Z_0 \frac{\cos(\omega t)}{\cos(\omega t - \theta)}$$

Equation 2.15

The impedance is therefore expressed in terms of magnitude, Z_0 , and phase difference, θ .

The expression for impedance is composed of real and imaginary parts and can be represented as a complex quantity, where,

$$Z = Z' + jZ''$$

Equation 2.16

where

- Z' = the real part of the impedance and is in phase
- Z'' = the imaginary part of the impedance and 90° out of phase
- $j = \sqrt{(-1)}$

The plot of Z' versus Z'' for a resistor and capacitor in parallel produces a complex plane plot and is shown in Figure 2.6. Each point on the plot is the impedance at one frequency. The impedance can be represented as a vector of length $|Z|$, and the angle between this vector and the x-axis is the phase shift, θ .

For pure resistance the phase shift, θ , is zero and the complex plane plot is a single point on the Z' axis at $Z' = R$. From the value of R at a specific temperature the resistivity of a material can be calculated, leading to determination of the oxide ion conductivity of the material.

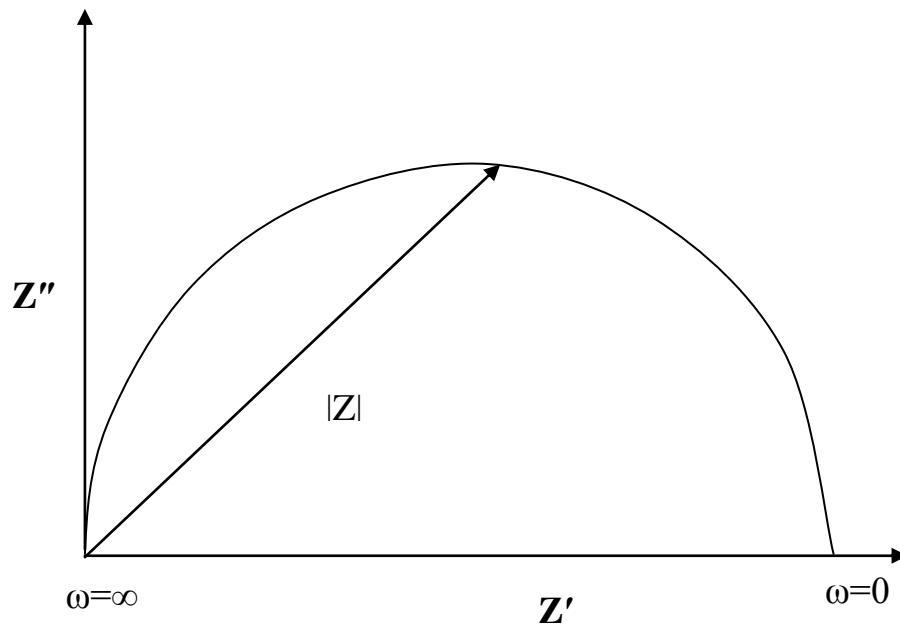


Figure 2.6 Complex plane representation of impedance for a resistor and capacitor in parallel.

2.4.1.2 Oxide Ion Conductivity Measurements

To determine the relative oxide ion conductivity at various temperatures, the powdered samples were compressed in a pellet press using an 8mm die and a pressure of $\sim 1.5 \text{ tonne cm}^{-2}$. The pellet was sintered at a temperature of 1123 K for 16 h with a heating and cooling rate of 60 K h^{-1} . Measurements of pellet diameter, d , thickness, l , and mass, m , were taken using a micrometer in order to determine the sintered density and calculate the conductivity or resistance.

Silver wire electrodes which were encased in a two holed ceramic sleeve were then attached to each side of the pellet using an even coating of silver dag conductive paste, as shown in Figure 2.7. The pellet and attached electrodes were heated to 373 K for 1 h, ensuring good adhesion.

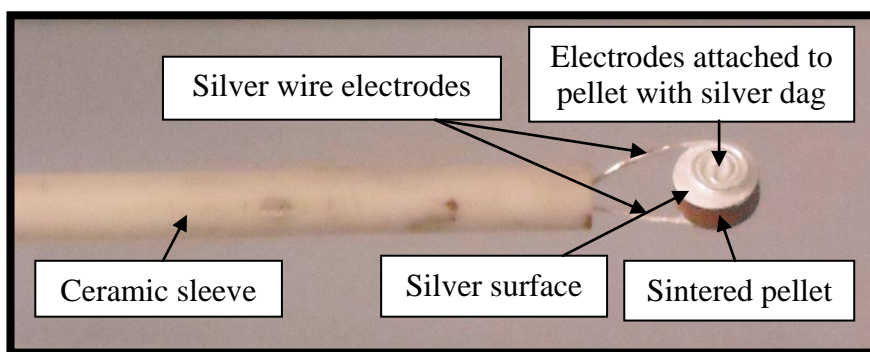


Figure 2.7 Arrangement of pellet with silver wire electrodes attached.

The prepared pellet was placed in a tube furnace next to a sensitive furnace thermocouple and the temperature was read through a digital temperature meter. The electrodes from the sample were attached to the input of a Solatron SI 1260 Impedance

Analysers. The sample was heated between 473 and 773 K and measurements were taken at intervals of 50 K, recorded once thermal equilibrium was achieved. The sample environment for impedance measurements is shown in Figure 2.8.

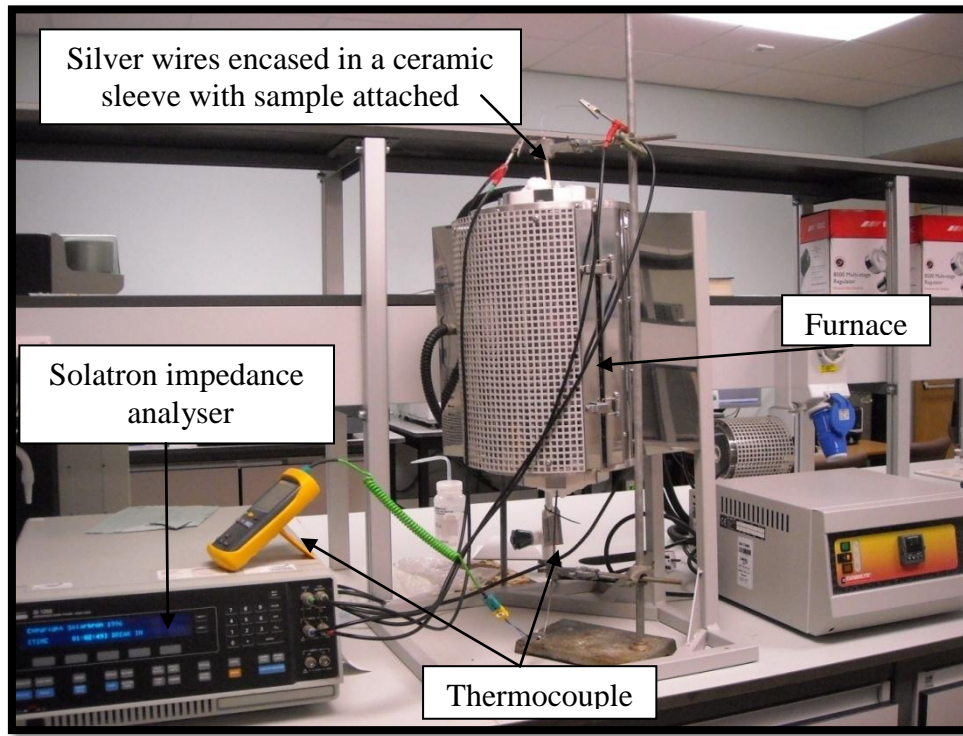


Figure 2.8 Sample environment for impedance measurements.

Using the data sets collected it was possible to construct a complex plane plot of Z' versus Z'' , using the program Zview. From this plot R was determined from the intercept along the Z' axis. At each temperature a value for the relative oxide ion conductivity can be determined as follows:

$$R = \rho l / A$$

Equation 2.17

$$\sigma = 1 / \rho$$

Equation 2.18

where

- R = resistance/ Ω
- ρ = resistivity
- l = thickness of pellet/ cm
- A = area of pellet / cm^2
- σ = conductivity/ $\Omega^{-1} \text{cm}^{-1}$

To calculate the Arrhenius energy of activation, E_a , for a material a plot of $\log \sigma$ versus $1000/T$ produces a negative slope. An example of a typical Arrhenius plot is given in Figure 2.9.

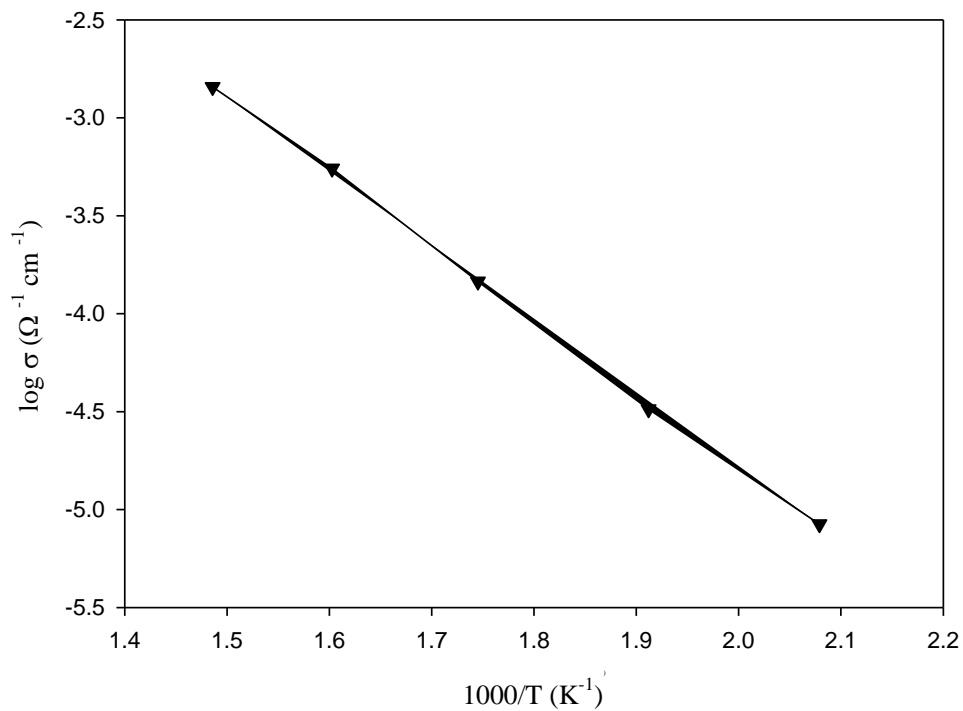


Figure 2.9 A typical Arrhenius plot.

$$\sigma = \sigma_0 e^{-E_a/RT}$$

Equation 2.19

$$\log \sigma = \log \sigma_0 - \frac{E_a}{2.303RT}$$

Equation 2.20

$$\text{slope} = -E_a / 2.303R$$

Equation 2.21

$$E_a = 2.303(-\text{slope} \times R)$$

Equation 2.22

where

- R = the gas constant (8.314 J K⁻¹ mol⁻¹). It is usual to convert E_a values in kJ mol⁻¹ into electron volts, eV (1eV = 96.485 kJ mol⁻¹).

2.4.2 X-ray Absorption Spectroscopy (XAS)

An X-ray is absorbed by an atom when the energy of the X-ray is transferred to a core-level electron which is ejected from the atom. X-ray absorption spectroscopy measures the variation in the element X-ray absorption coefficient at energies near and above an X-ray absorption edge. In addition to providing characteristic X-ray emission spectra, atoms also give characteristic X-ray absorption spectra, as the wavelengths at which absorption edges occur are dependent on the relative separation of the energy levels in an atom, which is in turn dependent upon atomic number. XAS therefore allows the investigation of the electronic and structural properties of a particular element in a material, and is broken into two categories:

- XANES –X-ray Absorption Near-Edge Spectroscopy
- EXAFS- Extended X-ray Absorption Fine Structure

2.4.2.1 Extended X-ray Absorption of Fine Structure (EXAFS)

EXAFS measures the variation of absorption energy extending from the absorption edge to higher energies. Ionised photoelectrons interact with neighbouring atoms, which in turn act as secondary scattering sources. This may lead to interference between adjacent scattered waves, which influences the probability of absorption of an incident X-ray photon. The degree of interference is determined by the local structure, including interatomic distances and coordination numbers in the region of the emitting atoms, in addition to the wavelength of the photoelectron. The absorption in EXAFS occurs as a ripple, as shown in Figure 2.10, from which it is possible to obtain information about the local environment of the excited atom. Using Fourier transform techniques, the ripple pattern may be analysed to obtain information such as bond distances and coordination numbers.

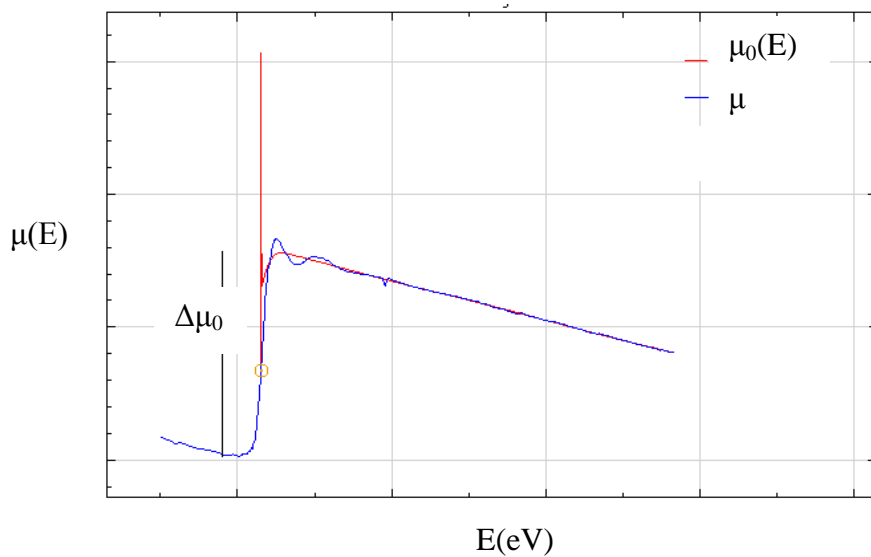


Figure 2.10 A typical K edge EXAFS spectrum.

XAS measures the energy dependence of the X-ray absorption coefficient, $\mu(E)$, at and above the absorption edge of a particular element. In this work, $\mu(E)$ was measured in transmission mode, whereby the absorption was measured directly by measuring transmission through the sample.

$$I = I_0 e^{-\mu(E)t}$$

Equation 2.23

$$\mu(E)t = -\ln(I/I_0)$$

Equation 2.24

where

- I = the intensity transmitted through the material
- I_0 = the X-ray intensity hitting the material
- $\mu(E)$ = absorption coefficient
- t = thickness of material the beam is passing through / cm

μ depends strongly on X-ray energy, E , atomic number, Z , density, ρ and atomic mass, A ;

$$\mu \approx \frac{\rho Z^4}{AE^3}$$

Equation 2.25

EXAFS may be defined as the normalised oscillatory part of $\mu(E)$,

$$\chi(E) = \frac{\mu(E) - \mu_0(E)}{\Delta\mu_0(E_0)}$$

Equation 2.26

where

- $\mu_0(E)$ = smooth background
- $\Delta\mu_0(E_0)$ = edge step

EXAFS is more conveniently expressed in terms of the photoelectron wavenumber, k , rather than X-ray energy, as EXAFS is an interference effect which depends on the wave-nature of the photoelectron.

$$k = \sqrt{\frac{2m(E - E_0)}{\hbar^2}}$$

Equation 2.27

In order to amplify the oscillations at high k , $\chi(k)$ is often shown weighted by k^2 or k^3 .

To model the EXAFS, the EXAFS equation is used,

$$\chi(k) = \sum_j \frac{N_j f_j(k) e^{-2k^2 \sigma_j^2}}{k R_j^2} \sin[2k R_j + \delta_j(k)]$$

Equation 2.28

where

- $f(k)$ = scattering amplitude
- $\delta(k)$ = phase-shift
- R = distance to neighbouring atom
- N = coordination number of neighbouring atom
- σ^2 = mean-square disorder of neighbour distance

$f(k)$ and $\delta(k)$ are photoelectron scattering properties of the neighbouring atoms and depend on atomic number, Z , of the scattering atom. The nature of the neighbouring atoms may therefore be determined. $\chi(k)$, $k^2 \chi(k)$ and $k^3 \chi(k)$ are composed of sine waves, which may be converted by Fourier Transform from k space to R space, $\chi(R)$ ¹².

Extended X-ray absorption fine structure (EXAFS) measurements were performed in transmission mode at The European Synchrotron Radiation Facility ESRF in Grenoble, France on Beamline 25 at 298 K. The raw data were background subtracted and normalised using the program ATHENA¹³. The EXAFS oscillations were isolated from the raw data, weighted by k^2 and fitted using the software package ARTEMIS¹³.

2.5 Differential Thermal Analysis (DTA)

Thermal analysis involves the measurement of properties of a solid as a function of temperature, rendering it a useful technique for the investigation of possible phase changes. A phase change produces either an absorption or evolution of heat. In DTA, the temperature of a sample is compared to that of an inert reference material during a programmed change of temperature. Both chambers are heated at a controlled uniform rate in a furnace and the temperatures of the two remain the same until a thermal event occurs and when the sample either gives out (exothermic) or takes in (endothermic) heat energy.

Experiments were performed with a Netzsch STA 449F1. The experimental arrangement is shown in Figure 2.11. A small mass of sample, ca. 40 mg, is accurately weighed into an alumina crucible and sealed with a lid. The sample and reference cell, which is simply an empty cell, are placed side by side in a heating block which is heated/cooled at a constant rate; identical thermocouples are placed in each. The system is purged to remove air

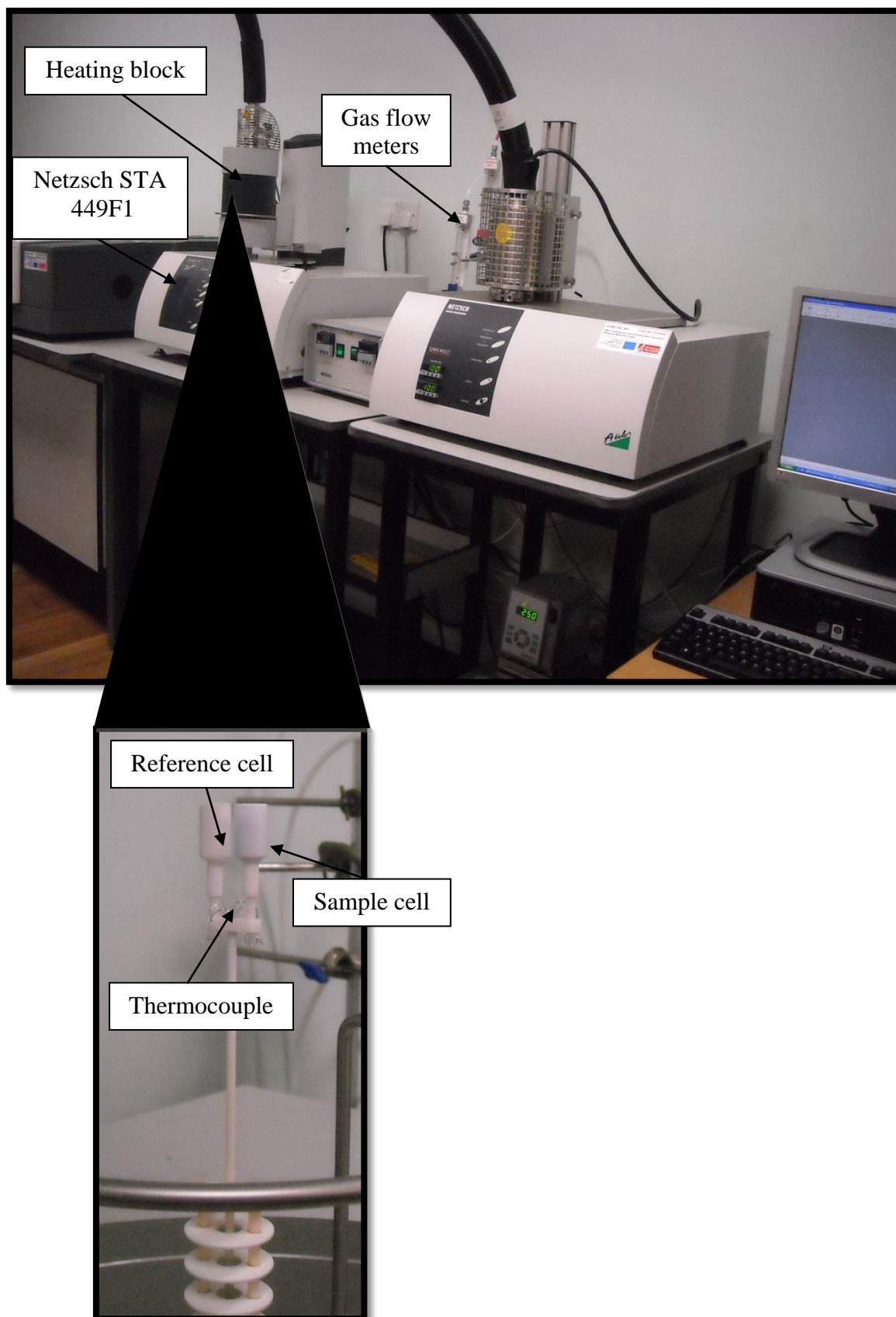


Figure 2.11 Netzsch STA 449F1 DTA experimental arrangement.

and the chamber is filled with nitrogen. A programmed cycle of heating/cooling is then applied. When the sample and reference are at the same temperature the net output from the pair of thermocouples is zero. The net voltage of the thermocouples detects when a thermal event occurs as a temperature difference, ΔT , between the sample and reference. The temperature of the heating block is monitored by a third thermocouple allowing the results to be plotted as ΔT versus temperature.

2.6 Electron Microscopy

High Resolution Electron Microscopy (HREM) was used to complement X-ray diffraction techniques to observe crystal defects and variations in local structure such as site occupancies and vacancies, thus confirming lattice symmetry and aiding structure determination. A thin sample (~200 nm), prepared by suspending the powder in ethanol and depositing this solution on a holey carbon grid, is subjected to a very high energy, high intensity electron beam. A two-dimensional projection of the sample is produced as the electrons which pass through the sample are detected, imaging the bulk structure, thus detecting crystal defects. Selected Area Electron Diffraction (SAED) patterns were recorded with a Phillips CM20 instrument, by Joke Hadermann at EMAT, University of Antwerp.

2.7 References

- 1 West, A. R. *Solid State Chemistry* 2nd edn. John Wiley and Sons, Ltd. England (1999)
- 2 Smart, L. E., Moore, E. A. *Solid State Chemistry: An Introduction* 3rd edn. Taylor and Francis Group (2005)
- 3 *Diffrac plus*, copyright of Bruker AXS
- 4 Greaves, C. *D-Space* The School of Chemistry, University of Birmingham
- 5 Louer, D; Vargas, R. *Index J. Appl. Cryst.* **15** (1982) 542 (modified by C. Greaves, The School of Chemistry, University of Birmingham)
- 6 Pye, M. F. *Cell*, University of Oxford (modified by C. Greaves, The School of Chemistry, University of Birmingham)
- 7 Larson, A. C.; Von Dreele, R. B. *General Structure Analysis System (GSAS)* Los Alamos National Laboratory, Los Alamos, NM (1994)
- 8 Rietveld, H. M. *Acta. Cryst.* **22** (1967) 151
- 9 <http://www.ill.eu>
- 10 Young, R. A. *The Rietveld Method* International Union of Crystallography, Oxford University Press (1993)
- 11 Barsoukov, E.; Macdonald, J. R. *Impedance Spectroscopy: Theory, experiment and applications* 2nd edn. John Wiley and Sons, Ltd. England (2005)
- 12 Newville, M. *Fundamentals of X-ray Absorption Fine Structure* version 1.6.1 (2004), Consortium for Advanced Radiation Sources, University of Chicago. Available online from: <http://www.xafs.org>
- 13 Ravel, B.; Newville, M. *J. Synchrotron Rad.* **12** (2005) 537

CHAPTER 3

The Structure, Ionic Conductivity and Local Environment of Cations in Bi₉ReO₁₇

3.1 Introduction

Previous studies in the Bi-Re-O system have revealed several Bi-rich materials with fluorite-related crystal structures, as discussed in Chapter 1. Bi₃ReO₈ was shown to crystallise in the cubic space group P2₁3 with $a = 11.590(1) \text{ \AA}$.

To investigate the possibility of single phases occurring within other Bi-rich compositions, samples with mole ratios between 6:1 (Bi:Re) to 16:1 (Bi:Re) were prepared by Crumpton *et al.*² 14:1 (Bi:Re) and 9:1 (Bi:Re) compositions were found to yield single phase products. As discussed in Chapter 1, the 14:1 phase, Bi₂₈Re₂O₄₉, was shown to have a fluorite-related superstructure with tetragonal symmetry where $a = 8.7216(1) \text{ \AA}$, $c = 17.4177(2) \text{ \AA}$ and space group I4/ m ³. The structure contains both octahedral ReO₆⁵⁻ and tetrahedral ReO₄⁻ units, comprising an ordered framework of linked BiO₄ trigonal bipyramids and square pyramids with discrete rhenium oxoanions at the origin and body centre of the unit cell. Despite its ordered structural framework, the compound displays relatively high conductivity ($5.4 \times 10^{-4} \Omega^{-1} \text{ cm}^{-1}$ at 673 K).

As a development of that work further studies of the structural and conduction properties of other fluorite-related superstructures in the bismuth-rich portion of the

Bi₂O₃-Re₂O₇ phase diagram were initiated, including the material of composition Bi₉ReO₁₇ which, when formed by quenching from high temperature, has been suggested⁴ to contain both ReO₄ and ReO₆ environments, similar to those observed in Bi₂₈Re₂O₄₉, although the actual ordered structure was not known at this time. However, during the course of this work the structure of Bi₉ReO₁₇ was described by Ling *et al.*⁵, and shown to display fluorite-related monoclinic symmetry where $a = 9.89917(5) \text{ \AA}$, $b = 19.70356(10) \text{ \AA}$, $c = 11.61597(6) \text{ \AA}$, $\beta = 125.302(2)^\circ$, space group P2₁/c . The structure features clusters of ReO₄ tetrahedra embedded in a distorted Bi-O fluorite-like network, and is shown in Figure 3.1.

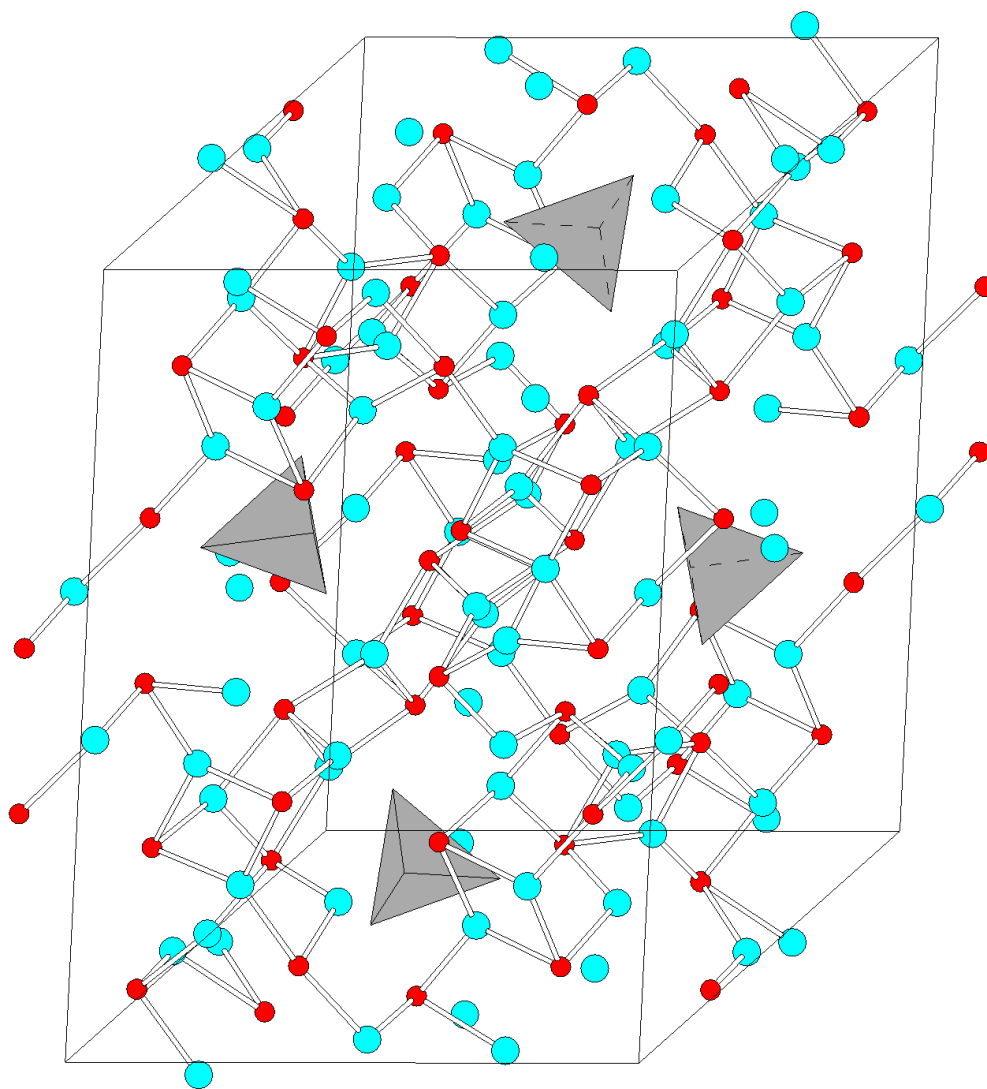


Figure 3.1 The structure of Bi₉ReO₁₇, where ReO₄ tetrahedra are shown as grey polyhedra.

Hence, this chapter reports a complementary structural study of $\text{Bi}_9\text{ReO}_{17}$ by X-ray- and neutron- powder diffraction together with the results of an examination of the local environments of the cations by extended X-ray absorption spectroscopy (EXAFS) and its oxide ion conduction properties.

3.2 Experimental

Stoichiometric amounts of Bi_2O_3 and NH_4ReO_4 were intimately ground and calcined for several periods of 12 h in air at 1073 K. Preliminary investigations were carried out by XPD to ensure a single phase product, with further characterisation made by NPD, EXAFS and impedance spectroscopy, as described in Chapter 2.

The material was also subjected to quenching by heating to 1073 K, followed by removal from the furnace and quickly cooling to room temperature in air, and in liquid nitrogen. $\text{Bi}_9\text{ReO}_{17}$ was additionally characterised by variable temperature XPD and DTA to further examine phase changes occurring on heating.

3.3 Results and Discussion

3.3.1 The Structure of $\text{Bi}_9\text{ReO}_{17}$

Neutron powder diffraction data were recorded from $\text{Bi}_9\text{ReO}_{17}$ at 3 K and 300 K, and refinement was based upon a structure with monoclinic symmetry, space group $\text{P2}_1/\text{c}$ ⁵. The low temperature data were recorded to provide better statistical precision, as it was envisaged that the reduction in thermal parameters could be useful for reducing thermal effects in the subsequent structure determination/refinement. Emphasis is therefore placed on the results

from this data set. The resultant unit cell parameters ($a = 9.8799(1)$, $b = 19.6116(2)$, $c = 11.5937(1)$ Å, $\beta = 125.2974(4)^\circ$ at 3 K and $a = 9.9030(2)$, $b = 19.7139(4)$, $c = 11.6212(2)$ Å, $\beta = 125.2988(7)^\circ$ at 300 K are consistent with the previous ambient temperature refinement⁵, where $a = 9.89917(5)$, $b = 19.70356(10)$, $c = 11.61597(6)$ Å, $\beta = 125.302(2)^\circ$. Refinement statistics for 159 variables were $R_p = 0.0233$, $R_{wp} = 0.0288$ and $\chi^2 = 2.730$ for the data recorded at 3 K, and $R_p = 0.0281$, $R_{wp} = 0.0359$ and $\chi^2 = 1.698$ for the data recorded at 300 K. The refined structural information for the data recorded at 3 K and 300 K is shown in Tables 3.1 and 3.2, respectively, and fitted NPD profiles shown in Figures 3.2 and 3.3, respectively, which show good agreement between observed and calculated profiles. The data are of high quality and no constraints on temperature factors were required. Whereas all refined temperature factors (Table 3.1) were reasonable for the 3 K dataset ($0.18 \text{ Å}^2 \leq 100U_{iso} \leq 1.0 \text{ Å}^2$), some high values were obtained for the 300 K data, as was found previously⁵. In particular, the O atoms forming the ReO_4^- tetrahedra (O1, O2, O3, O4) have a significantly enhanced U_{iso} at 300 K (average 2.65 Å^2) compared with the other O atoms which are bonded only to Bi (average 1.79 Å^2). This is probably related to librational dynamics of the ReO_4 groups, and is consistent with thermal analysis and conductivity data (*vide infra*).

Metal-oxygen distances in $\text{Bi}_9\text{ReO}_{17}$ at both 3 K and 300 K are given in Table 3.3, and allow comparison with the full range of distances provided in the earlier determination⁵. It can be seen that many of the Bi-O distances are very long, and are substantially larger than those which are normally ascribed to strong bonds. In fact, no significant discussion of the bismuth stereochemistry was provided in the previous structure determination⁵. It can be seen that for each Bi site, there are three or four short Bi-O distances, and Table 3.4 provides an evaluation based on a maximum bond distance of 2.4 Å (given that the ionic radius of

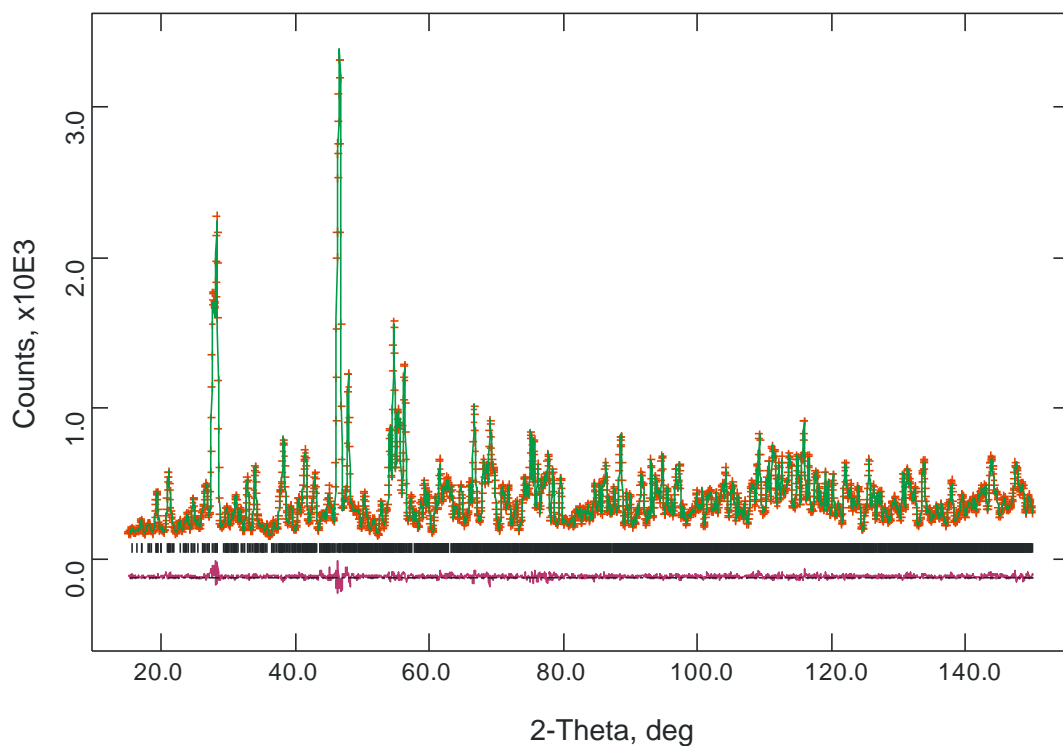


Figure 3.2 The observed (+), calculated (-) and difference NPD profile for the final Rietveld refinement of $\text{Bi}_9\text{ReO}_{17}$ at 3K.

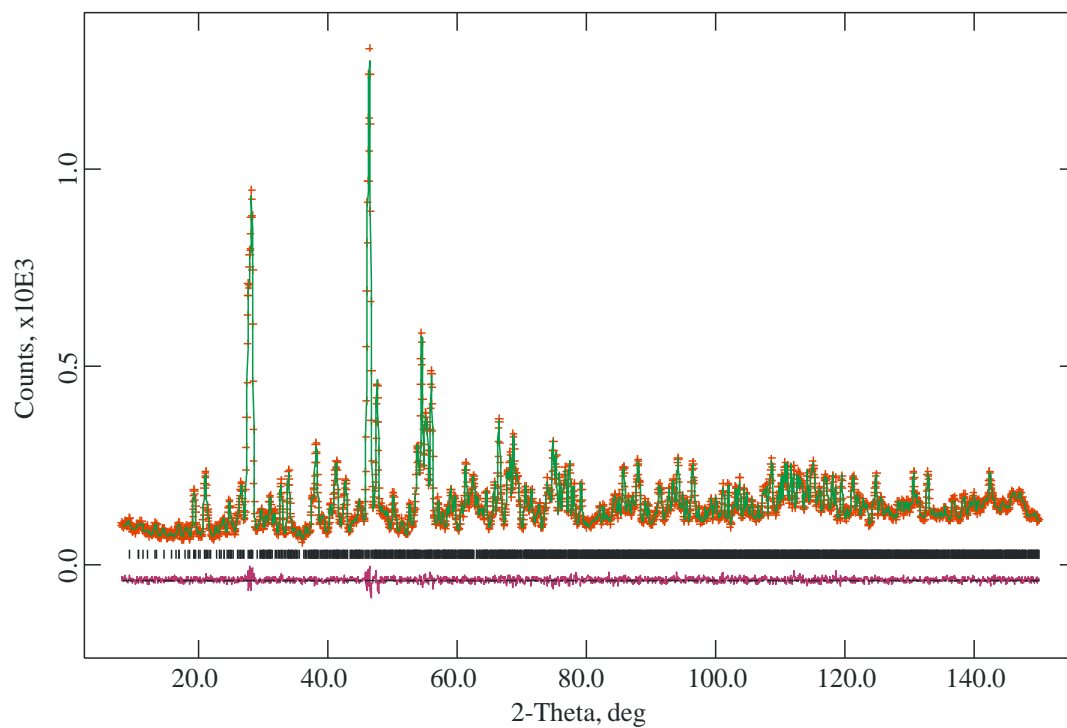


Figure 3.3 The observed (+), calculated (-) and difference NPD profile for the final Rietveld refinement of $\text{Bi}_9\text{ReO}_{17}$ at 300K.

Table 3.1 Refined structural parameters for Bi₉ReO₁₇ at 3K.

Atom	Site symmetry	<i>x</i>	<i>y</i>	<i>z</i>	Uiso x 100 / Å ²
Re	4	0.6342(4)	0.4394(2)	0.1799(3)	0.18(8)
Bi1	4	0.0841(2)	0.2535(2)	0.4041(4)	0.56(9)
Bi2	4	0.6061(5)	0.2734(2)	0.6839(4)	0.52(7)
Bi3	4	0.1060(4)	0.0530(3)	0.4396(3)	0.27(8)
Bi4	4	0.1355(4)	0.4473(2)	0.4406(4)	0.43(7)
Bi5	4	0.6184(4)	0.4522(2)	0.6769(4)	0.24(8)
Bi6	4	0.0848(5)	0.6461(2)	0.3924(4)	0.25(8)
Bi7	4	0.1104(5)	0.8458(2)	0.4466(4)	0.34(8)
Bi8	4	0.6612(4)	0.8441(2)	0.1943(4)	0.37(7)
Bi9	4	0.6239(5)	0.6649(2)	0.1881(4)	0.25(8)
O1	4	0.4565(6)	0.1061(3)	0.6240(6)	0.9(1)
O2	4	0.6413(6)	0.4556(3)	0.0365(5)	0.7(1)
O3	4	0.3599(7)	0.4861(3)	0.7416(6)	0.8(1)
O4	4	0.1965(7)	0.8895(3)	0.1981(6)	1.0(1)
O5	4	0.4482(6)	0.2425(3)	0.7600(6)	0.6(1)
O6	4	0.9096(6)	0.2495(3)	0.1705(6)	0.3(1)
O7	4	0.5205(7)	0.3630(3)	0.7222(6)	0.8(1)
O8	4	0.6739(7)	0.1313(3)	0.0999(6)	0.6(1)
O9	4	0.3113(7)	0.2419(3)	0.9000(6)	0.5(1)
O10	4	0.8291(6)	0.2729(3)	0.8887(5)	0.6(1)
O11	4	0.8904(7)	0.4386(3)	0.9280(6)	0.9(1)
O12	4	0.3688(7)	0.0323(2)	0.9823(6)	0.6(1)
O13	4	0.0853(7)	0.3520(3)	0.8324(6)	0.8(1)
O14	4	0.1522(6)	0.1573(3)	0.1177(5)	0.4(1)
O15	4	0.1082(7)	0.1305(3)	0.8105(6)	0.8(1)
O16	4	0.1277(6)	0.3345(3)	0.0929(5)	0.3(1)
O17	4	0.0297(7)	0.9759(3)	0.7791(6)	1.0(1)

Table 3.2 Refined structural parameters for Bi₉ReO₁₇ at 300K.

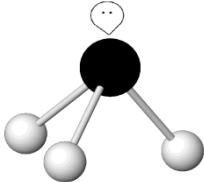
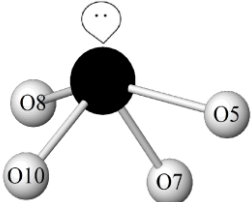
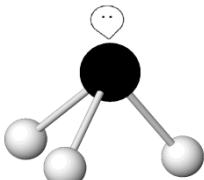
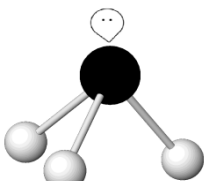
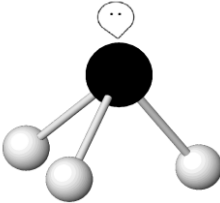
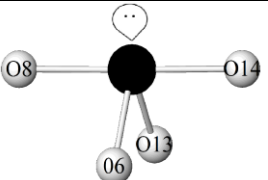
Atom	Site symmetry	<i>x</i>	<i>y</i>	<i>z</i>	Uiso x 100 / Å ²
Re	4	0.6326(6)	0.4389(3)	0.1805(5)	1.1(1)
Bi1	4	0.0830(8)	0.2537(4)	0.4025(7)	1.4(2)
Bi2	4	0.6098(8)	0.2728(3)	0.6858(7)	1.4(1)
Bi3	4	0.1033(7)	0.0514(4)	0.4357(5)	1.3(1)
Bi4	4	0.1381(6)	0.4477(4)	0.4412(5)	0.9(1)
Bi5	4	0.6223(7)	0.4516(4)	0.6778(6)	1.1(1)
Bi6	4	0.0838(8)	0.6475(3)	0.3929(7)	1.2(1)
Bi7	4	0.1115(8)	0.8455(4)	0.4479(7)	1.2(1)
Bi8	4	0.6612(7)	0.8440(3)	0.1949(6)	1.2(1)
Bi9	4	0.6216(9)	0.6656(3)	0.1891(7)	1.1(1)
O1	4	0.454(1)	0.1060(6)	0.625(1)	3.8(3)
O2	4	0.641(1)	0.4537(5)	0.0393(9)	2.1(2)
O3	4	0.360(1)	0.4874(5)	0.743(1)	0.8(1)
O4	4	0.202(1)	0.8901(6)	0.201(1)	3.9(3)
O5	4	0.446(1)	0.2426(5)	0.760(1)	1.9(1)
O6	4	0.911(1)	0.2493(5)	0.171(1)	1.6(2)
O7	4	0.523(1)	0.3628(5)	0.727(1)	1.9(2)
O8	4	0.673(1)	0.133(5)	0.097(1)	1.6(2)
O9	4	0.312(1)	0.2415(5)	0.900(1)	1.5(2)
O10	4	0.830(1)	0.2731(5)	0.8887(9)	1.2(2)
O11	4	0.890(1)	0.4377(6)	0.931(1)	2.5(2)
O12	4	0.370(1)	0.0335(4)	0.9839(9)	1.7(2)
O13	4	0.083(1)	0.3530(5)	0.831(1)	1.9(2)
O14	4	0.152(1)	0.1570(5)	0.116(1)	1.8(2)
O15	4	0.107(1)	0.1302(5)	0.811(1)	1.5(2)
O16	4	0.127(1)	0.3349(5)	0.0926(9)	1.3(2)
O17	4	0.035(1)	0.9759(5)	0.779(1)	2.9(2)

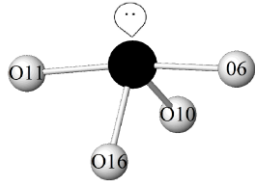
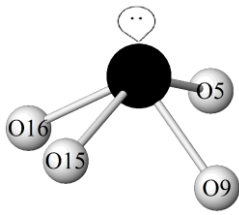
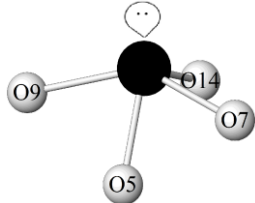
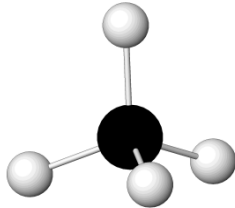
Table 3.3 Selected metal-oxygen bond distances (Å) in Bi₉ReO₁₇ at 3K and 300K.

Atom 1	Atom 2	3K	300K	Atom 1	Atom 2	3K	300K
Bi1	O4*	3.522(7)	3.57(1)	Bi5	O17	3.242(7)	3.17(1)
Bi1	O6	2.217(7)	2.20(1)	Bi6	O4*	3.121(7)	3.14(1)
Bi1	O9	2.275(7)	2.29(1)	Bi6	O6	2.165(7)	2.15(1)
Bi1	O10	2.475(7)	2.47(1)	Bi6	O8	2.352(7)	2.36(1)
Bi1	O13	2.233(7)	2.26(1)	Bi6	O10	3.294(6)	3.29(1)
Bi1	O14	2.777(7)	2.78(1)	Bi6	O13	2.135(7)	2.13(1)
Bi1	O15	2.589(8)	2.59(1)	Bi6	O14	2.287(6)	2.28(1)
Bi1	O16	2.621(7)	2.65(1)	Bi6	O17	2.631(7)	2.68(1)
Bi2	O1*	3.501(7)	3.52(1)	Bi7	O2*	3.184(6)	3.19(1)
Bi2	O4*	3.578(6)	3.56(1)	Bi7	O4*	3.549(7)	3.58(1)
Bi2	O5	2.274(7)	2.30(1)	Bi7	O6	2.268(7)	2.28(1)
Bi2	O6	3.123(6)	3.11(1)	Bi7	O7	3.460(6)	3.42(1)
Bi2	O7	2.105(7)	2.14(1)	Bi7	O10	2.174(7)	2.17(1)
Bi2	O8	2.374(7)	2.38(1)	Bi7	O11	2.332(7)	2.31(1)
Bi2	O9	2.885(7)	2.91(1)	Bi7	O15	2.515(7)	2.54(1)
Bi2	O10	2.109(6)	2.09(1)	Bi7	O16	2.132(6)	2.14(1)
Bi3	O1*	3.015(6)	3.04(1)	Bi8	O1*	3.095(6)	3.07(1)
Bi3	O2*	3.026(7)	3.06(1)	Bi8	O5	2.235(6)	2.23(1)
Bi3	O11	2.707(7)	2.71(1)	Bi8	O8	3.127(7)	3.12(1)
Bi3	O11	2.062(6)	2.09(1)	Bi8	O9	2.111(7)	2.12(1)
Bi3	O13	2.183(7)	2.19(1)	Bi8	O12	3.074(6)	3.08(1)
Bi3	O16	2.763(7)	2.81(1)	Bi8	O15	2.364(6)	2.39(1)
Bi3	O17	2.149(7)	2.11(1)	Bi8	O16	2.127(6)	2.13(1)
Bi4	O3*	2.954(7)	2.97(1)	Bi9	O1*	3.426(7)	3.48(1)
Bi4	O4*	2.922(7)	2.99(1)	Bi9	O2*	3.369(6)	3.37(1)
Bi4	O7	3.676(7)	3.70(1)	Bi9	O3*	3.051(6)	3.10(1)
Bi4	O12	2.102(6)	2.08(1)	Bi9	O5	2.159(7)	2.13(1)
Bi4	O14	2.839(7)	2.84(1)	Bi9	O7	2.265(7)	2.22(1)
Bi4	O15	2.050(7)	2.05(1)	Bi9	O9	2.356(7)	2.38(1)
Bi4	O17	2.147(7)	2.15(1)	Bi9	O13	3.035(7)	3.09(1)
Bi5	O3*	3.120(7)	3.17(1)	Bi9	O14	2.057(6)	2.08(1)
Bi5	O7	2.205(6)	2.24(1)	Re	O1	1.726(6)	1.73(1)
Bi5	O8	2.085(7)	2.11(1)	Re	O2	1.735(5)	1.714(9)
Bi5	O11	2.594(6)	2.59(1)	Re	O3	1.705(6)	1.69(1)
Bi5	O12	2.482(6)	2.51(1)	Re	O4	1.738(6)	1.70(1)
Bi5	O12	2.198(6)	2.21(1)				

* O atoms bonded to Re

Table 3.4 Selected metal-oxygen distances up to 2.4 Å (3 K), along with coordination polyhedra and bond angles. Some O atoms are labelled for clarity.

Bond lengths / Å			Stereochemistry	Bond angles/ °		BVS
Bi1	O6	2.217(7)		O6-Bi1-O9	93.2(2)	2.02
	O9	2.275(7)		O6-Bi1-O13	71.3(2)	
	O13	2.233(7)		O9-Bi1-O13	79.1(3)	
Bi2	O5	2.274(7)		O5-Bi2-O7	72.0(2)	3.01
	O7	2.105(7)		O5-Bi2-O8	142.0(3)	
	O8	2.374(7)		O5-Bi2-O10	93.8(3)	
	O10	2.109(6)		O7-Bi2-O8	70.9(2)	
				O7-Bi2-O10	93.0(3)	
				O8-Bi2-O10	96.1(3)	
Bi3	O11	2.062(6)		O11-Bi3-O13	98.2(3)	2.74
	O13	2.183(7)		O11-Bi3-O17	91.5(3)	
	O17	2.149(7)		O13-Bi3-O17	76.4(2)	
Bi4	O12	2.102(6)		O12-Bi4-O15	88.4(3)	2.97
	O15	2.050(7)		O12-Bi4-O17	89.1(3)	
	O17	2.147(7)		O15-Bi4-O17	95.1(3)	
Bi5	O7	2.205(6)		O7-Bi5-O8	74.8(3)	2.52
	O8	2.085(7)		O7-Bi5-O12	88.1(3)	
	O12	2.198(6)		O8-Bi5-O12	92.3(2)	
Bi6	O6	2.165(7)		O6-Bi6-O8	84.6(2)	2.81
	O8	2.352(7)		O6-Bi6-O13	74.2(2)	
	O13	2.135(7)		O6-Bi6-O14	96.8(3)	
	O14	2.287(6)		O8-Bi6-O14	178.3(3)	
				O13-Bi6-O14	82.8(3)	

Bi7	O6	2.268(7)		O6-Bi7-O10	82.1(3)	2.86
	O10	2.174(7)		O6-Bi7-O11	173.2(3)	
	O11	2.332(7)		O6-Bi7-O16	94.6(3)	
	O16	2.132(6)		O10-Bi7-O11	93.7(2)	
				O10-Bi7-O16	80.2(2)	
				O11-Bi7-O16	79.3(3)	
Bi8	O5	2.235(6)		O5-Bi8-O9	74.9(2)	3.04
	O9	2.111(7)		O5-Bi8-O15	140.4(3)	
	O15	2.364(6)		O5-Bi8-O16	86.7(2)	
	O16	2.127(6)		O9-Bi8-O15	75.1(2)	
				O9-Bi8-O16	101.3(3)	
				O15-Bi8-O16	74.5(2)	
Bi9	O5	2.159(7)		O5-Bi9-O7	71.2(2)	3.07
	O7	2.265(7)		O5-Bi9-O9	71.6(2)	
	O9	2.356(7)		O5-Bi9-O14	94.3(2)	
	O14	2.057(6)		O7-Bi9-O9	142.0(3)	
				O7-Bi9-O14	92.5(2)	
				O9-Bi9-O14	98.1(3)	
Re	O1	1.726(6)		O1-Re1-O2	109.3(3)	7.74
	O2	1.735(5)		O1-Re1-O3	110.9(3)	
	O3	1.705(6)		O1-Re1-O4	107.9(3)	
	O4	1.738(6)		O2-Re1-O3	110.3(3)	
				O2-Re1-O4	109.3(3)	
				O3-Re1-O4	109.1(3)	

Bi³⁺ = 117 pm and O²⁻ = 126 pm) for the 3 K data. The table also shows the individual bismuth coordination polyhedra and selected bond angles for each Bi and Re atom. Re is present as almost undistorted ReO₄ tetrahedra with an average Re-O bond of 1.726 Å. The bond distance criterion assumed provides two distinctly different coordination environments

for the Bi sites, both of which are fully consistent with those expected for ions with a stereochemically active lone pair (e) such as Bi^{3+} . Bi1, Bi3, Bi4 and Bi5 are three-coordinate with pyramidal coordination (tetrahedral including the lone pair, BiO_3e) with O-Bi-O angles all substantially less than the tetrahedral angle and consistent with significant lone pair – bond pair electron repulsions. The remaining Bi sites (Bi2, Bi6, Bi7, Bi8, Bi9) are four-coordinate with pseudo-trigonal bipyramidal coordination including an equatorial lone pair of electrons (BiO_4e). In all cases, Table 3.4 shows that the axial bonds, with largest O-Bi-O angle, are slightly longer than the equatorial bonds; this is in accordance with simple electron-pair repulsion theory and conforms with higher bond pair – lone pair electron repulsions for these bonds which are at 90° to the lone pair direction in the ideal undistorted trigonal bipyramid stereochemistry.

Bond valence sum (BVS) calculations⁶ for the cation sites (Table 3.4) reveal that the stereochemistries described completely satisfy the Bi^{3+} bonding requirements for the four-coordinate sites but are somewhat lower for the pyramidal sites. Bi1 is notably low at 2.02, and for this site, significant contributions to the bonding will be provided by slightly more distant O atoms. Indeed, Table 3.3 shows that at this position O10, O15 and O16 atoms are quite close to Bi1, and including these in the calculations provides a BVS of 2.88. The Re BVS is high (7.74) but still only ~ 10% different from that expected⁶.

The average Re-O bond distance (1.726 Å) is consistent with those previously reported in bismuth rhenium oxides^{1,3}. The Bi-O bonds and directional properties are all consistent with the short Bi-O bonds in other bismuth and bismuth rhenium oxides. In $\alpha\text{-Bi}_2\text{O}_3$ ⁷ and Bi_3ReO_8 ¹ for example, there are three short Bi-O bonds in a pyramidal arrangement. $\text{Bi}_{28}\text{Re}_2\text{O}_{49}$ ³ is described as having four coordinate BiO_4e sites with both trigonal bipyramidal and square pyramidal configurations.

Figure 3.4 shows the structure of $\text{Bi}_9\text{ReO}_{17}$ based on the stereochemistries described in Table 3.4: ReO_4 tetrahedra are displayed as polyhedra, and the stereochemical preference of each Bi atom is displayed. A Bi-O network is established which encapsulates isolated tetrahedral ReO_4 units.

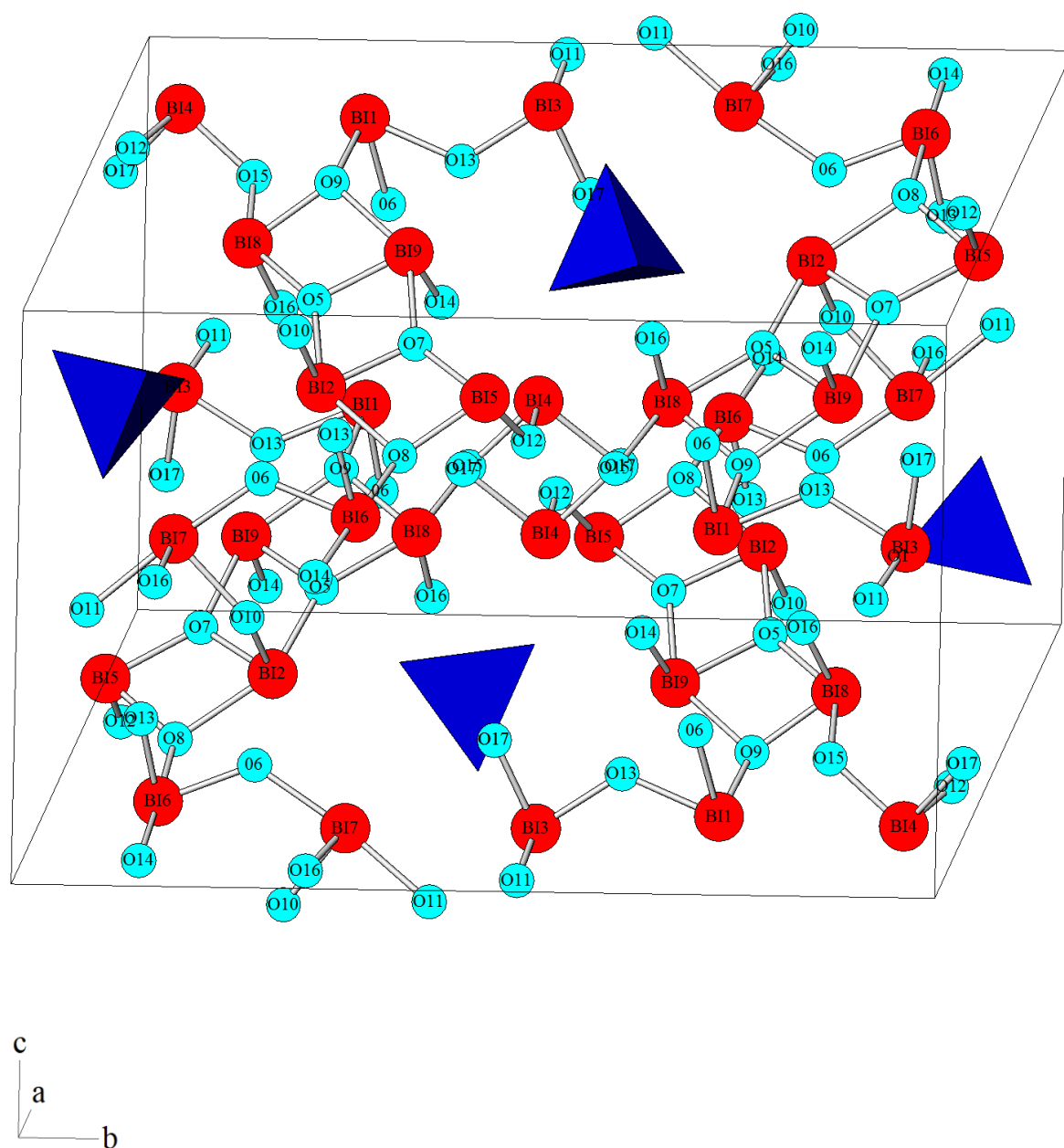


Figure 3.4 The structure of $\text{Bi}_9\text{ReO}_{17}$, where ReO_4 tetrahedra are shown as blue polyhedra.

3.3.2 Local Environment of Cations in Bi₉ReO₁₇

The refined Bi L_{III} edge EXAFS and corresponding fourier transform EXAFS pattern for the standard Bi_{12.5}Er_{1.5}ReO_{24.5} is shown in Figure 3.5, and refined data listed in Table 3.5. The refinement was based upon the structure reported by Greaves *et al.*^{8,9}, space group Fm $\bar{3}$ m. The Bi environment in Bi_{12.5}Er_{1.5}ReO_{24.5} is shown to have a first shell coordination number of 1.88 at a distance of 2.15 Å, and shows a similar outcome to the Bi L_{III} edge EXAFS recorded from Bi_{12.5}Er_{1.5}ReO_{24.5}⁹, where Bi is fitted to a first shell coordination of 1.84 oxygen atoms at a distance of 2.12 Å.

Table 3.5 Refined parameters to the Bi L_{III} edge EXAFS recorded from Bi_{12.5}Er_{1.5}ReO_{24.5}.

Edge	Coordination	R+0.03 /Å	2σ ² /Å ²
	number		
Bi L3	1.88	2.15	0.003

The Bi L_{III} edge EXAFS of Bi₉ReO₁₇ and corresponding Fourier transform is shown in Figure 3.6. The best fit parameters to the data are given in Table 3.6. The Bi L_{III} edge EXAFS were not amenable to fitting beyond a first shell coordination of 2.04 oxygen atoms at a distance of 2.14 Å. This result therefore appears to provide little support for the NPD data, for which the minimum coordination number is three. However, the Bi-O distance is quite similar to the average of all Bi-O distances less than 2.40 Å (Table 3.4), which is 2.20 Å, and the corresponding average coordination number is 3.6. The results are similar to those recorded from the Bi_{12.5}Er_{1.5}ReO_{24.5} standard. Bi_{12.5}Er_{1.5}ReO_{24.5} is highly disordered, with a

wide range of Bi-O distances⁸, and this was assumed to result in the EXAFS data being dominated by the shorter Bi-O distances. We believe a similar situation can explain the present results, even though we are now exploring a fully ordered structure. The nine individual Bi sites all have a different range of Bi-O distances, making the situation similar to that relating to a highly disordered system. The EXAFS data are therefore weighted in favour of the shorter bond distances. Indeed, using only the shorter Bi-O NPD distances – those from the three bonds of the pyramidal sites and the equatorial positions of the trigonal bipyramidal sites – we obtain an average Bi-O distance of 2.14 Å, and an average coordination of 2.4. These data are seen to be in good agreement with the EXAFS results and add support to the high sensitivity of the EXAFS data to the shorter distances.

Table 3.6 Best-fit parameters to the Bi L_{III} edge EXAFS recorded from Bi₉ReO₁₇.

Edge	Coordination		
	number	R+0.03 /Å	2σ² /Å²
Bi L3	2.04	2.14	0.005

Figure 3.7 shows the EXAFS and corresponding Fourier transform plot of the Re L_{III} edge for the purely tetrahedral coordination environment of Re in the standard KReO₄. Refined structural parameters are presented in Table 3.7. The Re environment in KReO₄ can be modelled with Re coordinated to 4 nearest neighbours at a distance of 1.73 Å, and shows a similar result to the literature value reported by Morrow for KReO₄, where 4-coordinate Re has a bond distance of 1.7688 Å¹⁰.

Table 3.7 Refined parameters to the Re L_{III} edge EXAFS recorded from KReO₄.

Edge	Coordination	$R \pm 0.03$ /Å	$2\sigma^2$ /Å ²
	number		
Re L3	4	1.73	0.001

Figure 3.8 shows the Re L_{III} edge EXAFS data of Bi₉ReO₁₇ and resultant Fourier transform. The best fit parameters are given in Table 3.8. The total number of atoms was constrained to 4, with the distance and the Debye-Waller factor allowed to vary, thus enabling construction of the radial distribution of oxygen atoms around the rhenium. The data were fitted pre-eminently to a first shell coordination of four oxygen atoms at a distance of 1.74 Å, similar to the Re L_{III} edge EXAFS recorded from Bi_{12.5}Er_{1.5}ReO_{24.5}⁹, where rhenium is tetrahedrally coordinated to the oxygen at 1.76 Å. This value is in excellent agreement with the Re-O bond lengths given in Table 3.4 from NPD data. Attempts to refine the first shell of the Re L_{III} edge EXAFS to six fold oxygen coordination gave unsatisfactory fits to the data, confirming the NPD results that rhenium exists only in tetrahedral coordination to oxygen in contrast to the local environment in Bi₂₈ReO₄₉³, which contains both octahedrally and tetrahedrally coordinated rhenium. As for the Bi L_{III} edge EXAFS data, the Re L_{III} edge EXAFS could not be fitted beyond a first shell. The small Debye-Waller factor for the rhenium coordination is consistent with the presence of rhenium in well defined, discrete ReO₄ tetrahedra.

Table 3.8 Best-fit parameters to the Re L_{III} edge EXAFS recorded from Bi₉ReO₁₇.

Edge	Coordination	$R \pm 0.03$ /Å	$2\sigma^2$ /Å ²
	number		
Re L3	4	1.74	0.001

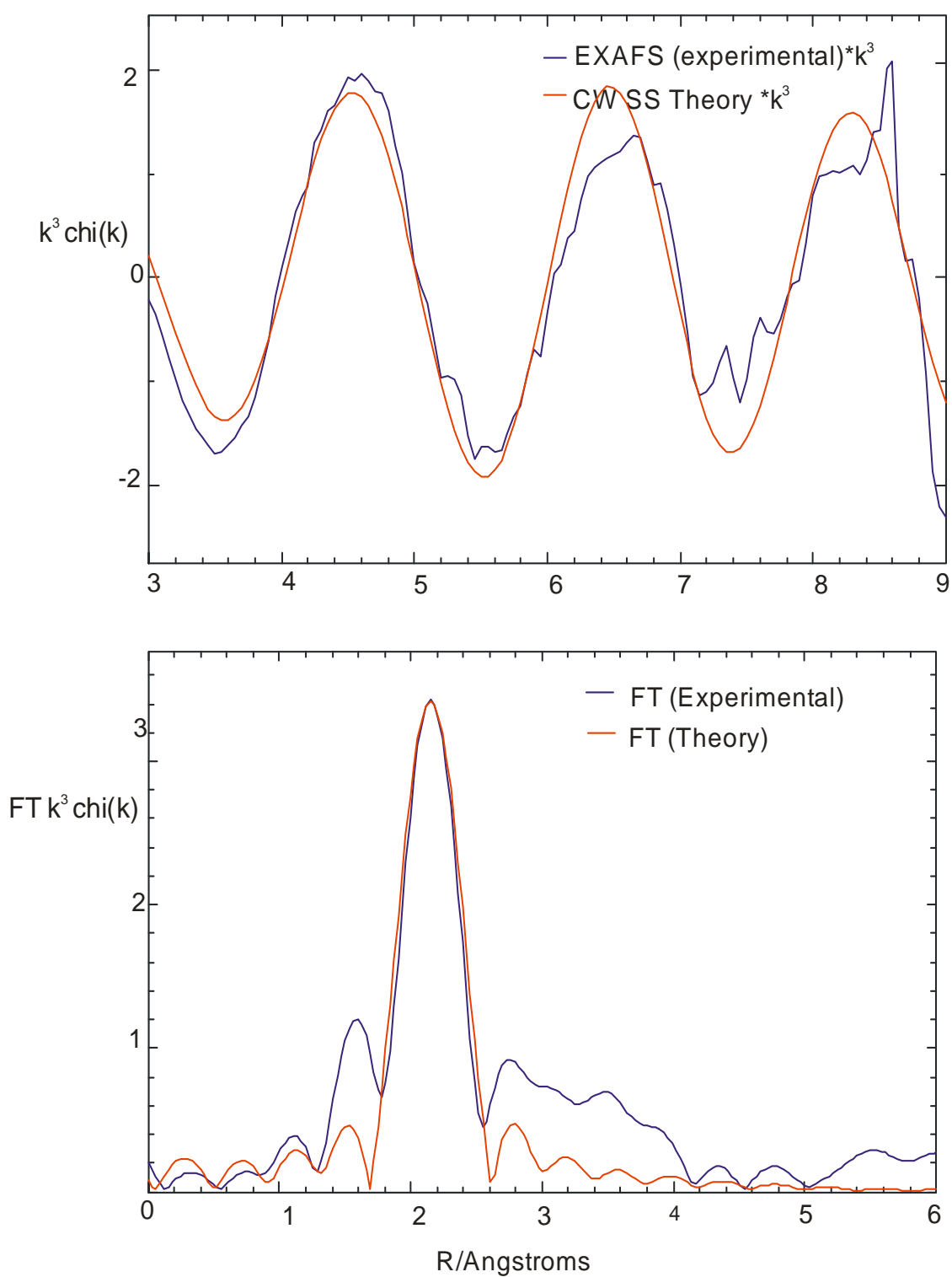


Figure 3.5 The Bi L_{III} edge EXAFS of Bi_{12.5}Er_{1.5}ReO_{24.5} and corresponding Fourier transform.

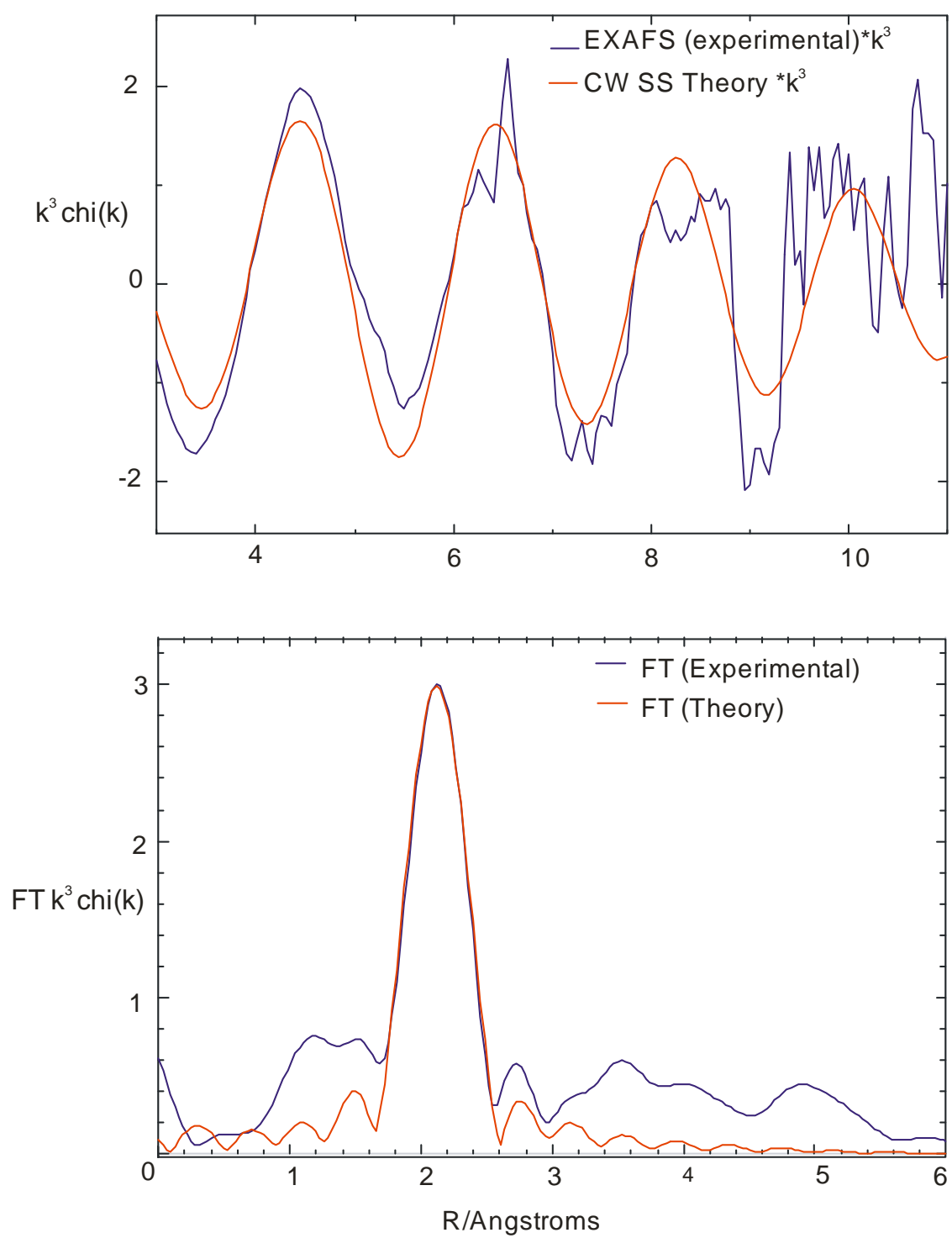


Figure 3.6 The Bi L_{III} edge EXAFS of Bi_9ReO_{17} and corresponding Fourier transform.

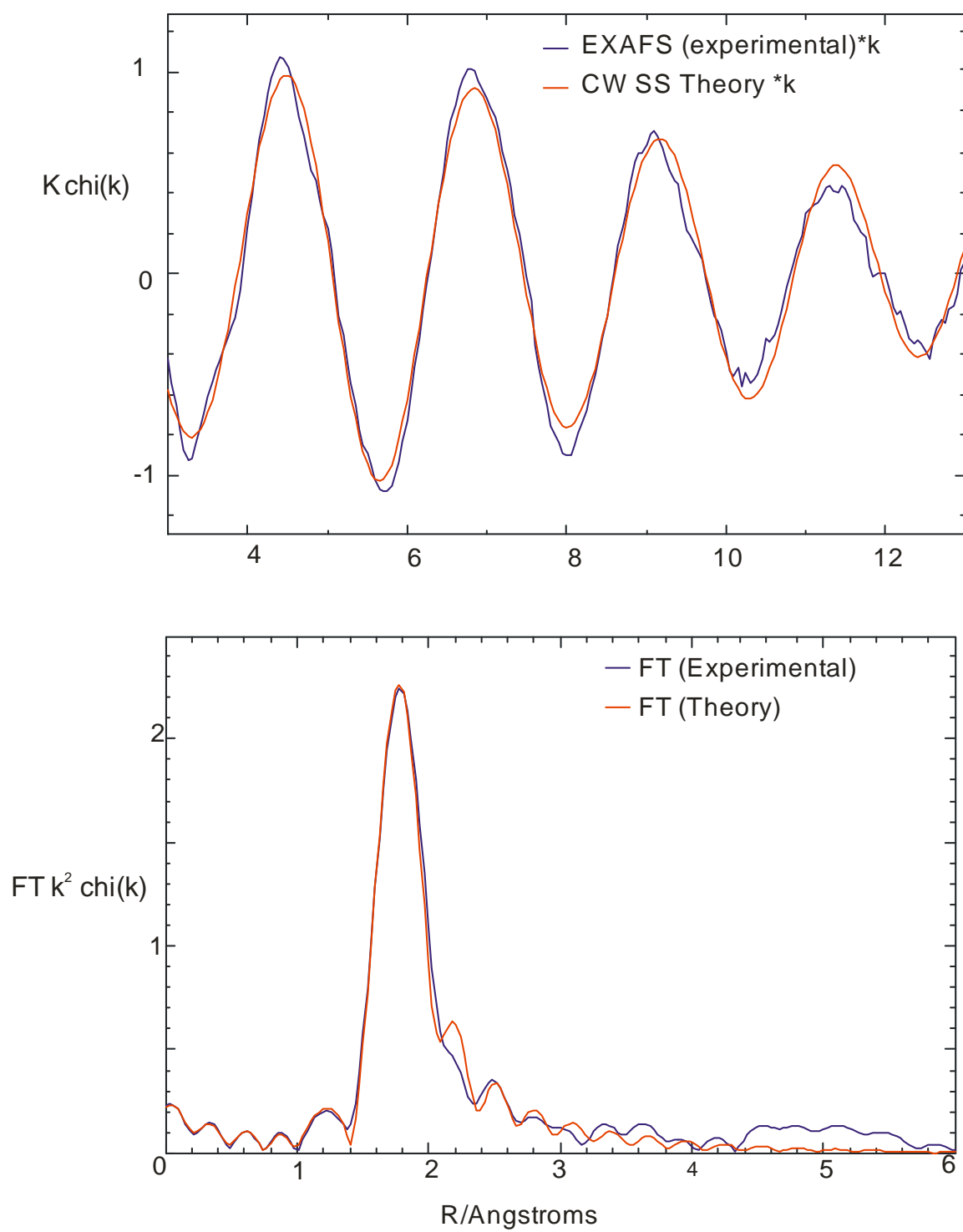


Figure 3.7 The Re L_{III} edge EXAFS of $KReO_4$ and corresponding Fourier transform.

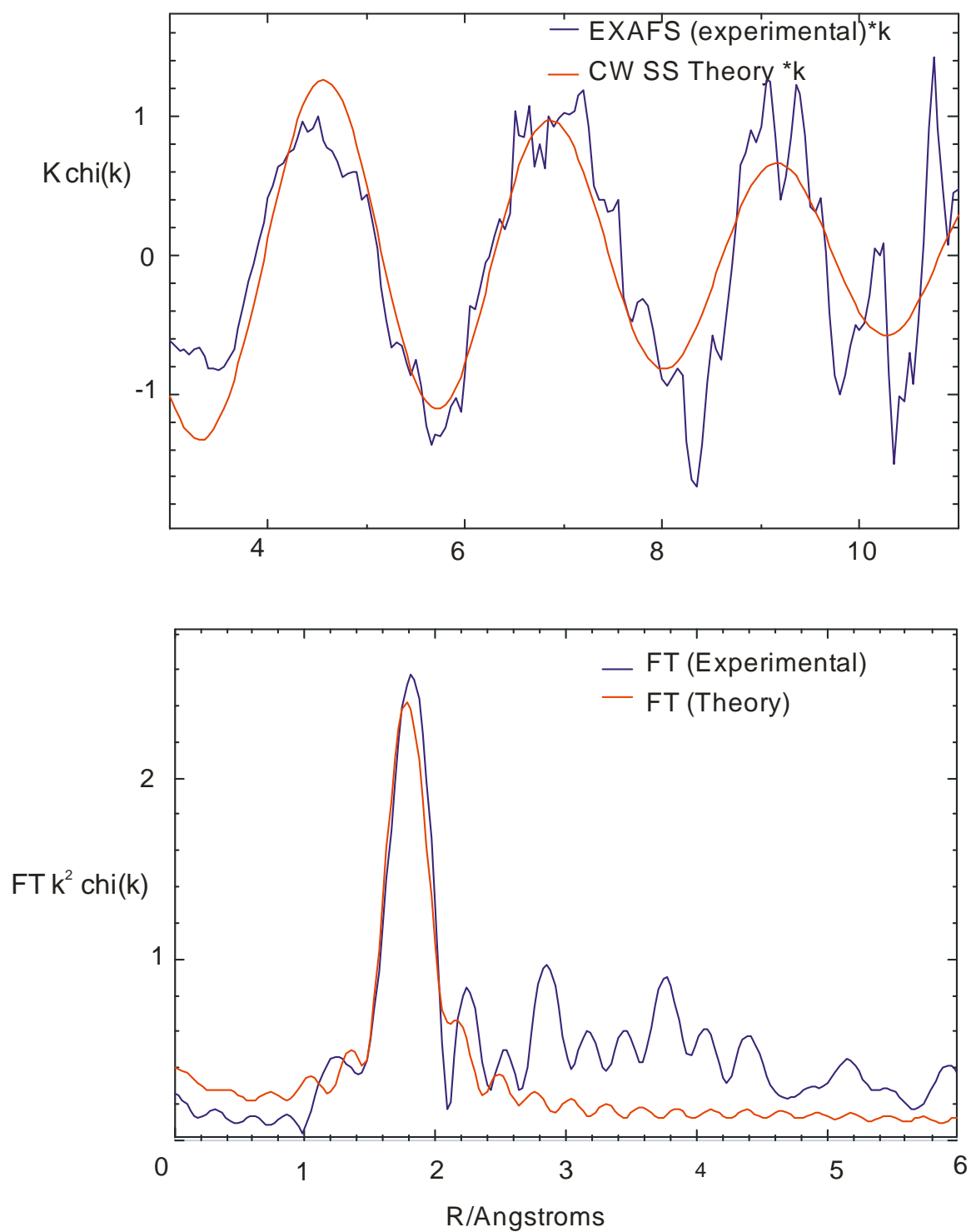


Figure 3.8 The Re L_{III} edge EXAFS of Bi_9ReO_{17} and corresponding Fourier transform.

3.3.3 High Temperature Structural Studies of $\text{Bi}_9\text{ReO}_{17}$

Investigations of possible structural transitions that may occur in $\text{Bi}_9\text{ReO}_{17}$ with variation of temperature were made using DTA, described in Section 2.5. Any phase changes were sought using heating and cooling cycles over a temperature range of 298 K to 1073 K, the results to which are displayed in Figure 3.9. An endothermic energy change with a peak onset at 996 K is apparent in the heating curve, suggestive of phase change. Marked hysteresis occurs, and the corresponding transition on cooling is seen with an onset at 940 K. DTA also reveals a broad endothermic peak in the heating curve, with a peak onset at 735 K. This may suggest that a gradual minor change in the structure occurs with increasing temperature until 996 K, where the material undergoes a more significant phase change, denoted by a much larger peak.

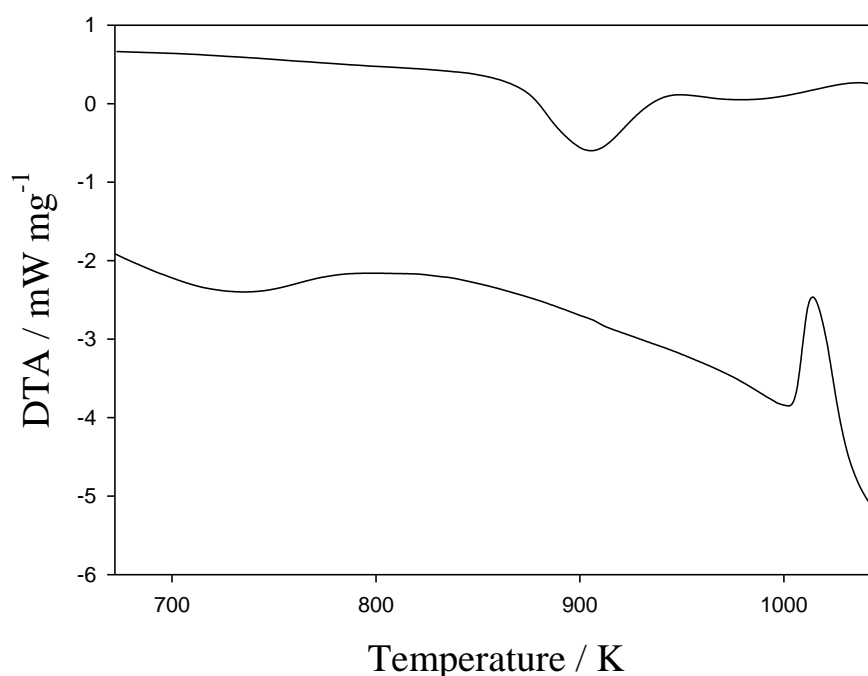


Figure 3.9 DTA results for $\text{Bi}_9\text{ReO}_{17}$, showing the heating curve (lower) and cooling curve (upper).

Variable temperature XPD, described in Section 2.2.1, was employed to support this evidence of phase change suggested by DTA, and to further explore the nature of this. XPD patterns were therefore recorded in the range of 298 K to 1123 K. Figure 3.10 shows the variable temperature XPD patterns recorded between 823 K and 1123 K. The results show little changes occur in the structure until >823 K, where a small peak begins to intensify in the XPD pattern, consistent with a gradual change in structure. This peak, which may be a consequence of a minor adjustment of the structure due to possible rotations of the ReO_4 tetrahedra, is illustrated more clearly in Figure 3.11, which shows variable temperature XPD

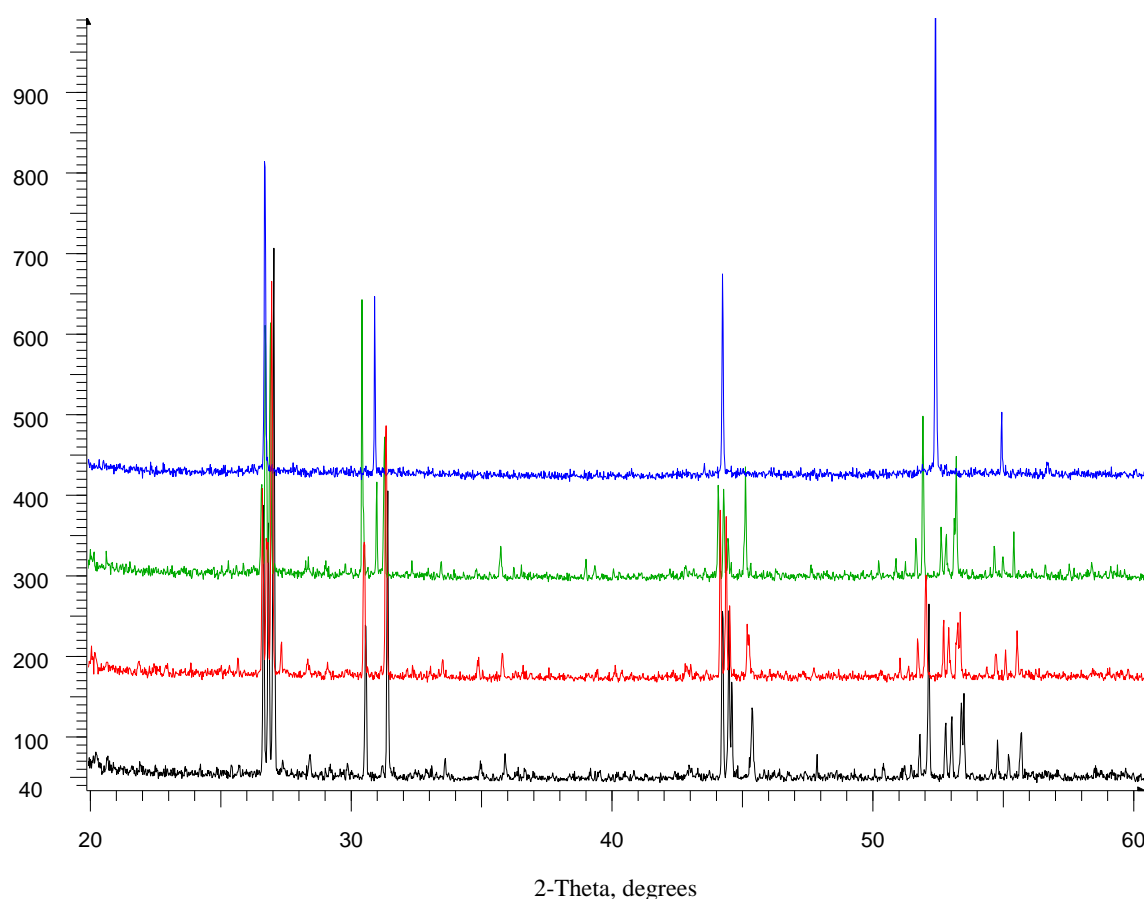


Figure 3.10 Variable temperature XPD results recorded for $\text{Bi}_9\text{ReO}_{17}$ at 823 K (black), 923 K (red), 1023 K (green) and 1123 K (blue).

results, between 25° and 30° 2θ , for the temperature range 823 K to 1023 K. The peak at around 27.3° becomes more apparent with increasing temperature, being most apparent at 923 K, corresponding with the broad endothermic curve revealed by DTA. Thereafter, this peak decreases as transformation to a face-centred cubic cell is evident by 1123 K.

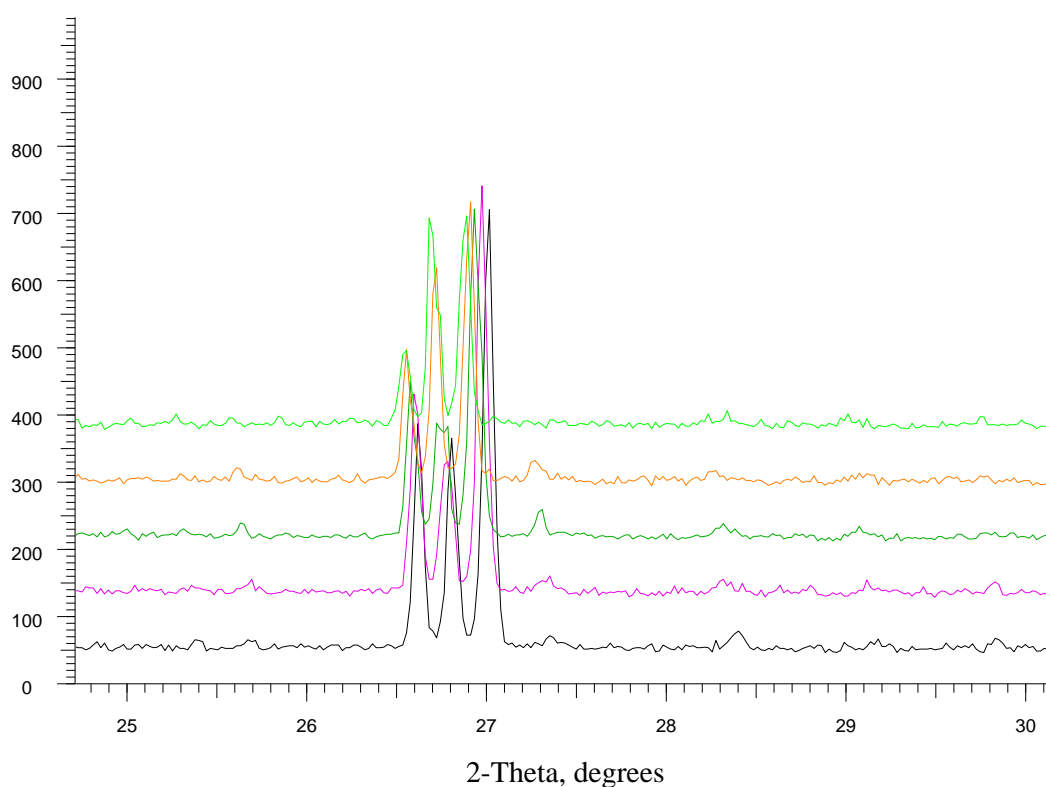


Figure 3.11 Variable temperature XPD results recorded for $\text{Bi}_9\text{ReO}_{17}$, between 25° and 30° 2θ , at 823 K (black), 873 K (purple), 923 K (dark green), 973 K (orange) and 1023 K (light green).

XPD results indicated that upon quenching of $\text{Bi}_9\text{ReO}_{17}$ from 1073 K in liquid nitrogen, the same cubic structure was formed that was shown by variable temperature XPD experiments at 1123 K. This high temperature phase could be indexed on a face-centred cubic unit cell, space group symmetry $\text{Fm}\bar{3}\text{m}$, with lattice parameter $a = 5.414(2)$ Å when cooled to room temperature, and $a = 5.779(2)$ Å for data collected at 1123 K.

DTA was again employed to investigate any phase changes that may occur in this face-centred cubic quenched form of $\text{Bi}_9\text{ReO}_{17}$, over a temperature range of 298 K to 1073 K. The results are displayed in Figure 3.12, where energy changes can be seen for both the heating curve (lower) and cooling curve (upper). A small but significant exothermic peak, with a peak onset at 773 K, superimposed on a similar broad endothermic curve as for the ordered $\text{Bi}_9\text{ReO}_{17}$ material, is apparent in the heating curve. This implies that the face-centred cubic material may decompose back to the monoclinic structure of ordered $\text{Bi}_9\text{ReO}_{17}$ at this temperature, and again undergo a gradual minor change in the structure with increasing temperature due to possible rotations of the ReO_4 tetrahedra in the monoclinic cell. The heating curve also shows a more considerable endothermic energy change, with a peak onset at 1005 K, suggestive of a phase change back to face-centred cubic. This phase change occurs at the same temperature as for the ordered $\text{Bi}_9\text{ReO}_{17}$ material. The cooling curve shows an exothermic energy change, with a peak onset at 941 K, again occurring at the same temperature as ordered $\text{Bi}_9\text{ReO}_{17}$, as the phase change is reversed and the structure reverts back to its room temperature form. As for the ordered $\text{Bi}_9\text{ReO}_{17}$ material, the large hysteresis is suggestive of a first order phase transition.

The structure of this material when heated to 798 K was confirmed to be the same as that of ordered $\text{Bi}_9\text{ReO}_{17}$ at the corresponding temperature, by XPD of the liquid nitrogen quenched fcc $\text{Bi}_9\text{ReO}_{17}$ material heated at 798 K for 3 h in air.

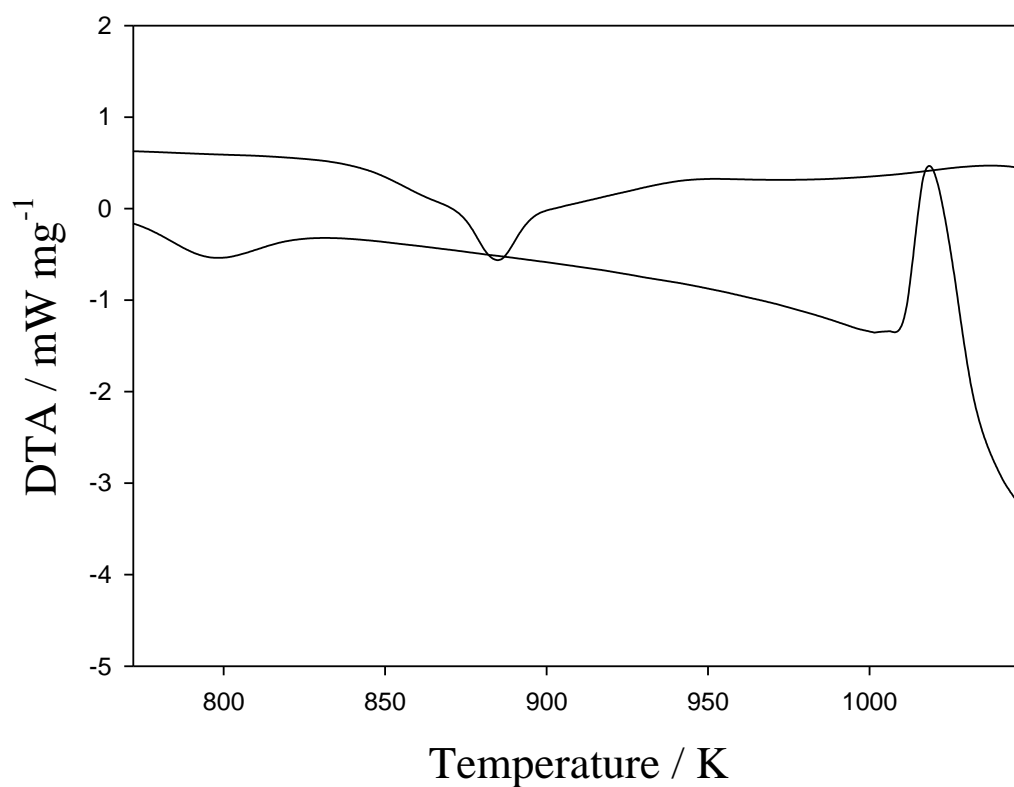


Figure 3.12 DTA results for face-centred cubic quenched $\text{Bi}_9\text{ReO}_{17}$, showing the heating curve (lower) and cooling curve (upper).

XPD results indicated that by quenching $\text{Bi}_9\text{ReO}_{17}$ in air down to room temperature, a different phase was produced to that of both the liquid nitrogen face centred cubic and the furnace-cooled ordered monoclinic forms. This metastable phase, which is undetected by variable temperature XPD, was observed by Ling *et al.*⁵ although the structure remained unsolved. Figure 3.13 shows the XPD pattern for this air quenched phase.

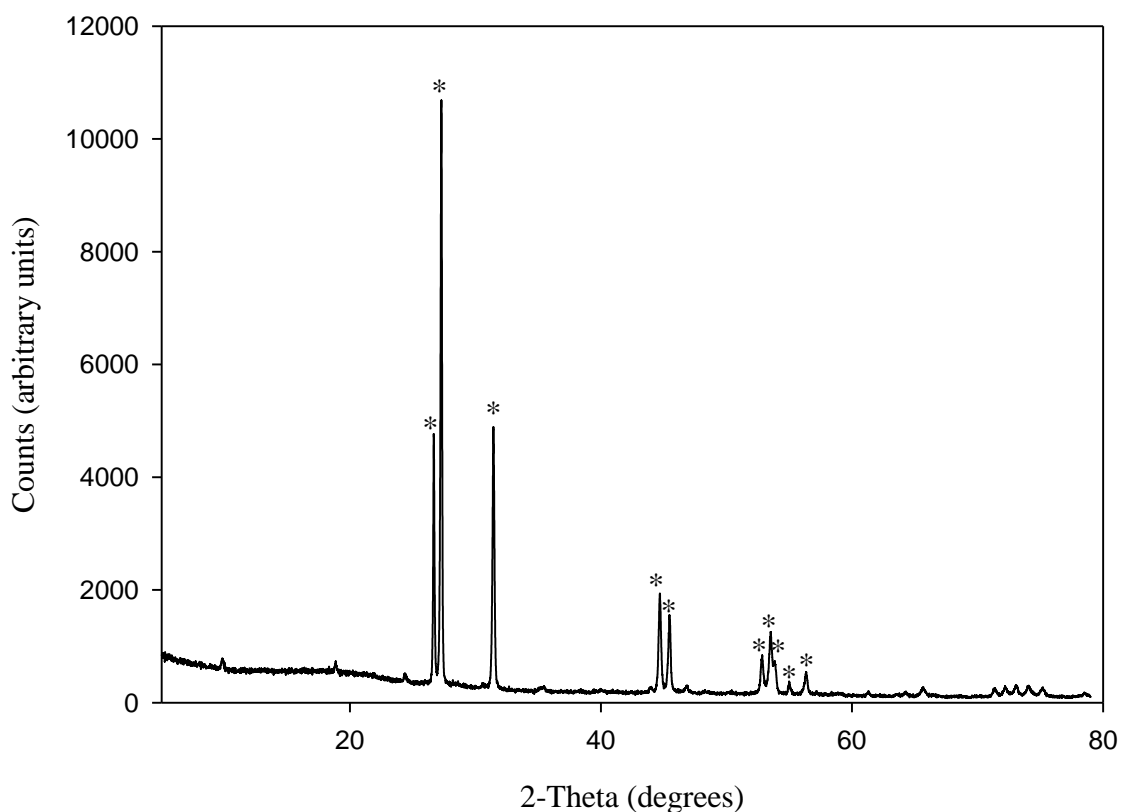


Figure 3.13 XPD pattern for air quenched $\text{Bi}_9\text{ReO}_{17}$.

The splittings of the cubic fluorite subcell peaks, indicated by *, were indicative of a rhombohedrally distorted subcell (cube stretched along a $[111]$ direction), with hexagonal parameters $a = 3.93(4)$ and $c = 9.78(9)$ Å. Subsequent indexing the XPD reflection peaks to a multiple of the subcell resulted in the supercell being ascertained, signifying a structure with monoclinic symmetry where $a = 9.770(8)$, $b = 3.974(6)$, $c = 9.897(10)$ Å with $\beta = 109.8(1)^\circ$.

The hexagonal subcell, displaying crystal symmetry $R\bar{3}m$, can be thought of as a ‘stretched’ fluorite cube, as shown in Figure 3.14, and is related to the fluorite edge length (a_f) by:

- $a_{subcell} = a_f / \sqrt{2} \text{ /Å}$

Equation 3.1

- $c_{subcell} = a_f \times \sqrt{3} \text{ /Å}$

Equation 3.2

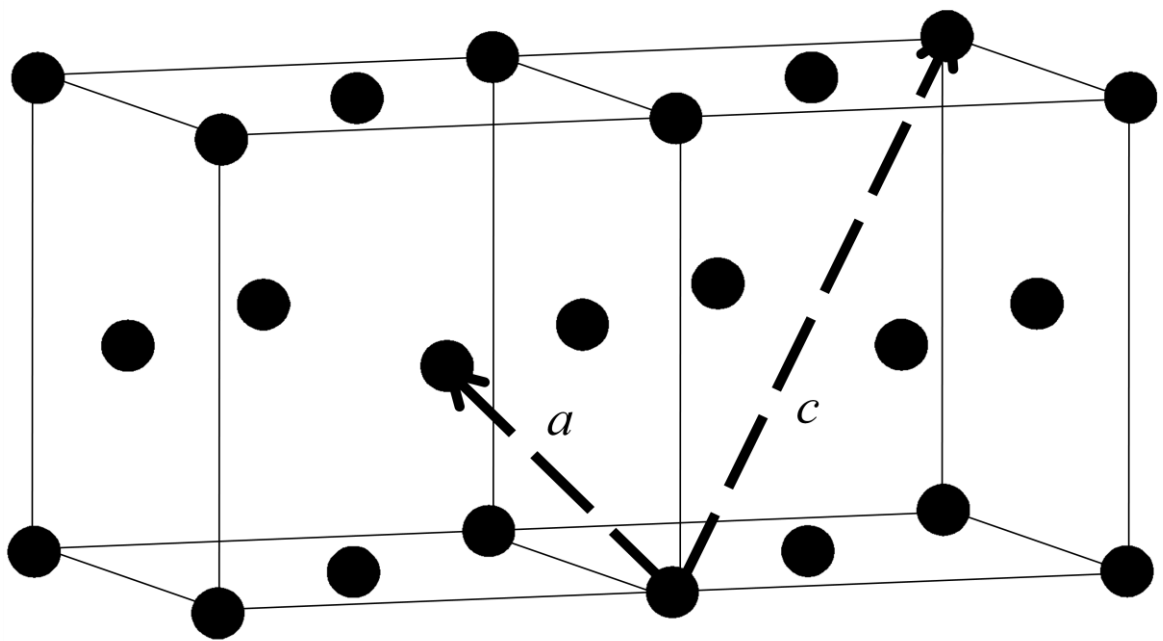


Figure 3.14 The relationship between fluorite and the subcell of air quenched $\text{Bi}_9\text{ReO}_{17}$.

The monoclinic supercell, having $P2_1/m$ space group symmetry, can be deliberated as having a relationship to the subcell whereby:

- $a_{supercell} = 4(\sqrt{3}a_{subcell}/3)/\cos(\beta - 90^\circ) \text{ /}\text{\AA}$

Equation 3.3

- $b_{supercell} = a_{subcell} \text{ /}\text{\AA}$

Equation 3.4

- $c_{supercell} = c_{subcell} \text{ /}\text{\AA}$

Equation 3.5

This relationship is illustrated in Figure 3.15.

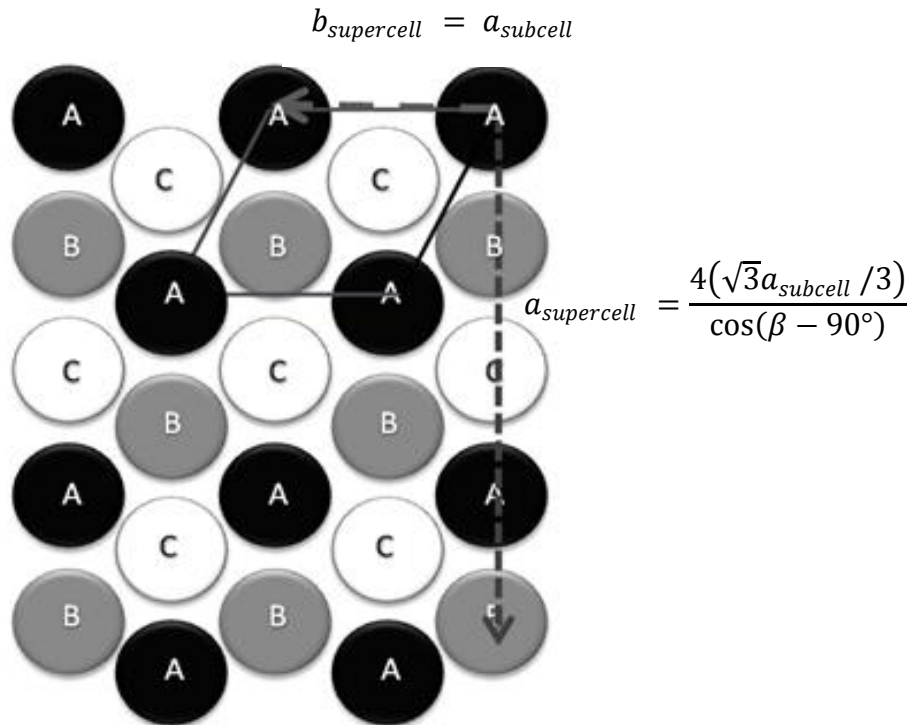


Figure 3.15 The hexagonal subcell, viewed along [001], highlighting the relationship between $a_{supercell}$, $b_{supercell}$ and $a_{subcell}$. $c_{supercell}$ is equivalent to $c_{subcell}$. The cubic close packed (ABC...) layers are shown.

Subsequent structural refinements were made using these XPD data, based on the Rietveld method¹², using the program GSAS¹³. The refinement was based on a structure with monoclinic symmetry and the space group $P2_1/m$, initially using idealised atom positions derived using the program Cryscon¹⁴ for this space group, inputting atom parameters from the hexagonal subcell along with the relationship between subcell and supercell, given in Equations 3.3-3.5. The atomic coordinates generated are listed in Table 3.9.

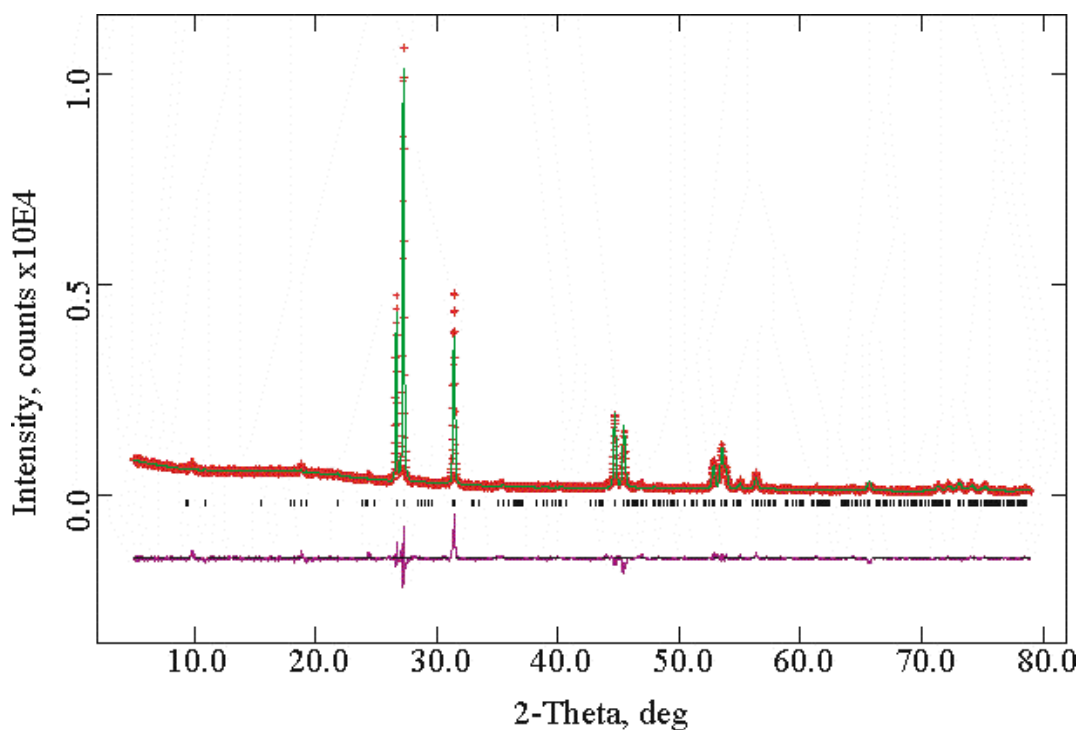
Table 3.9 Atomic coordinates generated by Cryscon¹⁴ with space group $P2_1/m$, where $a = 9.8$, $b = 4.0$, $c = 9.9$ Å, $\beta = 109.8^\circ$. All cations are represented by Bi.

Atom number	Atom Type	x	y	z	Multiplicity
1	Bi	0.0625	0.2500	0.1875	2
2	Bi	0.1875	0.7500	0.5625	2
3	Bi	0.5625	0.2500	0.6875	2
4	Bi	0.3125	0.2500	0.9375	2
5	O	0.0625	0.2500	0.4375	2
6	O	0.4375	0.7500	0.5625	2
7	O	0.1875	0.7500	0.3125	2
8	O	0.3125	0.2500	0.6875	2
9	O	0.3125	0.2500	0.1875	2
10	O	0.9375	0.7500	0.0625	2
11	O	0.1875	0.7500	0.8125	2
12	O	0.5625	0.2500	0.9375	2

Structural refinement of XPD data of the monoclinic quenched form of $\text{Bi}_9\text{ReO}_{17}$ was carried out. The final refined unit cell parameters were $a = 9.798(1)$, $b = 3.9843(5)$, $c = 10.0025(6)$ Å, $\beta = 109.91(1)^\circ$. Refinement statistics for 56 variables were $R_p = 0.087$, $R_{wp} = 0.061$, and $\chi^2 = 2.74$. Refined structural data are given in Table 3.10, and the fitted XPD profile shown in Figure 3.16. In the refinement, all cations were assigned a single variable temperature factor, but oxygen temperature factors were constrained to a sensible value for ambient temperature oxygen atoms. Cation positions were allowed to vary, but due to the insensitivity of oxygen atoms by XPD analysis in the presence of heavy Bi and Re, oxygen positions were constrained to their ideal sites, and their occupancies unrefined but constrained to be equal and to conform with the correct overall composition. The final refinement indicated a slight preference for Re to be located on the Bi1 site, but any Bi/Re order is very difficult to determine since their scattering factors for XPD are very similar. Clearly the refinement is incomplete for this material, since we cannot model the O positions reliably, and no attempt has been made to determine the O atoms that are linked to Re with very short Re-O bonds. The crystal structure of the monoclinic quenched form of $\text{Bi}_9\text{ReO}_{17}$ is shown in Figure 3.17.

Table 3.10 Refined structural information for air quenched monoclinic Bi₉ReO₁₇.

Atom	Site Symmetry	<i>x</i>	<i>y</i>	<i>z</i>	Fractional Occupancy	Uiso x 100 / Å ²
Bi1	2e	0.067(2)	0.25	0.185(2)	0.6	6.1(1)
Bi2	2e	0.172(2)	0.75	0.558(3)	1	6.1(1)
Bi3	2e	0.555(2)	0.25	0.679(2)	1	6.1(1)
Bi4	2e	0.325(2)	0.25	0.937(3)	1	6.1(1)
Re1	2e	0.067(2)	0.25	0.185(3)	0.4	6.1(1)
O1	2e	0.0625	0.25	0.4375	0.85	2.5
O2	2e	0.4375	0.75	0.5635	0.85	2.5
O3	2e	0.1875	0.75	0.3125	0.85	2.5
O4	2e	0.3125	0.25	0.6875	0.85	2.5
O5	2e	0.3125	0.25	0.1875	0.85	2.5
O6	2e	0.9375	0.75	0.0625	0.85	2.5
O7	2e	0.1875	0.75	0.8125	0.85	2.5
O8	2e	0.5625	0.25	0.9375	0.85	2.5

**Figure 3.16** The observed (+), calculated (-) and difference XPD profiles for the final Rietveld refinement of air quenched monoclinic Bi₉ReO₁₇.

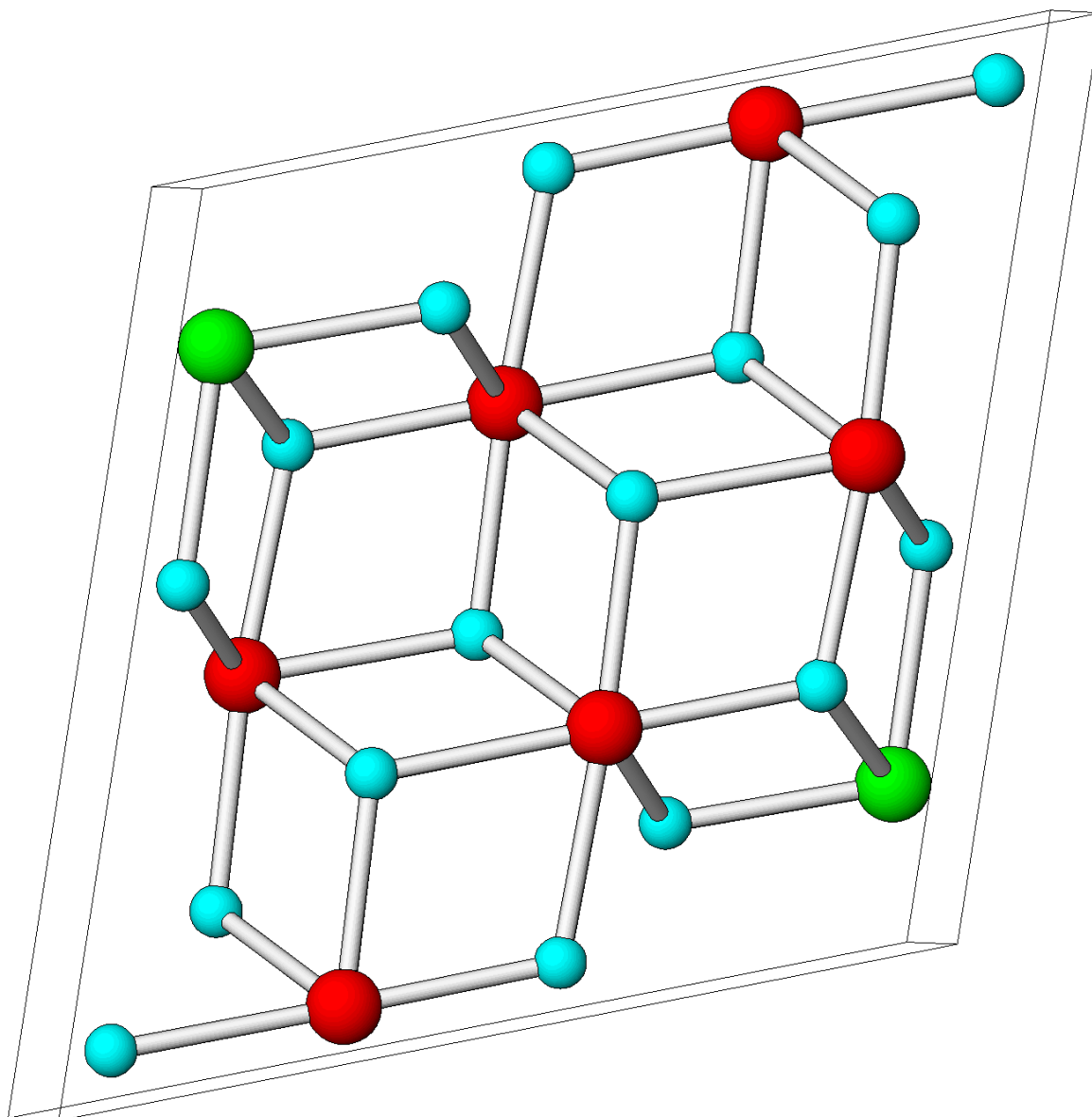


Figure 3.17 The crystal structure of air quenched $\text{Bi}_9\text{ReO}_{17}$, where the red spheres represent the pure bismuth sites, the green spheres represent the shared Bi/Re site and the blue spheres represent oxygen.

Any phase changes that may occur in this monoclinic quenched form of $\text{Bi}_9\text{ReO}_{17}$ were investigated by DTA, over a temperature range of 298 K to 1073 K. The results are displayed in Figure 3.18, where energy changes can be seen for both the heating curve (lower)

and cooling curve (upper). A phase change is suggested in the heating curve which shows an endothermic energy change, with a peak onset at 998 K, occurring at a similar temperature to that observed for ordered $\text{Bi}_9\text{ReO}_{17}$ and quenched fcc $\text{Bi}_9\text{ReO}_{17}$. As the phase change is reversed an exothermic energy change is seen in the cooling curve, with a peak onset at 908 K. This hysteresis is similar to that observed for the fully ordered and face-centred cubic materials and of course all materials would be expected to be identical when heated to 973 K, just below the transition to the fcc form. A broad endothermic peak in the heating curve, with a peak onset at 800 K, is also evident in the results, which again may relate to disordering of the ReO_4 tetrahedra. Interestingly, the exothermic curve suggests that upon cooling, structural

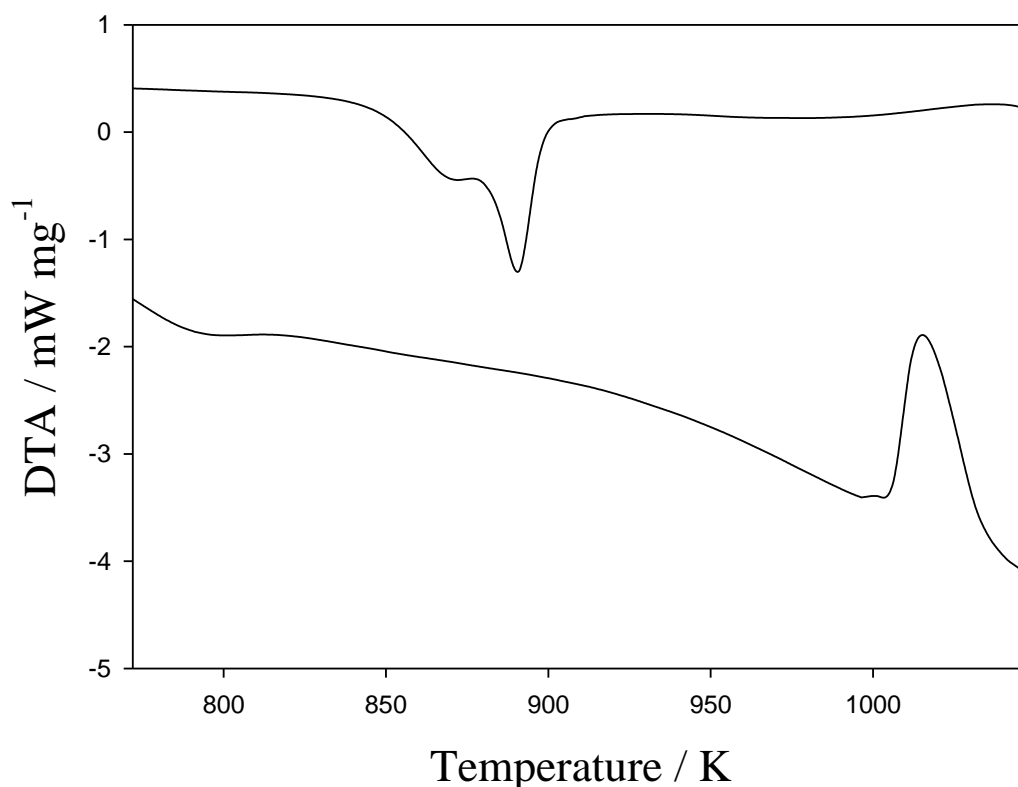


Figure 3.18 DTA results for monoclinic air quenched $\text{Bi}_9\text{ReO}_{17}$, showing the heating curve (lower) and cooling curve (upper).

changes transpire via a complex mechanism, appearing to occur in two stages. This mechanism remains unidentified at present.

The nature of this gradual transition to face-centred cubic upon heating was investigated by variable temperature XPD experiments. Figure 3.19 shows the variable temperature XPD patterns for the air quenched monoclinic form of $\text{Bi}_9\text{ReO}_{17}$, over a temperature range of 673 K to 1073 K. The results show that a phase change to a metastable intermediate form is occurring at 723 K, which remains stable until the phase change to the high temperature fcc form is observed at 1073 K. This monoclinic air quenched sample

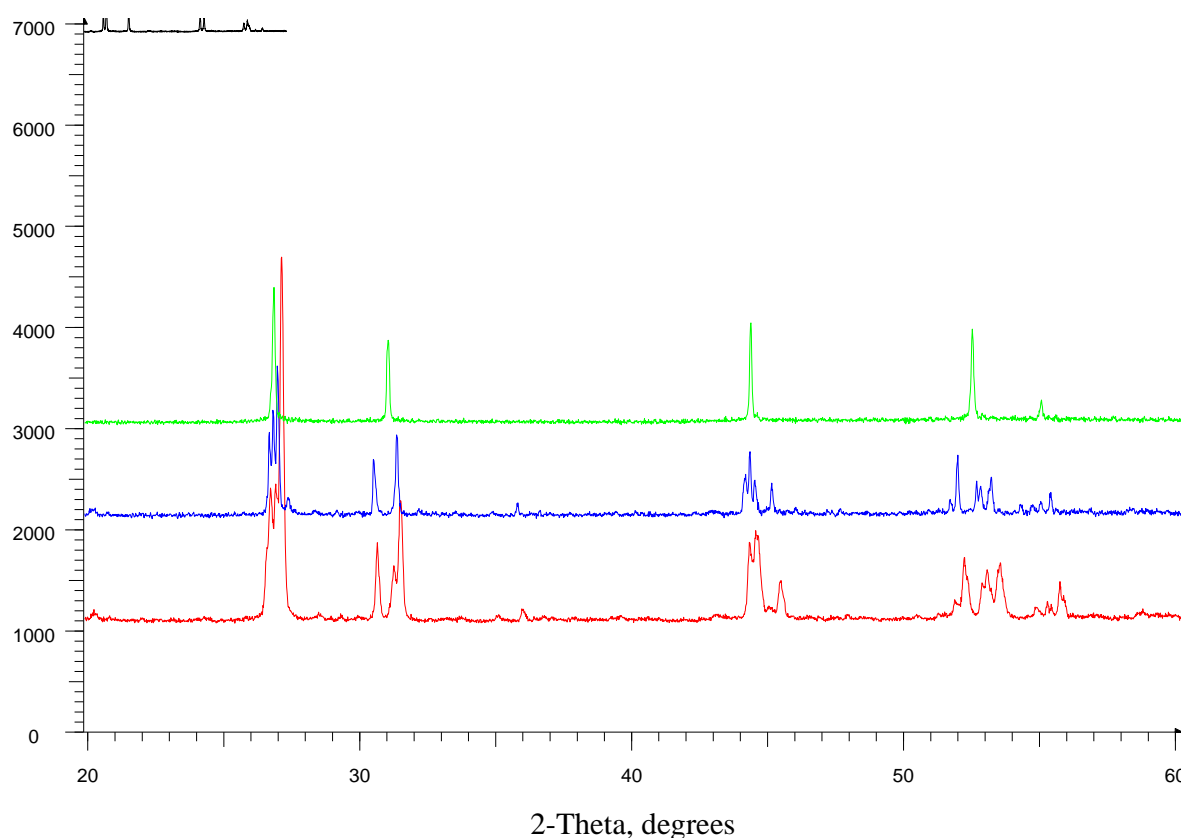


Figure 3.19 Variable temperature XPD results recorded for monoclinic air quenched $\text{Bi}_9\text{ReO}_{17}$ at 673 K (black), 723 K (red), 1023 K (blue) and 1073 K (green).

therefore clearly behaves in a very different way to that of the slow-cooled ordered $\text{Bi}_9\text{ReO}_{17}$ material, which would be expected, and upon heating, the structure transforms to give either a multiphase material or a material with an entirely different structure, the nature of which remains unidentified at present.

3.3.4 Ionic Conductivity

The quenched forms of $\text{Bi}_9\text{ReO}_{17}$ might be expected to exhibit high oxide ion conducting properties owing to the disordered nature of the system. Impedance spectroscopy was therefore employed to collect oxide ion conductivity data, with measurements made across a frequency range 1 Hz to 1×10^6 Hz and temperature range 473 to 773 K for $\text{Bi}_9\text{ReO}_{17}$, and 473 to 673 K for the quenched forms of $\text{Bi}_9\text{ReO}_{17}$ due to instability of these structures above this temperature, where transformation to a new, as yet incompletely characterised, structure occurs. XPD data confirmed that the fcc and monoclinic quenched structures had been retained throughout the impedance measurements. Materials were prepared and determinations made using the method outlined in Section 2.4.1. The density for each sample pellet was calculated and compared with the density of its unit cell, allowing the determination that all samples had a density in the range of 85 to 95 % of the theoretical.

The complex plane impedance plots could be fitted to a single semicircle (Figure 3.20) and resistance was therefore assigned to bulk effects; electronic contributions to conductivity was assumed to be negligible as previously found for similar bismuth rhenium oxides⁸. The conductivity was determined from the extrapolated intercept of the semicircle with the real axis in the complex plane plots. Figure 3.21 shows the plot of $\log \sigma$ versus $1000\text{K}/T$ for

$\text{Bi}_9\text{ReO}_{17}$, cubic quenched $\text{Bi}_9\text{ReO}_{17}$ and monoclinic quenched $\text{Bi}_9\text{ReO}_{17}$. The Arrhenius activation energies, E_a , for these materials determined from these plots are listed in Table 3.11.

Table 3.11 Activation energies, E_a , for $\text{Bi}_9\text{ReO}_{17}$, cubic quenched $\text{Bi}_9\text{ReO}_{17}$ and monoclinic quenched $\text{Bi}_9\text{ReO}_{17}$.

Material	E_a/eV
$\text{Bi}_9\text{ReO}_{17}$	0.99 (T<673 K)
cubic quenched $\text{Bi}_9\text{ReO}_{17}$	0.69
monoclinic quenched $\text{Bi}_9\text{ReO}_{17}$	0.76

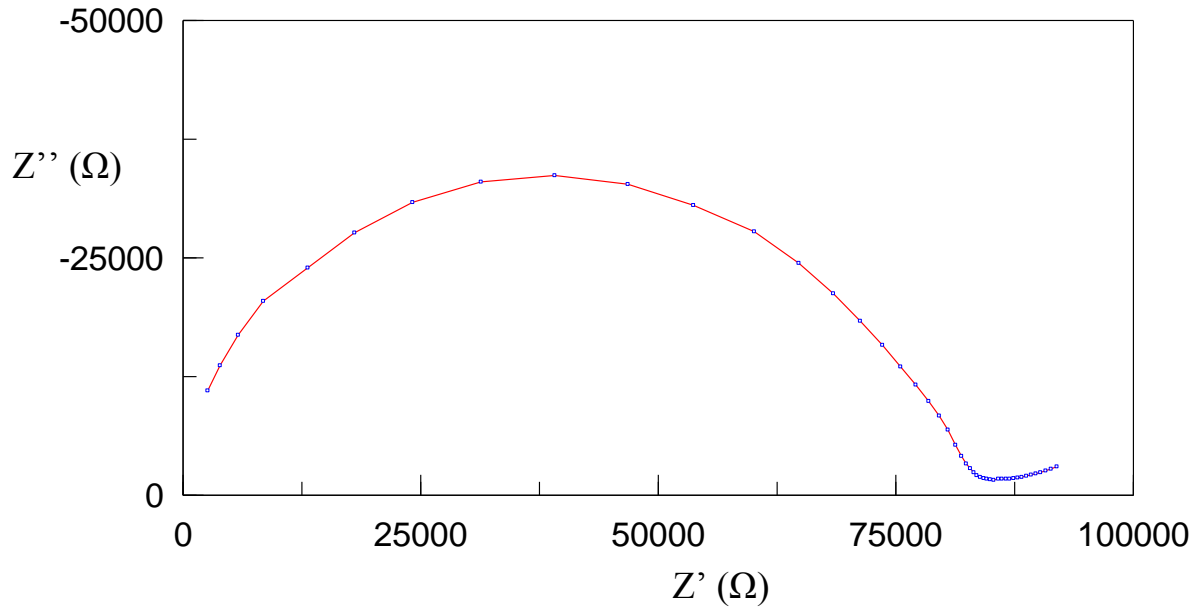


Figure 3.20 Complex plane impedance plot for monoclinic quenched $\text{Bi}_9\text{ReO}_{17}$ at 481 K.

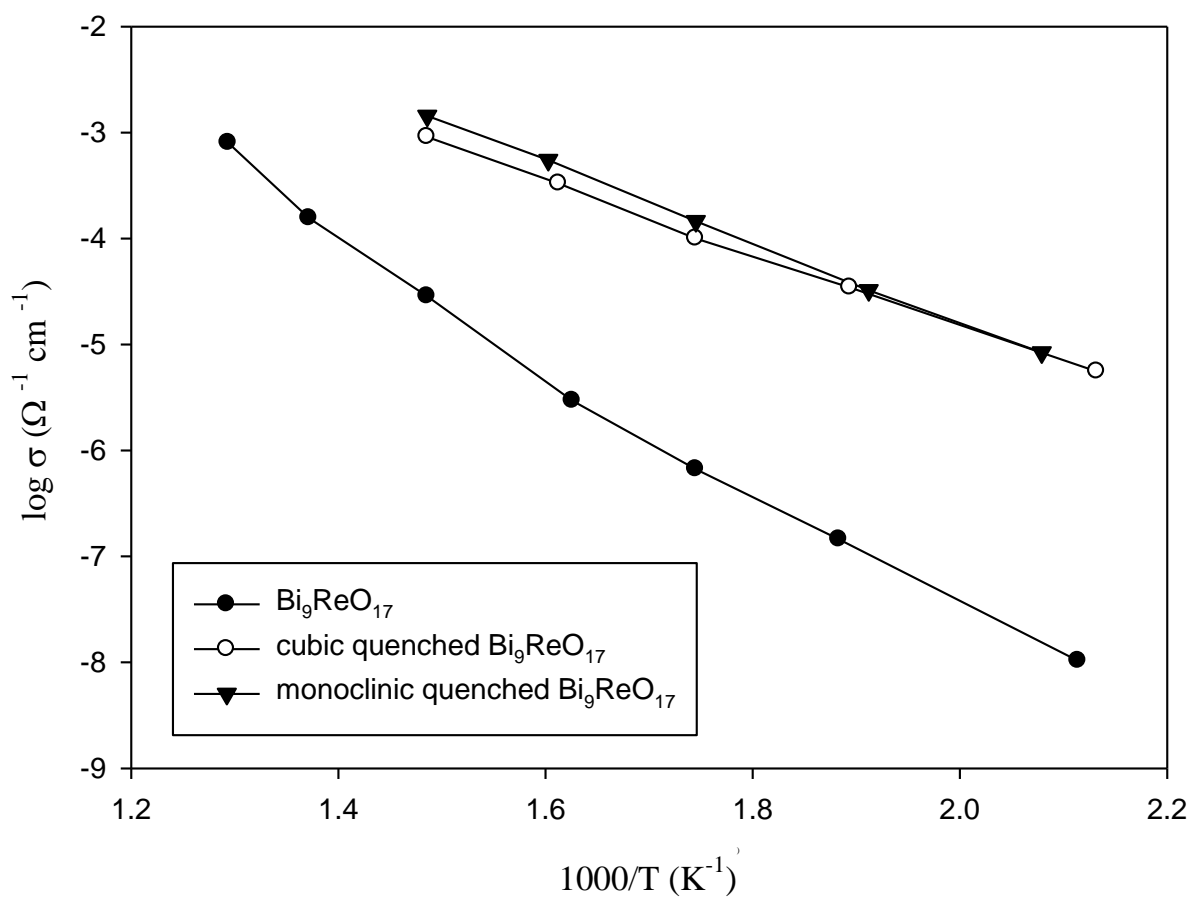


Figure 3.21 Arrhenius plots of conductivity determined by impedance spectroscopy for $\text{Bi}_9\text{ReO}_{17}$, cubic quenched $\text{Bi}_9\text{ReO}_{17}$ and monoclinic quenched $\text{Bi}_9\text{ReO}_{17}$.

The fully ordered $\text{Bi}_9\text{ReO}_{17}$ displays good oxide ion conductivity of $2.9 \times 10^{-5} \Omega^{-1} \text{cm}^{-1}$ at 673 K, but significantly lower than that of $\text{Bi}_{28}\text{Re}_2\text{O}_{49}$ at the same temperature, $5.4 \times 10^{-4} \Omega^{-1} \text{cm}^{-1}$ ³. This is consistent with the suggestion¹¹ that in doped bismuth oxide materials the conductivities decrease with increasing substituent oxide content, but may also indicate that the two different coordinations for Re in $\text{Bi}_{28}\text{Re}_2\text{O}_{49}$ (octahedral and tetrahedral) may be involved in its conduction mechanism as previously suggested³. The activation energy calculated for $\text{Bi}_9\text{ReO}_{17}$ is also considerably higher than that of $\text{Bi}_{28}\text{Re}_2\text{O}_{49}$, where $E_a = 0.62 \text{ eV}$ ³, suggesting a different mechanism and indicating that the conductivity of $\text{Bi}_9\text{ReO}_{17}$ at higher temperatures may in fact be greater than that of $\text{Bi}_{28}\text{Re}_2\text{O}_{49}$. The conductivity recorded for $\text{Bi}_9\text{ReO}_{17}$ at 773 K, $8.0 \times 10^{-4} \Omega^{-1} \text{cm}^{-1}$, is similar to that observed for other well characterised stabilised bismuth oxide ion conductors, and is just outside an order of magnitude of the fcc ionic conductor $(\text{Bi}_2\text{O}_3)_{0.8}(\text{Ta}_2\text{O}_5)_{0.2}$ which has a conductivity of $5.0 \times 10^{-3} \Omega^{-1} \text{cm}^{-1}$ at 773 K¹¹. There is a notable upturn in conductivity observed at 673 K for the ordered $\text{Bi}_9\text{ReO}_{17}$ material. This appears to relate to a minor structural change observed by DTA and VT-XRD experiments (discussed in Section 3.3.3), which may be due to enhanced libration / rotation of the ReO_4 groups within the otherwise ordered $\text{Bi}_9\text{ReO}_{17}$ structure.

The high temperature face-centred cubic and monoclinic forms of $\text{Bi}_9\text{ReO}_{17}$ show improved oxide ion conductivity, as expected for these disordered $\delta\text{-Bi}_2\text{O}_3$ related structures, being 1-2 orders of magnitude higher than that of ordered $\text{Bi}_9\text{ReO}_{17}$ over the temperature range studied, $473 \text{ K} < T < 673 \text{ K}$. This high level of anion disorder is undoubtedly responsible for the much improved conductivity in these materials with identical composition. The large difference in activation energy between the disordered and ordered forms of $\text{Bi}_9\text{ReO}_{17}$ confirms that different conductivity mechanisms apply. Both the face-centred cubic

quenched form of $\text{Bi}_9\text{ReO}_{17}$ ($\sigma = 9.1 \times 10^{-4} \Omega^{-1} \text{ cm}^{-1}$ at 673 K) and the monoclinic quenched form of $\text{Bi}_9\text{ReO}_{17}$ ($\sigma = 2.85 \times 10^{-5} \Omega^{-1} \text{ cm}^{-1}$ at 673 K), display conductivities which are greater than that displayed by $\text{Bi}_{28}\text{Re}_2\text{O}_{49}$ at the corresponding temperature ($5.4 \times 10^{-4} \Omega^{-1} \text{ cm}^{-1}$ at 673 K)³ in accordance with their disordered structures, despite having a higher cation substitution level.

3.4 References

- 1 Cheetham, A. K.; Rae Smith, A. R.; *Acta. Cryst.* **B41** (1985) 225
- 2 Crumpton, T. E. *PhD Thesis, The University of Birmingham*, (2003)
- 3 Crumpton, T. E.; Mosselmans, J. F. W.; Greaves, C. *J. Mater. Chem.* **15** (2005) 164
- 4 T. Fries, G. Lang, S. Kemmler-Sach, *Solid State Ionics* **89** (1996) 233
- 5 Sharma, N.; Withers, R. L.; Knight, K. S.; Ling, C. D. *J. Solid State Chem.* **182** (2009) 2468
- 6 I. D. Brown, D. Altermatt, *Acta Crystallogr.* **B41** (1985) 244
- 7 H. A. Harwig, *Z. Anorg. Chem.* **444** (1978) 151
- 8 Pun, R.; Feteira, A. M.; Sincliar, D. C.; Greaves, C. *J. Am. Chem. Soc.* **128** (2006) 15386
- 9 Pun, R.; Gameson, I.; Berry, F.; Greaves, C. *J. Phys. Chem. Solids* **69** (2008) 2687
- 10 Morrow, J. C. *Acta. Cryst.* **13** (1960) 443
- 11 Takahashi, T.; Iwahara, H. *Mat. Res. Bull.* **13** (1978) 1447
- 12 Young, R. A. *The Rietveld Method* International Union of Crystallography, Oxford University Press (1993)
- 13 Larson, A. C.; Von Dreele, R. B. *General Structure Analysis System (GSAS)* Los Alamos National Laboratory, Los Alamos, NM (1994)
- 14 Available from Shapessoftware: <http://www.shapesoftware.com/>

CHAPTER 4

The Structure and Ionic Conductivity of Two New Fluorite Related Rhenium and Calcium doped Bismuth Oxide Materials, $\text{Bi}_6\text{Ca}_3\text{ReO}_{15.5}$ and $\text{Bi}_{10}\text{Ca}_5\text{ReO}_{23.5}$

4.1 Introduction

The successful synthesis of materials containing Bi and small amounts of Re oxoanions, such as $\text{Bi}_{28}\text{Re}_2\text{O}_{49}$ ¹ and $\text{Bi}_9\text{ReO}_{17}$ ², discussed in Chapter 1, indicate that further doping might achieve interesting new phases.

The early work of Takahashi *et al.*³ found that the doping of Bi_2O_3 with calcium gave $\text{Bi}_{1-x}\text{Ca}_x\text{O}_{1.5-x/2}$, where $0.12 < x < 0.18$, with good ionic conductivity.

Since the addition of rhenium to bismuth oxide creates ion displacement onto the oxygen sites, substitution of a 2+ cation for 3+ bismuth would create a charge discrepancy that would be compensated by temperature independent extrinsic oxygen vacancies. The similarity in size of Ca^{2+} and Bi^{3+} (6-coordinate Ca^{2+} ionic radius = 114 pm, 6 co-ordinate Bi^{3+} ionic radius = 117 pm),⁴ suggests that Ca^{2+} might prove ideal in creating oxide ion vacancies in the structure.

This Chapter reports on two previously unreported Bi-Ca-Re oxides, both of which have fluorite-related structures. $\text{Bi}_6\text{Ca}_3\text{ReO}_{15.5}$ formed a face-centred cubic ($\text{Fm}\bar{3}\text{m}$) fluorite-

related structure ($a = 5.416 \text{ \AA}$), and $\text{Bi}_{10}\text{Ca}_5\text{ReO}_{23.5}$ a body-centred cubic ($I\bar{4}3d$) material ($a = 21.940 \text{ \AA}$) that is a superstructure of the $\text{Bi}_6\text{Ca}_3\text{ReO}_{15.5}$ phase. The structures and ionic conductivities of both materials were investigated.

4.2 Experimental

Stoichiometric amounts of Bi_2O_3 , CaCO_3 and NH_4ReO_4 were intimately ground and calcined for 12 h in air at 1073 K. It was necessary to carry out several subsequent cycles of regrinding and reheating to ensure complete reaction and the acquisition of single phase products. The materials were characterised by XPD, NPD, SAED and impedance spectroscopy, as described in Chapter 2.

$\text{Bi}_{10}\text{Ca}_5\text{ReO}_{23.5}$ was investigated further. The thermal stability was examined by annealing at 773 K. Post-annealing, the sample was examined by XPD to examine phase transformations. The material was also subjected to quenching by heating to 1073 K, followed by removal from the furnace and quickly cooling to room temperature. $\text{Bi}_{10}\text{Ca}_5\text{ReO}_{23.5}$ was additionally characterised by variable temperature XPD and DTA to further examine phase changes which occur on heating.

4.3 Results and Discussion

4.3.1 The Structure of $\text{Bi}_6\text{Ca}_3\text{ReO}_{15.5}$

Initial examination by XPD indicated $\text{Bi}_6\text{Ca}_3\text{ReO}_{15.5}$ to be single phase. The structure was indexed according to a face-centred cubic unit cell with space group symmetry $\text{Fm}\bar{3}\text{m}$ and lattice parameter $a = 5.50545(5) \text{ \AA}$. Figure 4.1 shows the XPD pattern recorded from this material.

Heavy bismuth and rhenium atoms scatter X-rays strongly compared to O atoms in the structure. Therefore, very little information could be obtained due to the insensitivity of the O atoms to X-rays using XPD techniques. Consequently, the XPD data were not amenable to refinement.

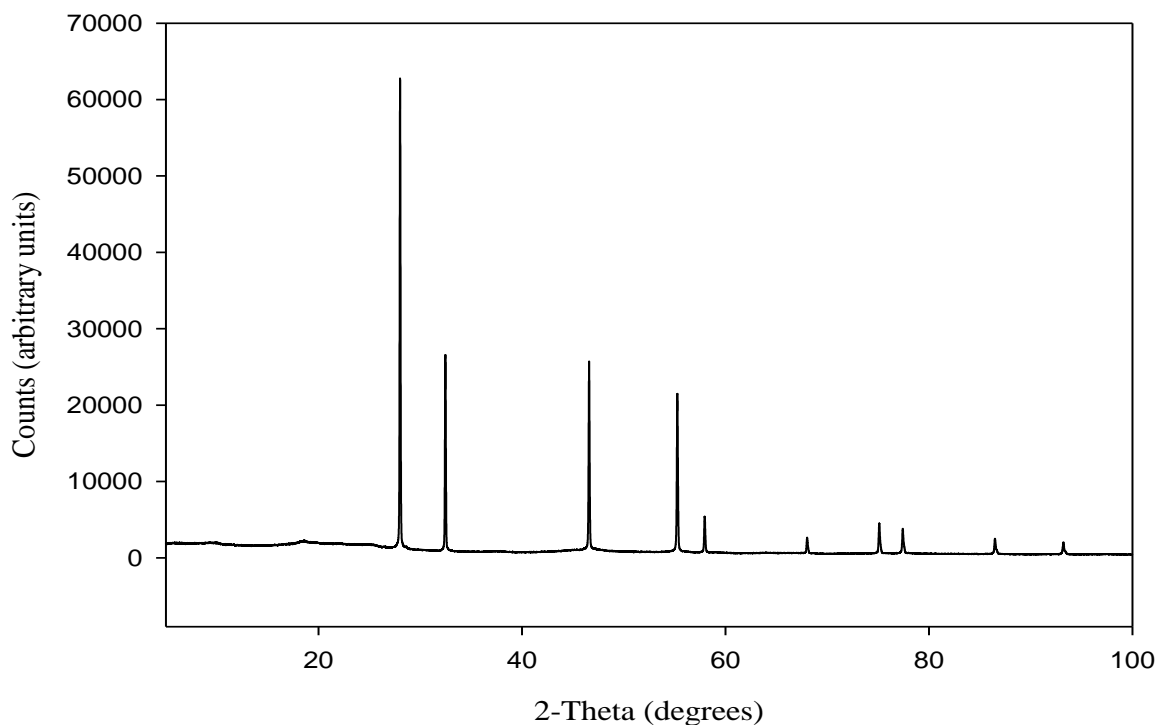


Figure 4.1 XPD pattern recorded from $\text{Bi}_6\text{Ca}_3\text{ReO}_{15.5}$.

Additional information on the structural details was achieved by high resolution NPD data collected at ambient temperature. This was specifically aimed at refining the fluorite-type oxygen site occupancies by exploiting the much greater sensitivity of NPD to oxygen atoms in the presence of the heavy metal atoms, Bi and Re. Consequent structural refinements were made using these data using the program GSAS⁵ based on the Rietveld method⁶.

A starting model for the refinement was based on that derived for pure $\delta\text{-Bi}_2\text{O}_3$ ⁷, space group $\text{Fm}\bar{3}\text{m}$, with the cations statistically distributed (Bi:Ca:Re = 6:3:1) at the $4a$ (0, 0, 0) sites and the oxygen atoms on their regular $8c$ ($\frac{1}{4}, \frac{1}{4}, \frac{1}{4}$) and interstitial $32f$ (x, x, x) sites. The final refined unit cell parameter in space group $\text{Fm}\bar{3}\text{m}$ was $a = 5.5092(2)$ Å. Refinement statistics for 53 variables were $R_p = 0.0125$, $R_{wp} = 0.0158$, and $\chi^2 = 1.392$. The fitted NPD profile, shown in Figure 4.2, indicates good agreement between observed and calculated profiles. The high level of disorder of the oxygen sublattice is reflected by both the presence of an extensive diffuse background and the decrease in peak intensities with 2θ . The refined structural information, shown in Table 4.1, also supports this with the high level of disorder being confirmed by the high thermal parameters for both cation and anion sites. Studies by Battle *et al.*⁷ suggested that, in doped $\delta\text{-Bi}_2\text{O}_3$ structures, the cations may shift along [100] from the $4a$ (0, 0, 0) site to the $24e$ ($x, 0, 0$). No strong evidence was found to support this, although the high cation temperature factor may be partly attributed to small displacements of this type. In the refinement all cations were assigned a single temperature factor, but separate values were used for the oxygen positions. Refinement suggests an oxygen content of $\text{Bi}_6\text{Ca}_3\text{ReO}_{14.9(7)}$, which agrees well with the expected composition assuming the presence of Re(VII), $\text{Bi}_6\text{Ca}_3\text{ReO}_{15.5}$. The refinement suggests that 52% of the oxide ions are displaced from their ideal fluorite site along [111] directions to the $32f$ (x, x, x) site. The position of the

$32f(x, x, x)$ interstitial oxygen site, where $x = 0.311(3)$, compares with other reported values of $x = 0.319(2)$ and $x = 0.32(1)$ for $(\text{Bi}_2\text{O}_3)_{0.8}(\text{Er}_2\text{O}_3)_{0.2}$ and $(\text{Bi}_2\text{O}_3)_{0.73}(\text{Y}_2\text{O}_3)_{0.27}$, respectively^{7,8}. However, these ternary oxides have a higher percentage of displaced oxide ions: 69% and 68% respectively. The structure of $\text{Bi}_6\text{Ca}_3\text{ReO}_{15.5}$ is shown in Figure 4.3.

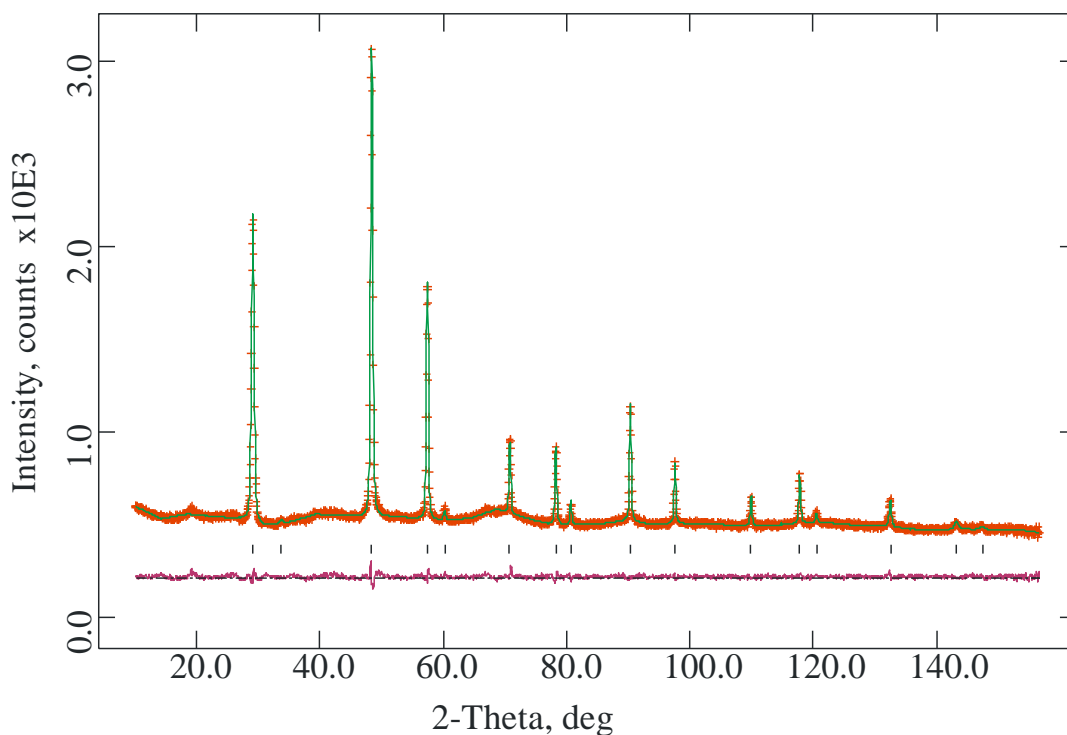


Figure 4.2 Observed (+), calculated (-), and difference NPD profiles for $\text{Bi}_6\text{Ca}_3\text{ReO}_{15.5}$.

Table 4.1 Refined structural information for NPD results of $\text{Bi}_6\text{Ca}_3\text{ReO}_{15.5}$, determined by Rietveld analysis.

Site					Fractional	Uiso x 100
Atom	Symmetry	x	y	z	occupancy	/ \AA^2
Bi	4a	0	0	0	0.6	5.44(4)
Ca	4a	0	0	0	0.3	5.44(4)
Re	4a	0	0	0	0.1	5.44(4)
O1	8c	0.25	0.25	0.25	0.35(3)	6.9(4)
O2	32f	0.311(3)	0.311(3)	0.311(3)	0.097(8)	16(1)

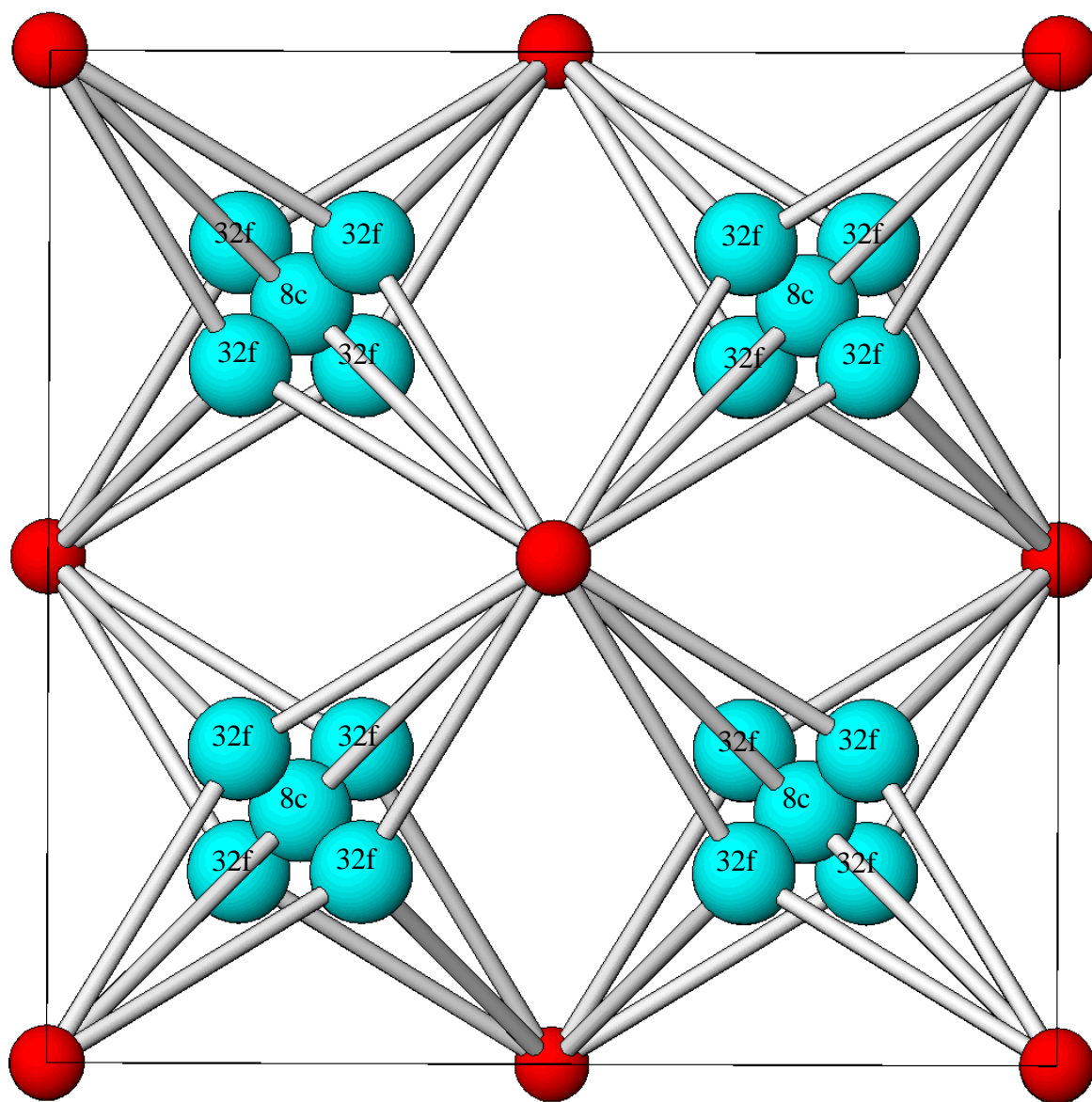


Figure 4.3 The structure of $\text{Bi}_6\text{Ca}_3\text{ReO}_{15.5}$ viewed along $[100]$, where the red spheres represent Bi/Ca/Re and the light blue spheres represent O.

4.3.2 The Structure of $\text{Bi}_{10}\text{Ca}_5\text{ReO}_{23.5}$

Inspection of the XPD pattern for $\text{Bi}_{10}\text{Ca}_5\text{ReO}_{23.5}$ indicated the presence of a superstructure which can be derived as $4 \times 4 \times 4$ superstructure of the subcell of $\text{Bi}_6\text{Ca}_3\text{ReO}_{15.5}$ with body centred cubic symmetry. Figure 4.4 shows the XPD pattern recorded from $\text{Bi}_{10}\text{Ca}_5\text{ReO}_{23.5}$. The subcell peaks, indicated by *, were indexed to a fcc structure where $a = 5.481(1) \text{ \AA}$. The supercell was then determined by indexing the XPD reflection peaks to a cell that was a multiple of the subcell, suggesting the structure to have a body centred cubic unit cell where $a = 21.940(14) \text{ \AA}$ and where $a_{\text{supercell}} = 4a_{\text{subcell}}$.

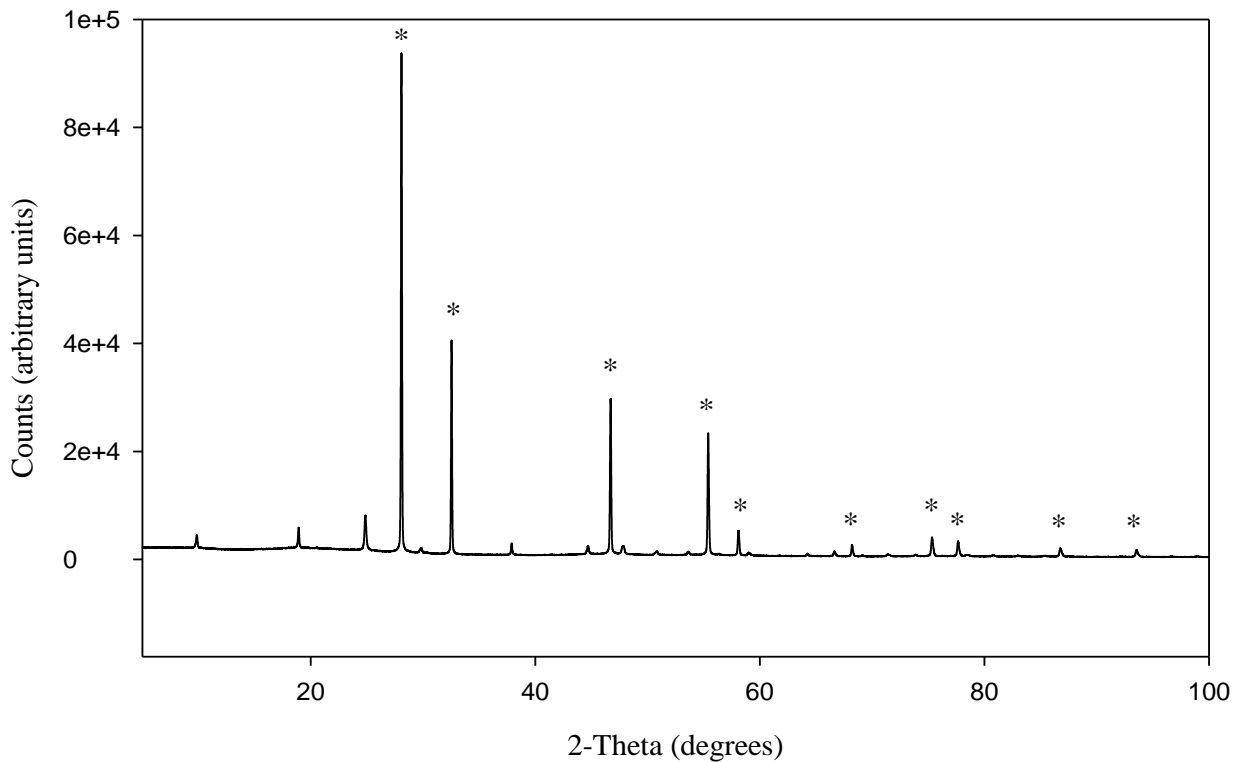


Figure 4.4 XPD pattern recorded from $\text{Bi}_{10}\text{Ca}_5\text{ReO}_{23.5}$.

This observation of a 4 x 4 x 4 superstructure of the fluorite subcell was confirmed by SAED. Figure 4.5 shows the observed SAED patterns for the 4 x 4 x 4 superlattice of $\text{Bi}_{10}\text{Ca}_5\text{ReO}_{23.5}$ viewed along [100], [111] and [110], allowing derivation of the reflection conditions hkl: $h+k+l = 2n$, 0kl: $k+l=2n$ and hhl: $2h+l=4n$. These correspond to the space group $\bar{I}43d$.

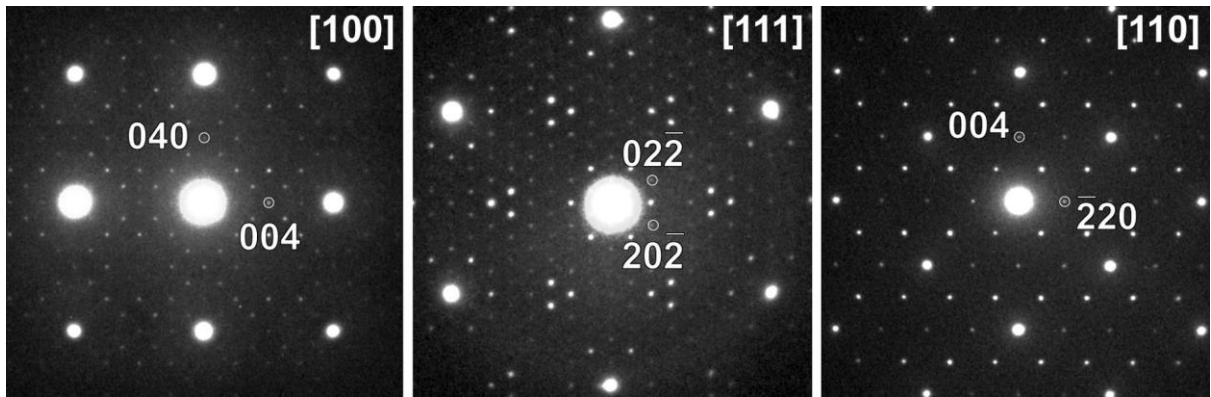


Figure 4.5 SAED patterns recorded from $\text{Bi}_{10}\text{Ca}_5\text{ReO}_{23.5}$.

Since XPD data are insensitive to order resulting from oxygen effects, Figure 4.4 shows that the superstructure found for the composition $\text{Bi}_{10}\text{Ca}_5\text{ReO}_{23.5}$ has a significant contribution from cation effects. Since cation order relating to Ca/Bi ions should have a more pronounced influence on the XPD pattern rather than the NPD pattern, a simultaneous refinement based on both X-ray and neutron data sets was employed.

Table 4.2 lists the atomic coordinates generated by the program Cryson⁹ for the space group $\bar{I}43d$. The subcell parameters were entered into the program, along with the relationship between the subcell and supercell, enabling the determination of atomic positions within the supercell. 256 cations were generated by Cryson, consistent with a unit cell of formula $\text{Bi}_{10}\text{Ca}_5\text{ReO}_{23.5}$.

Table 4.2 Atomic positions generated by Cryscon with space group $I\bar{4}3d$, $a = 21.940(14) \text{ \AA}$. All cations are represented by Bi.

Atom number	Atom Type	x	y	z	Multiplicity
1	Bi	0.7500	0.7500	0.7500	16
2	Bi	0.8750	0.8750	0.7500	48
3	Bi	0.0000	0.7500	0.7500	24
4	Bi	0.5000	0.7500	0.7500	24
5	Bi	0.1250	0.8750	0.7500	48
6	Bi	0.3750	0.8750	0.7500	48
7	Bi	0.6250	0.8750	0.7500	48
8	O	0.8125	0.8125	0.8125	16
9	O	0.9375	0.9375	0.8125	48
10	O	0.8125	0.8125	0.9375	48
11	O	0.9375	0.9375	0.9375	16
12	O	0.0625	0.8125	0.8125	48
13	O	0.3125	0.8125	0.8125	48
14	O	0.5625	0.8125	0.8125	48
15	O	0.5625	0.0625	0.8125	48
16	O	0.0625	0.8125	0.9375	48
17	O	0.3125	0.8125	0.9375	48
18	O	0.5625	0.8125	0.9375	48
19	O	0.0625	0.0625	0.9375	48

The refinement was based upon a structure with bcc cell symmetry and space group $I\bar{4}3d$ using the atomic positions generated from Cryscon in the starting model. The diffraction data were consistent with partial cation order but no oxygen order was apparent. Bi/Re order was very difficult to determine directly since the Bi and Re scattering factors are

similar for both X-ray and neutron diffraction. The overall composition suggests that the unit cell contains 16 Re atoms, and it was assumed that these atoms occupied the 16c site. The

Table 4.3 Refined structural information for Bi₁₀Ca₅ReO_{23.5}.

Site					Fractional	Uiso x 100
Atom	Symmetry	x	y	z	occupancy	/ Å ²
Re1	16c	0.7507(6)	0.7507(6)	0.7507(6)	1.000	4.45(4)
Bi2	48e	0.8716(8)	0.8691(8)	0.7469(8)	0.51(3)	4.45(4)
Bi3	24d	0.0000	0.7500	0.746(1)	0.29(2)	4.45(4)
Bi4	24d	0.5000	0.7500	0.752(1)	1.000	4.45(4)
Bi5	48e	0.1269(6)	0.8700(5)	0.7482(7)	1.000	4.45(4)
Bi6	48e	0.3763(5)	0.8823(3)	0.7501(6)	1.000	4.45(4)
Bi7	48e	0.6255(9)	0.8813(6)	0.751(1)	0.53(3)	4.45(4)
Ca2	48e	0.8716(8)	0.8691(8)	0.7469(8)	0.49(3)	4.45(4)
Ca3	24d	0.0000	0.7500	0.746(1)	0.71(2)	4.45(4)
Ca7	48e	0.6255(9)	0.8813(6)	0.751(1)	0.47(3)	4.45(4)
O1	16c	0.834(1)	0.834(1)	0.834(1)	0.678(7)	5.0(2)
O2	48e	0.934(2)	0.970(1)	0.809(2)	0.678(7)	5.0(2)
O3	48e	0.817(2)	0.826(2)	0.932(2)	0.678(7)	5.0(2)
O4	16c	0.925(2)	0.925(2)	0.925(2)	0.678(7)	5.0(2)
O5	48e	0.048(1)	0.824(2)	0.766(1)	0.678(7)	5.0(2)
O6	48e	0.307(2)	0.805(2)	0.812(2)	0.678(7)	5.0(2)
O7	48e	0.563(2)	0.797(2)	0.820(2)	0.678(7)	5.0(2)
O8	48e	0.568(2)	0.070(1)	0.813(2)	0.678(7)	5.0(2)
O9	48e	0.054(2)	0.798(2)	0.929(2)	0.678(7)	5.0(2)
O10	48e	0.309(2)	0.810(2)	0.927(2)	0.678(7)	5.0(2)
O11	48e	0.574(2)	0.806(2)	0.954(2)	0.678(7)	5.0(2)
O12	48e	0.067(2)	0.059(2)	0.943(2)	0.678(7)	5.0(2)

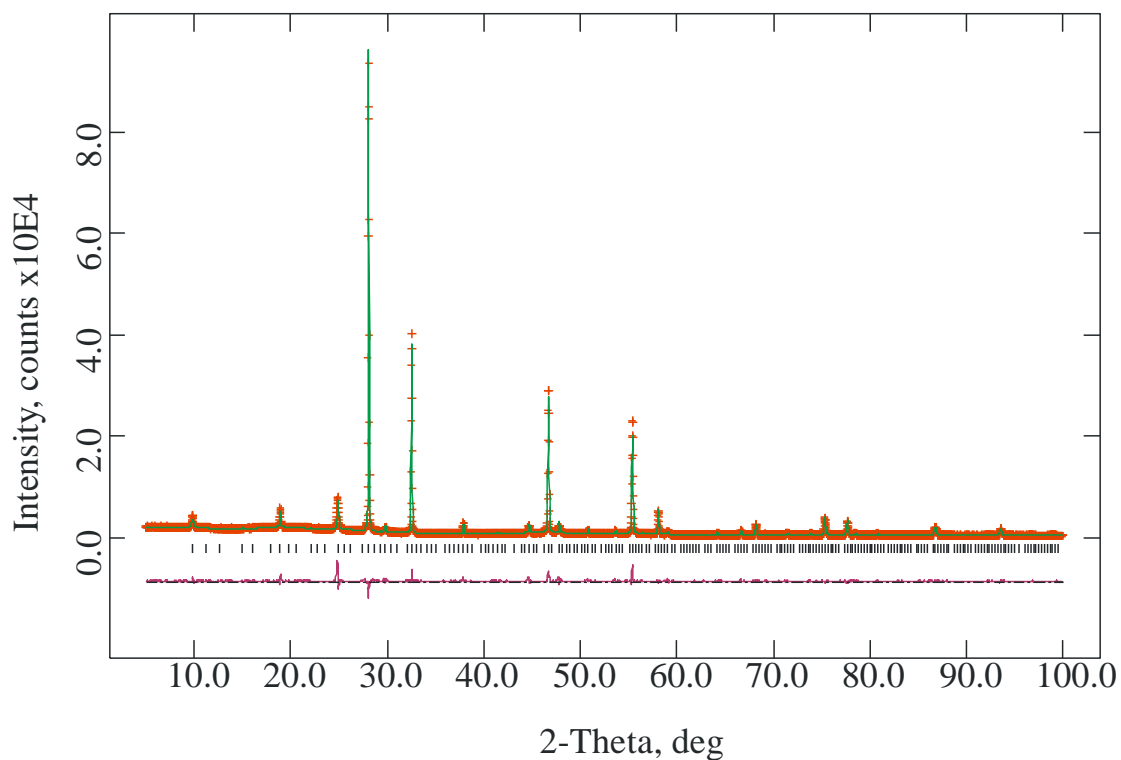


Figure 4.6 The observed (+), calculated (-) and difference XPD profiles for the final Rietveld refinement of $\text{Bi}_{10}\text{Ca}_5\text{ReO}_{23.5}$.

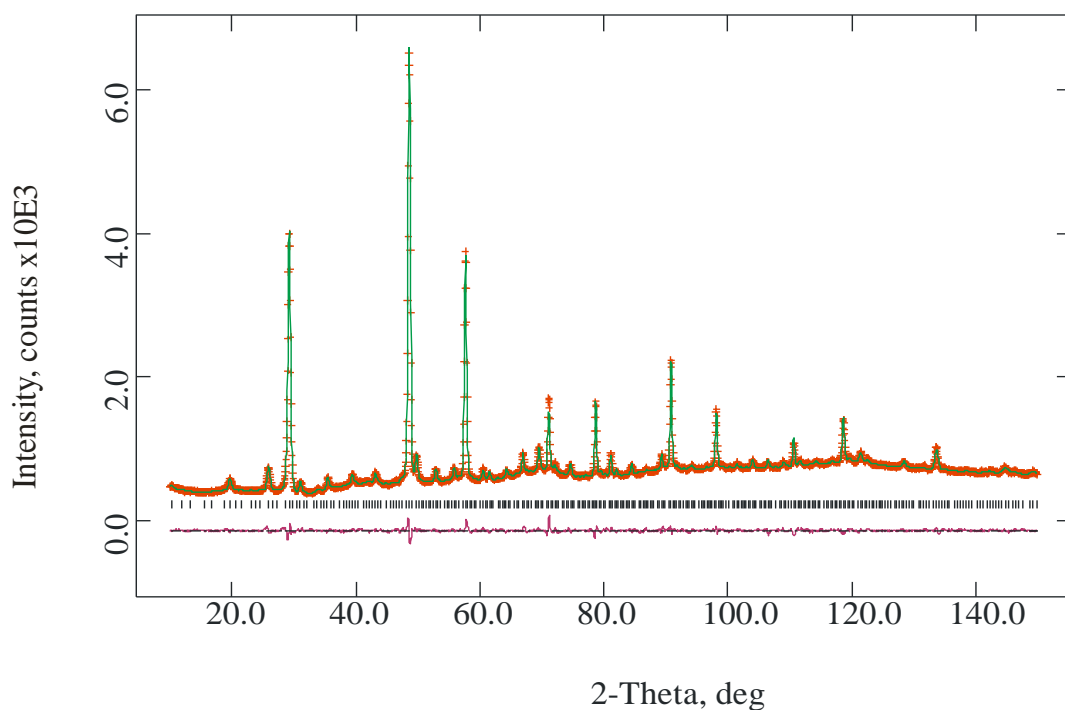


Figure 4.7 The observed (+), calculated (-) and difference NPD profiles for the final Rietveld refinement of $\text{Bi}_{10}\text{Ca}_5\text{ReO}_{23.5}$.

final refined unit cell parameter in space group $I\bar{4}3d$ was $a = 21.9575(4)$ Å. The oxygen atoms were assumed to be distributed randomly over all the available sites and were allowed to shift freely. All cations were assigned a single temperature factor as were all the individual oxygen atoms. For ease of refinement the oxygen site occupancies were constrained to be equal, as freeing showed no significant change. Refinement statistics for 151 variables were $R_p = 0.0475$, $R_{wp} = 0.0789$ for XPD data and $R_p = 0.0176$, $R_{wp} = 0.0238$ for NPD data, and $\chi^2 = 6.946$. The refined structural parameters are given in Table 4.3. The fitted XPD and NPD profiles (shown in Figures 4.6 and 4.7, respectively) indicate good agreement between observed and calculated profiles. As for $\text{Bi}_6\text{Ca}_3\text{ReO}_{15.5}$, an extensive diffuse background and decrease in peak intensities with 2θ indicates a high level of structural disorder, which is supported by high thermal parameters for both cation and anion sites. The final refinement shows exclusive occupation by Re of the 16c site, close to the origin of the unit cell, with Bi entirely occupying the Bi4, Bi5 and Bi6 sites and the remaining cation sites being shared between Bi and Ca. The overall composition corresponds to $\text{Bi}_{11.1(2)}\text{Ca}_{3.9(2)}\text{ReO}_{21.7(2)}$ and is in approximate agreement with the expected $\text{Bi}_{10}\text{Ca}_5\text{ReO}_{23.5}$ composition. The discrepancy probably relates to the necessary constraints that were applied to temperature factors and oxygen site occupancies, and the inherent high correlation that exists between such thermal factors and site occupancies. It should also be noted that the structure is incomplete, since the O atoms linked to the Re cations were not located. The oxygen sublattice therefore represents a simple model in which a single site is assigned to each O atom, in contrast with the split site assignments used for the basic $\delta\text{-Bi}_2\text{O}_3$ structure. The structure must therefore be regarded as an approximation to the precise local structure that exists within $\text{Bi}_{10}\text{Ca}_5\text{ReO}_{23.5}$. The structure is shown in Figure 4.8, projected along [100] and highlighting the Re distribution.

Table 4.4 Metal-oxygen bond lengths (Å) in the refined Bi₁₀Ca₅ReO_{23.5} structure.

Re1 - O6	2.21(4)	Bi5 - O7	2.15(4)
Re1 - O12	2.31(4)	Bi5 - O10	2.20(4)
Bi2 - O1	2.22(2)	Bi5 - O11	2.83(4)
Bi2 - O2	2.94(4)	Bi5 - O11	2.51(4)
Bi2 - O3	2.47(5)	Bi5 - O12	2.28(6)
Bi2 - O3	2.31(4)	Bi6 - O2	1.96(4)
Bi2 - O8	2.30(4)	Bi6 - O3	2.13(4)
Bi2 - O9	2.32(5)	Bi6 - O4	2.36(2)
Bi2 - O12	2.14(5)	Bi6 - O5	2.75(3)
Bi3 - O3	2.73(4)	Bi6 - O6	2.65(4)
Bi3 - O5	1.99(4)	Bi6 - O9	2.28(4)
Bi3 - O8	2.50(4)	Bi6 - O11	2.21(4)
Bi3 - O10	2.40(5)	Bi7 - O6	2.51(6)
Bi4 - O2	2.08(4)	Bi7 - O7	2.75(4)
Bi4 - O7	2.28(4)	Bi7 - O8	2.29(4)
Bi4 - O9	2.26(4)	Bi7 - O8	2.18(4)
Bi4 - O11	2.25(4)	Bi7 - O9	2.87(4)
Bi5 - O5	2.05(4)	Bi7 - O10	2.51(4)
Bi5 - O6	2.26(4)	Bi7 - O10	2.18(5)
Bi5 - O7	2.60(4)	Bi7 - O12	2.61(4)

Given the large size of the unit cell, the structural information available is insufficient to provide a definitive representation of the superstructure. Two O-O bond distances, O5-O10 (1.79(5) Å) and O2-O9 (1.86(5) Å) are unrealistically short, but the partial occupancy of all O sites does not prohibit such a model. It is clear, however, that the true oxygen sublattice is somewhat different from that deduced in this structure determination, and the metal-oxygen

bond distances provided (see Table 4.4) are therefore necessarily approximate, and the esds will substantially overestimate the true precision. However, it is clear that the structure has a highly disordered oxygen sublattice and the superstructure is derived principally from a non-random distribution of Ca and Bi within a fluorite framework.

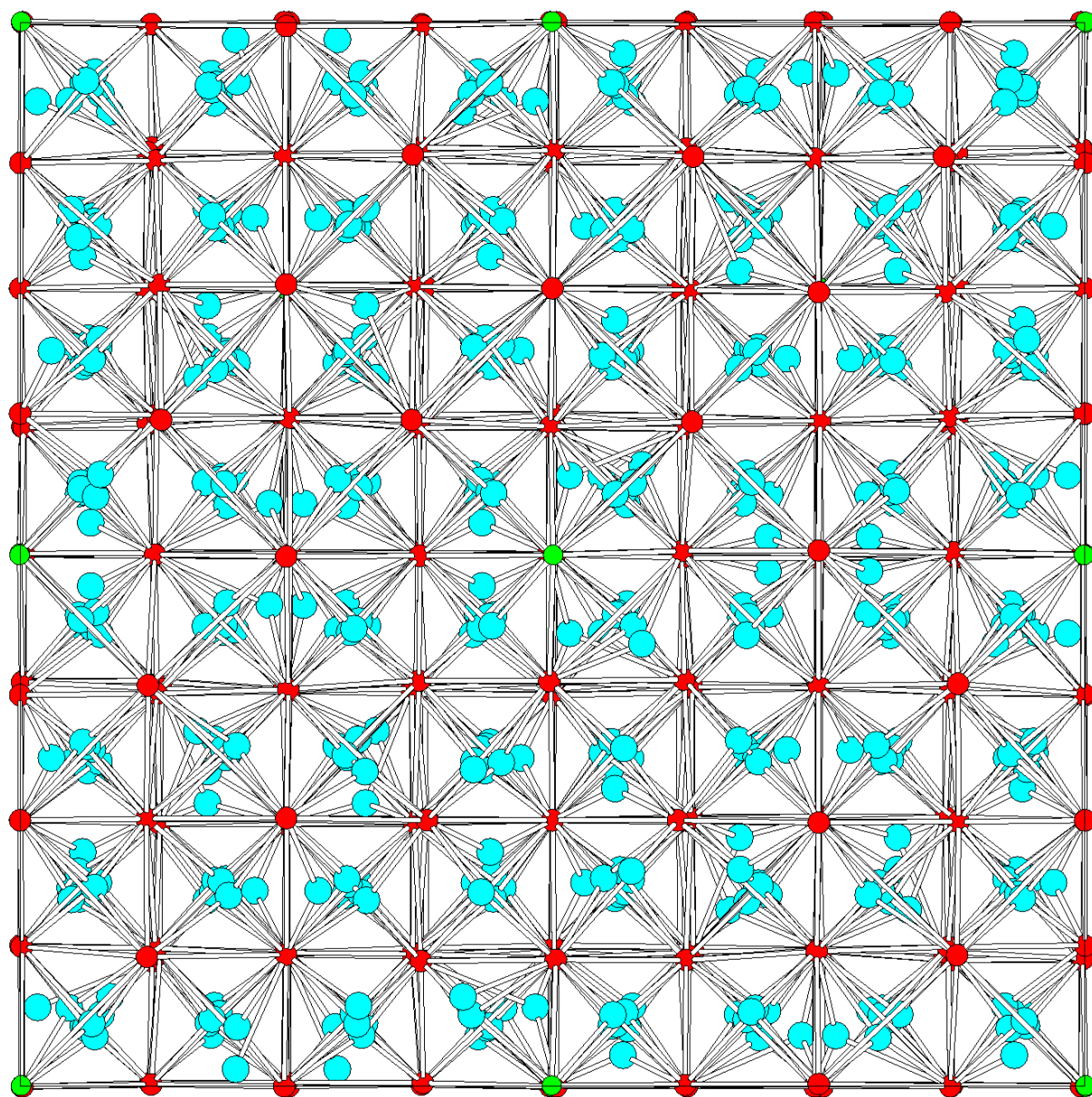


Figure 4.8 The structure of $\text{Bi}_{10}\text{Ca}_5\text{ReO}_{23.5}$, where the red spheres represent Bi/Ca, the green spheres represent Re and the light blue spheres represent O.

The unit cell for $\text{Bi}_6\text{Ca}_3\text{ReO}_{15.5}$ (5.416 Å) is slightly smaller than the subcell of $\text{Bi}_{10}\text{Ca}_5\text{ReO}_{23.5}$ ($21.940/4 = 5.485$ Å), and it is noted that the compositions represent two different levels of Re substitution in a mixed Bi/Ca oxide with a Bi:Ca ratio of 2:1. The change in unit cell size therefore reflects the introduction of the very small Re(VII) species into the structure.

4.3.3 Structural Changes in $\text{Bi}_{10}\text{Ca}_5\text{ReO}_{23.5}$

4.3.3.1 High Temperature Structural Studies of $\text{Bi}_{10}\text{Ca}_5\text{ReO}_{23.5}$

XPD results indicated that a high temperature phase was produced upon quenching of $\text{Bi}_{10}\text{Ca}_5\text{ReO}_{23.5}$ from 1073 K to room temperature. It was evident that this high temperature

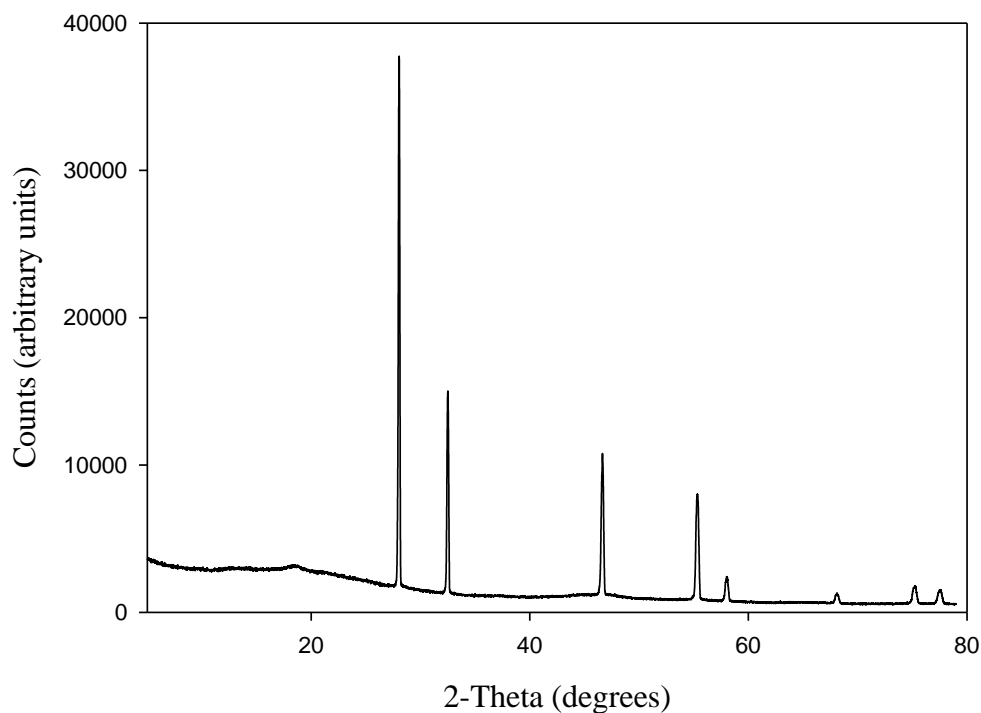


Figure 4.9 XPD pattern recorded from quenched $\text{Bi}_{10}\text{Ca}_5\text{ReO}_{23.5}$.

phase had a comparable XPD pattern to that of $\text{Bi}_6\text{Ca}_3\text{ReO}_{15.5}$, indicating that a similar fcc phase was formed. Indexing of the XPD data confirmed this structure to be face-centred cubic, with space group symmetry $\text{Fm}\bar{3}\text{m}$, and lattice parameter $a = 5.4978(7)$ Å. Figure 4.9 shows the XPD pattern obtained from this material.

Structural refinements were made using these XPD data and the program GSAS⁵ based on the Rietveld method⁶. A starting model for the refinement was based on that derived for pure $\delta\text{-Bi}_2\text{O}_3$ ⁷, space group $\text{Fm}\bar{3}\text{m}$, with the cations statistically distributed (Bi:Ca:Re = 10:5:1) at the $4a$ (0, 0, 0) site and the oxygen atoms on their regular $8c$ ($\frac{1}{4}, \frac{1}{4}, \frac{1}{4}$) and interstitial $32f$ (x, x, x) sites. The final refined unit cell parameter in space group $\text{Fm}\bar{3}\text{m}$ was $a = 5.4890(1)$ Å. Refinement statistics for 47 variables were $R_p = 0.0290$, $R_{wp} = 0.0452$, and $\chi^2 = 3.499$. The refined structural information is given in Table 4.5. The fitted XPD profile is shown in Figure 4.10 and demonstrates good agreement between observed and calculated profiles. An extensive diffuse background and decrease in peak intensities with 2θ is apparent, signifying a high level of disorder of the O sublattice which is supported by the high cation thermal parameters. In the refinement, all cations were assigned a single temperature factor, but oxygen temperature factors were constrained to allow a sensible refinement. Oxygen occupancies were allowed to vary. The final refinement shows 47% of oxide ions are displaced along [111] directions from their ideal $8c$ ($\frac{1}{4}, \frac{1}{4}, \frac{1}{4}$) site to the $32f$ (x, x, x) site, and compares well with the 52% of oxide ions that are shown to be displaced in $\text{Bi}_6\text{Ca}_3\text{ReO}_{15.5}$. The refinement allowed the $32f$ (x, x, x) atom site to shift freely and the position of the $32f$ (x, x, x) interstitial oxygen sites, where $x = 0.372(3)$, is significantly closer to the vacant octahedral site in the centre of the unit cell as compared to $\text{Bi}_6\text{Ca}_3\text{ReO}_{15.5}$ ($x = 0.311(3)$) and other reported values of $x = 0.319(2)$ and $x = 0.32(1)$ for $(\text{Bi}_2\text{O}_3)_{0.8}(\text{Er}_2\text{O}_3)_{0.2}$ and $(\text{Bi}_2\text{O}_3)_{0.73}(\text{Y}_2\text{O}_3)_{0.27}$, respectively^{7, 8}, and is approximately midway between the $8c$ ($\frac{1}{4}, \frac{1}{4}, \frac{1}{4}$)

site and the $(\frac{1}{2}, \frac{1}{2}, \frac{1}{2})$ site. This value of $x = 0.372(3)$ compares well with reported values of $x = 0.368(3)$, $x = 0.379(3)$ and $x = 0.368(3)$ for $\text{Bi}_{12.5}\text{Er}_{1.5}\text{ReO}_{24.5}$, $\text{Bi}_{12.5}\text{Nd}_{1.5}\text{ReO}_{24.5}$ and $\text{Bi}_{12.5}\text{Y}_{1.5}\text{ReO}_{24.5}$ ¹⁰, respectively. However, it is worth noting that this refined value for quenched $\text{Bi}_{10}\text{Ca}_5\text{ReO}_{23.5}$ could be inaccurate due to the poor sensitivity of XPD data to oxygen atoms in the presence of heavy Bi and Re. For this reason the oxygen occupancies were constrained to equal the sum of that expected in this refinement. As was the case for the structural refinement of $\text{Bi}_6\text{Ca}_3\text{ReO}_{15.5}$, little evidence was found to suggest displacement of the cations from their ideal $4a$ $(0, 0, 0)$ site to the $24e$ $(x, 0, 0)$ site, proposed by Battle *et al.*⁷.

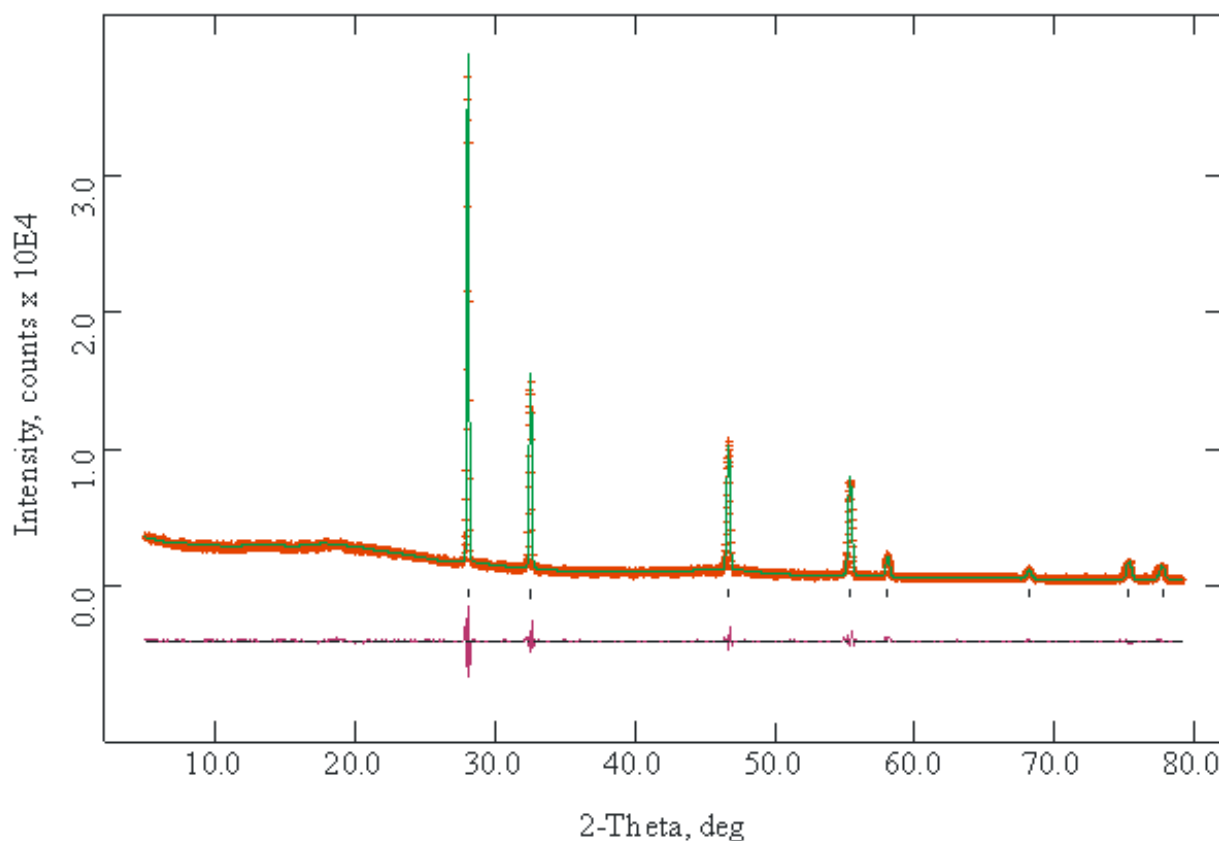


Figure 4.10 The observed (+), calculated (-) and difference XPD profiles for the final Rietveld refinement of quenched $\text{Bi}_{10}\text{Ca}_5\text{ReO}_{23.5}$.

Table 4.5 Refined structural information for XPD results of quenched $\text{Bi}_{10}\text{Ca}_5\text{ReO}_{23.5}$, determined by Rietveld analysis.

Site		Fractional			Uiso x 100	
Atom	Symmetry	<i>x</i>	<i>y</i>	<i>z</i>	occupancy	/ Å ²
Bi	4a	0	0	0	0.6250	3.90(5)
Ca	4a	0	0	0	0.3125	3.90(5)
Re	4a	0	0	0	0.0625	3.90(5)
O1	8c	0.25	0.25	0.25	0.39(1)	1.0
O2	32f	0.372(3)	0.372(3)	0.372(3)	0.086(3)	1.0

$\text{Bi}_{10}\text{Ca}_5\text{ReO}_{23.5}$ was examined by DTA, described in Section 2.5, in order to detect any phase changes. Heating and cooling cycles between 298 K and 1073 K were used. The DTA results for $\text{Bi}_{10}\text{Ca}_5\text{ReO}_{23.5}$ are shown in Figure 4.11. Small but significant energy changes can be seen for both the heating curve (lower) and cooling curve (upper). The heating curve shows an endothermic energy change, with a peak onset at 983 K, suggestive of a phase change. The cooling curve shows an exothermic energy change, with a peak onset at 951 K, as the phase change is reversed and the structure reverts back to its room temperature form. This large hysteresis is suggestive of a first order phase transition.

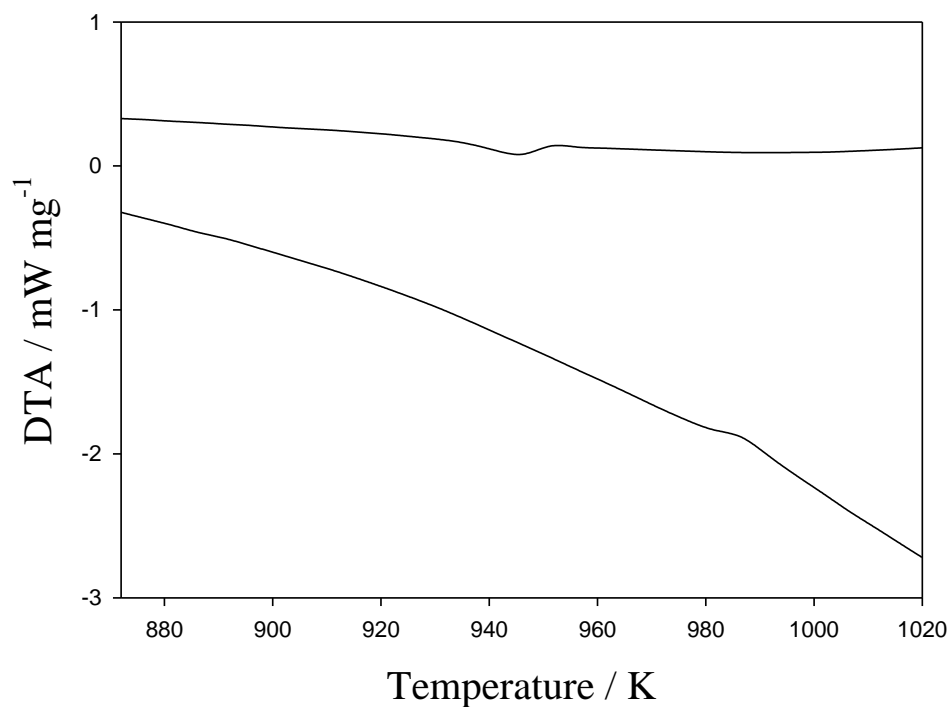


Figure 4.11 DTA results for $\text{Bi}_{10}\text{Ca}_5\text{ReO}_{23.5}$, showing the heating curve (lower) and cooling curve (upper).

Variable temperature XPD, as described in Section 2.2.1, was used to confirm that the phase change revealed by DTA corresponded to the transition to the simple fcc form. XPD patterns were recorded at a range of temperatures either side of the phase transition indicated by DTA and are shown in Figure 4.12. The variable temperature XPD results support the evidence of a phase change shown by DTA, with some peaks appearing to reduce in intensity at 923 K. By 973 K most of the superstructure peaks have disappeared and the phase change to fcc appears complete at 1023 K.

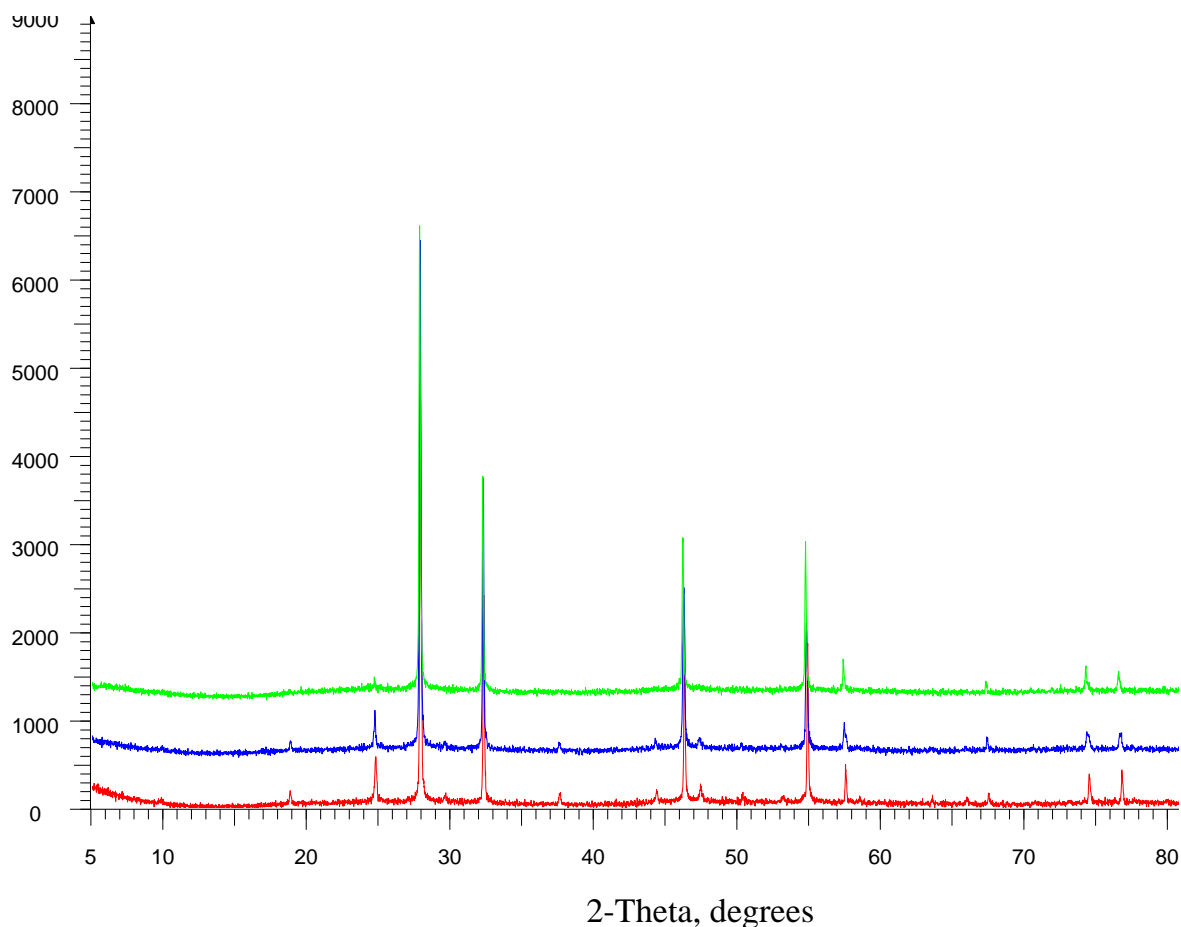


Figure 4.12 Variable temperature XPD results recorded from $\text{Bi}_{10}\text{Ca}_5\text{ReO}_{23.5}$ at 873 K (red), 923 K (blue), 973 K (green) and 1023 K (purple), showing the gradual phase change through this temperature range.

The presence of only two phases for $\text{Bi}_{10}\text{Ca}_5\text{ReO}_{23.5}$ – a high temperature fcc phase and a low temperature bcc phase – suggested by the presence of a single peak in both the heating and cooling curves in DTA, was confirmed by further variable temperature XPD experiments across a broader temperature range of 298 K to 1073 K with no further evidence of phase change being apparent.

4.3.3.2 Thermal Stability of $\text{Bi}_{10}\text{Ca}_5\text{ReO}_{23.5}$

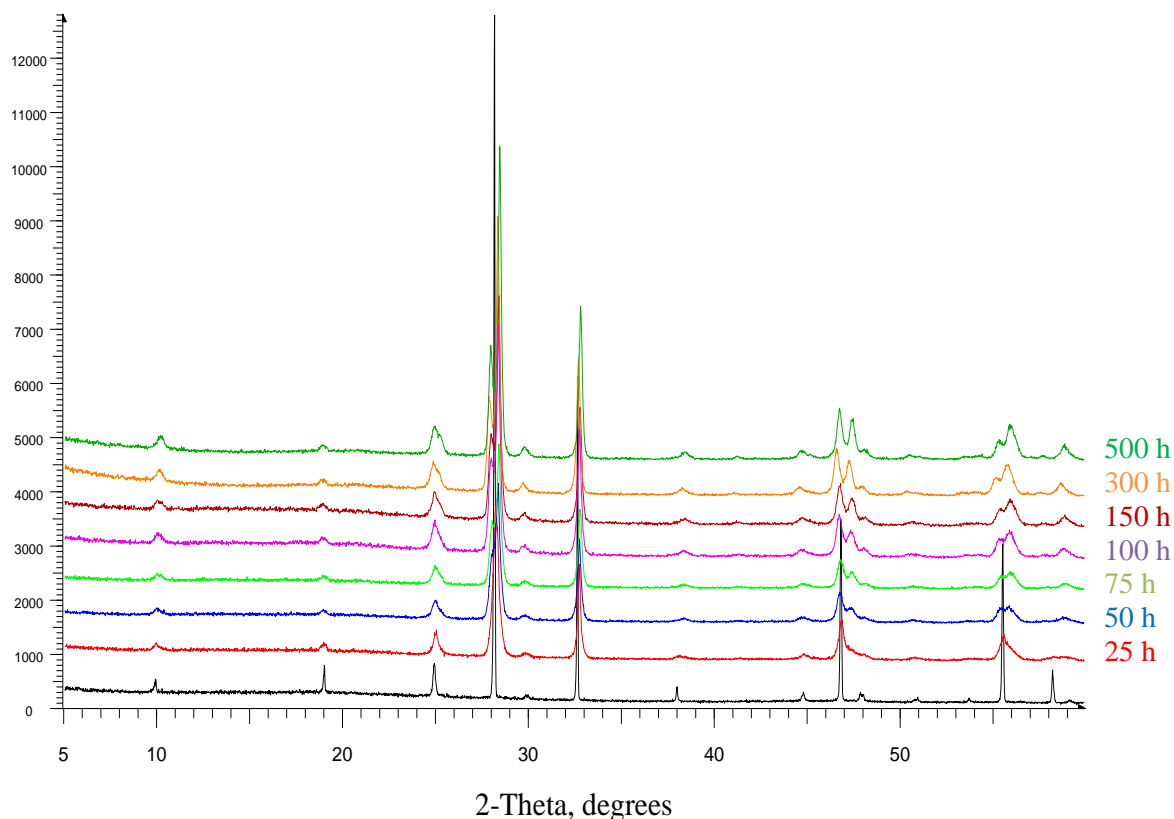


Figure 4.13 XPD patterns recorded from $\text{Bi}_{10}\text{Ca}_5\text{ReO}_{23.5}$ annealed at 773 K.

The XPD patterns shown in Figure 4.13 demonstrate the structural changes that occur to $\text{Bi}_{10}\text{Ca}_5\text{ReO}_{23.5}$ following annealing in air at 773 K. A phase transformation begins to emerge after 25 h where the peak reflections begin to broaden. This change continues with successive annealing and after 50 h a phase transformation is clearly evident by the appearance of additional peaks. The transformation is complete after 500 h, where $\text{Bi}_{10}\text{Ca}_5\text{ReO}_{23.5}$ converts to what was subsequently identified as a monoclinic phase.

Figure 4.14 shows the XPD pattern for the phase formed after annealing at 773 K and is derived as a monoclinic supercell based on a fluorite-related hexagonal subcell. This relationship is described in detail in Section 3.3.3, where the same structure is observed for a different material. The structure could be indexed to a cell with space group symmetry $P2_1/m$ and lattice parameters $a = 9.416(9) \text{ \AA}$, $b = 3.810(2) \text{ \AA}$, $c = 9.541(6) \text{ \AA}$, where $\beta = 109.7(1)^\circ$.

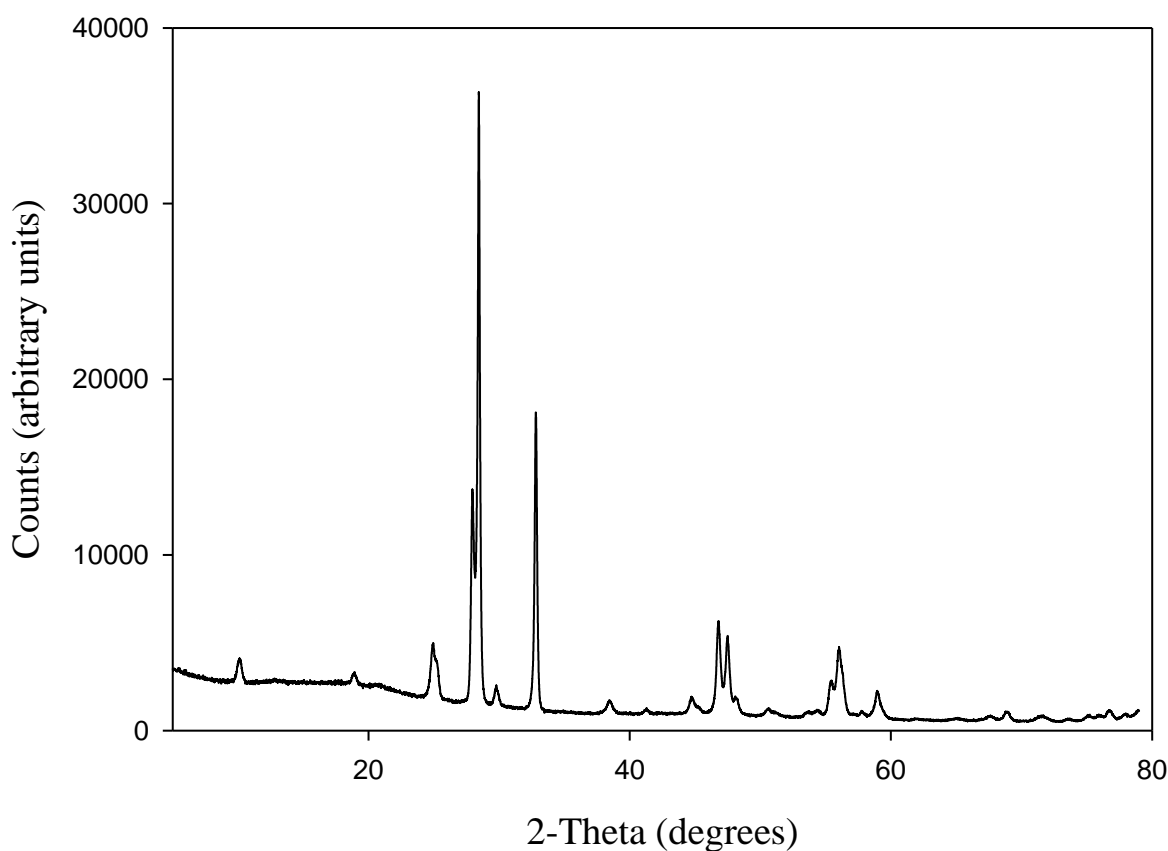


Figure 4.14 XPD pattern recorded from $\text{Bi}_{10}\text{Ca}_5\text{ReO}_{23.5}$ following annealing in air at 773 K.

Consequent structural refinements were made using these data, by the Rietveld method⁶ and the program GSAS⁵. The refinement was based on a structure with monoclinic symmetry and the space group $P2_1/m$, initially using idealised atom positions derived using

the program Cryscon⁹ for this space group, inputting atom parameters from the hexagonal subcell along with the relationship between subcell and supercell illustrated in Section 3.3.3 where the same relationship is observed for a different material. These atomic coordinates are listed in Table 4.6.

Table 4.6 Atomic coordinates generated by Cryscon with space group $P2_1/m$, where $a = 9.4 \text{ \AA}$, $b = 3.8 \text{ \AA}$, $c = 9.5 \text{ \AA}$, $\beta = 109.7^\circ$. All cations are represented by Bi.

Atom number	Atom Type	x	y	z	Multiplicity
1	Bi	0.0625	0.2500	0.1875	2
2	Bi	0.1875	0.7500	0.5625	2
3	Bi	0.5625	0.2500	0.6875	2
4	Bi	0.3125	0.2500	0.9375	2
5	O	0.0625	0.2500	0.4375	2
6	O	0.4375	0.7500	0.5625	2
7	O	0.1875	0.7500	0.3125	2
8	O	0.3125	0.2500	0.6875	2
9	O	0.3125	0.2500	0.1875	2
10	O	0.9375	0.7500	0.0625	2
11	O	0.1875	0.7500	0.8125	2
12	O	0.5625	0.2500	0.9375	2

The final refined unit cell parameters in space group $P2_1/m$ were $a = 9.4142(8) \text{ \AA}$, $b = 3.8129(3) \text{ \AA}$, $c = 9.5397(7) \text{ \AA}$ and $\beta = 109.730(4)$. Refinement statistics for 64 variables gave $R_p = 0.0625$, $R_{wp} = 0.0444$, and $\chi^2 = 7.171$. The refined structural information is given in Table 4.7. The fitted XPD profile is shown in Figure 4.15 and demonstrates good agreement between observed and calculated profiles. A decrease in the peak intensities with

increasing 2θ and an extensive diffuse background both reflect the high level of disorder of the oxygen sublattice. This is supported by high cation thermal parameters. In this refinement all cations were assigned a single temperature factor. The oxygen temperature factors were constrained, in addition to oxygen positions and occupancies, to allow a sensible refinement as it is difficult to locate oxygen atoms by XPD in the presence of heavy Bi and Re. Cation occupancies, however, were allowed to vary and the refinement suggests a cation content of $\text{Bi}_{9.9(2)}\text{Ca}_{5.1(2)}\text{Re}$ present in the unit cell, which agrees well with the expected composition. The final refinement suggests that all four cation sites are shared between either Bi and Ca or Bi and Re, with the Bi1, Bi2 and Bi4 sites being shared in varying proportions with calcium and the Bi3 site being shared with rhenium.

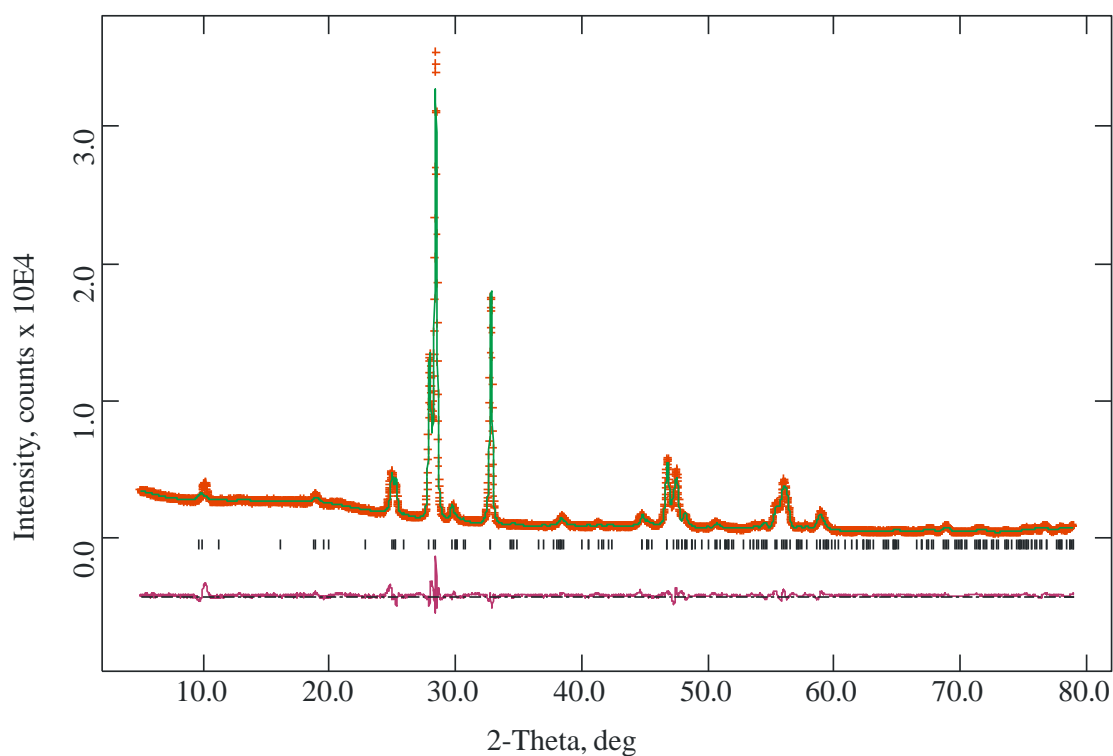


Figure 4.15 The observed (+), calculated (-) and difference XPD profiles for the final Rietveld refinement of $\text{Bi}_{10}\text{Ca}_5\text{ReO}_{23.5}$ annealed at 773 K.

Table 4.7 Refined structural information for XPD results of $\text{Bi}_{10}\text{Ca}_5\text{ReO}_{23.5}$ annealed at 773 K, determined by Rietveld analysis.

Atom	x	y	z	Fractional Occupancy	Uiso x 100 / \AA^2
Bi1	0.029(2)	0.25	0.167(2)	0.39(1)	5.4(2)
Bi2	0.174(1)	0.75	0.536(2)	0.68(2)	5.4(2)
Bi3	0.557(1)	0.25	0.695(1)	0.75	5.4(2)
Bi4	0.302(1)	0.25	0.910(1)	0.66(2)	5.4(2)
Ca1	0.029(2)	0.25	0.167(2)	0.61(1)	5.4(2)
Ca2	0.174(1)	0.75	0.536(2)	0.32(2)	5.4(2)
Re3	0.557(1)	0.25	0.695(1)	0.25	5.4(2)
Ca4	0.302(1)	0.25	0.910(1)	0.34(2)	5.4(2)
O1	0.0625	0.2500	0.4375	0.734	0.1
O2	0.4375	0.7500	0.5625	0.734	0.1
O3	0.1875	0.7500	0.3125	0.734	0.1
O4	0.3125	0.2500	0.6875	0.734	0.1
O5	0.3125	0.2500	0.1875	0.734	0.1
O6	0.9375	0.7500	0.0625	0.734	0.1
O7	0.1875	0.7500	0.8125	0.734	0.1
O8	0.5625	0.2500	0.9375	0.734	0.1

4.3.4 Ionic Conductivity

Both $\text{Bi}_6\text{Ca}_3\text{ReO}_{15.5}$ and $\text{Bi}_{10}\text{Ca}_5\text{ReO}_{23.5}$ are related to the fluorite face centred cubic unit cell of $\delta\text{-Bi}_2\text{O}_3$ which is known to have high oxide ion conducting properties at elevated temperatures. Furthermore, given the previous observations of high oxide ion conductivity in bismuth oxide based materials^{10,11} the two new phases were examined by oxide ion conduction measurements using impedance spectroscopy. Measurements were therefore

made between 473 K and 773 K and the frequency range 1 Hz to 1×10^6 Hz, in air. The materials were prepared and determinations made using the methods outlined in Chapter 2. The density for each sample pellet was calculated and compared with the density of its unit cell. From this it was determined that all samples had a density in the range 85 to 90 % of the theoretical.

The complex plane impedance plots could be fitted to a single semicircle with Warburg type impedance from electrode kinetic effects. Figure 4.16 gives an example of the complex plane plot for $\text{Bi}_{10}\text{Ca}_5\text{ReO}_{23.5}$ using the data obtained at 523 K. The conductivities were calculated from the bulk resistance determined from the minima in the complex plane plots. Plots of $\log \sigma$ versus $1000\text{K}/T$ for $\text{Bi}_6\text{Ca}_3\text{ReO}_{15.5}$, $\text{Bi}_{10}\text{Ca}_5\text{ReO}_{23.5}$, quenched $\text{Bi}_{10}\text{Ca}_5\text{ReO}_{23.5}$ and annealed $\text{Bi}_{10}\text{Ca}_5\text{ReO}_{23.5}$ are shown in Figure 4.17. The Arrhenius activation energies, E_a , for these materials were subsequently determined from these plots and are listed in Table 4.8.

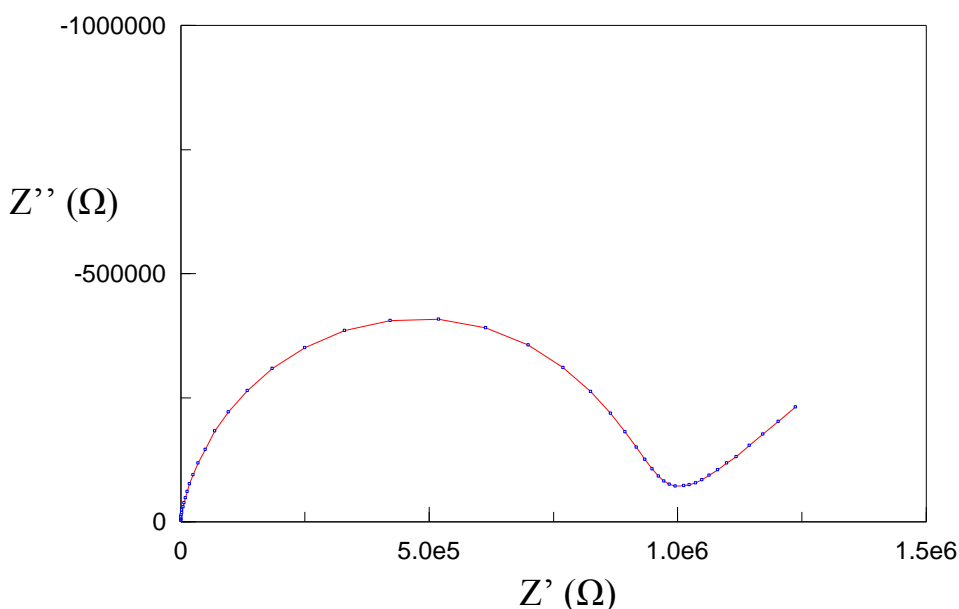


Figure 4.16 Complex plane impedance plot of real (Z') and imaginary (Z'') components, for $\text{Bi}_{10}\text{Ca}_5\text{ReO}_{23.5}$ at a temperature of 523 K.

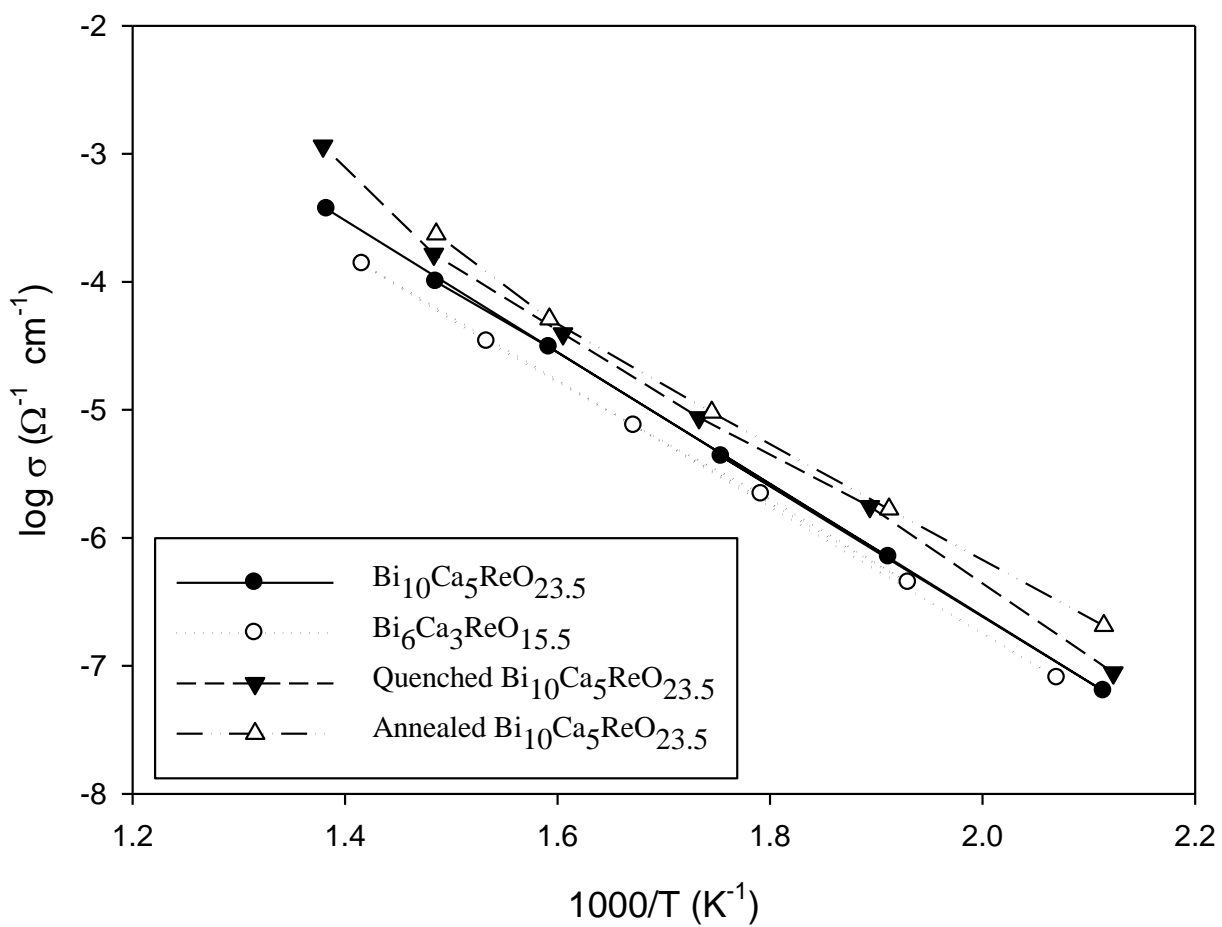


Figure 4.17 Arrhenius plots of conductivity determined by impedance spectroscopy for $\text{Bi}_6\text{Ca}_3\text{ReO}_{15.5}$, $\text{Bi}_{10}\text{Ca}_5\text{ReO}_{23.5}$, quenched $\text{Bi}_{10}\text{Ca}_5\text{ReO}_{23.5}$ and $\text{Bi}_{10}\text{Ca}_5\text{ReO}_{23.5}$ annealed at 773 K.

Table 4.8 Activation energies, E_a , for $\text{Bi}_6\text{Ca}_3\text{ReO}_{15.5}$, $\text{Bi}_{10}\text{Ca}_5\text{ReO}_{23.5}$, annealed $\text{Bi}_{10}\text{Ca}_5\text{ReO}_{23.5}$ and quenched $\text{Bi}_{10}\text{Ca}_5\text{ReO}_{23.5}$.

Material	E_a/eV
$\text{Bi}_6\text{Ca}_3\text{ReO}_{15.5}$	0.97
$\text{Bi}_{10}\text{Ca}_5\text{ReO}_{23.5}$	1.02
Quenched $\text{Bi}_{10}\text{Ca}_5\text{ReO}_{23.5}$	0.95
Annealed $\text{Bi}_{10}\text{Ca}_5\text{ReO}_{23.5}$	0.95

Both $\text{Bi}_{10}\text{Ca}_5\text{ReO}_{23.5}$ and $\text{Bi}_6\text{Ca}_3\text{ReO}_{15.5}$ show good oxide ion conductivity, with the conductivity of $\text{Bi}_{10}\text{Ca}_5\text{ReO}_{23.5}$ being marginally better than that of $\text{Bi}_6\text{Ca}_3\text{ReO}_{15.5}$. Conductivities are comparable to similar materials, with $\text{Bi}_{10}\text{Ca}_5\text{ReO}_{23.5}$ having a conductivity of $1.0 \times 10^{-4} \Omega^{-1} \text{cm}^{-1}$ at 673 K, compared to a conductivity of $5.4 \times 10^{-4} \Omega^{-1} \text{cm}^{-1}$ displayed by $\text{Bi}_{28}\text{Re}_2\text{O}_{49}$ at the same temperature¹¹. The conductivities of $\text{Bi}_{10}\text{Ca}_5\text{ReO}_{23.5}$ and $\text{Bi}_6\text{Ca}_3\text{ReO}_{15.5}$ were similar to that observed for well characterised stabilised bismuth oxide ion conductors, with $\text{Bi}_{10}\text{Ca}_5\text{ReO}_{23.5}$ displaying a conductivity of $3.51 \times 10^{-3} \Omega^{-1} \text{cm}^{-1}$ at 773 K, compared to $(\text{Bi}_2\text{O}_3)_{0.65}(\text{Gd}_2\text{O}_3)_{0.35}$, having a conductivity of $3.5 \times 10^{-3} \Omega^{-1} \text{cm}^{-1}$ at the same temperature, and is within a order of magnitude of the ionic conductor $(\text{Bi}_2\text{O}_3)_{0.75}(\text{Y}_2\text{O}_3)_{0.25}$ which has a conductivity of $1.3 \times 10^{-2} \Omega^{-1} \text{cm}^{-1}$ at 773 K¹². However, the activation energies calculated for these materials were significantly higher than those of $\text{Bi}_{28}\text{Re}_2\text{O}_{49}$ and $(\text{Bi}_2\text{O}_3)_{0.75}(\text{Y}_2\text{O}_3)_{0.25}$, where $E_a = 0.62 \text{ eV}$ and $E_a = 0.66 \text{ eV}$, respectively^{11,12}. Both materials have similar proportions of bismuth in the product - $\text{Bi}_6\text{Ca}_3\text{ReO}_{15.5}$ and $\text{Bi}_{10}\text{Ca}_5\text{ReO}_{23.5}$ have 60% and 62.5% Bi respectively. The results are consistent with previous

reports by Takahashi *et al.*¹² that, in doped bismuth oxide materials, the conductivities become lower as the added oxide content increased. The overall mechanism for the movement of O²⁻ ions through the oxygen sublattice is likely to be very similar for both materials despite the more complicated superstructure of Bi₁₀Ca₅ReO_{23.5}.

Both quenched and annealed samples of Bi₁₀Ca₅ReO_{23.5} show good oxide ion conductivity, similar to that of Bi₁₀Ca₅ReO_{23.5} but marginally better in both cases. The monoclinic structure formed upon annealing of Bi₁₀Ca₅ReO_{23.5} shows improved conductivity compared to the room temperature superstructure form, and displays the best ionic conductivity of all the Bi-Ca-Re-O phases. As expected, the high temperature fcc quenched form gave little improvement in conductivity, as is evident from a comparison of Bi₁₀Ca₅ReO_{23.5} with Bi₆Ca₃ReO_{15.5} (fcc). The marginally small improvement of quenched Bi₁₀Ca₅ReO_{23.5} over Bi₆Ca₃ReO_{15.5} could be due to the increased displacements observed for the interstitial 32*f*(*x*, *x*, *x*) site (*x* = 0.372(3) for quenched Bi₁₀Ca₅ReO_{23.5} compared to *x* = 0.311(3) for Bi₆Ca₃ReO_{15.5}). A greater (*x*, *x*, *x*) displacement may decrease the activation energy and increase the ionic conductivity if the pathway for ionic conduction is similar to that observed in the PbF₂ fluorite materials, as the 32*f* interstitial positions are located on the minimum energy conduction pathway calculated by Koto *et al.*¹³. This may also explain the lower activation energy of 0.95 eV for quenched Bi₁₀Ca₅ReO_{23.5} compared to values of 1.02 eV and 0.97 eV for Bi₁₀Ca₅ReO_{23.5} and Bi₆Ca₃ReO_{15.5}, respectively.

4.4 References

- 1 Crumpton, T. E.; Francesconi, M. G.; Greaves, C. *J. Solid State Chem.* **175** (2003) 197
- 2 Sharma, N.; Withers, R. L.; Knight, K. S.; Ling, C. D. *J. Solid State Chem.* **182** (2009) 2468
- 3 Takahashi, T.; Iwahara, H. *J. Appl. Electrochem.* **2** (1972) 97
- 4 Shannon, R. D. *Acta. Cryst.* **A32** (1976) 751
- 5 Larson, A. C.; Von Dreele, R. B. *General Structure Analysis System (GSAS)* Los Almos National Laboratory, Los Almos, NM (1994)
- 6 Young, R. A. *The Rietveld Method* International Union of Crystallography, Oxford University Press (1993)
- 7 Battle, P. D.; Catlow, C. R. A.; Drennan, J.; Murray, A. D. *J. Phys. C* **16** (1983) L561
- 8 Battle, P. D.; Catlow, C. R. A.; Moroney, L. M. *J. Solid State Chem.* **67** (1987) 42
- 9 Available from Shapessoftware: <http://www.shapesoftware.com/>
- 10 Punni, R.; Feteira, A. M.; Sincliar, D. C.; Greaves, C. *J. Am. Chem. Soc.* **128** (2006) 15386
- 11 Crumpton, T. E.; Mosselmans, J. F. W.; Greaves, C. *J. Mater. Chem.* **15** (2005) 164
- 12 Takahashi, T.; Iwahara, H. *Mat. Res. Bull.* **13** (1978) 1447
- 13 Koto, K.; Schultz, H.; Huggins, R. A. *Solid State Ionics* **1** (1980) 355

CHAPTER 5

The Structure and Ionic Conductivity of the Fluorite-Related Isostructural Materials $\text{Bi}_{20}\text{Ca}_7\text{NbO}_{39.5}$ and $\text{Bi}_{10.75}\text{Ca}_{4.375}\text{GaO}_{22}$

5.1 Introduction

The substitution of small amounts of Bi for metal oxoanions in Bi_2O_3 has been shown to lead to stable superstructures of the cubic fluorite unit cell, with some displaying relatively high oxide ion conducting properties. It has been revealed by previous studies at the bismuth-rich end of the $\text{Bi}_2\text{O}_3\text{-Re}_2\text{O}_7$ phase diagram that $\text{Bi}_{28}\text{Re}_2\text{O}_{49}$ adopts a superstructure of the cubic fluorite unit cell¹, comprising an ordered framework of linked BiO_4 trigonal bipyramids and square pyramids with discrete rhenium oxoanions at the origin and body centre of the unit cell. The compound displays relatively high conductivity ($5.4 \times 10^{-4} \Omega^{-1} \text{ cm}^{-1}$ at 673 K). In Chapter 3, recent studies of the structural and conduction properties of the fluorite-related superstructure of $\text{Bi}_9\text{ReO}_{17}$ in this bismuth-rich portion of the $\text{Bi}_2\text{O}_3\text{-Re}_2\text{O}_7$ phase diagram is described in detail.

In Chapter 4, the additional further substitution of Ca for Bi, forming the single phase materials $\text{Bi}_6\text{Ca}_3\text{ReO}_{15.5}$ and $\text{Bi}_{10}\text{Ca}_5\text{ReO}_{23}$, has also been shown to lead to superstructures of the simple fluorite subcell. $\text{Bi}_6\text{Ca}_3\text{ReO}_{15.5}$ formed a face-centred cubic ($\text{Fm}\bar{3}\text{m}$) fluorite-related structure ($a = 5.416 \text{ \AA}$), and $\text{Bi}_{10}\text{Ca}_5\text{ReO}_{23.5}$ a body-centred cubic ($\text{I}\bar{4}3\text{d}$) material ($a = 21.940 \text{ \AA}$) that is a $4 \times 4 \times 4$ superstructure of the $\text{Bi}_6\text{Ca}_3\text{ReO}_{15.5}$ phase. Both materials

are shown to display good oxide ion conductivity, having activation energies $E_a = 0.97$ eV and $E_a = 1.02$ eV for $\text{Bi}_6\text{Ca}_3\text{ReO}_{15.5}$ and $\text{Bi}_{10}\text{Ca}_5\text{ReO}_{23.5}$, respectively.

These successful syntheses suggested that similar fluorite-related phases might occur with other transition metal oxides. As discussed in Chapter 1, widespread studies into the stabilisation of $\delta\text{-Bi}_2\text{O}_3$ with transition metal cations have been reported, whereby isovalent and aliovalent dopants including Y, Ga, V, Nb, Ta and W have also been shown to stabilise $\delta\text{-Bi}_2\text{O}_3$ ^{2,3,4}. Therefore, the substitution of Nb and Ga for Re in Bi-Ca-Re-O were also investigated.

In this study two previously unreported isostructural doped calcium bismuth oxide materials which are monoclinically distorted superstructures of the fluorite-related hexagonal subcell are discussed. The structure of this phase along with oxide ion conductivity data are reported by means of XPD, NPD and impedance measurements. Thermal stability and high temperature structural studies have also been undertaken.

5.2 Experimental

Materials were prepared by reacting stoichiometric quantities of Bi_2O_3 (Aldrich, 99.9%), CaCO_3 (Aldrich, 99+%), Ga_2O_3 (Aldrich, 99.99+%) and Nb_2O_5 (Aldrich, 99.99%). Samples were intimately ground and calcined for a total of 36 h in air at 1073 K, with intermediate regrinding to ensure complete reaction and single phase products, as indicated by XPD.

The thermal stability of the materials was examined by annealing samples at 773 K. Materials were also subject to quenching, by heating to 1073 K, followed by removal from the furnace and quickly cooling to room temperature in both air and liquid nitrogen. Post

-annealing and -quenching, samples were examined by XPD to examine any phase transformations.

Further detailed characterisation was made by XPD, variable temperature XPD, NPD, DTA and impedance spectroscopy, as described in Chapter 2.

5.3 Results and Discussion

5.3.1 The Structure of $\text{Bi}_{20}\text{Ca}_7\text{NbO}_{39.5}$ and $\text{Bi}_{10.75}\text{Ca}_{4.375}\text{GaO}_{22}$

Initial examination by XPD showed both materials to be single phase, suggesting the presence of a fluorite-related superstructure, derived as a monoclinic supercell based on a fluorite-related hexagonal subcell. XPD patterns for $\text{Bi}_{20}\text{Ca}_7\text{NbO}_{39.5}$ and $\text{Bi}_{10.75}\text{Ca}_{4.375}\text{GaO}_{22}$ are shown in Figure 5.1 and 5.2, respectively.

The subcell peaks, indicated by *, could be indexed to a hexagonal cell where $a = 3.796(1)$ and $c = 9.622(3)$ Å for $\text{Bi}_{20}\text{Ca}_7\text{NbO}_{39.5}$; and $a = 3.973(7)$ and $c = 9.611(2)$ Å for $\text{Bi}_{10.75}\text{Ca}_{4.375}\text{GaO}_{22}$. Subsequent indexing the XPD reflection peaks to a multiple of the subcell resulted in the supercell being ascertained, signifying a structure with monoclinic symmetry where $a = 9.342(8)$, $b = 3.795(4)$, $c = 9.613(9)$ Å with $\beta = 110.10(6)^\circ$ for $\text{Bi}_{20}\text{Ca}_7\text{NbO}_{39.5}$; and where $a = 9.331(4)$, $b = 3.794(2)$, $c = 9.615(4)$ Å with $\beta = 110.08(4)^\circ$ for $\text{Bi}_{10.75}\text{Ca}_{4.375}\text{GaO}_{22}$.

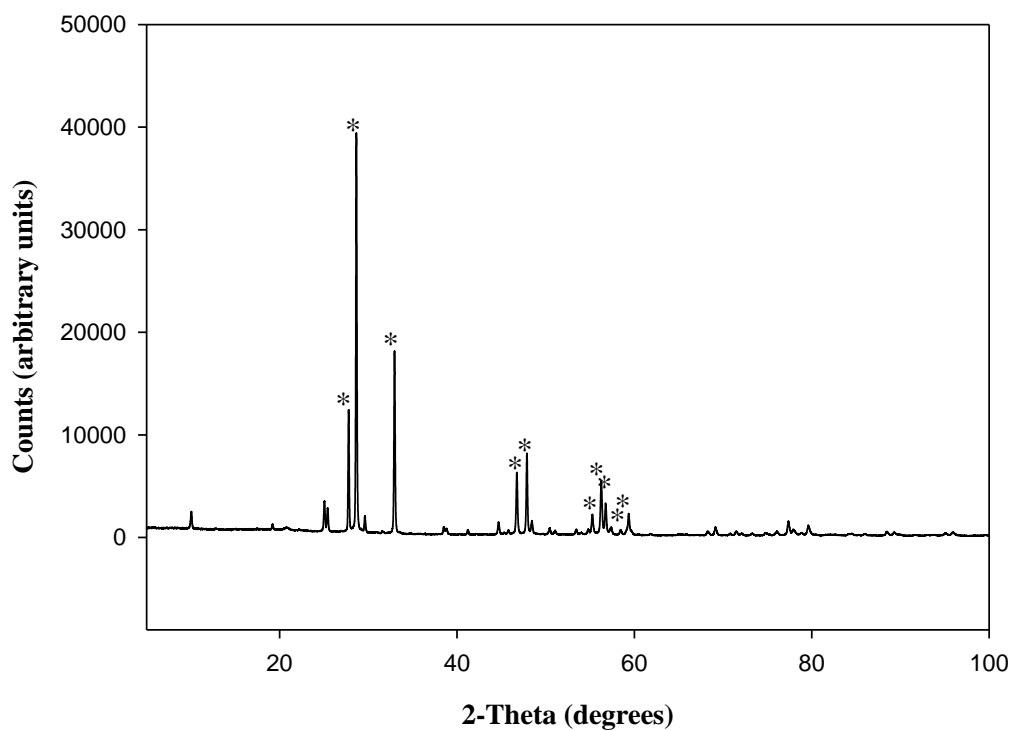


Figure 5.1 XPD pattern for $\text{Bi}_{20}\text{Ca}_7\text{NbO}_{39.5}$.

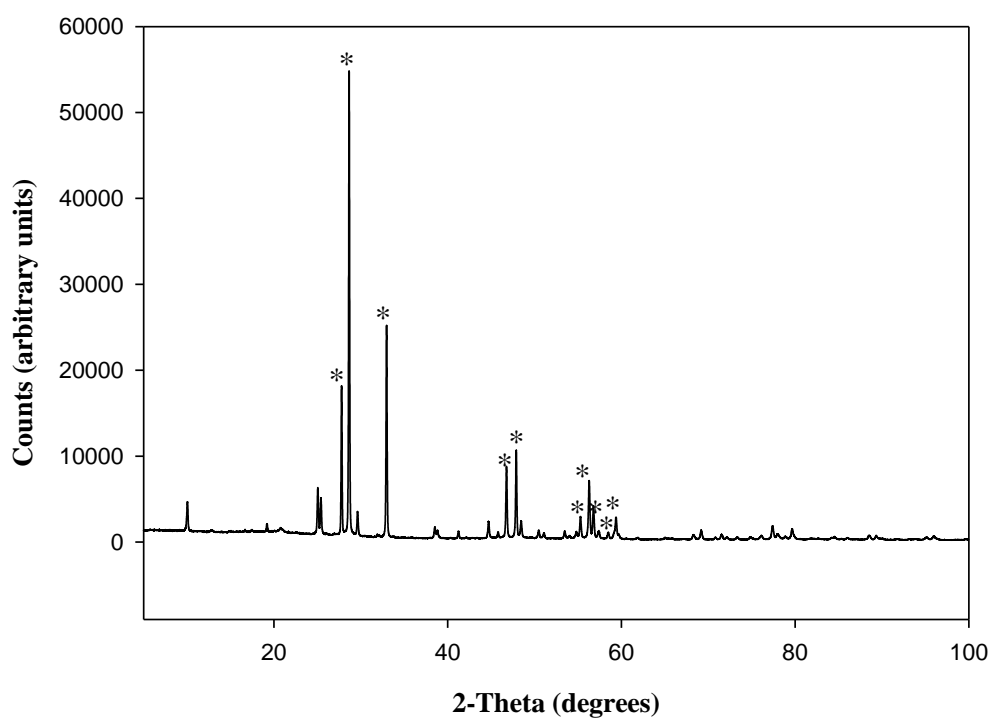


Figure 5.2 XPD pattern for $\text{Bi}_{10.75}\text{Ca}_{4.375}\text{GaO}_{22}$.

Since XPD data are insensitive to order resulting from oxygen effects in the presence of heavy metal atoms, additional information on the structural details were provided by high resolution NPD data collected at ambient temperature, thus enabling structural refinements to be carried out. Simultaneous refinements based on both X-ray and neutron data were carried out since cation order relating to Ca/Bi ions should have a more pronounced influence on the XPD pattern than the NPD pattern. The refinements were based on a structure with monoclinic symmetry and the space group $P2_1/m$, initially using idealised atom positions derived using the program Cryscon⁵ for this space group, inputting atom parameters from the hexagonal subcell along with the relationship between subcell and supercell, described in Section 3.3.3 where the same relationship is observed for a different material. Table 5.1 lists the atomic positions generated by Cryscon⁵.

Table 5.1 Atomic coordinates generated by Cryscon⁵ with space group $P2_1/m$, where $a = 9.3$, $b = 3.8$, $c = 9.6$ Å, $\beta = 110.1^\circ$. All cations are represented by Bi.

Atom number	Atom Type	x	y	z	Multiplicity
1	Bi	0.0625	0.2500	0.1875	2
2	Bi	0.1875	0.7500	0.5625	2
3	Bi	0.5625	0.2500	0.6875	2
4	Bi	0.3125	0.2500	0.9375	2
5	O	0.0625	0.2500	0.4375	2
6	O	0.4375	0.7500	0.5625	2
7	O	0.1875	0.7500	0.3125	2
8	O	0.3125	0.2500	0.6875	2
9	O	0.3125	0.2500	0.1875	2
10	O	0.9375	0.7500	0.0625	2
11	O	0.1875	0.7500	0.8125	2
12	O	0.5625	0.2500	0.9375	2

The ideal supercell has four cation positions and eight oxygen positions, all in 2e sites. The refinement suggested that one of the oxygen positions is totally empty, four are full and three are partially occupied. The final refined unit cell parameters for $\text{Bi}_{20}\text{Ca}_7\text{NbO}_{39.5}$ were $a = 9.3334(4)$, $b = 3.7956(1)$, $c = 9.6195(3)$ Å, $\beta = 110.101(2)^\circ$. Refinement statistics for 127 variables were $R_p = 0.052$, $R_{wp} = 0.070$ for XPD data, and $R_p = 0.024$, $R_{wp} = 0.030$ for NPD data, and $\chi^2 = 3.205$. Refined structural information is given in Table 5.2; fitted XPD and NPD profiles are shown in Figures 5.3 and 5.4, respectively, and demonstrate good agreement between observed and calculated profiles. Background undulation in the NPD data is consistent with a high level of disorder of the O sublattice, and this is supported by high thermal parameters for both cation and anion sites. In the refinement, oxygen occupancies were allowed to vary, with the final refinement showing O entirely occupying anion sites O1, O2, O3 and O6, with the remaining sites partially occupied, introducing O vacancies into the structure. All oxygen atoms were assigned a single temperature factor, as were all cations, and atom sites were allowed to shift freely. The final refinement shows Nb situated on the Bi4 site, with the remainder of the site being filled by Bi, Bi entirely occupying the Bi3 site, and the remaining cation sites being shared between Bi and Ca. The overall composition corresponds to $\text{Bi}_{21.3(2)}\text{Ca}_{6.28(9)}\text{Nb}_{1.0(1)}\text{O}_{39.8(6)}$. However, the esd values will be significantly underestimated, and the assumptions concerning the cation distribution may not be totally valid. For example there could be small amounts of Ca on the Bi/Nb4 site. The refined composition is therefore considered to agree satisfactorily with the expected $\text{Bi}_{20}\text{Ca}_7\text{NbO}_{39.5}$. Table 5.3 lists the metal-oxygen bond lengths in the refined $\text{Bi}_{20}\text{Ca}_7\text{NbO}_{39.5}$ structure. Overall, the structure is highly disordered, and the significant variations in atom positions from unit cell to unit cell are reflected in the high isotropic thermal parameters (Table 5.2).

Table 5.2 Refined structural information for Bi₂₀Ca₇NbO_{39.5}.

Site					Fractional	Uiso x 100
Atom	Symmetry	x	y	z	Occupancy	/ Å ²
Bi1	2e	0.0429(8)	0.25	0.1684(6)	0.432(5)	2.60(3)
Bi2	2e	0.1795(6)	0.75	0.5342(5)	0.689(8)	2.60(3)
Bi3	2e	0.565(5)	0.25	0.7076(5)	1	2.60(3)
Bi4	2e	0.3088(5)	0.25	0.9072(5)	0.86(2)	2.60(3)
Ca1	2e	0.0429(8)	0.25	0.1684(6)	0.568(5)	2.60(3)
Ca2	2e	0.1795(6)	0.75	0.5342(5)	0.311(8)	2.60(3)
Nb4	2e	0.3088(5)	0.25	0.9072(5)	0.14(2)	2.60(3)
O1	2e	0.044(2)	0.25	0.424(2)	1	5.8(1)
O2	2e	0.508(1)	0.75	0.530(2)	1	5.8(1)
O3	2e	0.217(3)	0.75	0.307(2)	1	5.8(1)
O4	2e	0.349(3)	0.25	0.678(2)	0.71(3)	5.8(1)
O5	2e	0.382(3)	0.25	0.226(3)	0.44(3)	5.8(1)
O6	2e	0.910(3)	0.75	0.057(2)	1	5.8(1)
O7	2e	0.195(5)	0.75	0.809(4)	0.42(3)	5.8(1)

Table 5.3 Selected bond distances (Å) for Bi₂₀Ca₇NbO_{39.5}.

Bi1-O1	2.46(2)	Bi3-O2	2.485(9)
Bi1-O3	2.56(1)	Bi3-O2	2.15(1)
Bi1-O6	2.32(1)	Bi3-O3	2.09(2)
Bi1-O6	2.35(2)	Bi3-O4	1.93(2)
Bi1-O7	2.30(4)	Bi3-O5	2.01(1)
Bi2-O1	2.33(1)	Bi4-O4	2.36(2)
Bi2-O1	2.25(2)	Bi4-O5	2.90(3)
Bi2-O3	2.33(2)	Bi4-O6	2.19(2)
Bi2-O4	2.55(2)	Bi4-O7	2.22(2)
Bi2-O7	2.60(4)		

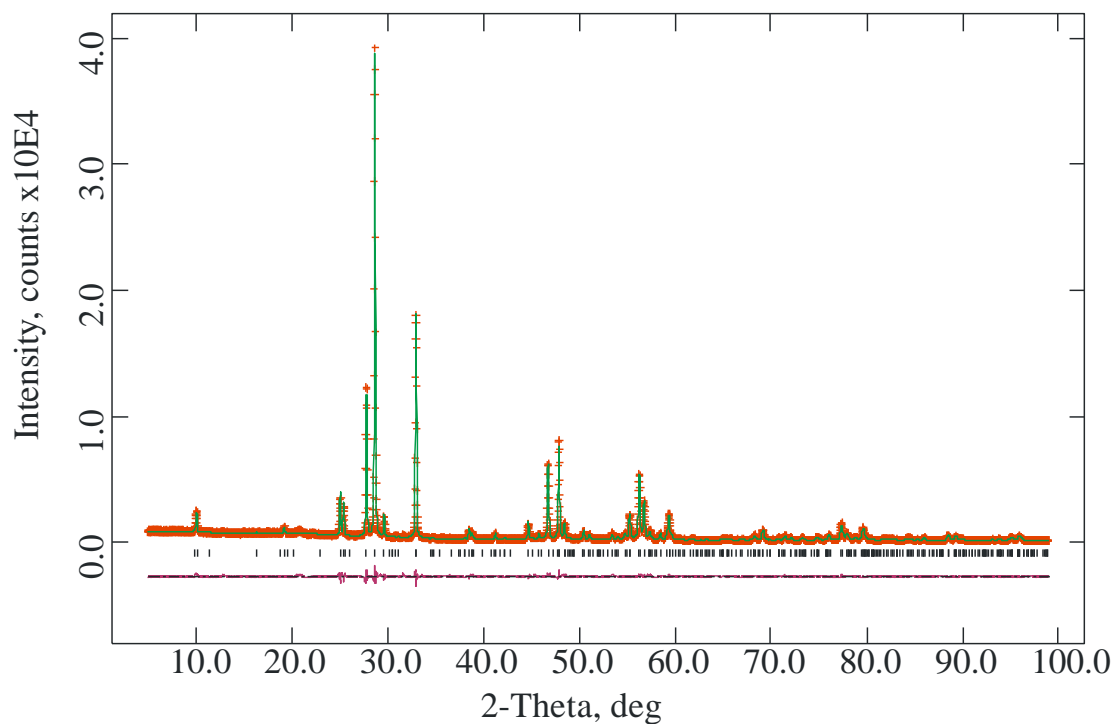


Figure 5.3 The observed (+), calculated (-) and difference XPD profiles for the final Rietveld refinement of $\text{Bi}_{20}\text{Ca}_7\text{NbO}_{39.5}$.

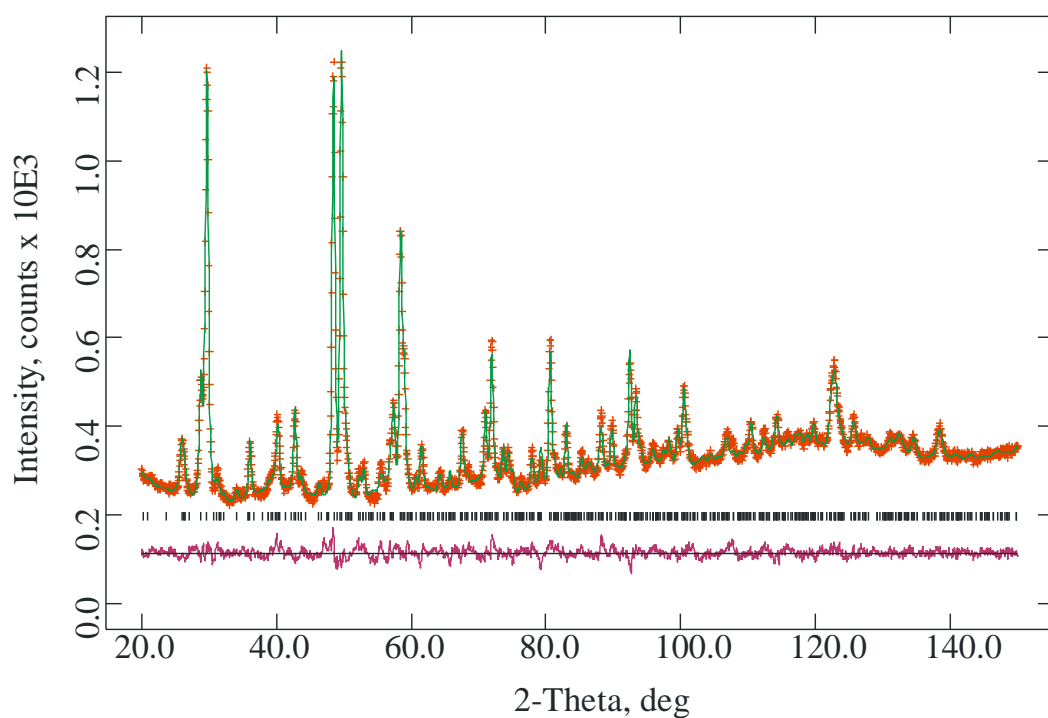


Figure 5.4 The observed (+), calculated (-) and difference NPD profiles for the final Rietveld refinement of $\text{Bi}_{20}\text{Ca}_7\text{NbO}_{39.5}$.

The phase $\text{Bi}_{10.75}\text{Ca}_{4.375}\text{GaO}_{22}$ was refined in a similar fashion and the final refined unit cell parameters were $a = 9.3293(3)$, $b = 3.7943(1)$, $c = 9.6136(2)$ Å, $\beta = 110.084(2)^\circ$. The same oxygen site was found to be vacant as was observed for the Bi-Ca-Nb-O phase, but now three sites are totally occupied and four have partial oxygen occupancy. Refinement statistics for 133 variables were $R_p = 0.051$, $R_{wp} = 0.072$ for XPD data, and $R_p = 0.031$, $R_{wp} = 0.042$ for NPD data, and $\chi^2 = 6.207$. Table 5.4 gives the refined structural parameters, and fitted XPD and NPD profiles are shown in Figures 5.5 and 5.6, respectively. As for $\text{Bi}_{20}\text{Ca}_7\text{NbO}_{39.5}$, a high level of structural disorder is indicated by the high thermal parameters for both cation and anion sites. The same cation site is occupied by Ga in $\text{Bi}_{10.75}\text{Ca}_{4.375}\text{GaO}_{22}$ that was occupied by Nb in $\text{Bi}_{20}\text{Ca}_7\text{NbO}_{39.5}$, with Ca again occupying Bi1 and Bi2 sites, and the Bi3 site uniquely occupied by Bi. The same constraints were used in both refinements, except that the Ga content was constrained to equal that expected, whereas Nb was allowed to vary in the refinement of $\text{Bi}_{20}\text{Ca}_7\text{NbO}_{39.5}$. The main differences between the two refinements are the lower Bi occupancy of the partially filled Bi sites in $\text{Bi}_{10.75}\text{Ca}_{4.375}\text{GaO}_{22}$, and the lower total oxygen occupancy as expected in this phase because of the higher Ca content and the absence of the Nb^{5+} cations. The overall composition corresponds to $\text{Bi}_{10.52(5)}\text{Ca}_{4.48(5)}\text{GaO}_{19.9(3)}$, in reasonable agreement with the expected composition, $\text{Bi}_{10.75}\text{Ca}_{4.375}\text{GaO}_{22}$. Table 5.5 lists the metal-oxygen bond lengths in the refined structure. The crystal structure of these materials is shown in Figure 5.7, displaying the stereochemistry of the different cation sites.

Table 5.4 Refined structural information for Bi_{10.75}Ca_{4.375}GaO₂₂.

Site		Fractional			Uiso x 100	
Atom	Symmetry	<i>x</i>	<i>y</i>	<i>z</i>	Occupancy	/ Å ²
Bi1	2e	0.047(1)	0.25	0.1680(8)	0.294(5)	3.07(4)
Bi2	2e	0.1764(8)	0.75	0.5313(6)	0.585(8)	3.07(4)
Bi3	2e	0.563(7)	0.25	0.7079(5)	1	3.07(4)
Bi4	2e	0.3089(7)	0.25	0.9076(5)	0.75	3.07(4)
Ca1	2e	0.047(1)	0.25	0.1680(8)	0.706(5)	3.07(4)
Ca2	2e	0.1764(8)	0.75	0.5313(6)	0.415(8)	3.07(4)
Ga4	2e	0.3089(7)	0.25	0.9076(5)	0.25	3.07(4)
O1	2e	0.051(2)	0.25	0.429(1)	1	4.2(1)
O2	2e	0.515(2)	0.75	0.553(2)	0.50(2)	4.2(1)
O3	2e	0.220(2)	0.75	0.308(2)	1	4.2(1)
O4	2e	0.358(2)	0.25	0.673(2)	0.67(2)	4.2(1)
O5	2e	0.390(4)	0.25	0.204(4)	0.32(2)	4.2(1)
O6	2e	0.910(2)	0.75	0.055(2)	1	4.2(1)
O7	2e	0.148(2)	0.75	0.766(2)	0.48(2)	4.2(1)

Table 5.5 Selected bond distances (Å) for Bi_{10.75}Ca_{4.375}GaO₂₂.

Bi1-O1	2.50(1)	Bi3-O2	2.36(1)
Bi1-O3	2.56(1)	Bi3-O2	2.36(2)
Bi1-O6	2.33(1)	Bi3-O3	2.08(2)
Bi1-O6	2.31(1)	Bi3-O4	1.82(2)
Bi1-O7	2.12(2)	Bi3-O5	2.06(1)
Bi2-O1	2.69(1)	Bi4-O4	2.46(2)
Bi2-O1	2.75(1)	Bi4-O5	2.69(3)
Bi2-O3	2.32(1)	Bi4-O6	2.20(2)
Bi2-O4	2.60(1)	Bi4-O7	2.51(1)
Bi2-O7	2.36(2)		

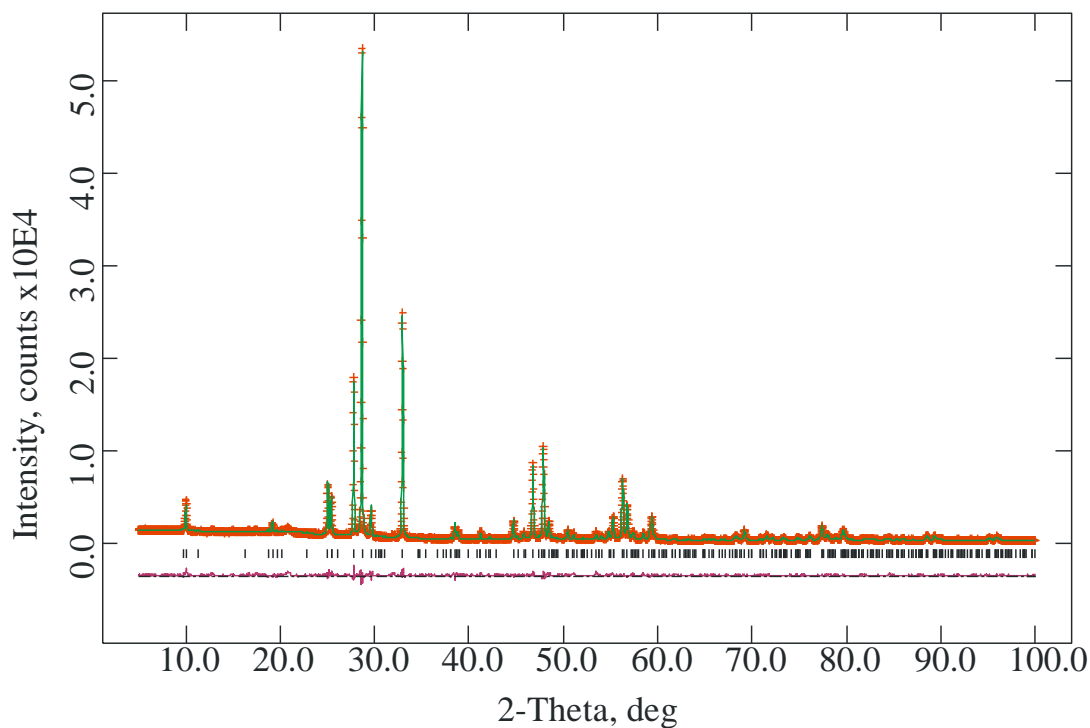


Figure 5.5 The observed (+), calculated (-) and difference XPD profiles for the final Rietveld refinement of $\text{Bi}_{10.75}\text{Ca}_{4.375}\text{GaO}_{22}$.

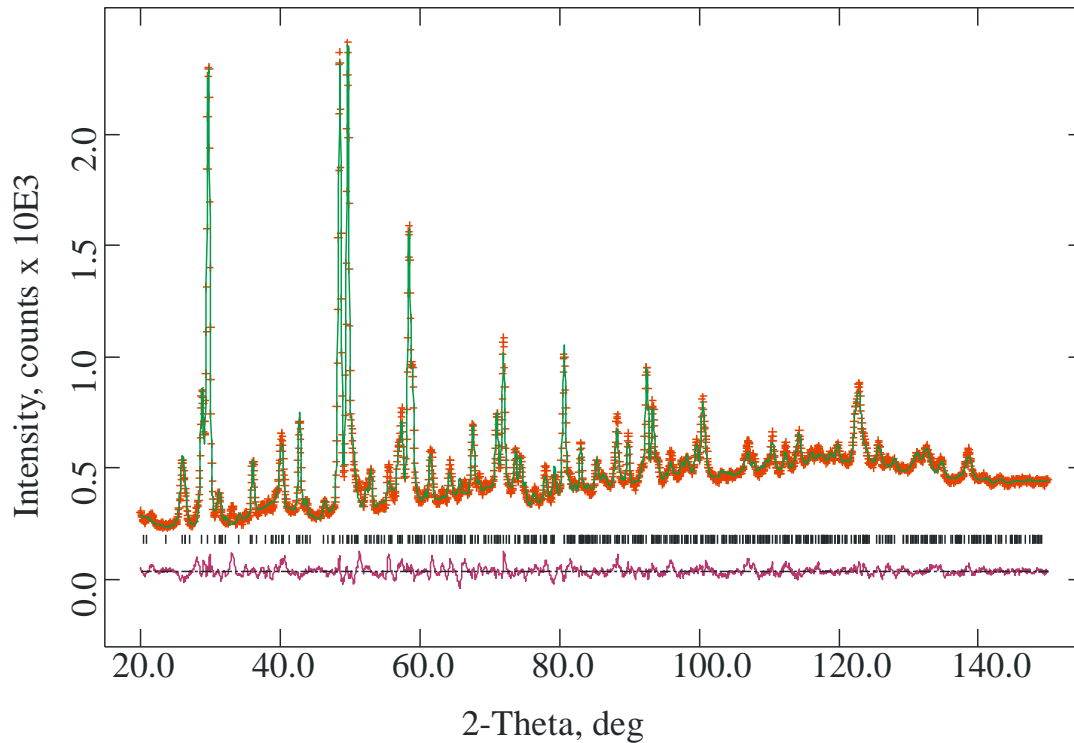


Figure 5.6 The observed (+), calculated (-) and difference NPD profiles for the final Rietveld refinement of $\text{Bi}_{10.75}\text{Ca}_{4.375}\text{GaO}_{22}$.

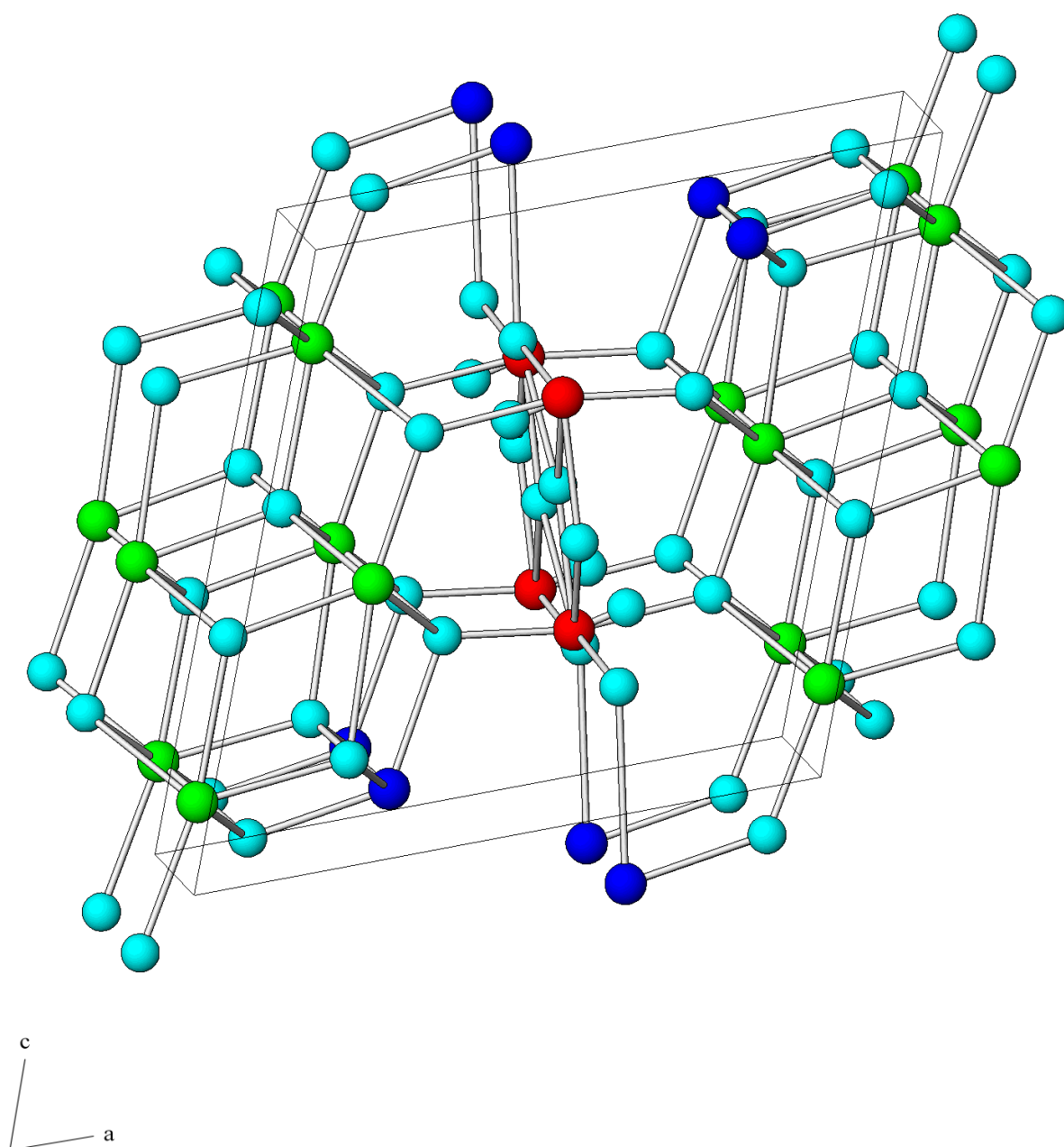


Figure 5.7 The crystal structure of $\text{Bi}_{20}\text{Ca}_7\text{NbO}_{39.5}$ and $\text{Bi}_{10.75}\text{Ca}_{4.375}\text{GaO}_{22}$, where the green spheres represent the shared Bi/Ca sites, red spheres represent the pure bismuth site, dark blue spheres represent the shared Bi/Nb or Bi/Ga site and light blue spheres represent oxygen.

5.3.2 Thermal Stability

After annealing samples of $\text{Bi}_{20}\text{Ca}_7\text{NbO}_{39}$ and $\text{Bi}_{10.75}\text{Ca}_{4.375}\text{GaO}_{22}$ for 750 h at 773 K no phase transformation was apparent by XPD analysis for either sample, allowing the conclusion that these materials remain stable after prolonged periods at this temperature.

5.3.3 High Temperature Structural Studies of $\text{Bi}_{20}\text{Ca}_7\text{NbO}_{39}$

Investigations of possible structure transitions that may occur in $\text{Bi}_{20}\text{Ca}_7\text{NbO}_{39}$ with variation of temperature were made using DTA, described in Section 2.5. Heating and cooling cycles between a temperature range of 298 K and 1073 K were therefore used to seek any phase changes, the results to which are displayed in Figure 5.8.

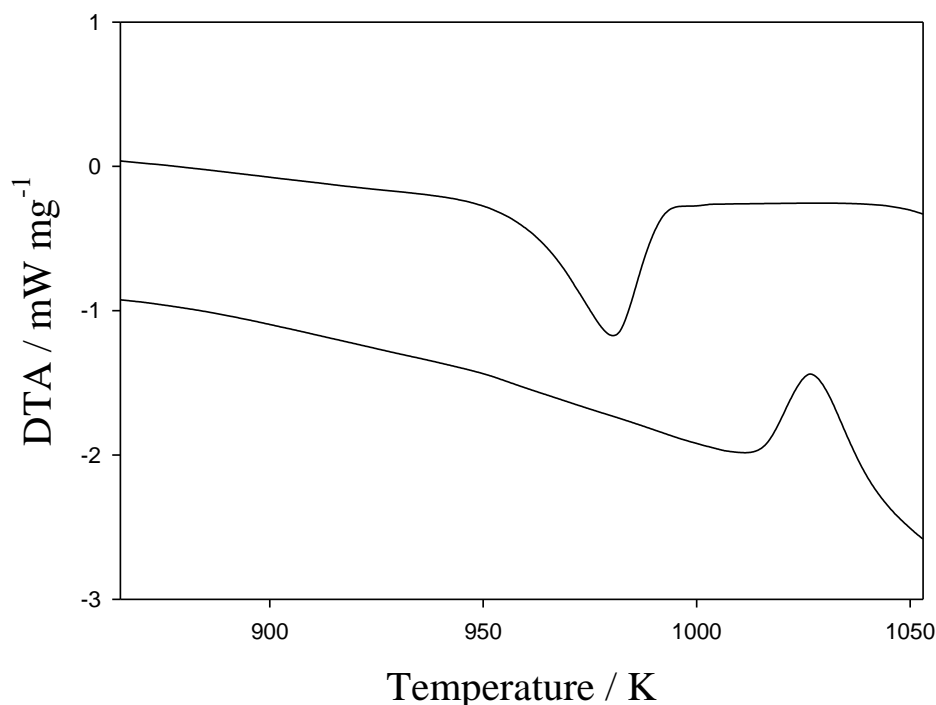


Figure 5.8 DTA results for $\text{Bi}_{20}\text{Ca}_7\text{NbO}_{39}$, showing the heating curve (lower) and cooling curve (upper).

An endothermic energy change with a peak onset at 1011 K is apparent in the heating curve, suggestive of phase change. The cooling curve shows an exothermic change, with a peak onset at 994 K, as the phase change is reversed and the structure reverts back to its room temperature form.

To support this evidence of phase change suggested by DTA, and to further explore the nature of this, variable temperature XPD, as described in Section 2.2.1, was employed. XPD patterns were therefore recorded at a range of temperatures either side of the phase transition indicated by DTA, and are shown in Figure 5.9.

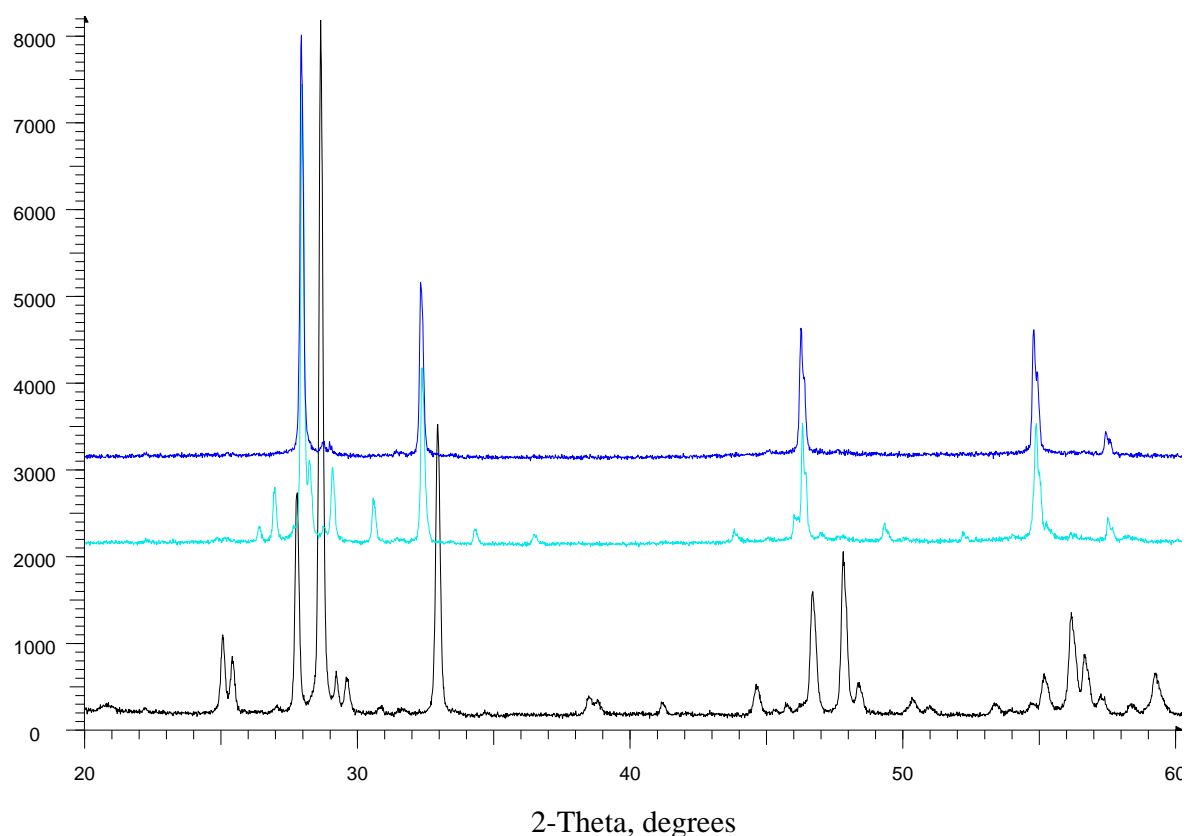


Figure 5.9 Variable temperature XPD results for $\text{Bi}_{20}\text{Ca}_7\text{NbO}_{39}$ at 298 K (black), 973 K (green), 1023 K (light blue) and 1073 K (dark blue).

The results of variable temperature XPD experiments support the evidence of phase change shown by DTA. At 1023 K the phase change is clearly occurring as many of the peaks are reduced in intensity and new peaks become apparent as an unidentified transitional phase appears to form. By 1073 K the structural change to a face-centred cubic material appears complete.

Variable temperature XPD experiments for $\text{Bi}_{20}\text{Ca}_7\text{NbO}_{39}$ across a broader temperature range of 298 K to 1073 K showed no further evidence of phase change, confirming the occurrence of only two well defined phases, suggested by the presence of a single peak in both the heating and cooling curves in DTA - a high temperature fcc phase and a low temperature monoclinic phase.

XPD results indicated that upon quenching of $\text{Bi}_{20}\text{Ca}_7\text{NbO}_{39}$ from 1073 K in liquid nitrogen, the same structure was formed that was shown by variable temperature XPD experiments at 1073 K. This high temperature phase could be indexed on a face-centred cubic unit cell, with space group symmetry $\text{Fm}\bar{3}\text{m}$, and lattice parameter $a = 5.476(2)$ Å. Figure 5.10 shows the XPD pattern obtained for this material. A slight impurity peak can be seen at around $29^\circ 2\theta$ in both the liquid nitrogen quenched sample, and the variable temperature XPD scan recorded at 1073 K. This relates to $\text{Bi}_5\text{Nb}_3\text{O}_{15}$.

Structural refinements were made using this XPD data, using the program GSAS⁷, based on the Rietveld method⁶. A starting model for the refinement was based on that derived for pure $\delta\text{-Bi}_2\text{O}_3$ ⁸, space group $\text{Fm}\bar{3}\text{m}$, with the cations statistically distributed ($\text{Bi}:\text{Ca}:\text{Nb} = 20:7:1$) at the $4a$ (0, 0, 0) site and the oxygen atoms on their regular $8c$ ($\frac{1}{4}, \frac{1}{4}, \frac{1}{4}$) and interstitial $32f$ (x, x, x) sites. The final refined unit cell parameter in space group $\text{Fm}\bar{3}\text{m}$ was $a = 5.4666(1)$ Å. Refinement statistics for 50 variables were $R_p = 0.0539$,

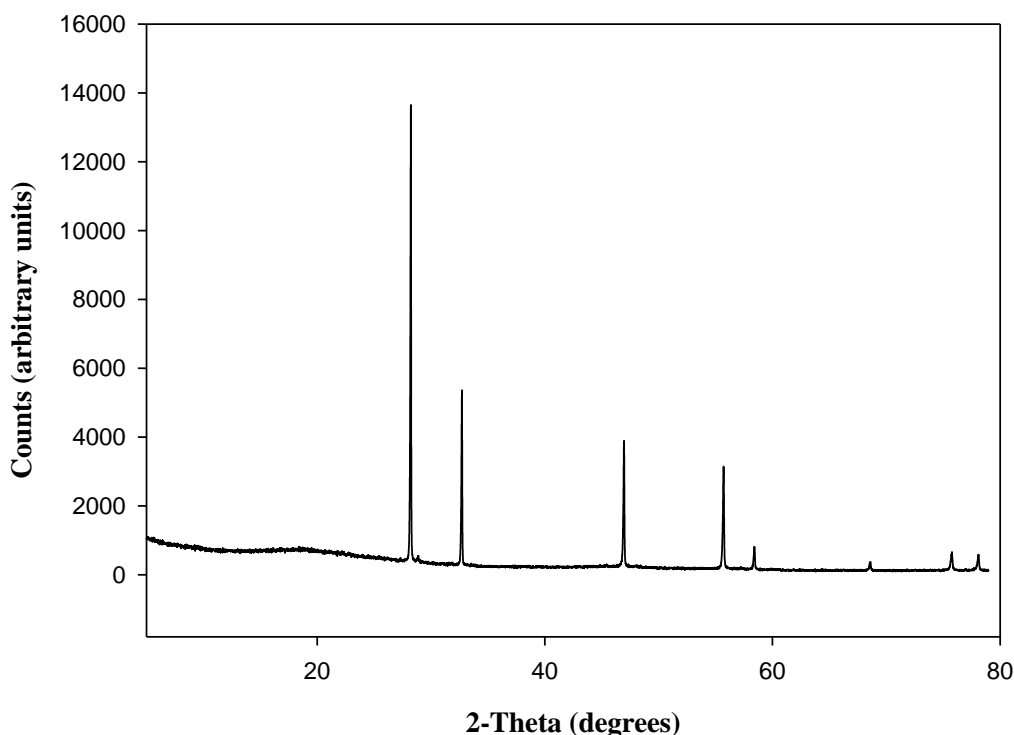


Figure 5.10 XPD pattern for liquid nitrogen quenched $\text{Bi}_{20}\text{Ca}_7\text{NbO}_{39}$.

$R_{\text{wp}} = 0.0790$, and $\chi^2 = 2.472$. Good agreement between observed and calculated profiles is evident in the fitted XPD profile shown in Figure 5.11, in which a decrease in peak intensities with 2θ is apparent, signifying a high level of disorder of the O sublattice. This is supported by high cation thermal parameters, listed in the refined structural information given in Table 5.6. In the refinement, all cations were assigned a single temperature factor, but oxygen temperature factors were constrained to allow a sensible refinement. Whilst being constrained to equal the sum of that expected in this refinement, oxygen occupancies were allowed to vary, as was the position of the $32f$ (x, x, x) interstitial oxygen site. The $32f$ (x, x, x) interstitial oxygen site, where $x = 0.356(6)$, is significantly closer to the vacant octahedral site in the centre of the unit cell compared to $\text{Bi}_6\text{Ca}_3\text{ReO}_{15.5}$ ($x = 0.311(3)$) (discussed in Chapter 4) and previous reported values of $x = 0.319(2)$ and $x = 0.32(1)$ for

$(\text{Bi}_2\text{O}_3)_{0.8}(\text{Er}_2\text{O}_3)_{0.2}$ and $(\text{Bi}_2\text{O}_3)_{0.73}(\text{Y}_2\text{O}_3)_{0.27}$, respectively^{8,9}. However, this refined value for $32f(x, x, x)$ could be inaccurate and therefore misleading due to the poor sensitivity of XPD data to oxygen atoms in the presence of heavy Bi and Nb. The final refinement shows 49% of oxide ions are displaced along $[111]$ directions from their ideal $8c(\frac{1}{4}, \frac{1}{4}, \frac{1}{4})$ site to the $32f(x, x, x)$ site, and compares well with the 52% and 47% of oxide ions that are shown to be displaced in face-centred cubic materials $\text{Bi}_6\text{Ca}_3\text{ReO}_{15.5}$ and quenched $\text{Bi}_{10}\text{Ca}_5\text{ReO}_{23.5}$, respectively (discussed in Chapter 4). As was the case for these aforementioned structural refinements, little evidence was found to suggest displacement of the cations from their ideal $4a(0, 0, 0)$ site to the $24e(x, 0, 0)$ site, proposed by Battle *et al.*⁹.

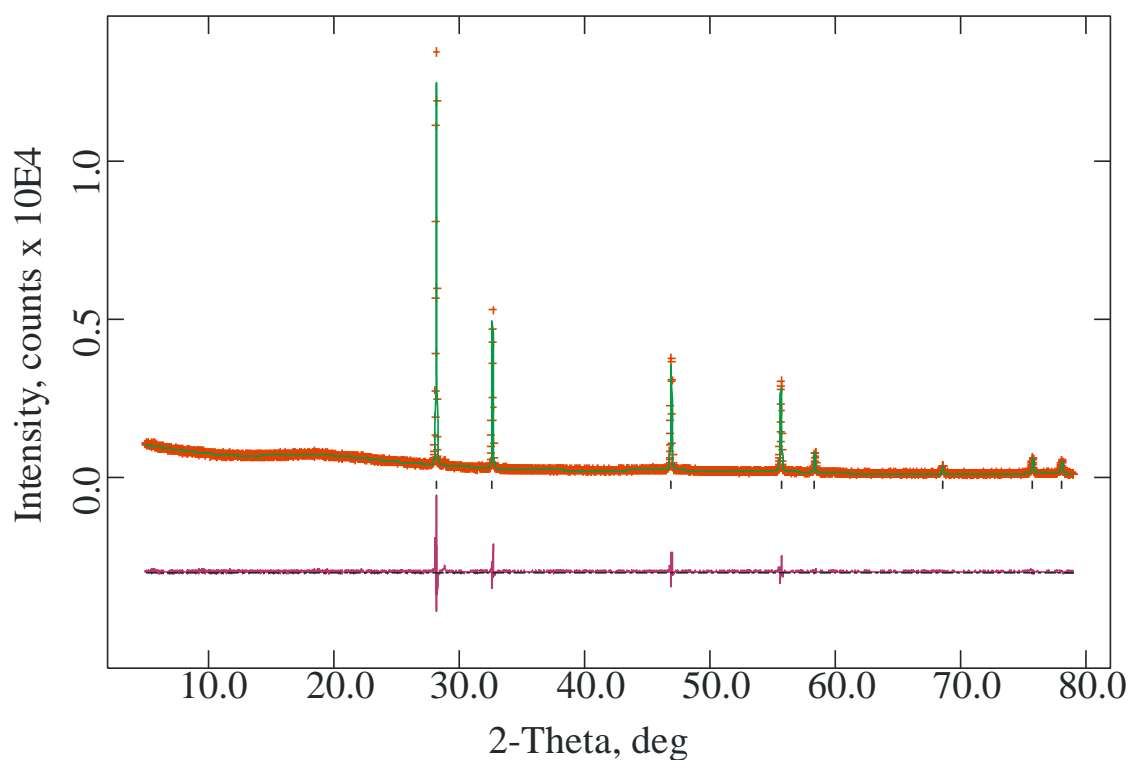


Figure 5.11 Observed (+), calculated (-), and difference XPD profiles for liquid nitrogen quenched $\text{Bi}_{20}\text{Ca}_7\text{NbO}_{39}$.

Table 5.6 Refined structural information from XPD data recorded from liquid nitrogen quenched $\text{Bi}_{20}\text{Ca}_7\text{NbO}_{39}$, determined by Rietveld analysis.

Site		Fractional			Uiso x 100 / \AA^2
Atom	Symmetry	x	y	z	
Bi	4a	0	0	0	4.43(8)
Ca	4a	0	0	0	4.43(8)
Nb	4a	0	0	0	4.43(8)
O1	8c	0.25	0.25	0.25	1
O2	32f	0.356(6)	0.356(6)	0.356(6)	1

XPD results indicated that by quenching $\text{Bi}_{20}\text{Ca}_7\text{NbO}_{39}$ in air down to room temperature, a different phase was produced to that of both the furnace-cooled and liquid nitrogen quenched samples, although it is closely related to the monoclinic furnace-cooled material. Figure 5.12 shows the XPD pattern for this air quenched phase.

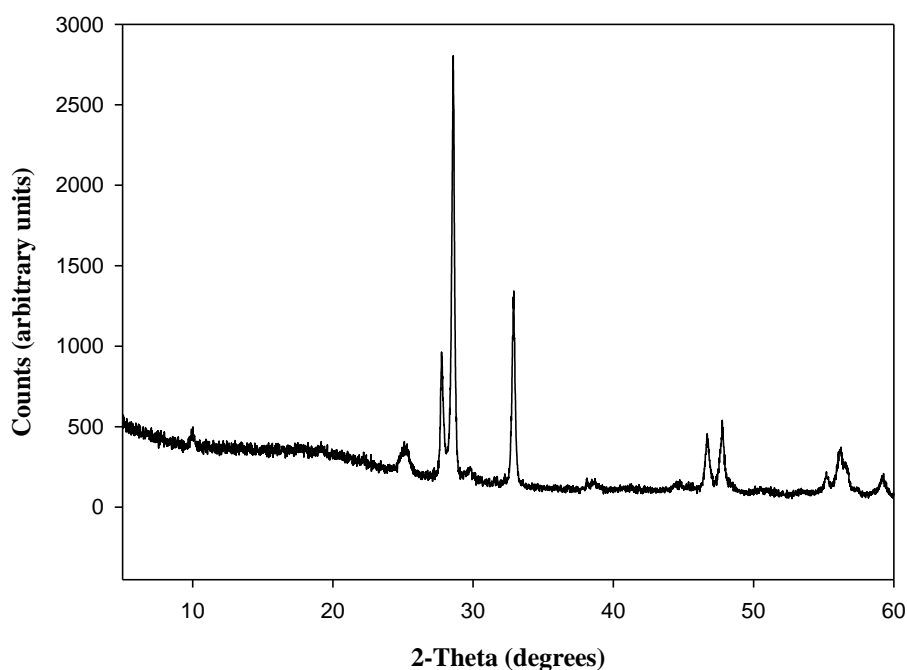


Figure 5.12 XPD pattern for air quenched $\text{Bi}_{20}\text{Ca}_7\text{NbO}_{39}$.

Careful indexing of these data suggests that these structural changes occur only in the supercell, and that the subcell maintains a distorted fluorite hexagonal $R\bar{3}m$ crystal symmetry, as for the furnace-cooled sample. The supercell of the air quenched sample appears to simplify, compared to the furnace-cooled sample, yet remains to have $P2_1/m$ space group symmetry, with fewer reflections shown in XPD data.

Consequent structural refinements were made using these XPD data, based on the Rietveld method⁶, using the program GSAS⁷. The refinement was based on a structure with monoclinic symmetry and the space group $P2_1/m$, initially using idealised atom positions derived using the program Cryscon⁵ for this space group, inputting atom parameters from the hexagonal subcell along with the relationship between subcell and supercell. The atomic coordinates generated are listed previously in Table 5.1.

The final refined unit cell parameters in space group $P2_1/m$ were $a = 9.382(5)$, $b = 3.807(3)$, $c = 9.597(6)$ Å and $\beta = 110.10(2)^\circ$. Refinement statistics for 63 variables were $R_p = 0.1161$, $R_{wp} = 0.1524$, and $\chi^2 = 1.273$. The refined structural information is given in Table 5.7 and the fitted XPD profile is shown in Figure 5.13, which demonstrates good agreement between observed and calculated profiles. A high level of disorder of the oxygen sublattice is suggested by both a decrease in peak intensities with increasing 2θ , and an extensive diffuse background. High cation thermal parameters also support this. As it is difficult to locate oxygen atoms by XPD in the presence of heavy Bi and Nb, oxygen temperature factors were constrained, in addition to oxygen positions and occupancies, to allow a sensible refinement. All cations were assigned a single temperature factor, and sites were allowed to shift freely. The final refinement suggests Bi to be the sole occupier of Bi1 and Bi2 sites, with Ca solely occupying the third cation site and the remaining site being

Table 5.7 Refined structural information from XPD data recorded from air quenched $\text{Bi}_{20}\text{Ca}_7\text{NbO}_{39}$, determined by Rietveld analysis.

Atom	x	y	z	Fractional Occupancy	Uiso x 100 / \AA^2
Bi1	0.059(5)	0.25	0.186(6)	1	5.6(7)
Bi2	0.193(4)	0.75	0.566(5)	1	5.6(7)
Ca3	0.54(2)	0.25	0.64(1)	1	5.6(7)
Nb4	0.326(9)	0.25	0.95(1)	0.143	5.6(7)
Bi4	0.326(9)	0.25	0.95(1)	0.857	5.6(7)
O1	0.0625	0.2500	0.4375	0.696	2.5
O2	0.4375	0.7500	0.5625	0.696	2.5
O3	0.1875	0.7500	0.3125	0.696	2.5
O4	0.3125	0.2500	0.6875	0.696	2.5
O5	0.3125	0.2500	0.1875	0.696	2.5
O6	0.9375	0.7500	0.0625	0.696	2.5
O7	0.1875	0.7500	0.8125	0.696	2.5
O8	0.5625	0.2500	0.9375	0.696	2.5

shared by Bi and Nb. This is in contrast to the refinement of the related furnace-cooled material, where Bi1 and Bi2 sites are jointly occupied by Bi and Ca, with Bi entirely occupying the Bi3 site and Nb and Bi sharing the Bi4 site. Therefore, despite many structural similarities between that of the air quenched and furnace-cooled samples, significant differences in the crystal structure are apparent. However, the refinement of this air quenched material was carried out solely using XPD data. Given this, despite doubts over the full reliability of the refinement, conductivity measurements carried out on both the air quenched and furnace-cooled samples do indeed confirm that regardless of many similarities, these two materials are likely to possess different structures due to the large difference in conductivity displayed. The conductivity measurements are discussed in detail in Section 5.3.4.

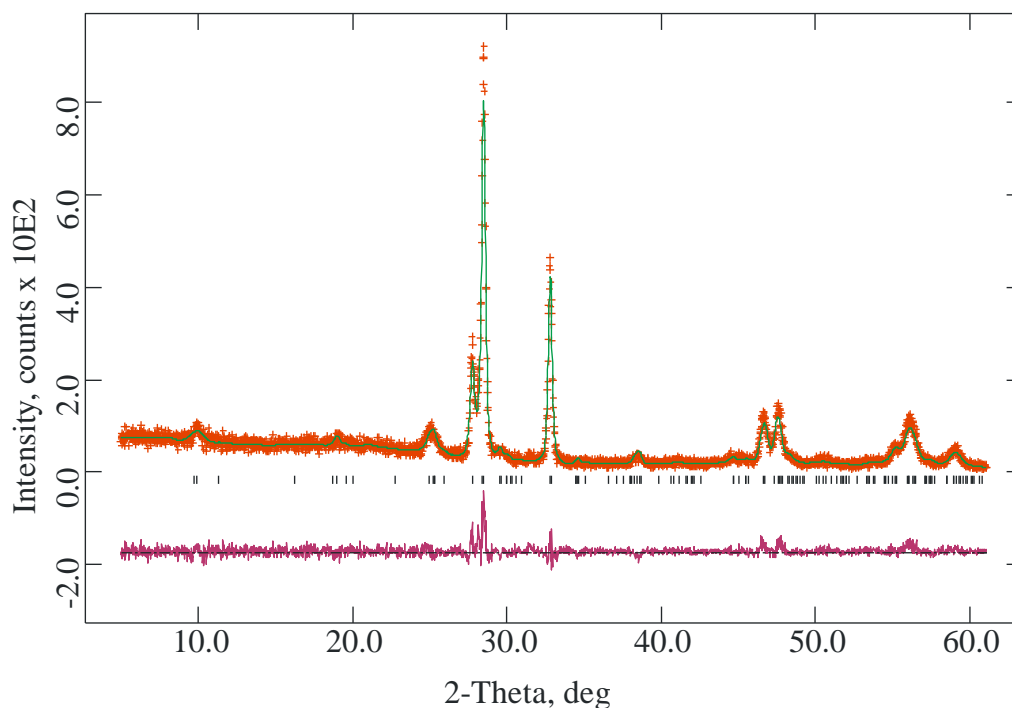


Figure 5.13 The observed (+), calculated (-) and difference XPD profiles for the final Rietveld refinement of air quenched $\text{Bi}_{20}\text{Ca}_7\text{NbO}_{39}$.

5.3.4 Ionic Conductivity

With previous observations of high oxide ion conductivity in fluorite-related bismuth oxide based materials, and with all materials discussed in this Chapter being related to the fluorite face-centred cubic unit cell of $\delta\text{-Bi}_2\text{O}_3$, these materials might be expected to exhibit high oxide ion conducting properties, owing to the high level of oxygen sublattice structural disorder present in all three phases. Oxide ion conductivity data were therefore collected by impedance spectroscopy, with measurements made between 473 K and 773 K and the frequency range 1 Hz to 1×10^6 Hz. Materials were prepared and determinations made using the method outlined in Chapter 2. The density for each sample pellet was calculated and

compared with the density of its unit cell. From this it could be determined that all samples had a density in the range 85 to 95 % of the theoretical.

The complex plane impedance plots could be fitted to a single semicircle and resistance was therefore assigned to bulk effects, with electronic contribution to conductivity assumed negligible. An example of a complex plane plot for $\text{Bi}_{20}\text{Ca}_7\text{NbO}_{39}$ is shown in Figure 5.14, using the data obtained at 528 K. The conductivities were calculated from the bulk resistance determined from the minima in the complex plane plots and plots of $\log \sigma$ versus $1000\text{K}/T$ for $\text{Bi}_{10.75}\text{Ca}_{4.375}\text{GaO}_{22}$, $\text{Bi}_{20}\text{Ca}_7\text{NbO}_{39}$, liquid nitrogen quenched fcc $\text{Bi}_{20}\text{Ca}_7\text{NbO}_{39}$ and air quenched monoclinic $\text{Bi}_{20}\text{Ca}_7\text{NbO}_{39}$ are shown in Figure 5.15. Table 5.8 lists the Arrhenius activation energies, E_a , for these materials that could subsequently be determined from these plots of $\log \sigma$ versus $1000\text{K}/T$.

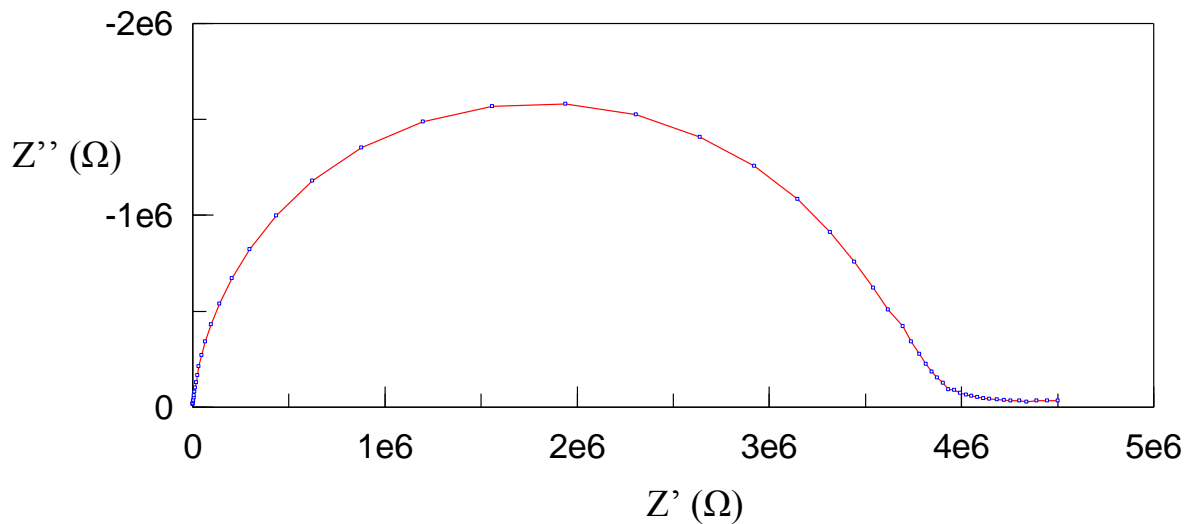


Figure 5.14 Complex plane impedance plot of real (Z') and imaginary (Z'') components, for $\text{Bi}_{20}\text{Ca}_7\text{NbO}_{39}$ at a temperature of 528 K.

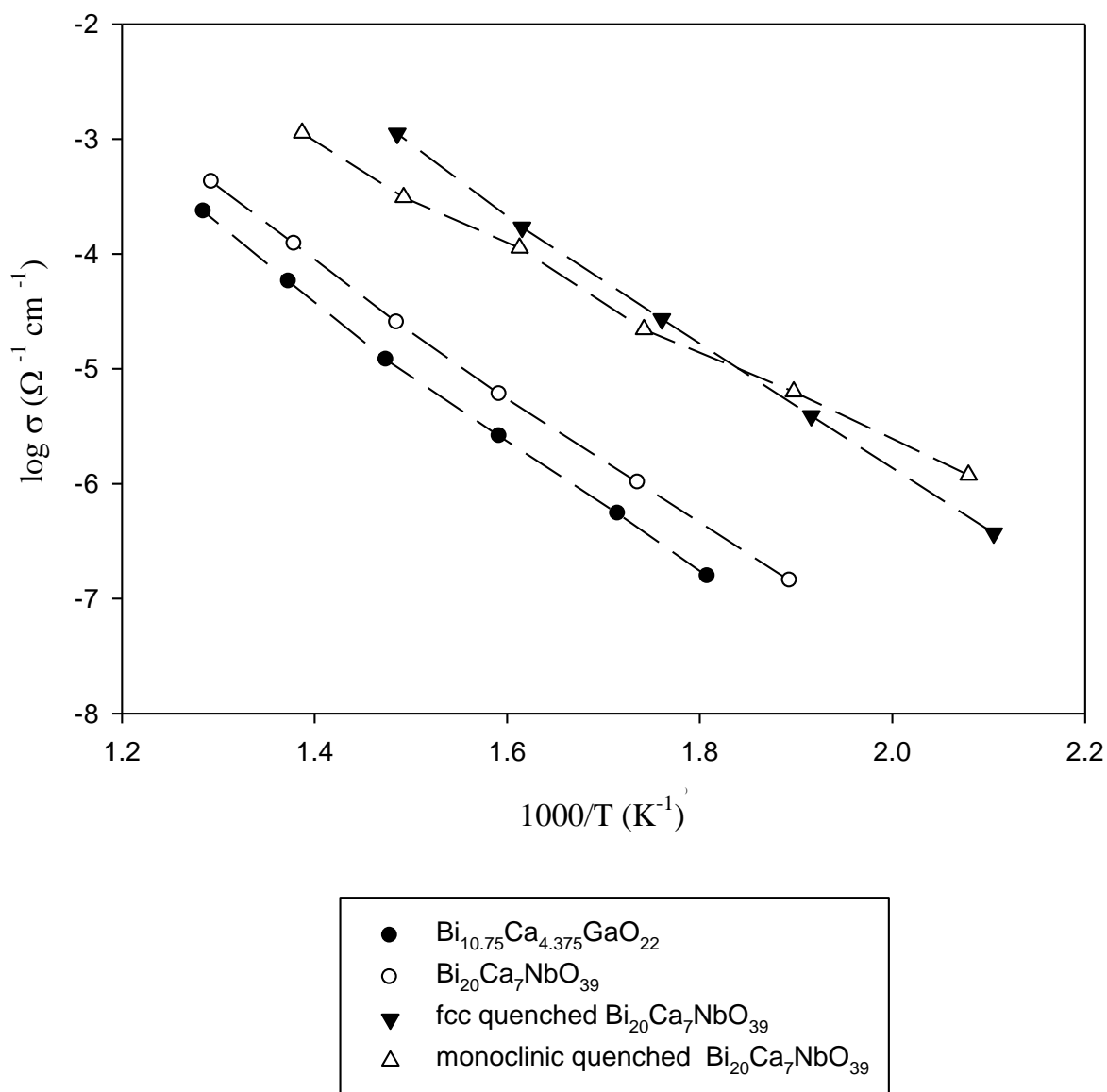


Figure 5.15 Arrhenius plots of conductivity determined by impedance spectroscopy for $\text{Bi}_{10.75}\text{Ca}_{4.375}\text{GaO}_{22}$, $\text{Bi}_{20}\text{Ca}_7\text{NbO}_{39}$, liquid nitrogen quenched fcc $\text{Bi}_{20}\text{Ca}_7\text{NbO}_{39}$ and air quenched monoclinic $\text{Bi}_{20}\text{Ca}_7\text{NbO}_{39}$.

Table 5.8 Activation energies, E_a , for $\text{Bi}_{10.75}\text{Ca}_{4.375}\text{GaO}_{22}$, $\text{Bi}_{20}\text{Ca}_7\text{NbO}_{39}$, liquid nitrogen quenched fcc $\text{Bi}_{20}\text{Ca}_7\text{NbO}_{39}$ and air quenched monoclinic $\text{Bi}_{20}\text{Ca}_7\text{NbO}_{39}$.

Material	E_a / eV
$\text{Bi}_{10.75}\text{Ca}_{4.375}\text{GaO}_{22}$	1.19
$\text{Bi}_{20}\text{Ca}_7\text{NbO}_{39}$	1.12
fcc quenched $\text{Bi}_{20}\text{Ca}_7\text{NbO}_{39.5}$	1.11
monoclinic quenched $\text{Bi}_{20}\text{Ca}_7\text{NbO}_{39}$	0.85

Both $\text{Bi}_{20}\text{Ca}_7\text{NbO}_{39.5}$ and $\text{Bi}_{10.75}\text{Ca}_{4.375}\text{GaO}_{22}$ display good oxide ion conductivity, with the conductivity of $\text{Bi}_{20}\text{Ca}_7\text{NbO}_{39.5}$ being marginally better than that of $\text{Bi}_{10.75}\text{Ca}_{4.375}\text{GaO}_{22}$. This could be a consequence of the relative amounts of bismuth present in the materials, despite niobium being a more highly charged cation than gallium (+5 as opposed to +3), decreasing the oxygen vacancies in this more conductive material. This supports previous reports by Takahashi *et al.*¹¹ that in doped bismuth oxide materials, the ionic conductivity decreases with added oxide content relative to bismuth. Conductivities are comparable to well characterised stabilised bismuth oxide ion conductors, with $\text{Bi}_{20}\text{Ca}_7\text{NbO}_{39.5}$ displaying a conductivity of $4.22 \times 10^{-4} \Omega^{-1} \text{cm}^{-1}$ at 773 K, being within an order of magnitude of the well known ionic conductors $(\text{Bi}_2\text{O}_3)_{0.65}(\text{Gd}_2\text{O}_3)_{0.35}$ and $(\text{Bi}_2\text{O}_3)_{0.78}(\text{MoO}_3)_{0.22}$, having conductivities of $3.5 \times 10^{-3} \Omega^{-1} \text{cm}^{-1}$ and $2.6 \times 10^{-3} \Omega^{-1} \text{cm}^{-1}$, respectively, at the same temperature¹¹.

Both air quenched monoclinic and liquid nitrogen quenched fcc forms of $\text{Bi}_{20}\text{Ca}_7\text{NbO}_{39}$ show a large improvement in ionic conductivity, compared to the furnace-

cooled form. Interestingly, the activation energy for the fcc quenched material ($E_a = 1.11$ eV) is very similar to that of the furnace-cooled form of $\text{Bi}_{20}\text{Ca}_7\text{NbO}_{39}$ ($E_a = 1.12$ eV), yet that of the monoclinic quenched material is considerably lower ($E_a = 0.85$ eV). The significantly lower activation energy for the monoclinic quenched sample implies that despite having a related structure to the furnace-cooled sample, the mechanism of conductivity is likely to be very different. This also explains the large increase in conductivity for this material, which is shown to be as good an ionic conductor as the liquid nitrogen quenched face-centred cubic form of $\text{Bi}_{20}\text{Ca}_7\text{NbO}_{39}$, with its much simpler $\delta\text{-Bi}_2\text{O}_3$ related structure. This fcc form of $\text{Bi}_{20}\text{Ca}_7\text{NbO}_{39}$ displays a conductivity of $1.11 \times 10^{-3} \Omega^{-1} \text{cm}^{-1}$ at 673 K, slightly better than that displayed by the quenched fcc $\text{Bi}_{10}\text{Ca}_5\text{ReO}_{23.5}$ material, discussed in Chapter 4, despite having a larger activation energy of $E_a = 1.11$ eV, compared to a value of $E_a = 0.95$ eV for quenched $\text{Bi}_{10}\text{Ca}_5\text{ReO}_{23.5}$. Both high temperature quenched forms of $\text{Bi}_{20}\text{Ca}_7\text{NbO}_{39}$, which display conductivities of $1.11 \times 10^{-3} \Omega^{-1} \text{cm}^{-1}$ and $1.11 \times 10^{-4} \Omega^{-1} \text{cm}^{-1}$ at 673 K for the fcc and monoclinic forms, respectively, exhibit conductivities greater than that displayed by $\text{Bi}_{28}\text{Re}_2\text{O}_{49}$ at the corresponding temperature ($\sigma = 5.4 \times 10^{-4} \Omega^{-1} \text{cm}^{-1}$ at 673 K)¹. In the case of the fcc $\text{Bi}_{20}\text{Ca}_7\text{NbO}_{39}$ material, this large difference is likely to be due to the simpler fluorite-related structure possessed by this quenched form.

5.4 References

- 1 Crumpton, T. E.; Mosselmans, J. F. W.; Greaves, C. *J. Mater. Chem.* **15** (2005) 164
- 2 Schumb, W. C.; Rittner, E. S. *J. Am. Chem Soc.* **65** (1943) 1055
- 3 Takahashi, T.; Iwahara, H. J.; Arao, T. *J. Appl. Electrochem.* **5** (1975) 187
- 4 Takahashi, T.; Iwahara, H. J.; Esaka, T. *J. Electrochem. Soc.* **124** (1977) 1563
- 5 Available from Shapessoftware: <http://www.shapessoftware.com/>
- 6 Young, R. A. *The Rietveld Method* International Union of Crystallography, Oxford University Press (1993)
- 7 Larson, A. C.; Von Dreele, R. B. *General Structure Analysis System (GSAS)* Los Almos National Laboratory, Los Almos, NM (1994)
- 8 Battle, P. D.; Catlow, C. R. A.; Drennan, J.; Murray, A. D. *J. Phys. C* **16** (1983) L561
- 9 Battle, P. D.; Catlow, C. R. A.; Moroney, L. M. *J. Solid State Chem.* **67** (1987) 42
- 10 Pun, R.; Feteira, A. M.; Sincliar, D. C.; Greaves, C. *J. Am. Chem. Soc.* **128** (2006) 15386
- 11 Takahashi, T.; Iwahara, H. *Mat. Res. Bull.* **13** (1978) 1447

CHAPTER 6

Preliminary Studies of Bismuth-Niobium-Oxygen Solid Solutions

6.1 Introduction

Much research has been carried out in recent years into bismuth oxide related materials doped with small amounts of niobium oxide, with many yielding fluorite-type phases based on superlattice ordering of the cubic subcell of δ -Bi₂O₃.

Castro *et al.*¹ have demonstrated that Bi₃NbO₇ exhibits a defect fluorite type structure which crystallizes in the cubic system, space group Fm $\bar{3}$ m. The system appears to show disorder in both the anionic and cationic lattices with 12.5% of the anion sites vacant. Impedance spectroscopy measurements demonstrated the material to have very good ionic conductivity up to 1148 K without undergoing any phase transformation. Ling and Johnson² have recently synthesized Bi₉₄Nb₃₂O₂₂₁, a slightly Nb rich composition of Bi₃NbO₇, which comprises an ordered tetragonal cell, space group I $\bar{4}$ m2. This work suggested that small differences in synthesis conditions can lead to a phase that shows significant tetragonal distortion of the cubic fluorite cell.

Due to the fluorite-related structures of many of the Bi₂O₃-Nb₂O₅ materials, good oxide ion conductivity is observed. The best known ionic conductor appears to be obtained at the lower limit of the fcc solid-solution formation range, determined by Takahashi *et al.*³, for the composition (Bi₂O₃)_{0.85}(Nb₂O₅)_{0.15} which exhibits a conductivity of $1.1 \times 10^{-2} \Omega^{-1} \text{ cm}^{-1}$ at 773 K. The conductivities of these systems decrease with increasing niobium dopant

concentration up to the maximum limit of the fcc solid solution range of $(\text{Bi}_2\text{O}_3)_{0.74}(\text{Nb}_2\text{O}_5)_{0.26}$.

The work described in this Chapter reports a face-centred cubic solid solution range beyond that previously identified³. The results show that when the niobium dopant concentration is decreased further, beyond the cubic solid solutions range, a group of materials with tetragonal symmetry are formed with a structure related to the fcc structure of the more niobium rich phase. The structures and ionic conductivities of both groups of materials have been investigated.

6.2 Experimental

Materials were prepared by reacting stoichiometric quantities of Bi_2O_3 (Aldrich, 99.9%) and Nb_2O_5 (Aldrich, 99.99%) to provide mixtures in the mole ratio of 6:1 (Bi:Nb) to 20:1 (Bi:Nb). Samples were intimately ground and calcined for a total of 36 h in air at 1073 K, with intermediate regrinding to ensure complete reaction and single phase products as indicated by XPD.

Materials were also subject to quenching and slow-cooling, by heating to 1073 K, followed by either removal from the furnace and rapid cooling to room temperature or by slow-cooling to room temperature at a rate of 24 K h^{-1} . The quenched and slow-cooled samples were examined by XPD to identify any phase transformations.

Further detailed characterisation was made by XPD, variable temperature XPD, DTA and impedance spectroscopy as described in Chapter 2.

6.3 Results and Discussion

6.3.1 Solid Solution Range

Initial examination by XPD suggested the niobium-rich range of the Bi-Nb-O solid solution to be single phase, the structure of which could be indexed on a face-centred cubic unit cell with space group symmetry $Fm\bar{3}m$ and lattice parameters ranging from $a = 5.506(2) \text{ \AA}$ for $\text{Bi}_6\text{NbO}_{11.5}$ to $a = 5.532(4) \text{ \AA}$ for $\text{Bi}_{13}\text{NbO}_{22}$ as shown in Table 6.1. Figure 6.1 shows the XPD patterns obtained for these materials.

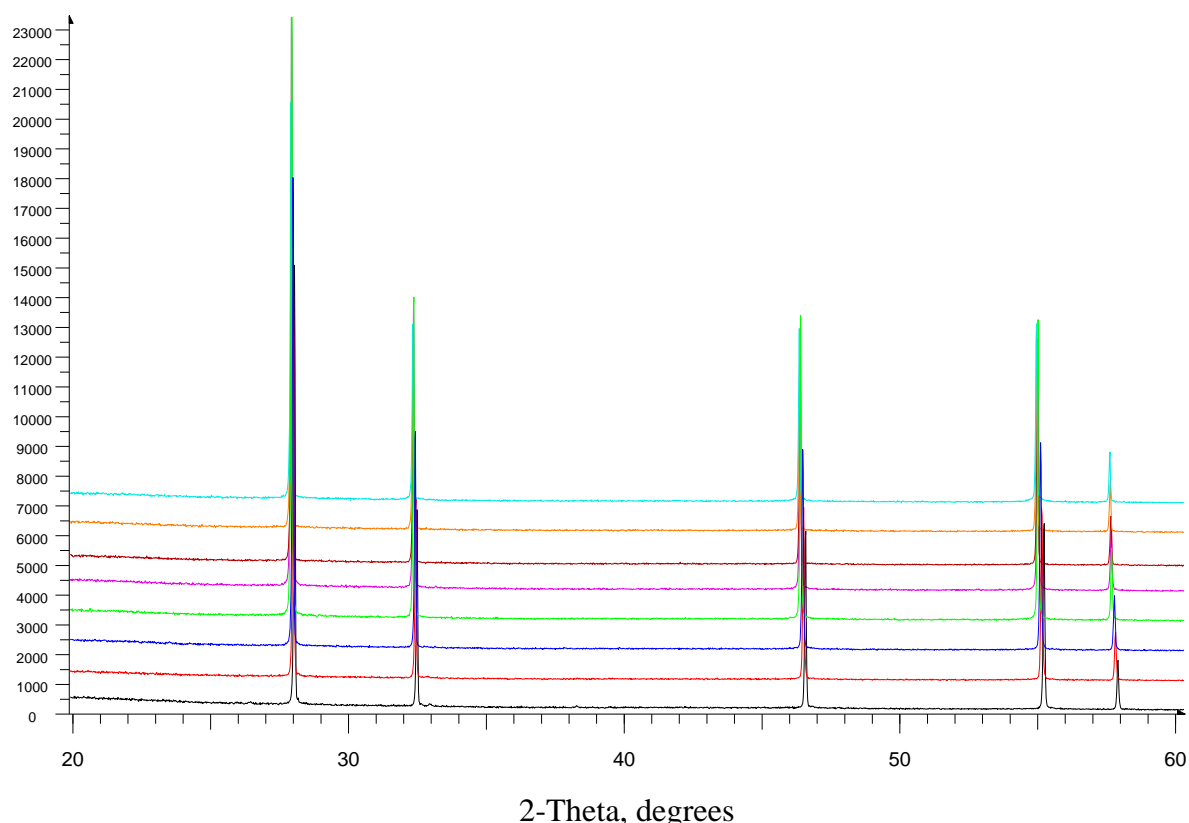


Figure 6.1 XPD patterns for niobium rich Bi-Nb-O solid solutions, showing $\text{Bi}_6\text{NbO}_{11.5}$ (black), $\text{Bi}_7\text{NbO}_{13}$ (red), $\text{Bi}_8\text{NbO}_{14.5}$ (dark blue), $\text{Bi}_9\text{NbO}_{16}$ (green), $\text{Bi}_{10}\text{NbO}_{17.5}$ (purple), $\text{Bi}_{11}\text{NbO}_{19}$ (brown), $\text{Bi}_{12}\text{NbO}_{20.5}$ (orange) and $\text{Bi}_{13}\text{NbO}_{22}$ (light blue).

Table 6.1 Lattice parameters for niobium rich Bi-Nb-O solid solutions.

Bi:Nb ratio	Lattice parameter a / Å
6Bi:1Nb	5.5062(24)
7Bi:1Nb	5.5112(19)
8Bi:1Nb	5.5170(12)
9Bi:1Nb	5.5231(10)
10Bi:1Nb	5.5240(5)
11Bi:1Nb	5.5273(29)
12Bi:1Nb	5.5289(16)
13Bi:1Nb	5.5324(35)

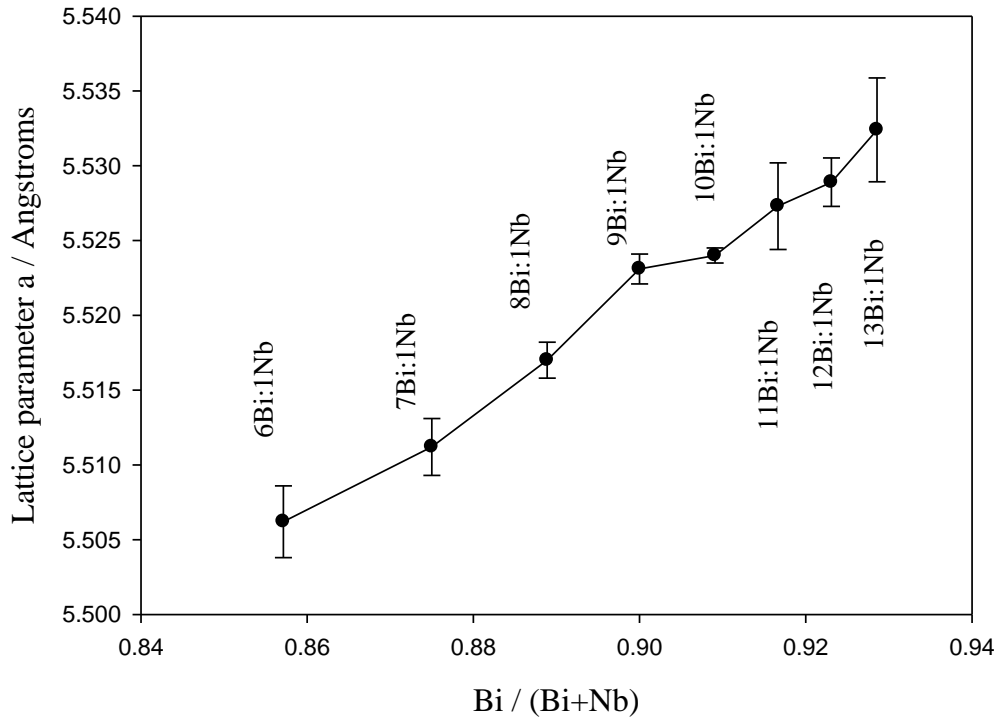


Figure 6.2 Variation of lattice parameter a with increasing percentage of Bi in the niobium-rich range of the Bi-Nb-O solid solution.

Figure 6.2 illustrates the increase in lattice parameter of the fcc materials with increased bismuth content. This increase in lattice parameter is as one would expect as the larger bismuth ion (ionic radius = 117 pm for 6 coordinate Bi^{3+})⁴ replaces the significantly smaller niobium (ionic radius = 78 pm for 6 coordinate Nb^{5+})⁴.

Increasing the bismuth content further, beyond 13Bi:1Nb, yields an alternative phase. Initial examination by XPD suggested the bismuth-rich range of the Bi-Nb-O solid solution to be single phase, the structure of which could be indexed on a tetragonal unit cell, space group I4/mmm, with a structure related to the fcc structure of the niobium rich phase. Figure 6.3 shows the XPD patterns obtained for these materials. Lattice parameters ranged from $a = 3.8729(16)$ Å and $c = 5.5755(25)$ Å for $\text{Bi}_{14}\text{NbO}_{23.5}$ to $a = 3.8661(8)$ Å and $c = 5.6005(1)$ Å for $\text{Bi}_{20}\text{NbO}_{32.5}$, as shown in Table 6.2.

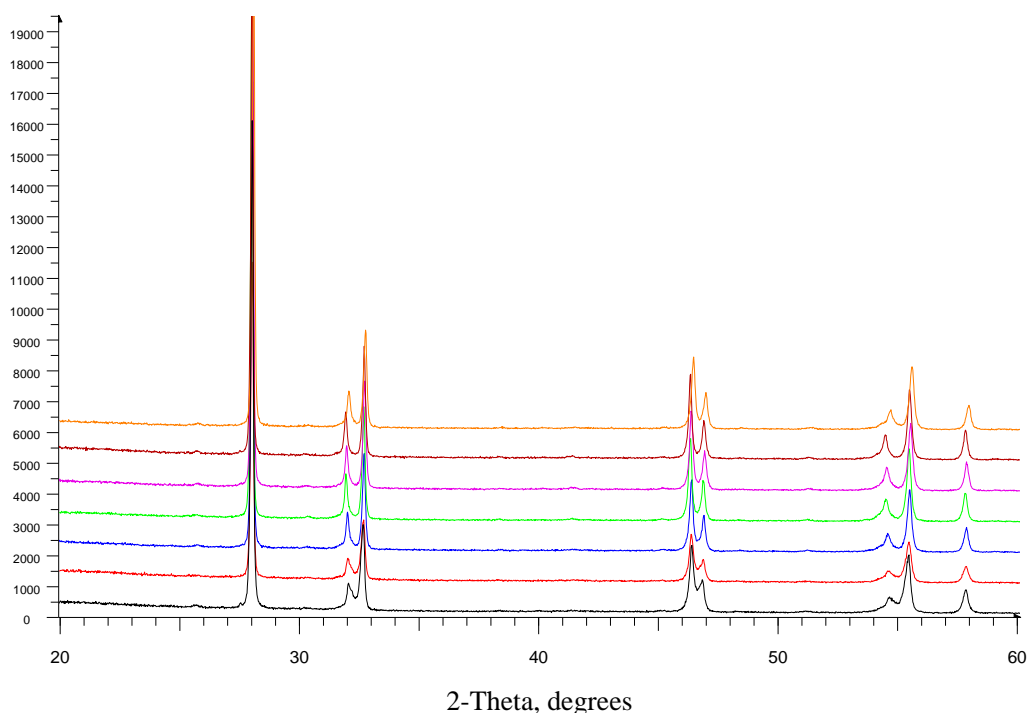


Figure 6.3 XPD patterns for bismuth-rich Bi-Nb-O solid solutions, showing $\text{Bi}_{14}\text{NbO}_{23.5}$ (black), $\text{Bi}_{15}\text{NbO}_{25}$ (red), $\text{Bi}_{16}\text{NbO}_{26.5}$ (dark blue), $\text{Bi}_{17}\text{NbO}_{28}$ (green), $\text{Bi}_{18}\text{NbO}_{29.5}$ (purple), $\text{Bi}_{19}\text{NbO}_{31}$ (brown) and $\text{Bi}_{20}\text{NbO}_{32.5}$ (orange).

The tetragonal cell, displaying crystal symmetry $I4/mmm$, can be thought of as a ‘squashed’ fluorite-related cube. The relationship of this cell to the face-centred cubic structure observed for the more niobium-rich phase, illustrated in Figure 6.4, is as follows:

- $a = a_{\text{fcc}} / \sqrt{2} \text{ \AA}$

Equation 6.1

- $c = a_{\text{fcc}} \text{ \AA}$

Equation 6.2

where a_{fcc} = the lattice parameter, a , for the face-centred cubic structure observed for the more Nb-rich Bi-Nb-O solid solution range.

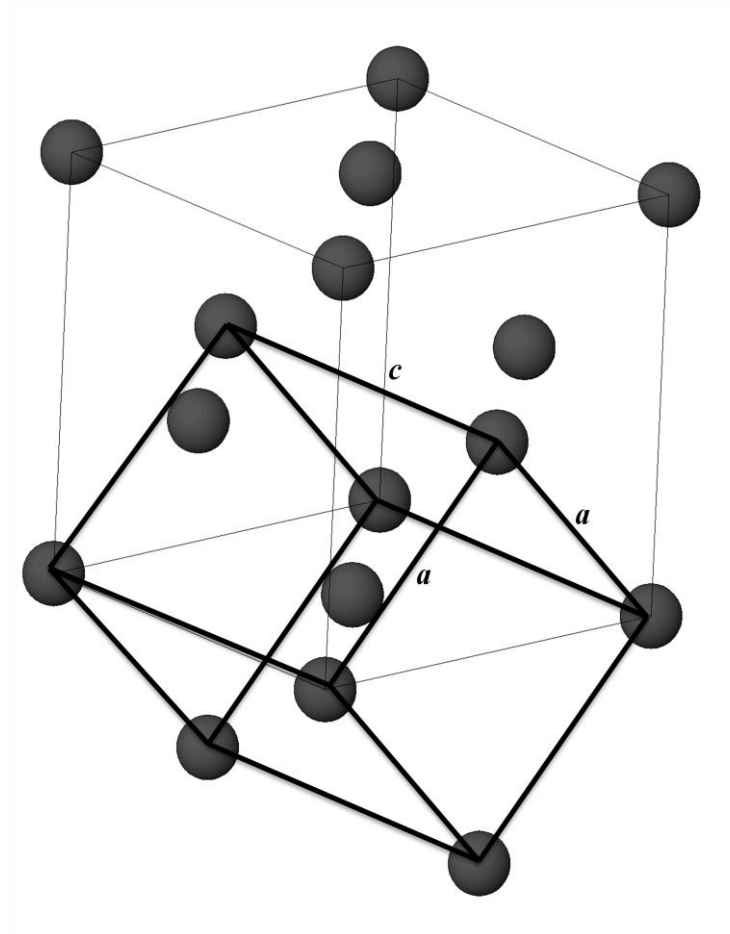


Figure 6.4 The relationship between the fluorite- and the tetragonal- unit cell of the Bi-rich Bi-Nb-O phase.

Table 6.2 Lattice parameters for bismuth rich Bi-Nb-O solid solutions.

Bi:Nb ratio	Lattice parameter $a/\text{\AA}$	Lattice parameter $c/\text{\AA}$
14Bi:1Nb	3.8729(16)	5.5755(25)
15Bi:1Nb	3.8709(15)	5.5817(23)
16Bi:1Nb	3.8688(9)	5.587(13)
17Bi:1Nb	3.8678(4)	5.5939(6)
18Bi:1Nb	3.868(6)	5.5965(9)
19Bi:1Nb	3.8676(4)	5.5992(6)
20Bi:1Nb	3.8661(8)	5.6005(10)

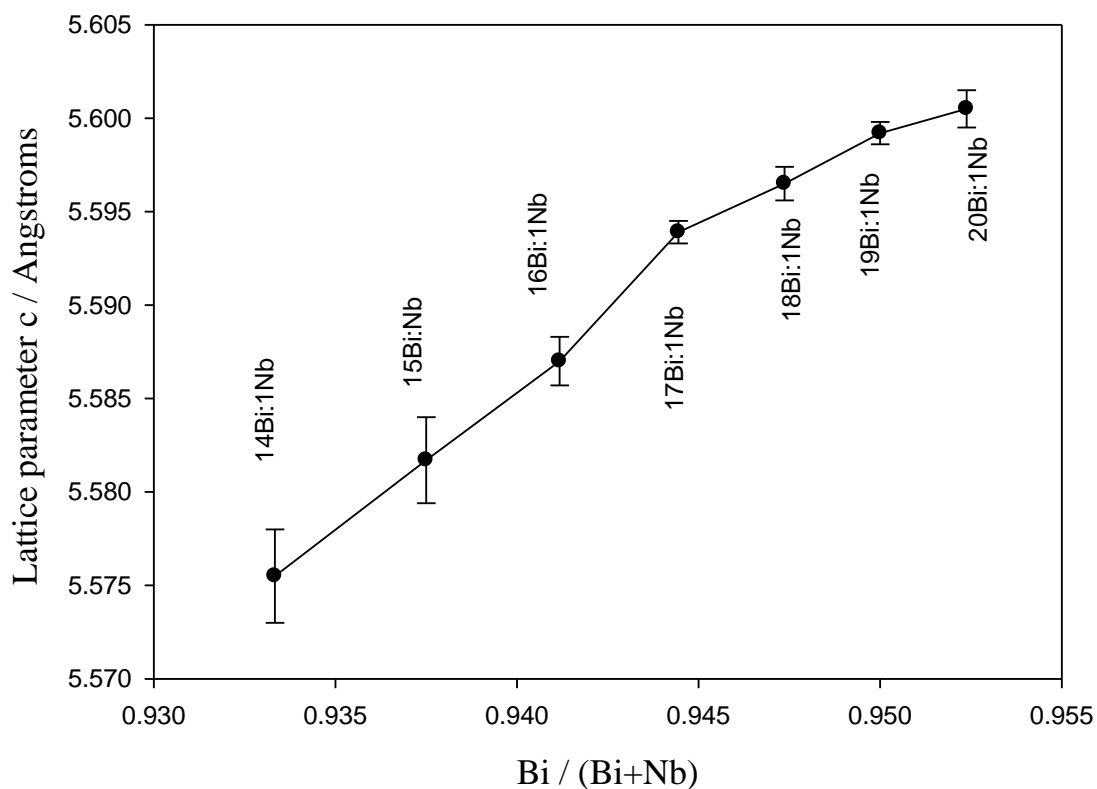


Figure 6.5 Variation of lattice parameter, c , with increasing percentage of Bi in the bismuth-rich range of the Bi-Nb-O solid solution.

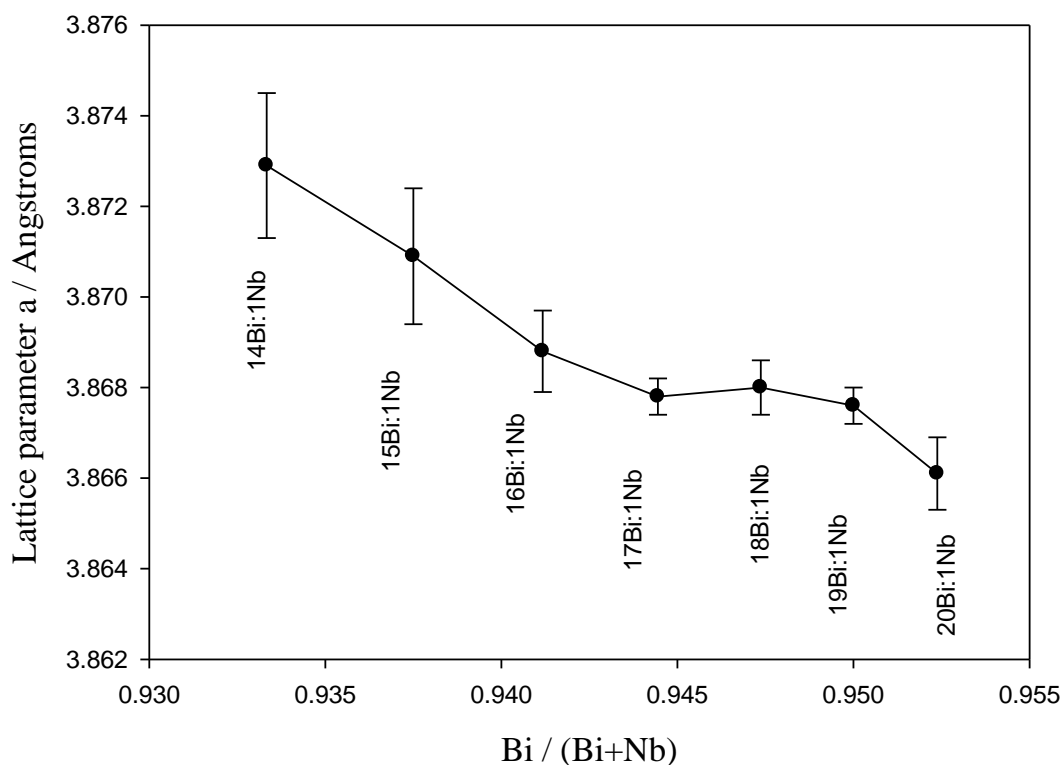


Figure 6.6 Variation of lattice parameter, a , with increasing percentage of Bi in the bismuth-rich range of the Bi-Nb-O solid solution.

Figure 6.5 illustrates the expected increase in c parameter of the bismuth rich range of the Bi-Nb-O solid solution with increasing bismuth content. This increase in lattice parameter is - in a similar manner to the increase in lattice parameter of the niobium-rich materials - expected, as the larger bismuth ion (ionic radius = 117 pm for 6 coordinate Bi^{3+})⁴ is replacing the significantly smaller niobium (ionic radius = 78 pm for 6 coordinate Nb^{5+})⁴. In contrast to this trend, Figure 6.6 shows a decrease in lattice parameter a with increasing bismuth content. As a consequence of this, no overall volume change is observed within the standard deviation with increasing bismuth content.

6.3.2 Niobium-Rich Phase

Structural refinements were made using XPD data on $\text{Bi}_{10}\text{NbO}_{17.5}$ using the program GSAS⁵, based on the Rietveld method⁶. In the starting model, cations were statistically distributed ($\text{Bi:Nb} = 10:1$) at the $4a$ (0, 0, 0) site and the oxygen atoms on the $32f$ (x, x, x) and $48i$ ($\frac{1}{2}, x, x$) sites, with space group symmetry $\text{Fm}\bar{3}m$.

The final refined unit cell parameter in space group $\text{Fm}\bar{3}m$ was $a = 5.52660(4)$ Å. Refinement statistics for 52 variables were $R_p = 0.0612$, $R_{wp} = 0.0876$, and $\chi^2 = 2.414$. The fitted XPD profile for $\text{Bi}_{10}\text{NbO}_{17.5}$, shown in Figure 6.7, indicates good agreement between observed and calculated profiles. The refined structural information, shown in Table 6.3, is consistent with a high level of disorder confirmed by the high thermal parameters for cation sites. In the refinement, all cations were assigned a single temperature factor but oxygen temperature factors were fixed at a sensible value of 1.00 Å^2 ($100U_{iso}$) to assist the refinement. Oxygen occupancies were allowed to vary, but constrained to equal the sum of that expected. The position of the $32f$ (x, x, x) oxygen site, where $x = 0.296(3)$, compares well with other reported values in related Bi-Nb-O materials of $x = 0.2966(2)$ in $\text{Bi}_{1.78}\text{Nb}_{0.22}\text{O}_{3.22}$ ⁷ and $x = 0.2891(4)$ in $\text{Bi}_{3.111}\text{Nb}_{0.889}\text{O}_{6.889}$ ⁸. The position of the $48i$ ($\frac{1}{2}, x, x$) site, where $x = 0.112(9)$, is slightly closer to the origin compared to other values of $x = 0.185(2)$ for $\text{Bi}_{1.78}\text{Nb}_{0.22}\text{O}_{3.22}$ ⁷ and $x = 0.231(4)$ in $\text{Bi}_{3.111}\text{Nb}_{0.889}\text{O}_{6.889}$ ⁸. However, this could be a consequence of a reduced amount of niobium in the material, as the value of x in the $48i$ ($\frac{1}{2}, x, x$) site does appear to vary with niobium content in these reported values. The final refinement shows 72% of the oxide ions located on the $32f$ site, with the remainder on the $48i$ site, which is slightly less than previous reports of 85% in $\text{Bi}_{1.78}\text{Nb}_{0.22}\text{O}_{3.22}$ ⁷ and 86% in $\text{Bi}_{3.111}\text{Nb}_{0.889}\text{O}_{6.889}$ ⁸. However, it is worth noting that these stated oxygen positions and

occupancies could be inaccurate due to the poor sensitivity of XPD data to oxygen atoms in the presence of heavy bismuth atoms. Studies by Castro *et al.*¹ reported that in Bi_3NbO_7 , the oxygen atoms were located exclusively on the 48g site, whereas this refinement showed a preference for the oxygen atoms to be located mainly on the 32f site, with the remainder on the 48i site - as is reported for other niobium doped $\delta\text{-Bi}_2\text{O}_3$ materials^{7,8}. Studies by Battle *et al.*⁹ suggested that in doped $\delta\text{-Bi}_2\text{O}_3$ structures, the cations may shift along [100] from the 4a (0, 0, 0) site to the 24e (x, 0, 0) site. No strong evidence was found to support this. Despite being undetected by XPD data, it is likely that this material forms an incommensurate type II lattice, as previously observed for materials with compositions ranging from $12\text{Bi}_2\text{O}_3\text{:Nb}_2\text{O}_5$ to $4\text{Bi}_2\text{O}_3\text{:Nb}_2\text{O}_5$, by neutron powder diffraction or electron microscopy experiments^{1,7,8}. The structure of $\text{Bi}_{10}\text{NbO}_{17.5}$ is shown in Figure 6.8.

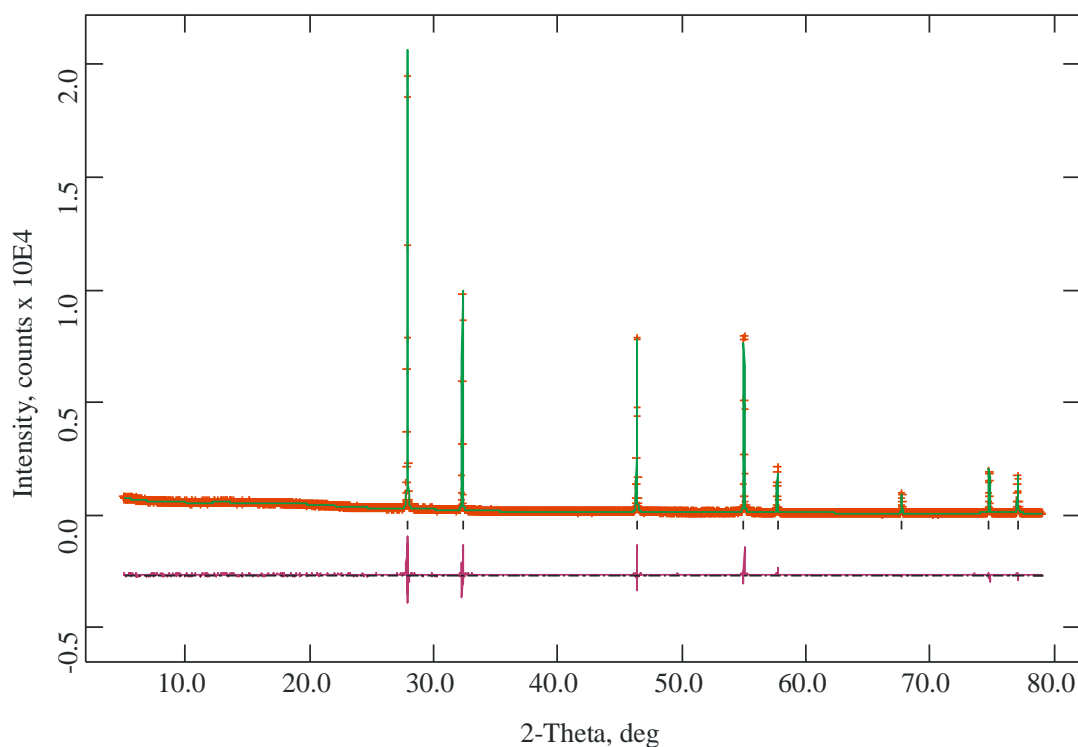


Figure 6.7 Observed (+), calculated (-), and difference XPD profiles for $\text{Bi}_{10}\text{NbO}_{17.5}$.

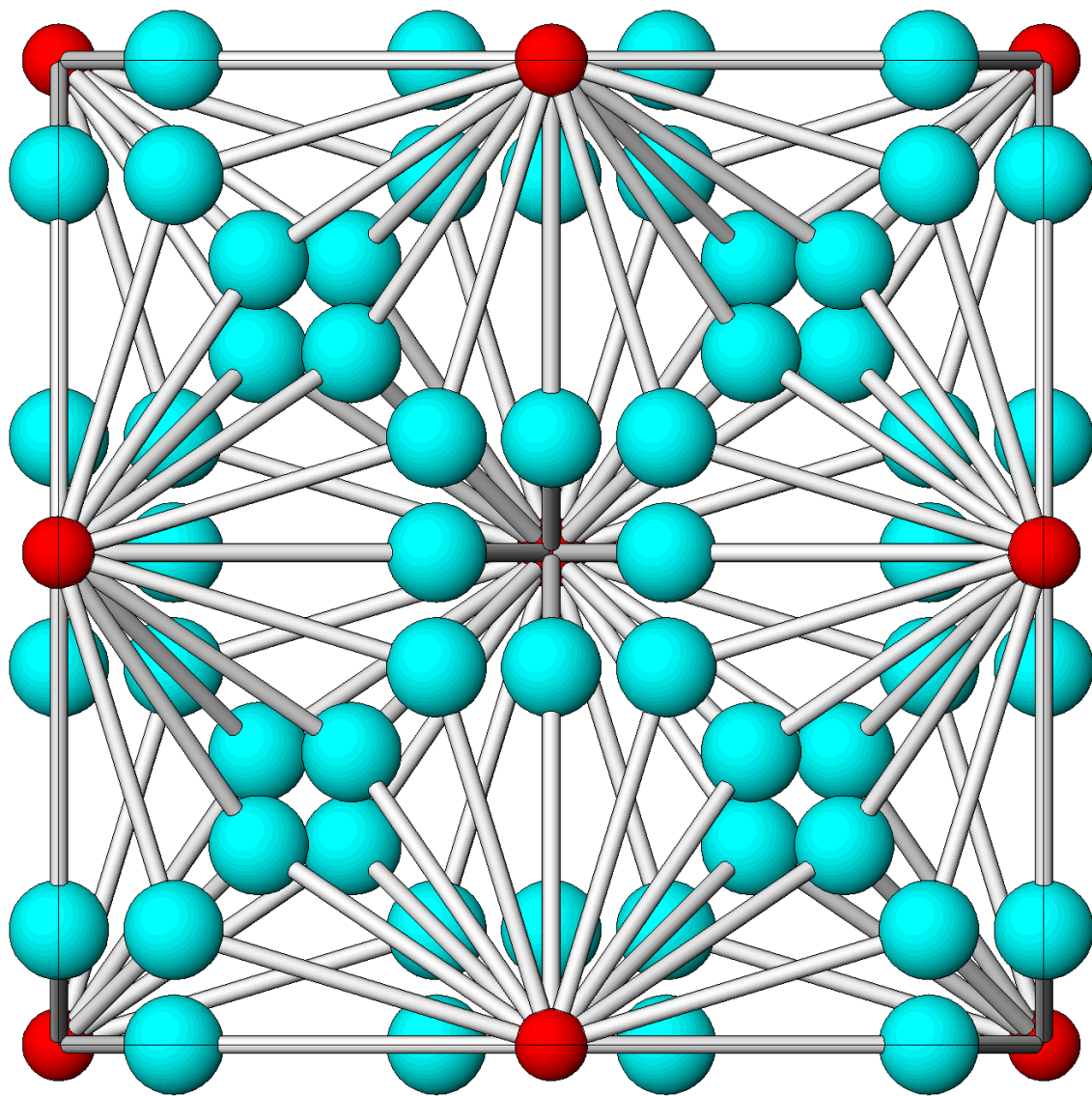


Figure 6.8 The structure of $\text{Bi}_{10}\text{NbO}_{17.5}$, viewed along $[100]$, where the red spheres represent the Bi/Nb site and the blue spheres represent oxygen.

Table 6.3 Refined structural information from XPD data recorded from Bi₁₀NbO_{17.5}, as determined by Rietveld analysis.

Site		Fractional			Uiso x 100	
Atom	Symmetry	<i>x</i>	<i>y</i>	<i>z</i>	occupancy	/ Å ²
Bi	4a	0	0	0	0.91	1.91(5)
Nb	4a	0	0	0	0.09	1.91(5)
O1	32f	0.296(3)	0.296(3)	0.296(3)	0.144(6)	1.00
O2	48i	0.5	0.112(9)	0.112(9)	0.037(4)	1.00

6.3.3 Bismuth-Rich Phase

Structural refinements were made using XPD data on Bi₁₄NbO_{23.5} using the program GSAS⁵, based on the Rietveld method⁶. The refinement was based upon a structure with tetragonal symmetry and the space group I4/mmm, initially using atom positions derived using the program Cryscon¹⁰ for this space group and inputting the parameters from the face-centred cubic cell observed for the more niobium-rich phase along with the relationship between the two phases described in Equations 6.1 and 6.2. Cations were statistically distributed (Bi:Nb = 14:1) at the *2a* (0, 0, 0) site with the oxygen atoms on the *4d* (0, ½, ¼) site. The final refined unit cell parameters in space group I4/mmm were *a* = 3.8781(2) Å and *c* = 5.5764(3) Å. Refinement statistics for 51 variables were R_p = 0.0663, R_{wp} = 0.0919 and $\chi^2 = 2.757$. The refined structural information is given in Table 6.4, along with the fitted XPD

Table 6.4 Refined structural information from XPD data recorded from $\text{Bi}_{14}\text{NbO}_{23.5}$, as determined by Rietveld analysis.

Site					Fractional	Uiso x 100
Atom	Symmetry	<i>x</i>	<i>y</i>	<i>z</i>	occupancy	/ Å ²
Bi	2a	0	0	0	0.9333	2.68(8)
Nb	2a	0	0	0	0.0667	2.68(8)
O1	4d	0	0.5	0.25	0.7833	1.00

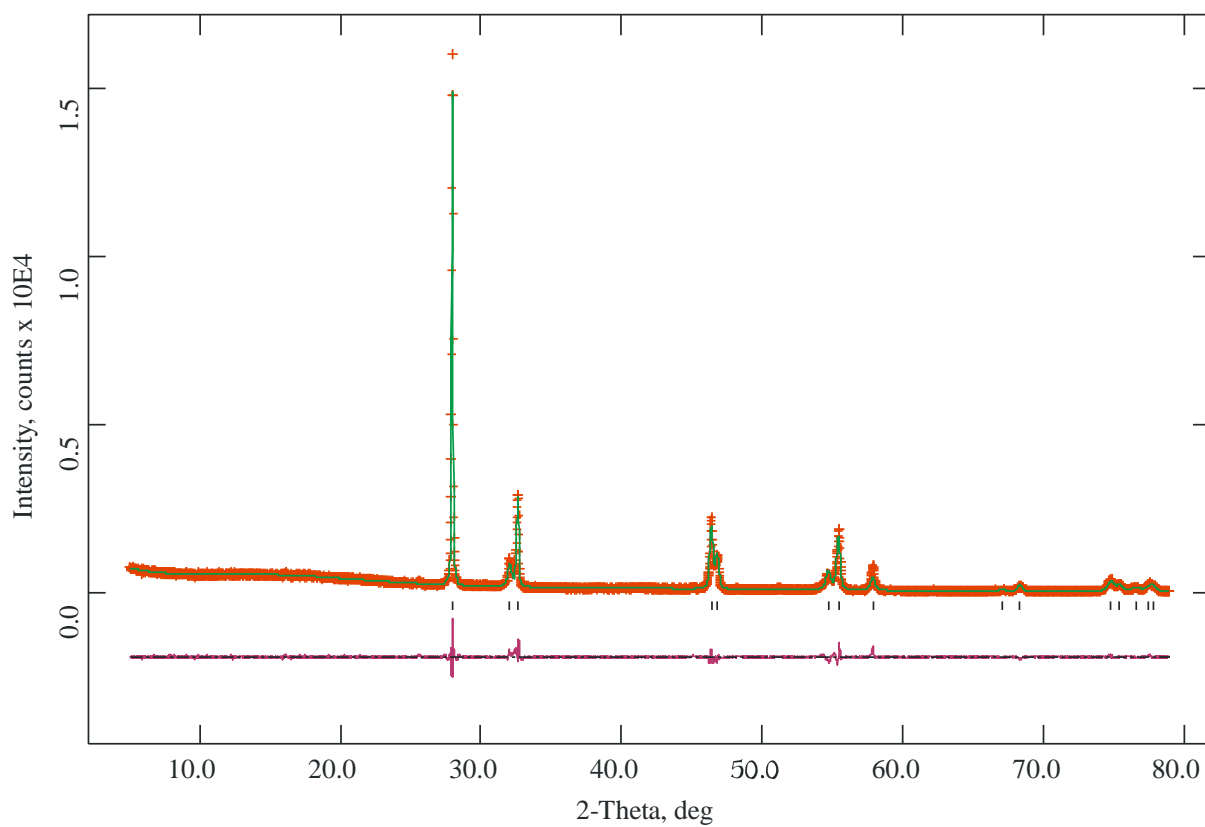


Figure 6.9 Observed (+), calculated (-), and difference XPD profiles for $\text{Bi}_{14}\text{NbO}_{23.5}$.

profile shown in Figure 6.9. Refinement of scale factors and cation site isotropic temperature factors produced a good fit between observed and calculated profiles. Due to the insensitivity of the O atoms to X-rays using XPD techniques, the oxygen occupancy and temperature factor were not refined. Attempts to refine the oxygen temperature factor gave very high values, and it was therefore fixed at 1.00 \AA^2 ($100U_{\text{iso}}$). Attempts to refine the oxygen cell occupancy also gave an extremely high value and it was therefore fixed at the expected oxygen content, assuming the presence of Bi^{3+} and Nb^{5+} .

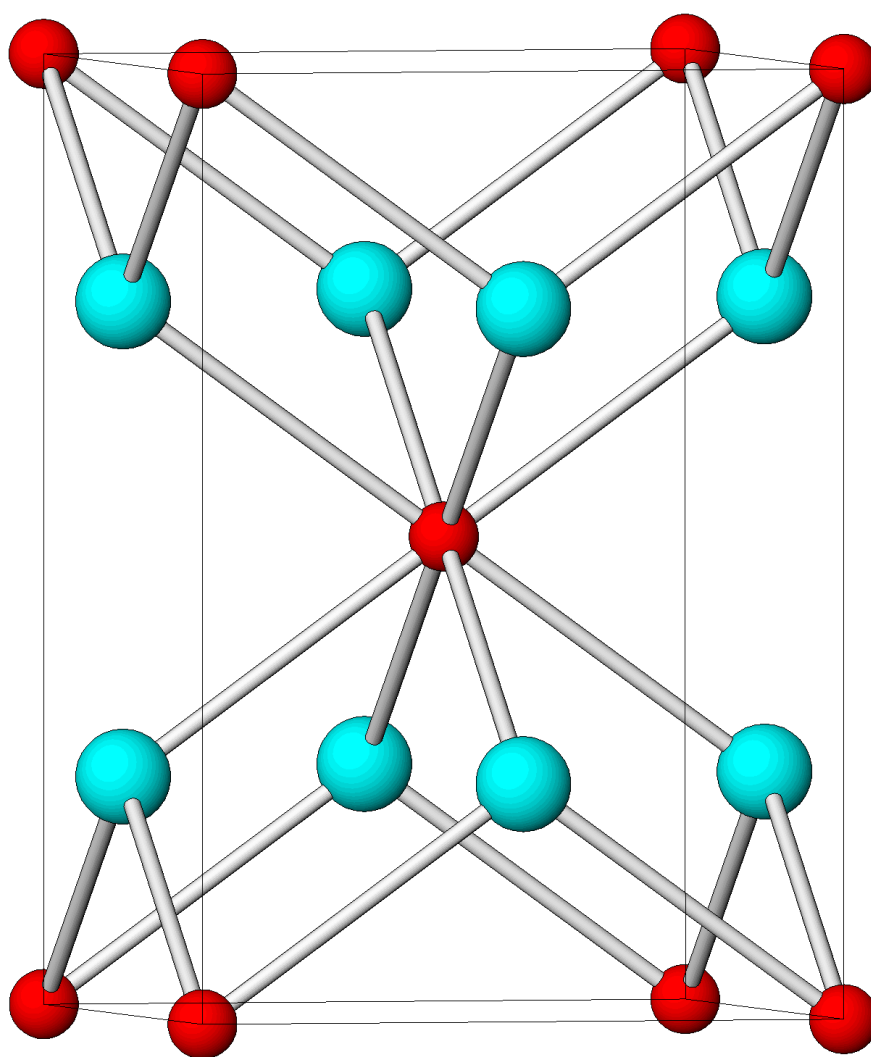


Figure 6.10 The structure of $\text{Bi}_{14}\text{NbO}_{23.5}$, where the red spheres represent the Bi/Nb site and the blue spheres represent oxygen.

6.3.4 Structural Stability of Bi-Nb-O

6.3.4.1 High Temperature Structural Studies on $\text{Bi}_{14}\text{NbO}_{23.5}$

Examination of XPD data revealed that a high temperature phase was produced upon quenching of $\text{Bi}_{14}\text{NbO}_{23.5}$ from 1073 K. This high temperature phase had a comparable XPD pattern to that of the more niobium-rich phase, described in 6.3.1 and 6.3.2, indicating that a similar fcc phase had been formed. This suggests that the Bi-Nb-O solid-solution range depends upon synthesis conditions in combination with the Bi:Nb ratio. Indexing of the XPD data confirmed this structure to be face-centred cubic, with space group symmetry $\text{Fm}\bar{3}\text{m}$, and lattice parameter $a = 5.536(2)$ Å.

XPD structural data for quenched $\text{Bi}_{14}\text{NbO}_{23.5}$ were refined using the program GSAS⁵, based on the Rietveld method⁶. The starting model was based on $\text{Bi}_{10}\text{NbO}_{17.5}$, using space group $\text{Fm}\bar{3}\text{m}$, with the cations statistically distributed on the $4a$ (0, 0, 0) site and the anions on the $32f$ (x , x , x) and $48i$ ($1/2$, x , x) sites.

Refinement of the scale factors, positions and occupancy of the anion sites and isotropic temperature factors of the cation sites produced a good fit between the calculated and observed profiles, shown in Figure 6.11. The high level of disorder in this structure, indicated by a decrease in peak intensities with 2θ , is confirmed by the high cation thermal parameters listed in the refined structural information given in Figure 6.5. Concurrent to the $\text{Bi}_{10}\text{NbO}_{17.5}$ refinement (Section 6.3.2) all cations were assigned a single temperature factor, but oxygen temperature factors were fixed to allow a sensible refinement. Oxygen occupancies were allowed to vary but constrained to equal the sum of that expected.

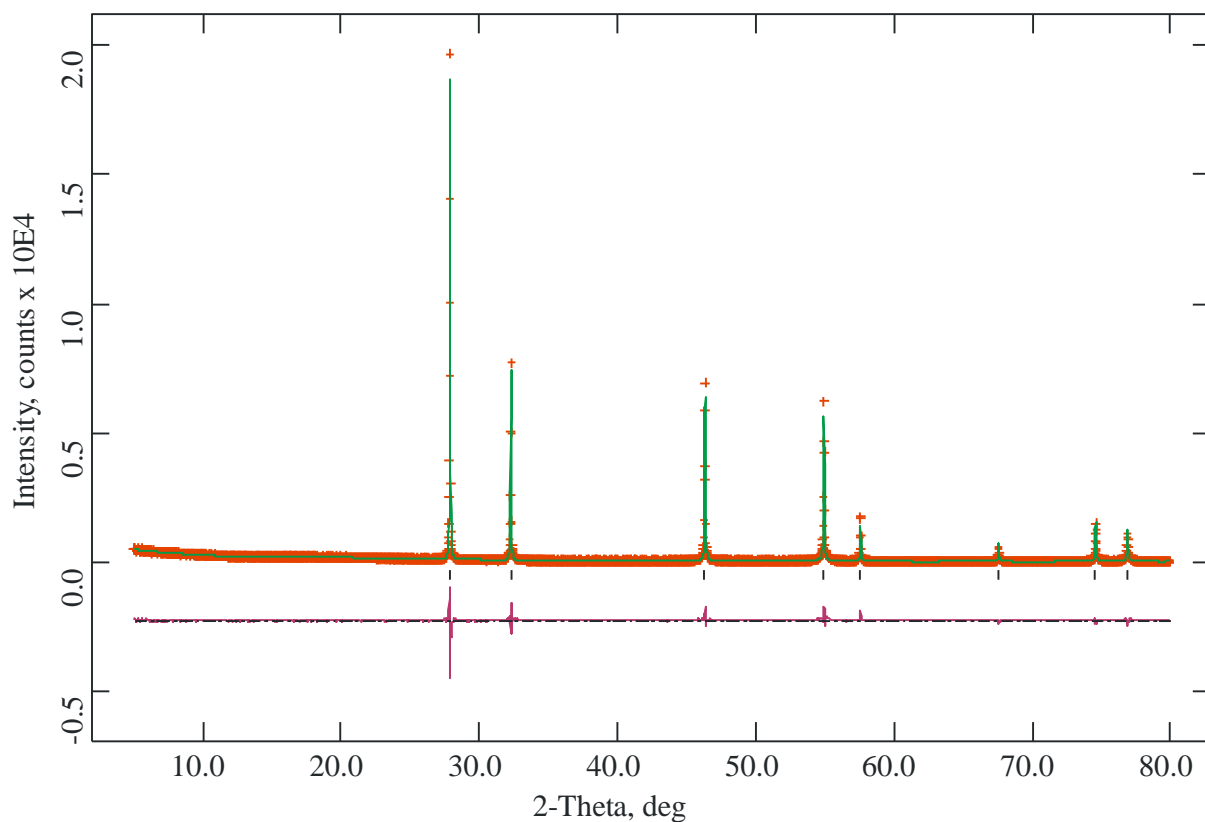


Figure 6.11 Observed (+), calculated (-), and difference XPD profiles for quenched $\text{Bi}_{14}\text{NbO}_{23.5}$.

Table 6.5 Refined structural information from XPD data recorded from quenched $\text{Bi}_{14}\text{NbO}_{23.5}$, as determined by Rietveld analysis.

Site					Fractional	Uiso x 100
Atom	Symmetry	<i>x</i>	<i>y</i>	<i>z</i>	occupancy	/ Å ²
Bi	4a	0	0	0	0.9333	2.59(7)
Nb	4a	0	0	0	0.0667	2.59(7)
O1	32f	0.291(4)	0.291(4)	0.291(4)	0.157(8)	1.00
O2	48i	0.5	0.120(16)	0.120(16)	0.026(5)	1.00

The final refined unit cell parameter in space group $Fm\bar{3}m$ was $a = 5.53991(5)$ Å. Refinement statistics for 50 variables were $R_p = 0.0925$, $R_{wp} = 0.1272$, and $\chi^2 = 3.008$. The final refinement of quenched $Bi_{14}NbO_{23.5}$ produced similar results to that of $Bi_{10}NbO_{17.5}$. The position of the $48i$ ($\frac{1}{2}, x, x$) site, where $x = 0.120(16)$, compares well with that of $x = 0.112(9)$ for $Bi_{10}NbO_{17.5}$. The $32f$ (x, x, x) site was located at $x = 0.291(4)$, comparable to $x = 0.296(3)$ for $Bi_{10}NbO_{17.5}$, with 80% of the oxide ions located on this site. This value is larger than that of 72% given for $Bi_{10}NbO_{17.5}$, and is more comparable to previous reports of 85% in $Bi_{1.78}Nb_{0.22}O_{3.22}$ ⁷ and 86% in $Bi_{3.111}Nb_{0.889}O_{6.889}$ ⁸. However, bismuth atoms scatter X-rays very strongly compared to O atoms in the structure. As a result of this, very little information can be obtained from the insensitivity of O atoms to X-rays using XPD techniques. Therefore, these stated oxygen positions and occupancies could be inaccurate. As for the refinement of $Bi_{10}NbO_{17.5}$, no evidence was found to support previous suggestions that the cations may shift along [100] from the $4a$ (0, 0, 0) site to the $24e$ ($x, 0, 0$) site⁹ or that the oxygen atoms were located exclusively on the $48g$ site¹. As for the face-centred cubic $Bi_{10}NbO_{17.5}$ material (Section 6.3.2), the presence of an undetected incommensurate type II lattice is also predicted.

DTA, described in Section 2.5, was employed to trace any phase changes in $Bi_{14}NbO_{23.5}$. Heating and cooling cycles were followed in a temperature range between 298 K and 1073 K. The results are shown in Figure 6.12. Large energy changes can be seen for both heating (lower) and cooling (upper) curves and suggest the occurrence of a phase change. A large endothermic energy change is apparent in the heating curve, with a peak onset at 846 K, indicating that at this temperature the material begins to transform to another

phase. The cooling curve shows a large energy change with a peak onset at 744 K, as the structure reverts back to its room temperature form and the phase change is reversed.

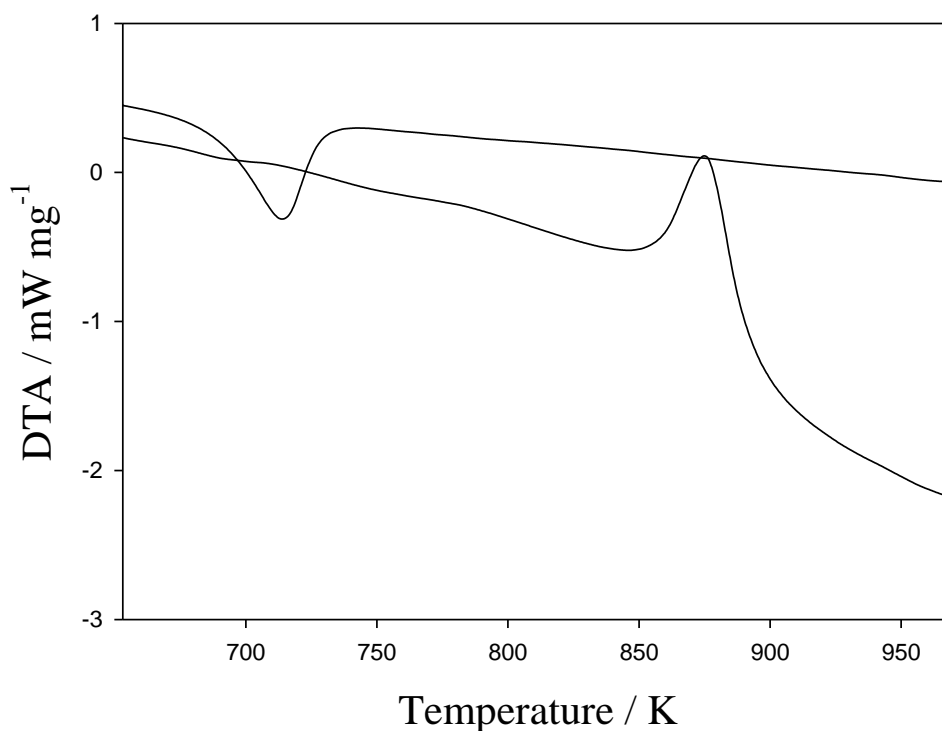


Figure 6.12 DTA results recorded from $\text{Bi}_{14}\text{NbO}_{23.5}$, showing the heating curve (lower) and the cooling curve (upper).

Variable temperature XPD, described in Section 2.2.1, was undertaken in order to examine the nature of the phase change revealed by DTA. The presence of two well defined phases for $\text{Bi}_{14}\text{NbO}_{23.5}$ – a high temperature fcc phase and a low temperature tetragonal phase – suggested by the presence of a single peak in both the heating and cooling curves in DTA, was confirmed by variable temperature XPD experiments over the temperature range 298 K to 1073 K.

Figure 6.13 displays the XPD patterns recorded at a range of temperatures either side of the phase transition indicated by DTA. These results support the evidence of phase change

shown by DTA, with peaks beginning to broaden significantly at 773 K. At 873 K, the material appears to undergo a change of phase to an as yet unidentified metastable intermediate and, by 973 K, the phase change to fcc appears complete.

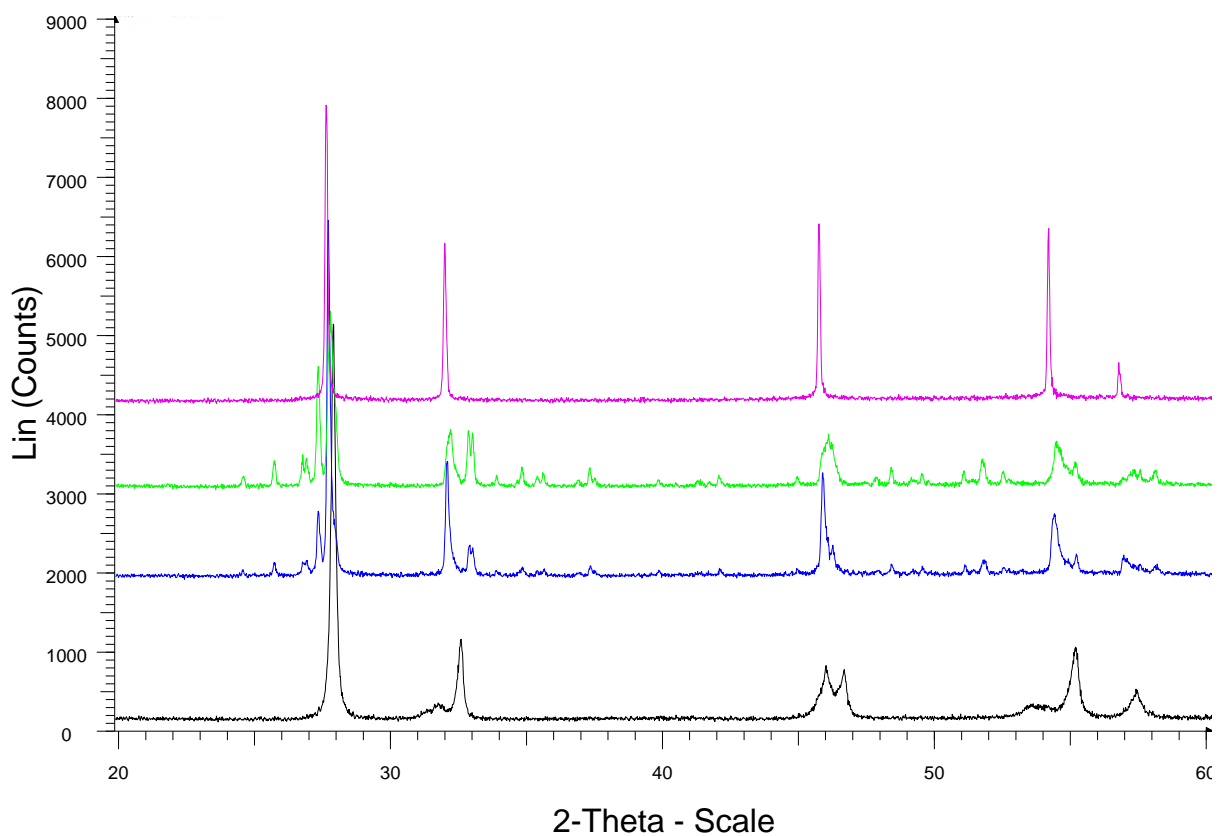


Figure 6.13 Variable temperature XPD results recorded from $\text{Bi}_{14}\text{NbO}_{23.5}$ between 20° and 60° , 2θ , at 773 K (black), 823 K (red), 873 K (blue), 923 K (green) and 973 K (purple).

Table 6.6 shows the variation of lattice parameters with temperature for $\text{Bi}_{14}\text{NbO}_{23.5}$ as determined by analysis of the variable temperature XPD data. Figures 6.14 and 6.15 illustrate the relationship between lattice parameters c and a , with temperature. An increase in temperature is shown to result in an increase in both the c and a parameters. Lattice parameter c (Figure 6.14) is shown to have a directly proportional relationship to temperature, as the lattice parameter increases in a near-linear manner with increasing temperature. Figure 6.15, however, shows that a variation to this linear trend occurs at temperatures up to 373 K and also post 473 K for lattice parameter a . The data (Figure 6.15) show little increase in the cell a direction at temperatures up to 373 K. The decrease in cell parameter a at 773 K may be attributed to the broadening of peaks in the variable temperature XPD data (Figure 6.13) that commence at this temperature, and correlates with the cell beginning to undergo a phase

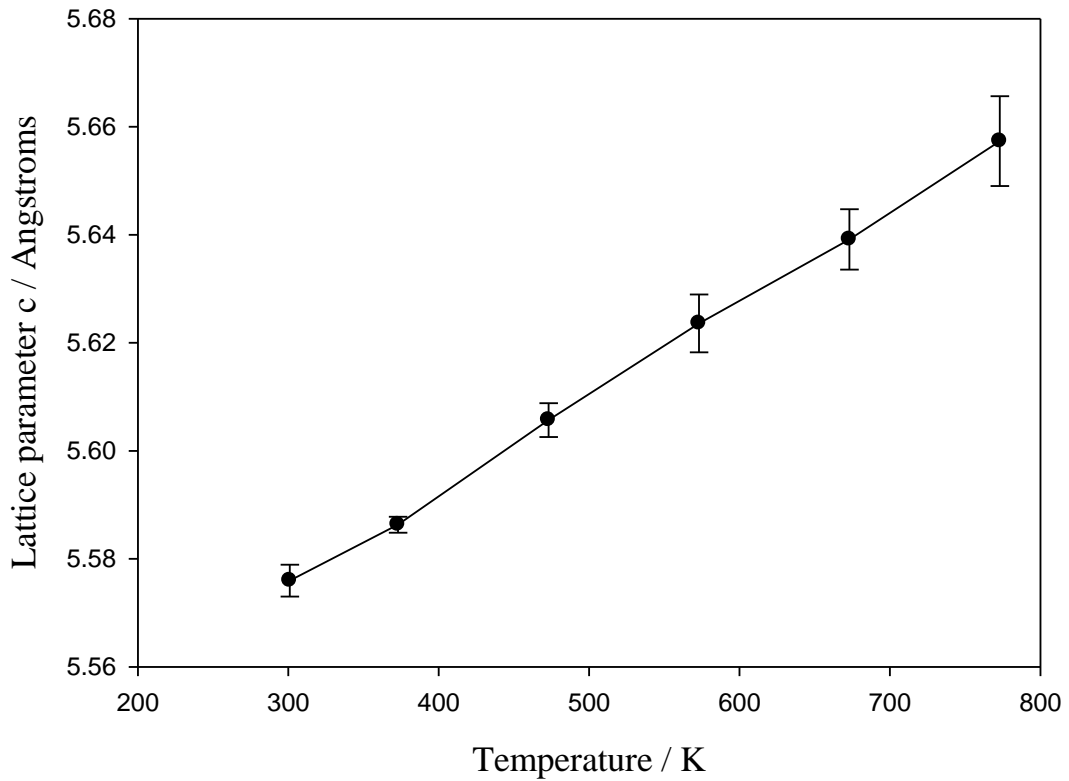
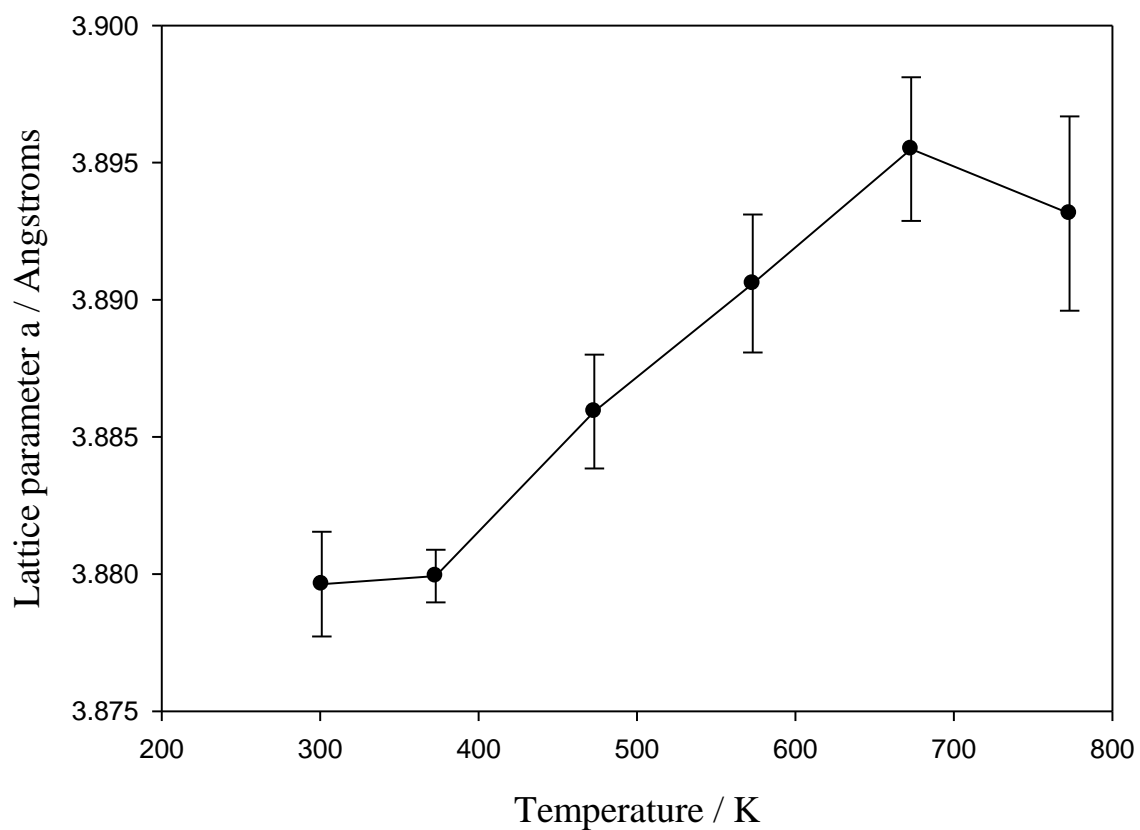


Figure 6.14 Variation of lattice parameter, c , with increasing temperature for $\text{Bi}_{14}\text{NbO}_{23.5}$.

Table 6.6 Variation of lattice parameters with temperature for $\text{Bi}_{14}\text{NbO}_{23.5}$.

Temperature / K	Lattice parameter a / Å	Lattice parameter c / Å
301	3.8796(19)	5.576(3)
373	3.8799(10)	5.586(1)
473	3.8859(21)	5.606(3)
573	3.8906(25)	5.624(5)
673	3.8955(26)	5.639(6)
773	3.8931(35)	5.657(8)

**Figure 6.15** Variation of lattice parameter, a , with increasing temperature for $\text{Bi}_{14}\text{NbO}_{23.5}$.

transformation to face-centred cubic. However, it is worth noting that the esds will be substantially underestimated and may therefore render the decrease in lattice parameter a at 773 K insignificant.

6.3.4.2 Structural Studies on $\text{Bi}_{13}\text{NbO}_{22}$

XPD results indicated that, upon slow-cooling of $\text{Bi}_{13}\text{NbO}_{22}$ at a rate of 24 K h^{-1} , a different phase was produced to that of the furnace-cooled sample. It was evident that this phase had a comparable XPD pattern to that of the more bismuth-rich phase, described in Section 6.3.3, indicating that a similar tetragonal phase formed. This confirmed the suggestion made when studying quenched $\text{Bi}_{14}\text{NbO}_{23.5}$ (Section 6.3.4.1) that the Bi-Nb-O solid-solution range depends upon synthesis conditions in combination with the Bi:Nb ratio. Indexing of the XPD data confirmed this structure to be of tetragonal symmetry, with space group symmetry $I4/\text{mmm}$ and lattice parameters $a = 3.879(2) \text{ \AA}$ and $c = 5.571(4) \text{ \AA}$.

Structural refinements were subsequently made using these XPD data and the program GSAS⁵ based on the Rietveld method⁶. The starting model was based upon $\text{Bi}_{14}\text{NbO}_{23.5}$, using space group $I4/\text{mmm}$, with the cations statistically distributed on the $2a$ site $(0, 0, 0)$ and the anions on the $4d$ $(0, \frac{1}{2}, \frac{1}{4})$ sites. The final refined unit cell parameters in space group $I4/\text{mmm}$ were $a = 3.8811(2) \text{ \AA}$ and $c = 5.5721(4) \text{ \AA}$. Refinement statistics for 49 variables were $R_p = 0.0724$, $R_{wp} = 0.0998$ and $\chi^2 = 2.085$. The fitted XPD profile, shown in Figure 6.16, produced a good fit between observed and calculated profiles. The high cation thermal parameters, given in Table 6.7, and decrease in peak intensities with 2θ reflects the high level of disorder of the oxygen sublattice. The oxygen occupancy and temperature factor were not refined as a consequence of the insensitivity of the O atoms to X-rays using XPD techniques.

Table 6.7 Refined structural information from XPD data recorded from slow-cooled $\text{Bi}_{13}\text{NbO}_{22}$ as determined by Rietveld analysis.

Site					Fractional	Uiso x 100
Atom	Symmetry	x	y	z	occupancy	/ \AA^2
Bi	2a	0	0	0	0.9286	2.15(8)
Nb	2a	0	0	0	0.0714	2.15(8)
O1	4d	0	0.5	0.25	0.7857	1.00

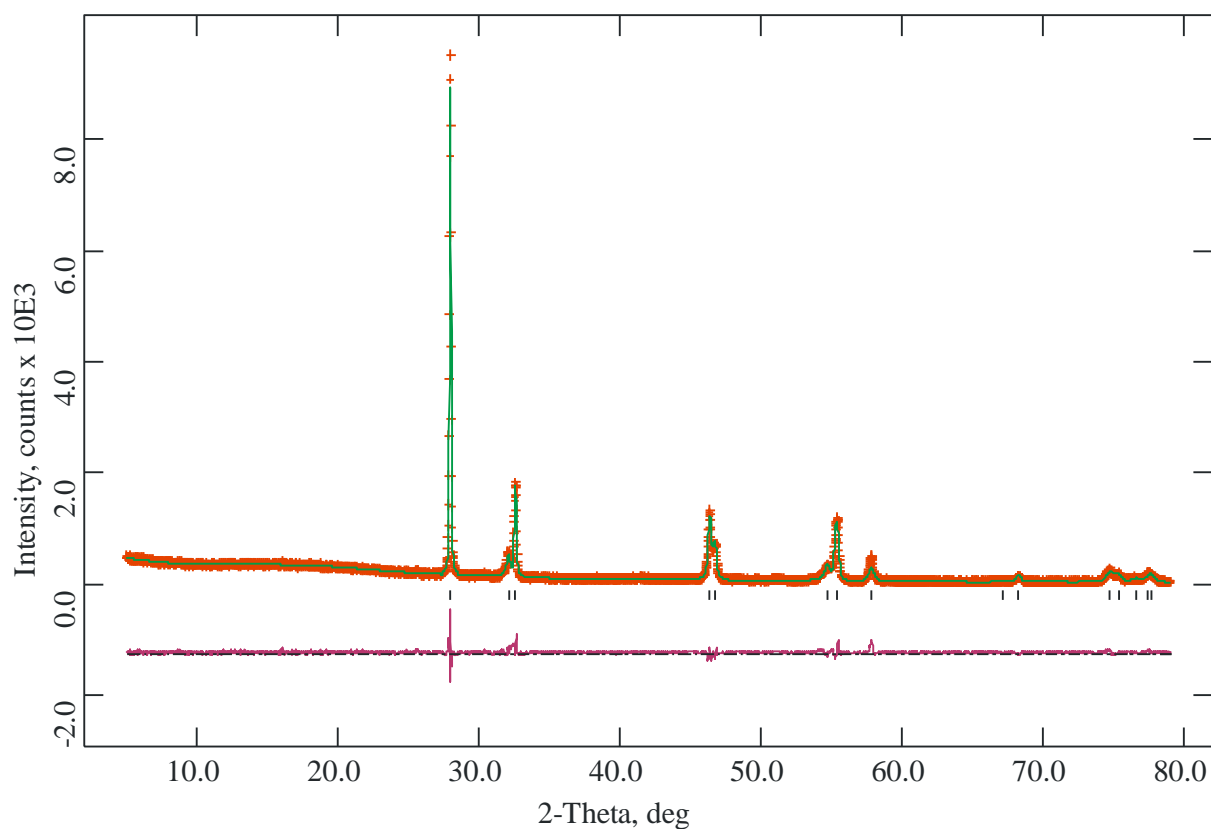


Figure 6.16 Observed (+), calculated (-), and difference XPD profiles for slow-cooled $\text{Bi}_{13}\text{NbO}_{22}$.

6.3.5 Ionic Conductivity

Impedance spectroscopy was employed to give oxide ion conductivity measurements from this group of materials, as they have structures related to the fluorite face-centred cubic unit cell of δ -Bi₂O₃ which is known to have high oxide ion conducting properties at elevated temperatures. Furthermore, previous observations of high oxide ion conductivity in bismuth oxide based materials^{7-9,11} suggest that these Bi-Nb-O materials might be expected to exhibit high oxide ion conducting properties.

Conductivity measurements were made between 473 K and 773 K in air across the frequency range 1 Hz to 1 x 10⁶ Hz. Materials were prepared and determinations made using the method outlined in Chapter 2. The density for each sample pellet was calculated and compared with the density of its unit cell, and it was determined that all samples had a density in the range 80 to 90 % of the theoretical.

The complex plane impedance plots could be fitted to a single semicircle with Warburg type impedance and resistance was therefore assigned to bulk effects, with the electronic contribution to conductivity assumed negligible. An example of a complex plane plot is shown in Figure 6.17, where data are displayed for Bi₁₀NbO_{17.5} at 483 K. The conductivities were calculated from the minima in the complex plane plots, and plots of log σ versus 1000K/T for Bi₁₀NbO_{17.5}, Bi₁₃NbO₂₂, slow-cooled Bi₁₃NbO₂₂, Bi₁₄NbO_{23.5}, quenched Bi₁₄NbO_{23.5} and Bi₂₀NbO_{32.5} are shown in Figure 6.18. The Arrhenius activation energies, E_a , for these materials determined from these plots are listed in Table 6.8.

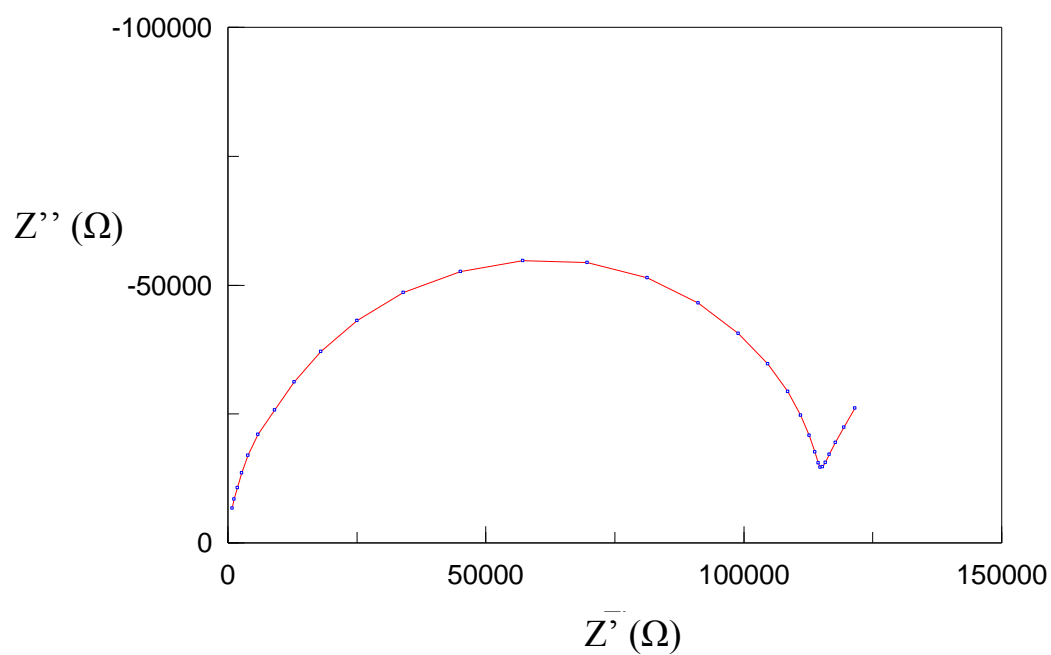


Figure 6.17 Complex plane impedance plot of real (Z') and imaginary (Z'') components, for $\text{Bi}_{10}\text{NbO}_{17.5}$ at a temperature of 483 K.

Table 6.8 Activation energies, E_a , for $\text{Bi}_{10}\text{NbO}_{17.5}$, $\text{Bi}_{13}\text{NbO}_{22}$, slow-cooled $\text{Bi}_{13}\text{NbO}_{22}$, $\text{Bi}_{14}\text{NbO}_{23.5}$, quenched $\text{Bi}_{14}\text{NbO}_{23.5}$ and $\text{Bi}_{20}\text{NbO}_{32.5}$.

Material	E_a/eV
$\text{Bi}_{10}\text{NbO}_{17.5}$	1.09
$\text{Bi}_{13}\text{NbO}_{22}$	1.13
Slow cooled $\text{Bi}_{13}\text{NbO}_{22}$	1.07
$\text{Bi}_{14}\text{NbO}_{23.5}$	1.02
Quenched $\text{Bi}_{14}\text{NbO}_{23.5}$	1.11
$\text{Bi}_{20}\text{NbO}_{32.5}$	1.00

All materials show very good oxide ion conductivity, with the conductivity of some materials being exceptionally high. $\text{Bi}_{10}\text{NbO}_{17.5}$, $\text{Bi}_{13}\text{NbO}_{22}$ and quenched $\text{Bi}_{14}\text{NbO}_{23.5}$ display conductivities of 2.61×10^{-2} , 1.89×10^{-2} and $2.23 \times 10^{-2} \Omega^{-1} \text{cm}^{-1}$, respectively, at 726 K and compare well with other reported bismuth-niobium-oxide materials, the conductivities and activation energies of which are listed in Table 6.9, at 773 K. Although a direct comparison cannot be made due to the difference in temperatures, it is evident that the conductivities of the measured materials compare well with that of $(\text{Bi}_2\text{O}_3)_{0.85}(\text{Nb}_2\text{O}_5)_{0.15}$ and are considerably greater than that of the other materials listed^{1,3}. The conductivities displayed by this group of materials are also significantly greater than that of other well known ionic conductors, such as $(\text{Bi}_2\text{O}_3)_{0.65}(\text{Gd}_2\text{O}_3)_{0.35}$ and $(\text{Bi}_2\text{O}_3)_{0.78}(\text{MoO}_3)_{0.22}$, which display conductivities of $3.5 \times 10^{-3} \Omega^{-1} \text{cm}^{-1}$ and $2.6 \times 10^{-3} \Omega^{-1} \text{cm}^{-1}$, respectively, at 773 K³.

Table 6.9 Conductivity at 773 K and activation energies for $\text{Bi}_2\text{O}_3\text{-Nb}_2\text{O}_5$ materials^{1,3}.

Composition	$\sigma / \Omega^{-1} \text{cm}^{-1}$	E_a / eV
$(\text{Bi}_2\text{O}_3)_{0.85}(\text{Nb}_2\text{O}_5)_{0.15}$	1.1×10^{-2}	0.9
$(\text{Bi}_2\text{O}_3)_{0.78}(\text{Nb}_2\text{O}_5)_{0.22}$	2.3×10^{-4}	1.2
$(\text{Bi}_2\text{O}_3)_{0.75}(\text{Nb}_2\text{O}_5)_{0.25}$	4.2×10^{-4}	0.88
$(\text{Bi}_2\text{O}_3)_{0.70}(\text{Nb}_2\text{O}_5)_{0.30}$	2.3×10^{-5}	1.4

It is clear from Figure 6.18 that the conductivities of this group of materials fall into two bands with $\text{Bi}_{14}\text{NbO}_{23.5}$, $\text{Bi}_{20}\text{NbO}_{32.5}$ and the slow-cooled $\text{Bi}_{13}\text{NbO}_{22}$ material forming the first band, displaying very good ionic conductivity. The second band, which display exceptional oxide ion conductivity, contains $\text{Bi}_{10}\text{NbO}_{17.5}$, $\text{Bi}_{13}\text{NbO}_{22}$ and quenched

$\text{Bi}_{14}\text{NbO}_{23.5}$. This categorisation appears to relate to the structure of the material being measured, rather than the ratio of Bi:Nb, with the band of exceptional oxide ion conductors being materials with the simpler face-centred cubic structure, and the other containing materials of the tetragonal structure. This signifies that the overall mechanism for movement of O^{2-} ions through the oxygen sublattice is different for the two phases, and that the pathway for ionic conduction is less complicated in the simpler fcc structure.

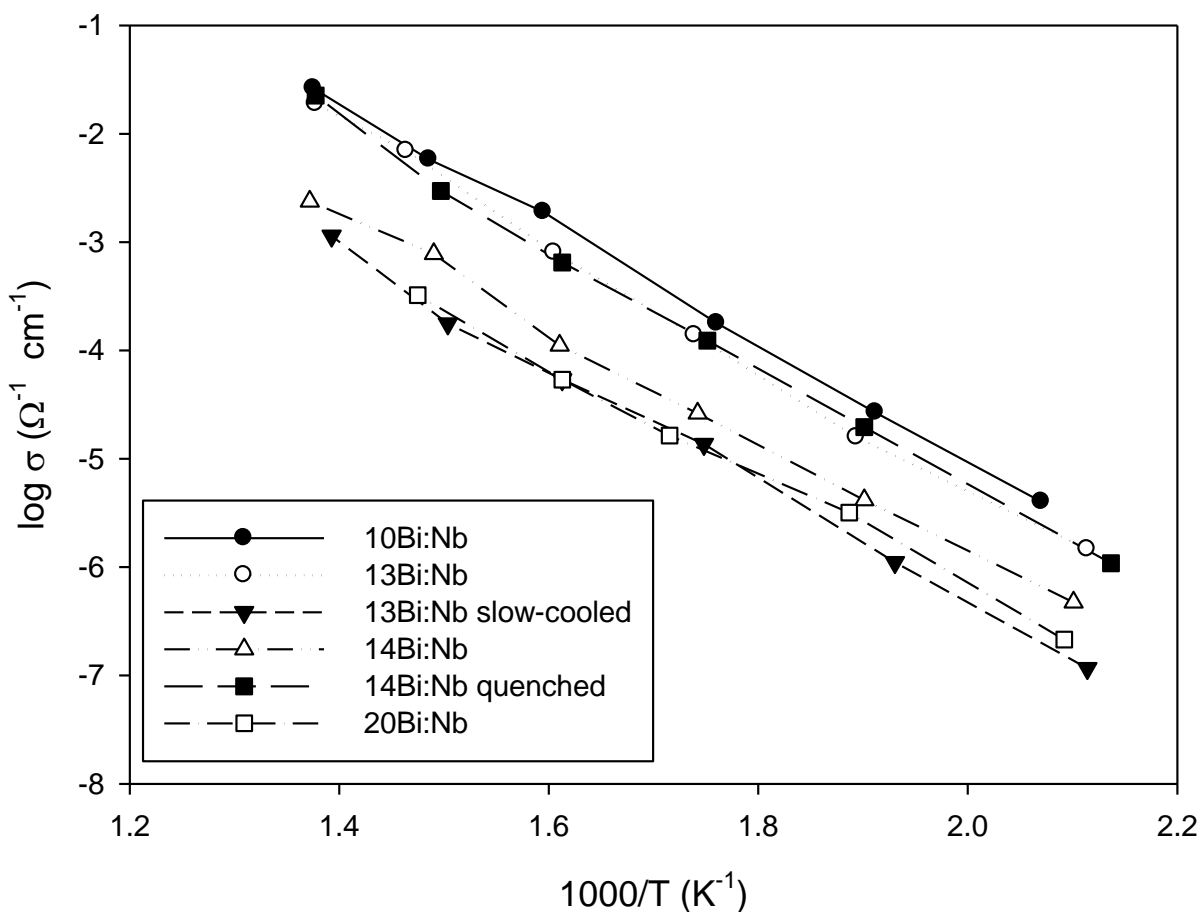


Figure 6.18 Arrhenius plots of conductivity determined by impedance spectroscopy for $\text{Bi}_{10}\text{NbO}_{17.5}$, $\text{Bi}_{13}\text{NbO}_{22}$, slow-cooled $\text{Bi}_{13}\text{NbO}_{22}$, $\text{Bi}_{14}\text{NbO}_{23.5}$, quenched $\text{Bi}_{14}\text{NbO}_{23.5}$ and $\text{Bi}_{20}\text{NbO}_{32.5}$.

6.4 References

- 1 Castro, A.; Aguado, E.; Rojo, J. M.; Herrero, P.; Enjalbert, R.; Galy, J. *Mat. Res. Bull.* **33** (1998) 31
- 2 Ling, C. D.; Johnson, M. *J. Solid State Chem.* **177** (2004) 1838
- 3 Takahashi, T.; Iwahara, H. *Mat. Res. Bull.* **13** (1978) 1447
- 4 Shannon, R. D. *Acta. Cryst.* **A32** (1976) 751
- 5 Larson, A. C.; Von Dreele, R. B. *General Structure Analysis System (GSAS)* Los Almos National Laboratory, Los Almos, NM (1994)
- 6 Young, R. A. *The Rietveld Method* International Union of Crystallography, Oxford University Press (1993)
- 7 Abrahams, I.; Krok, F.; Wrobel, W.; Kozanecka-Szmigiel, A.; Chan, S. C. M.; *Solid State Ionics* **179** (2008) 2
- 8 Krok, F.; Abrahams, I.; Holdynski, M.; Kozanecka-Szmigiel, A.; Malys, M.; Struzik, M.; Liu, X.; Dygas, J. R. *Solid State Ionics* **179** (2008) 975
- 9 Battle, P. D.; Catlow, C. R. A.; Drennan, J.; Murray, A. D. *J. Phys. C* **16** (1983) L561
- 10 Available from Shapessoftware: <http://www.shapesoftware.com/>
- 11 Abrahams, I.; Kozanecka-Szmigiel, A.; Krok, F.; Wrobel, W.; Chan, S. C. M.; Dygas, J. R. *Solid State Ionics* **177** (2006) 1761

CHAPTER 7

Conclusions and Further Work

In order to develop new materials with high oxide ion conducting properties, sintered bulk samples of novel stabilised δ - Bi_2O_3 materials have been synthesised by conventional solid state reaction and their structure and oxide ion conduction properties examined. This thesis has reported the results of these investigations.

The previously reported material $\text{Bi}_{28}\text{Re}_2\text{O}_{49}$ prompted these investigations since new materials containing bismuth and small amounts of rhenium oxoanions could be synthesized. As a development of that work, further studies of the structural and conduction properties of other fluorite-related superstructures in the bismuth-rich portion of the Bi_2O_3 - Re_2O_7 phase diagram have been investigated, including the material of composition $\text{Bi}_9\text{ReO}_{17}$. However, during the course of this work the structure of $\text{Bi}_9\text{ReO}_{17}$ was described. Hence a complementary study of the structural characterisation of $\text{Bi}_9\text{ReO}_{17}$, together with the results of an examination of the local environments of the cations, is reported. The structure of $\text{Bi}_9\text{ReO}_{17}$ previously reported was confirmed using NPD and EXAFS data, with Re being present as Re(VII) in regular tetrahedral coordination. However, the local bismuth coordination was reappraised in this study and a model presented which more fully reflects the importance of a stereochemically active $6s^2$ lone pair of electrons on all Bi atoms. Four of the nine bismuth sites are best described as pyramidal BiO_3e , whereas the other five are trigonal bipyramidal BiO_4e . EXAFS data are consistent with this analysis, but demonstrate that the data are dominated by the shorter Bi-O distances. The local environments of the

cations are similar to those in $\text{Bi}_{12.5}\text{Er}_{1.5}\text{ReO}_{24.5}$ with rhenium adopting tetrahedral coordination forming ReO_4 clusters and dissimilar to the situation found in $\text{Bi}_{28}\text{Re}_2\text{O}_{49}$. Further investigations of this material demonstrate that in addition to a high temperature disordered face-centred cubic phase (space group $\text{Fm}\bar{3}\text{m}$, $a = 5.414(2)$ Å, formed upon quenching from 1073 K in liquid nitrogen), a high temperature disordered monoclinic phase also exists (formed upon quenching from 1073 K in air), derived as a monoclinic supercell based on a fluorite-related hexagonal subcell (space group $\text{R}\bar{3}\text{m}$, $a = 3.93(4)$, $c = 9.78(9)$ Å), where $a_{\text{supercell}} = 4(\sqrt{3}a_{\text{subcell}}/3)/\cos(\beta - 90^\circ)/\text{Å}$, $b_{\text{supercell}} = a_{\text{subcell}}/\text{Å}$, and $c_{\text{supercell}} = c_{\text{subcell}}/\text{Å}$. The monoclinic supercell was refined in space group $\text{P}2_1/\text{m}$, where $a = 9.789(2)$, $b = 3.9873(6)$, $c = 9.9979(5)$ Å, $\beta = 109.82(1)^\circ$. Both the ordered and disordered forms of $\text{Bi}_9\text{ReO}_{17}$ display relatively high oxide ion conductivity, with that of the disordered structures being 1-2 orders of magnitude higher over the temperature range studied, $473 \text{ K} < T < 673 \text{ K}$.

Solid state reactions between bismuth, rhenium and calcium were undertaken and the structure and physical properties of any single-phase products investigated. The structure and ionic conductivity of fluorite-related $\text{Bi}_6\text{Ca}_3\text{ReO}_{15.5}$ and $\text{Bi}_{10}\text{Ca}_5\text{ReO}_{23.5}$ were studied by neutron powder diffraction, X-ray powder diffraction, electron diffraction and impedance spectroscopy. $\text{Bi}_6\text{Ca}_3\text{ReO}_{15.5}$ formed a face-centred cubic ($\text{Fm}\bar{3}\text{m}$) fluorite-related structure ($a = 5.416$ Å), and $\text{Bi}_{10}\text{Ca}_5\text{ReO}_{23.5}$ a body-centred cubic ($\text{I}\bar{4}3\text{d}$) material ($a = 21.940$ Å) that is a $4 \times 4 \times 4$ superstructure of the $\text{Bi}_6\text{Ca}_3\text{ReO}_{15.5}$ phase. It was revealed that upon quenching of $\text{Bi}_{10}\text{Ca}_5\text{ReO}_{23.5}$ from 1073 K in air, a face-centred cubic material was formed, refined in space group $\text{Fm}\bar{3}\text{m}$, where $a = 5.4890(1)$ Å. The onset phase transition temperature was determined using DTA to be 983 K, and was confirmed by variable temperature XPD to relate to the structural change from bcc to fcc. Annealing of $\text{Bi}_{10}\text{Ca}_5\text{ReO}_{23.5}$ at 773 K was shown to

induce a structural change of the material, and after 500 h a transition to a structure related to that of air quenched $\text{Bi}_9\text{ReO}_{17}$ became apparent, composing a monoclinic supercell based on a hexagonal subcell. Data were refined in space group $P2_1/m$, where $a = 9.4142(8)$, $b = 3.8129(3)$, $c = 9.5397(7)$ Å, $\beta = 109.730(4)^\circ$. All materials were shown to display good oxide ion conductivity, having activation energies $E_a = 0.97$ eV, $E_a = 1.02$ eV, $E_a = 0.95$ eV and $E_a = 0.95$ eV for $\text{Bi}_6\text{Ca}_3\text{ReO}_{15.5}$, $\text{Bi}_{10}\text{Ca}_5\text{ReO}_{23.5}$, quenched $\text{Bi}_{10}\text{Ca}_5\text{ReO}_{23.5}$ and annealed $\text{Bi}_{10}\text{Ca}_5\text{ReO}_{23.5}$, respectively.

Two previously unreported isostructural doped calcium bismuth oxide materials, $\text{Bi}_{20}\text{Ca}_7\text{NbO}_{39.5}$ and $\text{Bi}_{10.75}\text{Ca}_{4.375}\text{GaO}_{22}$, which have monoclinically distorted superstructures of the fluorite-related hexagonal subcell are also discussed in this thesis. The structure of these phases along with oxide ion conductivity data are reported by means of XPD, NPD and impedance measurements. As for monoclinic quenched $\text{Bi}_9\text{ReO}_{17}$, the structure was derived as a monoclinic supercell based on a fluorite - related hexagonal subcell, where $a_{\text{supercell}} = 4(\sqrt{3} a_{\text{subcell}} / 3) / \cos(\beta - 90^\circ) / \text{\AA}$, $b_{\text{supercell}} = a_{\text{subcell}} / \text{\AA}$, and $c_{\text{supercell}} = c_{\text{subcell}} / \text{\AA}$. The monoclinic supercell was refined in space group $P2_1/m$, where $a = 9.3334(4)$, $b = 3.7956(1)$, $c = 9.6195(3)$ Å, $\beta = 110.101(2)^\circ$ for $\text{Bi}_{20}\text{Ca}_7\text{NbO}_{39.5}$ and $a = 9.3293(3)$, $b = 3.7943(1)$, $c = 9.6136(2)$ Å, $\beta = 110.084(2)^\circ$ for $\text{Bi}_{10.75}\text{Ca}_{4.375}\text{GaO}_{22}$. Thermal stability studies were also undertaken, with results concluding that these materials remained stable after prolonged periods at 773 K. High temperature structural studies of $\text{Bi}_{20}\text{Ca}_7\text{NbO}_{39.5}$ revealed that, as for $\text{Bi}_9\text{ReO}_{17}$, two different high temperature forms exist: a phase formed upon quenching $\text{Bi}_{20}\text{Ca}_7\text{NbO}_{39.5}$ from 1073 K in air to form a simpler monoclinic structure, yet remaining in space group $P2_1/m$, where $a = 9.382(5)$, $b = 3.807(3)$, $c = 9.597(6)$ Å, $\beta = 110.10(2)^\circ$; and a face-centred cubic phase formed upon quenching $\text{Bi}_{20}\text{Ca}_7\text{NbO}_{39.5}$ from 1073 K in liquid nitrogen (space group $\text{Fm}\bar{3}m$, $a = 5.476(2)$ Å). DTA

results from $\text{Bi}_{20}\text{Ca}_7\text{NbO}_{39.5}$ revealed the onset phase transition temperature to be 1011 K. This was confirmed by variable temperature XPD to relate to the structural change from monoclinic to fcc. All materials were shown to display good oxide ion conductivity, with the values for the quenched monoclinic and fcc materials being slightly higher. Activation energies were $E_a = 1.19$ eV, $E_a = 1.12$ eV, $E_a = 1.11$ eV and $E_a = 0.85$ eV for $\text{Bi}_{10.75}\text{Ca}_{4.375}\text{GaO}_{22}$, $\text{Bi}_{20}\text{Ca}_7\text{NbO}_{39.5}$, fcc quenched $\text{Bi}_{20}\text{Ca}_7\text{NbO}_{39.5}$ and monoclinic quenched $\text{Bi}_{20}\text{Ca}_7\text{NbO}_{39.5}$, respectively.

An investigation into the Bi-Nb-O solid solution range was also explored, reporting a face-centred cubic solid solution range beyond that previously identified. Lattice parameters were shown to range from $a = 5.506(2)$ Å for $\text{Bi}_6\text{NbO}_{11.5}$ to $a = 5.532(4)$ Å for $\text{Bi}_{13}\text{NbO}_{22}$ in space group $\text{Fm}\bar{3}\text{m}$, displaying an increasing trend in lattice parameter with increasing Bi content as the larger bismuth is replacing the significantly smaller niobium. The results show that when the niobium dopant concentration is decreased further, beyond the cubic solid solutions range, a group of materials with tetragonal symmetry (space group I4/mmm) are formed with a structure related to the fcc structure of the more niobium rich phase, whereby $a = a_{\text{fcc}}/\sqrt{2}$ Å and $c = a_{\text{fcc}}$ Å. Lattice parameters ranged from $a = 3.873(2)$ Å and $c = 5.576(3)$ Å for $\text{Bi}_{14}\text{NbO}_{23.5}$ to $a = 3.8661(8)$ Å and $c = 5.601(1)$ Å for $\text{Bi}_{20}\text{NbO}_{32.5}$, with an expectant increase in c parameter with increasing Bi content as the larger Bi is replacing the smaller Nb, yet decrease in a parameter. The boundaries of the fcc-tetragonal solid solution range are shown to be partially dependant on cooling conditions, in that slow-cooling $\text{Bi}_{13}\text{NbO}_{22}$ formed a tetragonal cell ($a = 3.879(2)$ Å and $c = 5.571(4)$ Å) as for the more Bi-rich materials, and quenched $\text{Bi}_{14}\text{NbO}_{23.5}$ produced a face-centred cubic material as for the lower Bi content materials ($a = 5.536(2)$ Å). Investigations on $\text{Bi}_{14}\text{NbO}_{23}$ by DTA revealed the onset phase transition temperature to be 846 K. This was confirmed by variable

temperature XPD to relate to the structural change from tetragonal to fcc. All materials were shown to display excellent oxide ion conductivity, with that of the face-centred cubic materials being slightly better than that of the tetragonal, signifying that the overall mechanism for movement of O^{2-} ions through the oxygen sublattice is different for the two phases, and that the pathway for ionic conduction is less complicated in the simpler fcc structure.

The research undertaken in this thesis demonstrates the possibility to form $\delta\text{-Bi}_2\text{O}_3$ related materials, stabilised by Ca, Ga, Nb and Re. Further work is required to achieve a better understanding of these complex materials. Specifically, further variable temperature experiments are required for all materials discussed to identify structural changes that occur on cooling. In particular, DTA revealed that for quenched $\text{Bi}_9\text{ReO}_{17}$ materials, structural changes appear to occur upon cooling via a two-step mechanism. The structure of this intermediate would be of interest. High temperature NPD data would be useful to assist structure elucidation as it is difficult to locate oxygen atoms in the presence of heavy bismuth by XPD. For this reason, NPD data would also be advantageous for the Bi-Nb-O materials investigated. Additionally, XAFS measurements would be of interest for these materials to confirm the oxidation state of niobium. Energy calculations for oxide migration would be beneficial for all materials investigated in this research. This would show the effect of atomic positions on conduction and allow determination of favourable energy pathways. Further ratios of Bi:Ca:Ga/Nb/Re could be investigated in an attempt to synthesise other single phase materials, which may prove to have different structures. It may also be worthwhile examining the substitution of alternative oxoanions into these systems, such as SO_4^{2-} for ReO_4^- , whilst substituting F^- for O^{2-} to balance the charge. Furthermore, it is possible that new materials could be synthesised using a combination of different oxoanions. There are consequently

considerable supplementary investigations required as a continuation of the work reported in this thesis.

Publications Arising from this Thesis

As a result of work presented in this thesis, the following papers have been produced,

The Ionic Conductivity and Local Environment of Cations in $\text{Bi}_9\text{ReO}_{17}$.

M. Thompson, T. Herranz, B. Santos, J. F. Marco, F. J. Berry and C. Greaves.

J. Solid State Chemistry, in press.

The Structure and Ionic Conductivity of Two New Fluorite Related Bismuth Calcium Rhenium Oxides, $\text{Bi}_6\text{Ca}_3\text{ReO}_{15.5}$ and $\text{Bi}_{10}\text{Ca}_5\text{ReO}_{23.5}$.

M. Thompson, J. Hadermann and C. Greaves.

Solid State Ionics, submitted for publication.

The Structure and Ionic Conductivity of the Fluorite-Related Isostructural Materials $\text{Bi}_{20}\text{Ca}_7\text{NbO}_{39.5}$, $\text{Bi}_{10.75}\text{Ca}_{4.375}\text{GaO}_{22}$ and Quenched $\text{Bi}_9\text{ReO}_{17}$.

M. Thompson and C. Greaves.

Solid State Ionics, submitted for publication.